In Search of Lost Time:

Development of Rapid Magnetic Resonance Methods to Probe Time-Varying Diffusion

Teddy Xuke Cai

Linacre College

University of Oxford

A thesis submitted for the degree of

Doctor of Philosophy

Trinity 2023

Acknowledgements

This thesis is a result of fruitful collaboration between many individuals, and to all of them I owe my thanks.

First and foremost I would like to thank my supervisors Dr. Peter Basser and Prof. Karla Miller. Your advice and guidance are deeply appreciated, and you both have been an invaluable wellspring of knowledge. Learning from you and others about diffusion MR has been a pleasure. Peter I would like to thank for welcoming me into his lab when I was, at the time, just a wide-eyed chemical engineering student, and for entertaining some of my wilder theories and proposed methods. Karla I would like to thank for giving me the opportunity to study at Oxford as part of this unique, joint program, through which I have met a wonderful group of students and researchers across the pond, so to speak.

A special thanks is owed to my closest collaborators Drs. Nathan Williamson, Rea Ravin, and Mohamed Tachrount, from whom I have learned a great deal about MR and biological experimentation, and who have collectively helped to save innumerable hours of potential troubleshooting. The experiments throughout this thesis would not have been possible without your help. In particular, Nathan's deep knowledge of practical MR experimentation on the PM-10 and Rea's expertise in neurobiology were critical in our investigations of exchange in mouse spinal cord. Mohamed's mastery of pulse sequence programming was an essential part of getting the *in vivo* experiments up and running.

Additionally, thanks are owed to various collaborators and colleagues with whom I have had stimulating and useful discussions: Drs. Dan Benjamini, Michal (Miki) Komlosh, Alexandru Avram, Velencia Witherspoon, Magdoom Kulam, and Aaron Hess, as well as Julian Rey.

I also would like to extend my thanks to the administrators Drs. Katie Stagliano and Kara Rothberg of the NIH-Oxford Cambridge Scholars program, which provided part of the funding for my studies.

Abstract

Diffusion MR methods are a powerful means to probe tissue microstructural features. Most diffusion MR methods and signal representations, however, do not explicitly acknowledge the inherent time-dependence of diffusion, although it is precisely this time-dependence which reveals the characteristics of the microstructure. More advanced diffusion MR methods have emerged to study time-dependent phenomena. Diffusion exchange spectroscopy (DEXSY) measures exchange between diffusive microenvironments, and temporal diffusion spectroscopy (TDS) measures the time-dependence of diffusion directly. These methods, while powerful, have various limitations, particularly in their high data requirement.

This thesis details the development and validation of rapid, information-rich methods to probe exchange and time-dependent diffusion and which improve upon DEXSY and TDS. To improve upon DEXSY, a rapid sub-sampling scheme called the 'curvature' method is developed to isolate exchange from other effects such as restriction, while requiring as few as 5 total acquisitions. The speed of the method enables the study of exchange in near real-time and also permits the study of *distributed* exchange times, revealing new insights about the nature of exchange in tissue. To improve upon TDS, a single-shot method is developed to probe diffusion over sub-millisecond timescales while also avoiding off-resonance effects, called the static gradient, time-incremented echo train acquisition (SG-TIETA).

The methods are tested using a tabletop, permanent magnet system with a strong static gradient as well as pre-clinical scanners capable of imaging. Studies of simple liquids, tissue phantoms, yeast, *ex vivo* neonatal mouse spinal cord under various perturbations, and *in vivo* mice are presented to support the feasibility and utility of the developed methods. Of note, the exchange time is found to be linked to steady-state, metabolic activity in tissue, representing a potentially useful biomarker. Overall, novel diffusion MR methods sensitive to exchange and time-dependent diffusion are developed and validated in a series of pre-clinical experiments.

Contents

List of Figures *vi*

1 Introduction **1**
1.1 Motivation . . . 1
1.2 Thesis outline . . . 3

2 Diffusion Magnetic Resonance **5**
2.1 Principles of diffusion MR . . . 6
2.1.1 Precession, excitation, and relaxation . . . 6
2.1.2 Field inhomogeneity, echoes, and coherence selection . . . 12
2.1.3 Imaging . . . 22
2.1.4 Working with permanent magnets . . . 26
2.2 Diffusion MR signal modelling . . . 28
2.2.1 Free diffusion and the *b*-value . . . 28
2.2.2 The Gaussian phase approximation . . . 29
2.2.3 Limiting regimes of signal behavior . . . 37
2.2.4 Time-dependent diffusion . . . 39
2.3 Diffusion in neural tissue . . . 42
2.3.1 Compartment models . . . 42
2.3.2 Permeability and exchange . . . 44

3 Rapid Isolation of Exchange **50**
3.1 Introduction . . . 50
3.1.1 Chapter outline and related works . . . 51
3.2 Diffusion Exchange Spectroscopy (DEXSY) . . . 53
3.2.1 The DEXSY pulse sequence . . . 54
3.2.2 Conventional DEXSY analysis . . . 56
3.3 The 'curvature' method . . . 58
3.3.1 The bi-exponential signal model . . . 58
3.3.2 Validation on a tissue phantom . . . 62
3.3.3 Correspondence in fixed spinal cord . . . 66
3.3.4 Normalization approaches . . . 76
3.4 Disentangling restriction and exchange . . . 81
3.4.1 Signal scaling for non-Gaussian diffusion . . . 81
3.4.2 Two-compartment model with restriction . . . 85
3.4.3 Artifacts in diffusion-diffusion spectra due to restriction . . . 87
3.4.4 Measuring restriction from curvature . . . 90
3.5 Comparison to 'Filter Exchange' methods . . . 92

4 Distributed Exchange Times and Activity **97**
4.1 Introduction . . . 97
4.1.1 Chapter outline and related works . . . 99
4.2 Evidence for active exchange in live tissue . . . 101
4.2.1 Activation energies in live vs. fixed tissue . . . 101
4.2.2 Suppression of the sodium-potassium pump . . . 105
4.2.3 Oxygen-glucose deprivation model . . . 106
4.3 Measuring a distribution of exchange times . . . 109
4.3.1 Signal modelling . . . 110
4.3.2 Phase cycling in DEXSY experiments . . . 111
4.3.3 Distributions in live tissue . . . 116
4.4 Effects on the distribution under perturbations . . . 124
4.4.1 Temperature variation . . . 124
4.4.2 Suppression of the sodium-potassium pump . . . 126
4.4.3 Tissue 'rundown' . . . 128
4.4.4 Fixation . . . 130
4.4.5 Osmolarity perturbation after ouabain . . . 132
4.5 Discussion . . . 136

5 Imaging of *In Vivo* Exchange in Mice **140**
5.1 Introduction . . . 140
5.1.1 Chapter outline and related works . . . 141
5.2 Pulsed gradient exchange imaging . . . 142
5.2.1 Stimulated echo DEXSY sequence . . . 142
5.2.2 Choosing experimental parameters . . . 144
5.2.3 Analysis pipeline . . . 149
5.3 Exchange contrast and parameter maps . . . 152
5.3.1 Apparent exchange contrast at a single mixing time . . . 152
5.3.2 Total exchange and exchange rate maps . . . 154
5.3.3 Repeatability . . . 161
5.4 Discussion . . . 166

6 Rapid measurement of sub-millisecond, time-dependent diffusion **174**
6.1 Introduction . . . 174
6.1.1 Chapter outline and related works . . . 177
6.2 Time-incremented echo train . . . 178
6.2.1 Avoiding off-resonances . . . 178
6.2.2 Estimating the instantaneous diffusivity . . . 184
6.3 Experimental findings . . . 188
6.3.1 Findings in simple liquids . . . 188
6.3.2 Findings in yeast . . . 194
6.4 Discussion . . . 197

7 Future Work and Conclusions **199**
7.1 Revisiting the 'curvature' method 199
7.2 Further experiments 203

A Additional derivations **208**

B DEXSY phase cycles **211**

C Difference maps *in vivo* **215**

List of Figures

2.1 Resonant excitation 10
2.2 Off-resonance pulse 14
2.3 Spin echo formation 15
2.4 Decomposing the effect of 90°- and 180° pulses 16
2.5 Decomposing the effect of off-resonant pulses 17
2.6 Gradient echoes 22
2.7 Echo planar imaging sequence 25
2.8 PM-10 NMR-MOUSE shematic 26
2.9 Pulse sequences and b-values 30
2.10 Calculation of cumulative gradient autocorrelation 36
2.11 Summary of diffusion regimes 47

3.1 DEXSY pulse sequences 55
3.2 DEXSY inverse Laplace transform 56
3.3 Contour maps for bi-exponential signal model 59
3.4 Glass capillary array tissue phantom 63
3.5 Curvature and exchange in glass capillary array phantom 64
3.6 Exchanging signal fraction images in glass capillary array phantom . 66
3.7 Technical drawing of a PM-10 NMR-MOUSE with spinal cord sample 67
3.8 Curvature and signal difference in fixed spinal cord 70
3.9 Full DEXSY spectra in fixed spinal cord 73
3.10 Curvature and exchange in fixed spinal cord 74
3.11 Normalization approaches in the curvature method 77
3.12 Diffusion data in spinal cord compared to theoretical models 83
3.13 Diffusion-diffusion spectra in the presence of restriction 88
3.14 Measuring restriction using the curvature method in fixed spinal cord 91
3.15 Comparison to FEXSY 93

4.1 Activation energies for exchange, diffusion in fixed vs. live spinal cord 104
4.2 Effect of ouabain over time in live spinal cord 106
4.3 Oxygen-glucose deprivation in live spinal cord 108

4.4 Simulated exchange time distributions 117
4.5 Floor removal in simulated exchange data 118
4.6 Floor removal in spinal cord data 119
4.7 Bi- vs. monoexponential fit of exchange signal 120
4.8 Repeatability of exchange time distributions in live spinal cord 122
4.9 Feasibility of sub-sampling mixing times 122
4.10 Distributions at different temperature in live spinal cord 125
4.11 Distributions with ouabain in live spinal cord 128
4.12 Distributions during tissue 'rundown' 129
4.13 Distributions in fixed vs. live spinal cord 131
4.14 Distributions with ouabain and sucrose live spinal cord 133

5.1 Pulsed gradient, stimulated echo DEXSY sequence 143
5.2 Exchange-weighted difference maps across *b*-values 146
5.3 Exchange-weighted difference maps across mixing times and *b*-values 148
5.4 Exchange contrast and structural images, *in vivo* 153
5.5 Total exchange and exchange time maps, *in vivo* 154
5.6 Fit to the slice mean 155
5.7 Exemplar fitting residuals 155
5.8 Fits to individual voxels 157
5.9 Scan-to-scan repeats for one animal 162
5.10 Scan-to-scan repeats for another animal 164

6.1 Static gradient, time-incremented echo train (SG-TIETA) sequence . 179
6.2 Simulated MSD and fit for instantaneous diffusivity using SG-TIETA . 187
6.3 Echo shapes for CPMG vs. SG-TIETA in 1-octanol 190
6.4 Zoomed SG-TIETA signal decay in 1-octanol 192
6.5 Pulse accuracy estimation in simple liquids 193
6.6 Instantaneous diffusivity measured in yeast 196

7.1 Weighting of the instantaneous diffusivity by the curvature method . 200

Preface

Declaration of the contributions of others

The work presented in this thesis was performed at two sites as part of the NIH-Oxford Cambridge Scholars Program and supervisory duties were shared between two groups:

- Section on Quantitative Imaging and Tissue Sciences, *Eunice Kennedy Shriver* National Institute of Child Health and Human Development, National Institutes of Health (NIH), Bethesda, MD, USA — supervised by Dr. Peter J. Basser
- Wellcome Centre for Integrative Neuroimaging, Oxford Centre for Functional MRI of the Brain (FMRIB), Nuffield Department of Clinical Neurosciences, University of Oxford, UK — supervised by Prof. Karla L. Miller with additional supervision by Dr. Mohamed Tachrount

The development of the theory, data analysis, and writing for all first-authored works was carried out by myself, while the experimental work and methodological development was carried out in collaboration with others. The experiments using a permanent magnet system, comprising Chapters 3, 4, and 6, were performed at the NIH in collaboration with Drs. Nathan H. Williamson and Rea Ravin, primarily. The *in vivo* experiments using a pre-clinical scanner, comprising Chapter 5, were performed at FMRIB in collaboration with Dr. Mohamed Tachrount. Each chapter containing novel results will begin with an outline detailing the relevant work(s) and contributions.

List of publications arising from or related to this thesis

The first-authored works and related co-authored works are listed here, in reverse chronological order within each category.

In preparation

- **Cai, T. X.**, Williamson, N. H., Basser, P. J., Miller, K. L.*, & Tachrount, M.* *In vivo* imaging of the apparent exchange rate in mice under AQP4 suppression using equally diffusion-weighted double diffusion encodings.

- **Cai, T. X.**, Williamson, N. H., Ravin, R., & Basser, P. J. Multiexponential analysis of exchange times in neural tissue reveals a bimodal distribution of distinct exchange processes.

First-authored journal articles

- **Cai, T. X.**, Williamson, N. H., Ravin, R., & Basser, P. J. (2022). Disentangling the effects of restriction and exchange with diffusion exchange spectroscopy. *Frontiers in Physics*, *10*, 805793.
- **Cai, T. X.**, Williamson, N. H., Witherspoon, V., Ravin, R., & Basser, P. J. (2021). A single-shot measurement of time-dependent diffusion over sub-millisecond timescales using static field gradient NMR. *The Journal of Chemical Physics*, *154*, 111105.
- [†]**Cai, T. X.**, Benjamini, D., Komlosh, M. E., Basser, P. J., & Williamson, N. H. (2018). Rapid detection of the presence of diffusion exchange. *Journal of Magnetic Resonance*, *297*, 17–22.

  [†]Published before the start of the degree. This work is included because the results are vital to the other works presented in this thesis. Furthermore, additional analyses are developed and presented here which significantly expand the original scope of the work and thus merit inclusion in this thesis.

Co-authored articles

- Williamson, N. H., Witherspoon, V., **Cai, T. X.**, Ravin, R., Horkay, F., & Basser, P. J. (2023). Low-field, high-gradient NMR shows diffusion contrast consistent with localization or motional averaging of water near surfaces. *Magnetic Resonance Letters*, *3*(2), 90–107.
- Williamson, N. H.[*], Ravin, R.[*], **Cai, T. X.**, Falgairolle, M., O'Donovan, M. J., & Basser, P. J. (2023) Magnetic Resonance measurements of steady-state transmembrane water exchange detect cellular activity and homeostasis in central nervous system tissue. *PNAS Nexus*, *2*(3), pgad056.

  [*]Indicates equal contribution
- Williamson, N. H., Ravin, R., **Cai, T. X.**, Benjamini, D., Falgairolle, M., O'Donovan, M. J., & Basser, P. J. (2020) Real-time measurement of diffusion exchange rate in biological tissue. *Journal of Magnetic Resonance*, *317*, 106782.

- Williamson, N. H., Ravin, R., Benjamini, D., Merkle, H., Falgairolle, M., O'Donovan, M. J., Blivis, D., Ide, D., **Cai, T. X.**, Ghorashi, N. S., Bai, R., & Basser, P. J. (2019). Magnetic resonance measurements of cellular and sub-cellular membrane structures in live and fixed neural tissue. *eLife*, *8*, e51101.

Conference proceedings

- **Cai, T. X.**, Williamson, N. H., Ravin, R., & Basser, P. J. Multiexponential analysis of diffusion exchange times reveals a distinct exchange process associated with metabolic activity. (2023, June). *Proceedings of the 32nd Annual Meeting of the ISMRM*, Toronto, Canada, Abstract #5017.

- **Cai, T. X.**, Williamson, N. H., Ravin, R., & Basser, P. J. Isolating restriction and exchange in gray matter using double and single diffusion encodings with equal diffusion weighting. (2022, June). [Oral Presentation]. *Proceedings of the 31st Annual Meeting of the ISMRM*, London, England, U.K., Abstract #252.

- **Cai, T. X.**, Williamson, N. H., Witherspoon, V. W., Ravin, R., & Basser, P. J. Single-shot measurement of sub-millisecond, time-dependent diffusion using optimized, unequal pulse spacings in a static field gradient. (2021, May). *Proceedings of the 30th Annual Meeting of the ISMRM*, Online, Abstract #2468.

Patents

- Ravin, R., Williamson, N. H., **Cai., T.X.**, & Basser, P. J. Methods of determining homeostatic perturbations. International Patent Application No. PCT/US2022/-049542. Filed on 2022-11-10.

1 Introduction

1.1 Motivation **1**
1.2 Thesis outline **3**

1.1 Motivation

Diffusion magnetic resonance (MR) probes molecular displacements. In systems with a confined fluid that is detectable via MR — namely, water within the membranes of biological tissue — diffusion MR provides a means to non-invasively probe the surrounding microenvironment. Molecules diffusing within a confined space interact with and "[feel] the boundary" [1]. The confining structure of the microenvironment leads to a deviation from Brownian motion, which manifests itself as a non-linear time-dependence in the ensemble-averaged, net mean-squared-displacement. This time-dependence is rich in information. As such, diffusion MR methods have the potential to probe microstructural features such as overall geometry [2, 3], the surface-to-volume ratio [4–6], and permeability [7–10]. In practice, however, such features are difficult to measure and more difficult still to disambiguate because of the highly degenerate nature of microstructural parameter estimation in diffusion MR. Historically, methods that measure a simple, apparent parameter such as an

isotropic diffusion coefficient [11, 12] or an anisotropic diffusion tensor [13] — thereby ignoring the inherent time-dependence of the diffusion MR signal — have sufficed to offer biomedical utility [12].

More advanced methods hope to realize the full potential of diffusion MR to characterize biological and especially neural tissue via the time-dependence of the diffusion process. Here, we consider two classes of advanced diffusion MR methods: (i) diffusion exchange measurements, which probe the exchange of molecules between compartments of differing mobility, and (ii) time-dependent diffusion measurements. Diffusion exchange and time-dependence are conventionally measured using diffusion exchange spectroscopy (DEXSY) [14] and temporal diffusion spectroscopy (TDS) [15–17], respectively. DEXSY and TDS can reveal contrasts or effects that are largely invisible to standard diffusion MR methods. For example, DEXSY or derivative methods have been used to discriminate porous breast cancer tissue [18] and to track the expression of membrane channels via their water co-transport [19]. TDS can resolve specific timescales and can, through iterative measurements, yield the time-dependence of the diffusion process. TDS has been shown to produce highly accurate geometric parameters such as microcapillary (mimicking axons) [20] and cell [21] diameters. However, both DEXSY and TDS have significant experimental limitations. Both methods require large amounts of data and, in the case of DEXSY, make non-physical modelling assumption(s). Thus, these methods have limited biological and clinical translatability, as well as generalizability in their proposed forms.

This thesis describes the author's work in developing novel variations of diffusion exchange and time-dependent diffusion measurements, with an emphasis on diffusion exchange methods. These methods aim to minimize the data requirement and maximize experimental sensitivity whilst making as few modelling assumptions as possible. To that end, novel data acquisition schemes, pulse sequences, and analysis methods are proposed. Results from non-living and living specimen acquired using tabletop magnets and pre-clinical MR imaging systems are presented to support the feasibility of these methods. Further, we make the case that these methods provide unique sensitivity and have the potential to serve as quantitative imaging biomarkers with clinical utility, once we establish that exchange is linked to metabolic activity.

In summary, this thesis aims to put forth time- and signal-efficient variations of exchange and time-dependent measurements which improve upon DEXSY and TDS and pave the way for further development and future applications.

1.2 Thesis outline

We introduce in **Chapter 2** the concepts underlying diffusion MR and MRI. Signal models and acquisition methods are described, with an emphasis on time-dependent models of the diffusion signal that can rigorously describe the effects of barriers. Neural tissue microstructure and the relevance of permeability are also discussed.

In **Chapter 3**, we propose a novel experimental protocol and modelling approach to rapidly measure exchange whilst isolating the measurement from other effects such as restriction. The method requires many-fold fewer data points than DEXSY and is, to our knowledge, the fastest possible such measurement. Data collected on a white-matter tissue phantom validate the approach. Findings in *ex vivo* neonatal mouse spinal cord using a permanent magnet system indicate that exchange may be very rapid in gray matter tissue, with residence times on the order of ~10 ms.

In **Chapter 4** we expand upon the findings in Chapter 3 by developing a method to measure *distributed* exchange times. We present findings which suggest the presence of multiple different exchange processes linked, perhaps, to passive diffusion and its interaction with active metabolism. Findings in *ex vivo* neonatal mouse spinal cord support the existence of a bimodal distribution of exchange times in tissue. Upon the suppression of metabolic activity using a sodium-potassium channel blocker, only the faster of the two exchange peaks is decreased, suggesting that metabolic activity is linked to a fast exchange process with an exchange time on the order of ~5 ms. These findings indicate that exchange may be a biomarker for tissue homeostasis (i.e., steady-state metabolic activity).

Chapter 5 describes preliminary efforts to translate the methods described in Chapters 3 – 4 to pre-clinical *in vivo* imaging. A bespoke pulsed gradient sequence and acquisition scheme is developed to measure exchange. Apparent exchange maps are produced for wild-type mice and compared within subjects and between subjects.

While repeatability in the parameter maps remains challenging, these results serve as a preliminary demonstration of the feasibility of pairing our method(s) with *in vivo* imaging. Avenues of future development are described.

In **Chapter 6**, we change course to the measurement of time-dependent diffusion. We propose a single echo-train approach under a static gradient, wherein the echo times are successively incremented to simultaneously probe many timescales and avoid off-resonance effects. Combined with the strong, static gradients available on a permanent magnet system, such an approach permits the measurement of sub-millisecond diffusion in potentially a single shot. Findings in simple liquids of different diffusivity demonstrate the avoidance of off-resonance effects. Findings in yeast suspensions are also presented.

Finally, in **Chapter 7** we discuss future directions and synthesize some of the concepts previously presented. Of note, we point out that the exchange measurement can also be viewed as a time-dependent diffusion measurement, which provides a new perspective on exchange measurement.

2

Diffusion Magnetic Resonance

2.1 Principles of diffusion MR 6
2.1.1 Precession, excitation, and relaxation 6
2.1.2 Field inhomogeneity, echoes, and coherence selection 12
2.1.3 Imaging 22
2.1.4 Working with permanent magnets 26
2.2 Diffusion MR signal modelling 28
2.2.1 Free diffusion and the *b*-value 28
2.2.2 The Gaussian phase approximation 29
2.2.3 Limiting regimes of signal behavior 37
2.2.4 Time-dependent diffusion 39
2.3 Diffusion in neural tissue 42
2.3.1 Compartment models 42
2.3.2 Permeability and exchange 44

This chapter provides background for the theoretical and experimental advances presented in later chapters. The contributions in this thesis build upon conventional acquisition and analysis of diffusion MR data as applied to the study of neural tissue. As such, attention is given to parsing the differences between model representations of the diffusion MR signal. In addition, because the experiments in this work span disparate MR systems — from low-field spectroscopy to rapid, high-field imaging — hardware differences and pulse sequence development are detailed. This chapter includes: (1) an overview of MR theory and methodology, (2) empirical

and analytical models of the diffusion MR signal, and (3) a discussion of diffusion and permeability in neural tissue.

2.1 Principles of diffusion MR

Nuclear magnetic resonance encompasses experimental methods that manipulate spin-bearing nuclei oriented within a constant magnetic field. The physical principles of the MR phenomenon can be divided into precession, excitation, and relaxation. Field inhomogeneities must also be considered in MR experimentation and can be addressed using various experimental techniques such as echo formation. The downstream methods of magnetic resonance imaging (MRI) and diffusion MR/MRI use spatiotemporal magnetic field gradients to sensitize the one-dimensional signal to location and molecular mobility, respectively. To limit the scope of this section, we will focus only on signal arising from protons (^{1}H) on water and on aspects relevant to diffusion MR. The content of this section is adapted primarily from Ref. [22].

2.1.1 Precession, excitation, and relaxation

Atomic nuclei have intrinsic spin $\mathbf{S}$ and an associated magnetic dipole moment $\boldsymbol{\mu}$:

$$\boldsymbol{\mu} = \gamma \mathbf{S}, \tag{2.1.1}$$

where γ is the gyromagnetic ratio. Here, we consider the spin-$\frac{1}{2}$ nucleus ^{1}H for which $\gamma = 2.6752 \times 10^8$ rad/s/T, where T denotes Teslas. We henceforth refer to ^{1}H nuclei as 'spins'.

The Zeeman effect

When placed in a constant, external magnetic field $\mathbf{B}_0$, spins experience the Zeeman effect. Spins interact with $\mathbf{B}_0$ according to the Hamiltonian:

$$H = -\boldsymbol{\mu} \cdot \mathbf{B}_0, \tag{2.1.2}$$

resulting in energy splitting with eigenvalues

$$E_\pm = \pm \hbar \gamma B_0 / 2, \tag{2.1.3}$$

where E_+ and E_- correspond to the z-component of the spin dipoles being parallel or anti-parallel to $\mathbf{B}_0$, respectively, $\hbar$ is the reduced Planck constant, and B_0 is the magnitude of $\mathbf{B}_0$.

The above holds for singular spins near absolute zero temperature. In practical NMR experimentation, however, an ensemble of spins undergoing rapid thermal motion is measured with total magnetization $\mathbf{M} = \sum \boldsymbol{\mu}$. Spins may take any orientation under such motion and the spin eigenstates (2.1.3) serve as a basis. The probability of each eigenstate can be considered using classical Boltzmann statistics:

$$P(E_j) = \frac{\exp\left(E_j/k_BT\right)}{\sum_j \exp\left(E_j/k_BT\right)}, \tag{2.1.4}$$

where j indexes the eigenstates, k_B is Boltzmann's constant, and T is the absolute temperature. The difference in eigenstate probabilities is

$$P(E_+) - P(E_-) = \frac{\exp\left(-\hbar\omega_0/2k_BT\right) - \exp\left(\hbar\omega_0/2k_BT\right)}{\exp\left(-\hbar\omega_0/2k_BT\right) + \exp\left(\hbar\omega_0/2k_BT\right)} = \tanh\left(-\frac{\hbar\gamma B_0}{2k_BT}\right). \tag{2.1.5}$$

To simplify further, note that the energy splitting ($\Delta E = \hbar\gamma B_0$) is very small compared to thermal motion (k_BT) at room temperature for any attainable B_0 (i.e., the Curie regime). In this regime, $\tanh(x) \approx x$, yielding M_0, the approximate amplitude of the z-component of $\mathbf{M}$:

$$M_0 \approx \frac{\rho\hbar^2\gamma B_0}{4k_BT}, \tag{2.1.6}$$

where ρ is the number of spins per unit volume, a.k.a. the proton density. Thus, the Zeeman effect produces a net magnetization of magnitude M_0 along $\mathbf{B}_0$.

The Zeeman effect also results in precession of $\mathbf{M}$ about $\mathbf{B}_0$. This can be seen by taking a semi-classical point of view, wherein the magnetic field $\mathbf{B}$ exerts a torque on spins with angular momentum $\boldsymbol{\mu}/\gamma$:

$$\frac{d(\boldsymbol{\mu}/\gamma)}{dt} = \boldsymbol{\mu} \times \mathbf{B}. \tag{2.1.7}$$

Summing over spins and multiplying by γ,

$$\frac{d\mathbf{M}}{dt} = \gamma \mathbf{M} \times \mathbf{B}, \tag{2.1.8}$$

or recast in matrix form:

$$\frac{d}{dt}\begin{bmatrix} M_x \\ M_y \\ M_z \end{bmatrix} = \begin{bmatrix} 0 & \gamma B_z & -\gamma B_y \\ -\gamma B_z & 0 & \gamma B_x \\ \gamma B_y & -\gamma B_x & 0 \end{bmatrix} \begin{bmatrix} M_x \\ M_y \\ M_z \end{bmatrix}. \tag{2.1.9}$$

Note that the above semi-classical description, in which the ensemble magnetization $\mathbf{M}$ is represented as a vector, is equivalent to the quantum description for un-coupled, spin-$\frac{1}{2}$ systems [22, 23]. As such, the following treatment(s) may proceed classically without reservation. For $\mathbf{B} = B_0\hat{\mathbf{k}}$ along the z-axis,

$$\frac{d}{dt}\begin{bmatrix} M_x \\ M_y \\ M_z \end{bmatrix} = \begin{bmatrix} 0 & \gamma B_0 & 0 \\ -\gamma B_0 & 0 & 0 \\ 0 & 0 & 0 \end{bmatrix} \begin{bmatrix} M_x \\ M_y \\ M_z \end{bmatrix}, \tag{2.1.10}$$

and

$$\frac{dM_x}{dt} = \gamma B_0 M_y \tag{2.1.11a}$$

$$\frac{dM_y}{dt} = -\gamma B_0 M_x. \tag{2.1.11b}$$

To solve for the evolution $\mathbf{M}(t)$, it is convenient to consider separately the longitudinal (z) and transverse (xy-plane) components. Writing the transverse component of $\mathbf{M}$ as a complex sum,

$$M_{xy} = M_x + iM_y, \tag{2.1.12}$$

we can re-write (2.1.11) as

$$\frac{dM_{xy}}{dt} = -i\gamma B_0 M_{xy}, \tag{2.1.13}$$

with solution:

$$M_{xy}(t) = M_{xy}(0)\exp\left(-i\gamma B_0 t\right). \tag{2.1.14}$$

Therefore, the transverse magnetization M_{xy} precesses about $\mathbf{B}_0$ (clockwise) at the Larmor frequency of

$$\omega_0 = \gamma B_0. \tag{2.1.15}$$

For typically achievable B_0 values (ranging from $0.05-28$ T), the Larmor frequency ω_0 lies in the radiofrequency (RF) regime (≈ 2 MHz to 1.2 GHz).

In summary, the Zeeman effect causes (i) any transverse magnetization M_{xy} to precess about $\mathbf{B}_0$ at the Larmor frequency $\omega_0 = \gamma B_0$ and (ii) produces a net magnetization M_0 along $\mathbf{B}_0$ proportional to the field magnitude B_0 (2.1.6). This net magnetization can be manipulated via excitation, providing a means to probe the spin ensemble.

Resonant excitation

Resonant excitation occurs when a magnetic field transverse to the longitudinal axis, $\mathbf{B}_1$, is applied at the Larmor frequency using electromagnetic coil(s). This field can be expressed as

$$\mathbf{B}_1(t) = B_1 \cos(\omega_0 t)\,\hat{\mathbf{i}} - B_1 \sin(\omega_0 t)\,\hat{\mathbf{j}}. \tag{2.1.16}$$

The total field becomes

$$\mathbf{B}(t) = B_1 \cos(\omega_0 t)\,\hat{\mathbf{i}} - B_1 \sin(\omega_0 t)\,\hat{\mathbf{j}} + B_0\,\hat{\mathbf{k}}, \tag{2.1.17}$$

and

$$\frac{d}{dt}\begin{bmatrix} M_x \\ M_y \\ M_z \end{bmatrix} = \begin{bmatrix} 0 & \omega_0 & \omega_1 \sin(\omega_0 t) \\ -\omega_0 & 0 & \omega_1 \cos(\omega_0 t) \\ -\omega_1 \sin(\omega_0 t) & -\omega_1 \cos(\omega_0 t) & 0 \end{bmatrix}\begin{bmatrix} M_x \\ M_y \\ M_z \end{bmatrix}, \tag{2.1.18}$$

where $\omega_1 = \gamma B_1$. With initial condition $\mathbf{M}(t=0) = M_0\,\hat{\mathbf{k}}$, this solves to [22]:

$$M_{xy}(t) = M_0 \sin(\omega_1 t) \exp(-i\gamma B_0 t) \tag{2.1.19a}$$

$$M_z(t) = M_0 \cos(\omega_1 t). \tag{2.1.19b}$$

The application of an excitation field $\mathbf{B}_1$(t) — called an RF pulse — tips the equilibrium longitudinal magnetization M_0 into the transverse plane by a 'flip' angle determined by the duration, amplitude, and shape of the pulse. For a hard, rectangular pulse of duration τ_p, the flip angle α is given by

$$\alpha = \frac{180^\circ}{\pi} \cdot \omega_1 \tau_p, \tag{2.1.20}$$

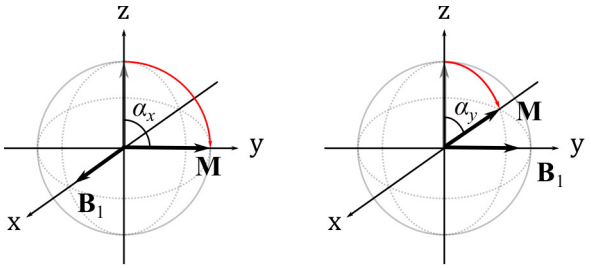

Figure 2.1: In the rotating frame of reference with ω_0, **M** rotates clockwise about $\mathbf{B}_1$ by a flip angle α. (left) For $\mathbf{B}_1$ along the $+x$-axis, **M** rotates in the yz-plane towards $+y$. (right) For $\mathbf{B}_1$ along the $+y$ axis, **M** rotates in the xz-plane towards $-x$. Flip angles are denoted by α sub-scripted with the axis of $\mathbf{B}_1$. Flip angles of $\alpha = 90°$ are illustrated.

for $\gamma = 2.6752 \times 10^8$ rad/s/T. More generally, α is given by the integral of the envelope of the pulse:

$$\alpha = \frac{180°}{\pi} \cdot \gamma \int_0^{\tau_p} B_1(t)dt. \tag{2.1.21}$$

A flip angle of 90° produces the maximal $M_{xy} = M_0$. Following the RF pulse, signal is detected as an electromotive force induced in the pickup or receive coil by the precessing transverse magnetization [24]. This 'transmit-receive' paradigm forms the basis of signal formation and measurement in MR.

From now on, we will assume that the transmission and receiver frequencies are the same and can thereby operate in a frame of reference rotating with ω_0 such that (2.1.19) becomes

$$M_{xy}(t) = M_0 \sin(\omega_1 t) \tag{2.1.22}$$

The x- and y-components no longer refer to spatial orientations but to a *phase* relative to the on-resonance signal. Typically, the detected signal is mixed with two reference signals that are 90° out-of-phase to separate the real and imaginary parts of M_{xy}. This is known as quadrature detection. In this frame, **M** rotates about a stationary $\mathbf{B}_1$ by the flip angle α, as illustrated in Fig. 2.1, in which $\mathbf{B}_1$ is oriented along $+x$ or $+y$.

As shown in the figure, pulses can also be applied about different axes by manipulating the phase of the components of $\mathbf{B}_1$. Pulses are typically denoted by the axis about which they induce rotation, called a pulse phase (e.g., $90°_x$). The first pulse creates a frame of reference and is conventionally defined to be along $+x$,

inducing a rotation of **M** from $+z$ towards $+y$. We will use this convention throughout. Subsequent pulses may have a phase relative to the first pulse. Likewise, the detection or receiver phase can be specified, changing the axis along which the real part of M_{xy} is positive. Manipulation of pulse and receiver phase(s) is an important experimental tool for phase cycling, discussed in Sec. 2.1.2.

Finally, it is important to note that in practice, pulses are not purely sinusoidal, but have an envelope with an associated frequency spectrum via Fourier transform (i.e., bandwidth) over which they excite magnetization. For example, a Gaussian-shaped pulse will excite a Gaussian band and a hard, rectangular pulse will excite a sinc-shaped band.

Relaxation: The Bloch Equations

After excitation, the spin ensemble will interact with the surrounding environment, or 'lattice', and magnetization will relax back to thermal equilibrium: $M_z = M_0$. This 'spin-lattice' or longitudinal relaxation process is exponential with characteristic time T_1 [24]. Simultaneously, M_{xy} decays to 0 with characteristic 'spin-spin' relaxation time T_2. This spin-spin relaxation time differs from T_1 due to interactions between nearby spins. These interactions produce transient deviations from the Larmor frequency at the micro- to nano- spatial scales, resulting in loss of coherence. Thus, $T_2 \leq T_1$ in all practical applications. For pure liquids, relaxation is well-described by Bloembergen-Purcell-Pound theory [25].

In biological tissue, the mechanisms underlying relaxation are sophisticated, and no comprehensive model yet exists. We note, however, that relaxation rates will vary based on interactions with macromolecules and boundaries. Smaller structures produce more interactions with the boundary in the same period of time; this effect is called surface relaxivity and is proportional to the surface-to-volume ratio (S/V) of the structure [22, 26]. These effects shorten T_1 and T_2 compared to the pure liquid and vary depending on the local environment. As a result, different types of tissue may have different relaxivities, and relaxation rates provide an important source of tissue-type contrast in MR [27].

Altogether, precession, excitation, and the subsequent relaxation processes (within which, surface relaxivity and macromolecular interactions play a part) are described by the phenomenological Bloch equations [24]:

$$\frac{d\mathbf{M}}{dt} = \gamma \mathbf{M} \times \mathbf{B}_0 - \frac{M_x \hat{\mathbf{i}} + M_y \hat{\mathbf{j}}}{T_2} - \frac{M_z - M_0}{T_1} \hat{\mathbf{k}}. \tag{2.1.23}$$

Under the field in (2.1.17), one obtains:

$$\frac{d}{dt} \begin{bmatrix} M_x \\ M_y \\ M_z \end{bmatrix} = \begin{bmatrix} -\frac{1}{T_2} & 0 & \omega_1 \\ 0 & -\frac{1}{T_2} & \omega_1 \\ -\omega_1 & -\omega_1 & -\frac{1}{T_1} \end{bmatrix} \begin{bmatrix} M_x \\ M_y \\ M_z \end{bmatrix} + \begin{bmatrix} 0 \\ 0 \\ \frac{M_0}{T_1} \end{bmatrix}. \tag{2.1.24}$$

Looking at M_{xy} and M_z following some degree of excitation,

$$\frac{dM_{xy}}{dt} = \frac{M_{xy}}{T_2}, \tag{2.1.25a}$$

$$\frac{dM_z}{dt} = \frac{M_z - M_0}{T_1}. \tag{2.1.25b}$$

Thus, relaxation proceeds as follows:

$$\frac{M_{xy}(t)}{M_{xy}(0)} = \exp\left(\frac{-t}{T_2}\right) \tag{2.1.26a}$$

$$M_z(t) = M_0 - [M_0 - M_z(t)] \exp\left(\frac{-t}{T_1}\right), \tag{2.1.26b}$$

absent other signal evolution mechanisms.

2.1.2 Field inhomogeneity, echoes, and coherence selection

Additional mechanisms can affect the experimentally measured signal, however, necessitating a more detailed view. These mechanisms are a result of deviations from the Larmor frequency due to factors such as inhomogeneous $\mathbf{B}_0$ and $\mathbf{B}_1$ fields, among others. It is important to account for these effects and isolate the intended magnetization evolution by means of various experimental techniques — namely, echoes and coherence selection. As several of the results in this thesis involve novel coherence selection methods (Chapters 4, 6), a detailed treatment is given here.

$\mathbf{B}_0$ inhomogeneity and T_2^* dephasing

Inhomogeneities in the $\mathbf{B}_0$ field result in a loss of coherence between spins at the *macro*scale, accelerating the relaxation of M_{xy} beyond the intrinsic T_2. The experimentally observed T_2 is shorter, and is called T_2^*. This decay of M_{xy} with T_2^* is called free induction decay (FID). To describe the loss of coherence, we introduce the concept of phase accrual. A spin isochromat — i.e., a group of spins which precess at the same frequency, $\omega(t)$ — acquires a phase, $\phi(t) \in [0, 2\pi]$, of

$$\phi(t) = \int_0^t \Delta\omega(t')dt', \tag{2.1.27}$$

where $\Delta\omega(t) = \omega(t) - \omega_0$ is the offset from the Larmor frequency (in rad/s). The resulting loss of ensemble coherence is called dephasing. The dephasing of M_{xy} can be expressed as the expected value of $\phi(t)$ across isochromats:

$$\frac{M_{xy}(t)}{M_{xy}(0)} = \exp\left(\frac{-t}{T_2}\right)\mathbb{E}\left[\exp\left(i\phi(t)\right)\right] \tag{2.1.28}$$

Visually, dephasing is a spreading of the magnetization in the transverse plane.

$\mathbf{B}_1$ inhomogeneity and off-resonance

The signal may also be affected by imperfections in pulses, i.e., in the frequency they are applied (ω_1) and the resulting flip angle ($\alpha \propto \omega_1\tau_p$). If pulses are applied off-resonance ($\omega_1 \neq \omega_0$), then in the rotating frame, the magnetization does not rotate about $\mathbf{B}_1$ but rather about an effective field $\mathbf{B}_{\text{eff}}$,

$$\mathbf{B}_{\text{eff}} = \mathbf{B}_1 + \Delta\mathbf{B}, \tag{2.1.29}$$

where $\Delta\mathbf{B} = \gamma(\omega_0 - \omega_1)\hat{\mathbf{k}}$ is the field offset [22, 28]. Thus, a different trajectory is realized, as shown in Fig. 2.2. Off-resonance pulses result in smaller effective flip angles — i.e., some longitudinal magnetization remains — and M_{xy} also acquires a phase during the application of the pulse. The effect can be quantified by the angle θ between $\mathbf{B}_{\text{eff}}$ and $\Delta\mathbf{B}$, given by

$$\theta = \sin^{-1}\left(\frac{B_1}{B_{\text{eff}}}\right) = \tan^{-1}\left(\frac{B_1}{\Delta B}\right). \tag{2.1.30}$$

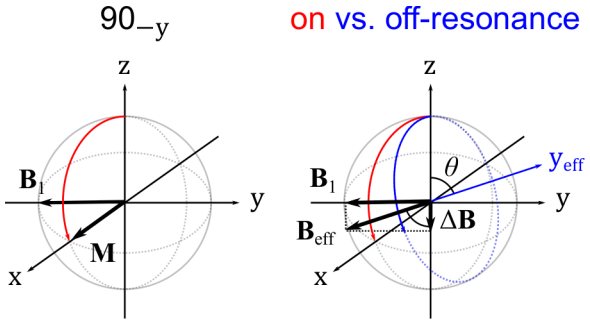

Figure 2.2: Effects of applying a pulse off-resonance. The effect of a 90°_{-y} pulse is shown for on- (red) and off-resonance (blue) cases. In the off-resonance case, the magnetization rotates about $\mathbf{B}_{\text{eff}}$ (2.1.29), taking on a different trajectory. This trajectory leads to a reduced amount of transverse magnetization and phase accrual due to the pulse, characterized by θ (2.1.30). Visually, the rotation occurs along a circular cross-section of the sphere orthogonal to $\mathbf{B}_{\text{eff}}$ and intersecting the z-axis at M_0.

For an intended flip angle of $\alpha = 90^\circ$, the total amount of transverse magnetization $|M_{xy}|$ and its phase ϕ is given by

$$|M_{xy}(\alpha = 90^\circ, \theta)| = \sqrt{M_0^2 \sin^2\theta(1+\cos^2\theta)} \tag{2.1.31a}$$

$$M_z(\alpha = 90^\circ, \theta) = M_0 \cos^2\theta \tag{2.1.31b}$$

$$\phi = \tan^{-1}(\cos\theta) \tag{2.1.31c}$$

Note that for large $|\Delta B|$ compared to B_1, θ approaches 0° and $\mathbf{B}_1$ is unable to rotate M_0 away from $\mathbf{B}_0$; little to no transverse magnetization is produced as $\sin^2\theta \to 0$. Taking the magnitude of the transverse magnetization $|M_{xy}|$ is often preferred in practice because doing so mitigates phase issues but *does not* address the flip angle effect of off-resonance pulses. Furthermore, the $\mathbf{B}_1$ field amplitude can vary within the coil depending on its design, introducing additional flip angle variation, though coil design details are beyond the scope of this text.

Off-resonance effects are compounded by $\mathbf{B}_0$ inhomogeneities. The shape (and resulting frequency spectrum) of the pulse and the $\mathbf{B}_1$ field will interact with any spatial variations in $\mathbf{B}_0$. Taken together, these effects can potentially lead to a huge variety of flip angles for different spin isochromats within the excited volume and result in a complicated ensemble magnetization evolution, particularly when slice-selective pulses (discussed in Sec. 2.1.3) and/or multiple pulses are applied.

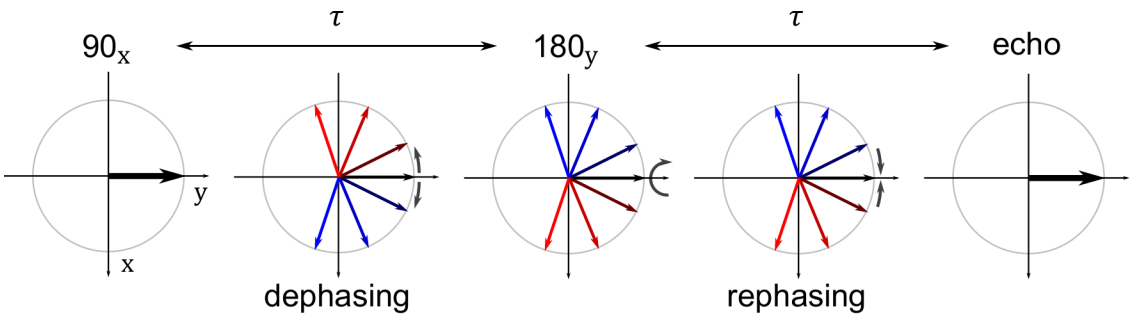

Figure 2.3: Schematic representation of a spin echo (SE). Following a 90°_x pulse, the excited magnetization spreads in the transverse plane due to static $\mathbf{B}_0$ field inhomogeneities. Spin isochromats accrue positive (red) and negative (blue) phase ϕ, depending on the sign and magnitude of the frequency offset $\Delta\omega$ (2.1.27). A 180°_y-pulse rotates the magnetization about the xz-plane after time τ. Magnetization rephases and forms an echo when $\mathbb{E}[\phi] = 0$ at the echo time, $\mathrm{TE} = 2\tau$.

Echoes

There exist experimental methods to mitigate the effects of field inhomogeneities. Echo formation is a means to reverse T_2^* dephasing via additional pulses, which was first developed by Hahn [29]. In the case of *static* $\mathbf{B}_0$ field inhomogeneities, i.e., assuming that $\Delta\omega$ for each isochromat is constant, the reversal is complete. More specifically, a spin echo (SE) can be formed by introducing a 180°, or refocusing pulse following excitation. In the example provided in Fig. 2.3, a 180°_y-pulse rotates the magnetization in the xz-plane and inverts the phase ϕ of all isochromats about the y-axis. The phase accrual of each isochromat then proceeds such that for a 180°_y-pulse applied at a time τ following excitation, an SE forms at 2τ along the $+y$-axis (Fig. 2.3), whence the effects of static field inhomogeneities are removed. By utilizing spin echoes of various echo times ($\mathrm{TE} = 2\tau$) the intrinsic T_2 can be measured. In a natural extension of this idea, the magnetization can be repeatedly refocused and measured with a series of equally-spaced 180°-pulses, which forms the Carr-Purcell-Meiboom-Gill (CPMG) sequence [30, 31].

Echoes can also be formed by other pulse sequences. For instance, three 90°_x-pulses in succession produce a stimulated echo (STE) [29, 32]. The evolution of the magnetization, however, is more complicated than for SEs. Before returning to STEs, let us first introduce a framework for more general perturbations.

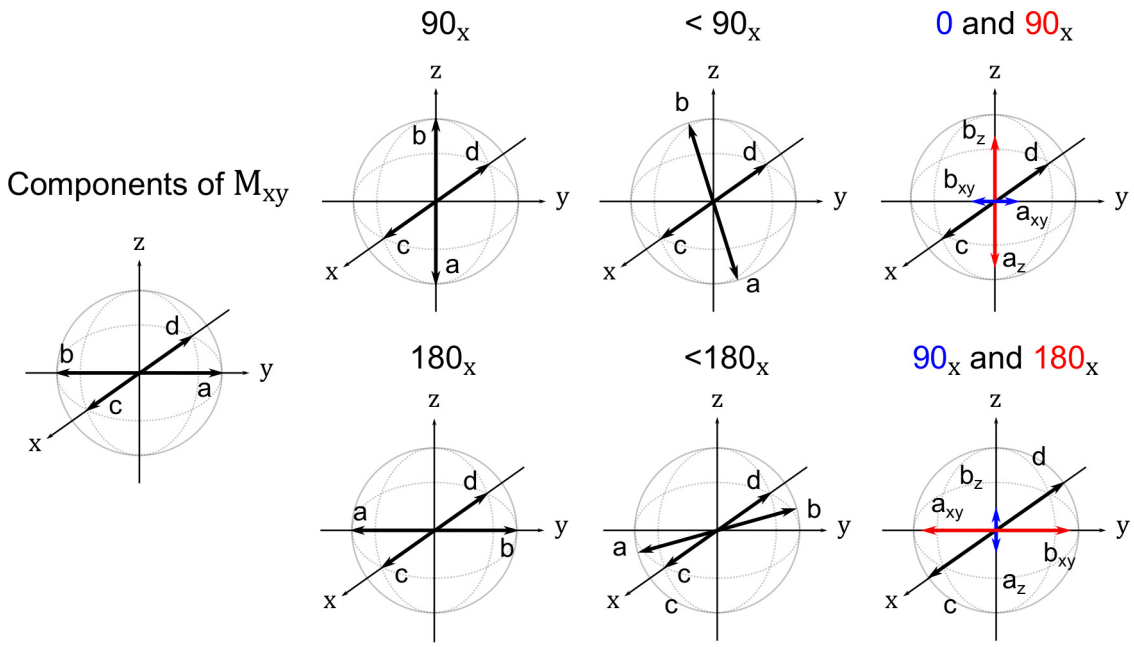

Figure 2.4: Evolution of decomposed transverse magnetization M_{xy} under (top) 90°_x- and (bottom) 180°_x-pulses, following complete dephasing after an initial excitation. Also shown are flip angles less than 90° and 180°. In the case of these smaller flip angles, the effect can be decomposed in terms of 0° (no rotation), 90°_x and 180°_x components.

Woessner decomposition

We would like to be able to account for flip angles other than 90° and 180°, as well as off-resonant pulses. First, let us presume that the transverse magnetization M_{xy} has been fully dephased following a 90°_x-pulse such that there is no net magnetization after some time $\tau \gg T_2^*$. The transverse magnetization M_{xy} can now be decomposed into four equal components based on their rate of phase accrual: a component which (a) does not acquire phase, (b) $\phi(\tau) = 180°$, and (c, d) $\phi(\tau) = \pm 90°$, shown on the left side of Fig. 2.4 [33].

This permits a simple visualization of the effects of subsequent pulses. A second 90°_x-pulse rotates (a) and (b) onto the longitudinal axis, where they are 'stored' and evolve by T_1 relaxation towards $+z$ (top row of Fig. 2.4). The (c) and (d) components are unaffected. Note that this leads to the observation that only half the signal (a, b) can be stored by 90°-pulses in such a manner [33], presuming complete dephasing beforehand. A 180°_x-pulse flips the position of (a) and (b), after which (b), (c), and

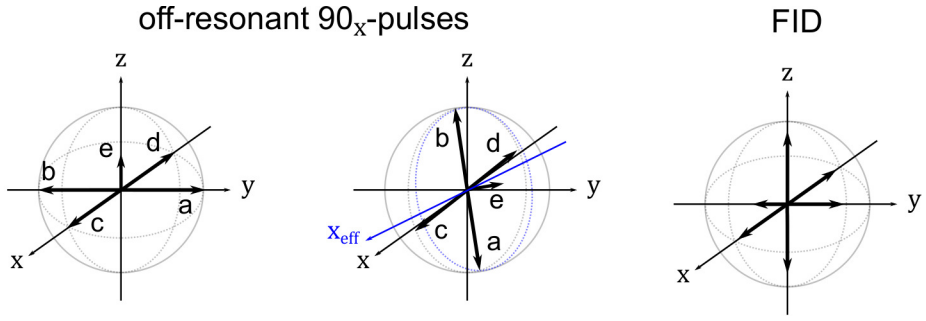

Figure 2.5: Evolution of decomposed magnetization after an off-resonant 90°_x-pulse, dephasing and a second off-resonant 90°_x-pulse pulse. In this case, some longitudinal magnetization (e) remains after the initial excitation (2.1.31). The magnetization after the second pulse can again be decomposed in the same way shown in Fig. 2.4. Following the second pulse, an FID is produced from the component of (e) in the transverse plane.

(d) will continue to evolve such that a spin echo is formed at time 2τ along $-y$ (bottom row of Fig. 2.4). What of other flip angles? We see that for a flip angle smaller than 90°_x, the effects of such a pulse can be decomposed into signal fractions which undergo an 'effective' 0°-pulse (i.e., no rotation, blue), wherein a fraction of (a) and (b) remain in the xy-plane, and which undergo a 90°_x-pulse (red). Likewise, for a flip angle less than 180°, the rotation can be decomposed into fractions which undergo a 90°_x- (blue) and a 180°_x-pulse (red). Note that pulse phase is preserved. These effects are visualized in Fig. 2.4.

For off-resonant pulses, the intuition proceeds similarly, illustrated in Fig. 2.5. Following an off-resonant 90°_x excitation pulse, M_{xy} will again dephase completely over time, but a longitudinal component (e) will remain, given by (2.1.31), and representing the effect of the field offset $\Delta\mathbf{B}$ (2.1.28). A second off-resonant 90°_x-pulse results in a complicated rotation of these different components, but they can again be decomposed into fractions aligned along each axis, just as in Fig. 2.4. In this case, a net magnetization is produced along $+y$ by the second pulse, yielding an FID (see Fig. 2.5), which arises principally from (e). The transverse part of (e) will then proceed to dephase, generating a new set of components (a – d).

We thus arrive, by geometric intuition, at the concept of Woessner decomposition [32] or the 'partitioning effect of an RF pulse' [33, 34], applicable to uncoupled, spin-$\frac{1}{2}$ systems. That is, the effects of any pulse after the first can be decomposed

into signal fractions which undergo effective pulses of (1) 0°, (2) 90°, and (3) 180°, wherein pulse phase is preserved. Put another way, transverse magnetization either (1) continues dephasing, (2) is stored longitudinally, or (3) begins rephasing to form an echo. The proportion of each of these 'pathways' depends on the flip angle and the degree of off-resonance.

Woessner decomposition is a powerful framework to analyze pulse sequences. This framework allows the potentially complicated ensemble magnetization to be treated as consisting of fractional pathways or 'coherences' [28] that undergo conventional RF pulses $(0, 90, 180°)$. These pathways may be considered individually, *regardless* of how they arise (e.g., field inhomogeneity). In practice, one generally wishes to 'select' a single, desired pathway while suppressing all others. Let us now return to the STE as an instructive example for techniques to suppress unwanted pathways.

Coherence selection via phase cycling

An STE sequence consists of three 90°-pulses, each with some pulse phase φ, separated by times τ_1 and τ_2. First, let us consider three 90°_x-pulses:

$$90^\circ_x - \tau_1 - 90^\circ_x - \tau_2 - 90^\circ_x - \tau_1 - \text{echo}.$$

The STE forms at a time τ_1 after the final pulse and along $-y$, as determined by the pulse phases. The maximal signal for this STE is given (approximately) by

$$\frac{M_{xy}(\text{TE} = 2\tau_1 + \tau_2)}{M_0} = \frac{1}{2}\exp\left(-\frac{2\tau_1}{T_2} - \frac{\tau_2}{T_1}\right), \tag{2.1.32}$$

acknowledging that only half the signal is stored during τ_2 (see Fig. 2.4). A variety of other pathways leading to single and double spin echoes can also arise, however, due to off-resonance effects. These can be enumerated via Woessner decomposition and are summarized in Table 2.1. Also shown is the location of each pathway during each interval, i.e., whether it lies in the transverse plane or is stored longitudinally — denoted T and L, respectively — and the axis of echo formation. Additionally, FIDs result from each pulse (not shown).

Thus, even a simple three-pulse sequence such as this can result in five echoes [35]. Depending on the timings used (τ_1, τ_2), the various SEs and FIDs may overlap

Table 2.1: Echoes formed by an STE sequence.

Pathway	Effective pulses	Location	Time of echo	Echo axis
STE	90°_x — 90°_x — 90°_x	T — L — T	$2\tau_1+\tau_2$	$-y$
SE_1	90°_x — 180°_x — 0°	T — T — T	$2\tau_1$	$-y$
SE_2	90°_x — 0° — 180°_x	T — T — T	$2(\tau_1+\tau_2)$	$-y$
SE_3	0° — 90°_x — 180°_x	L — T — T	$\tau_1+2\tau_2$	$-y$
SE-SE	90°_x — 180°_x — 180°_x	T — T — T	$2\tau_1+2(\tau_1-\tau_2)$	$+y$

Table 2.2: Exemplar 2-step STE phase cycle.

Step	φ_1	φ_2	φ_3	φ_{rec}
1	0	0	0	π
2	0	π	0	0

with the STE. A straightforward approach to isolate the STE pathway is to select timings that sufficiently separate it from the SE pathways, as well as a long enough τ_1 to dephase the FID from the last pulse. Isolation via timings is not always possible nor desirable, however. Other means to isolate the desired coherence are available, and are based on exploiting the different *effective* pulses between pathways.

Phase cycling is the manipulation of pulse and receiver phases over multiple repetitions of the experiment such that the repetitions add coherently for the desired pathway and destructively for undesired pathways. Let us consider a 2-step phase cycle in which we alternate the phase of the second pulse, φ_2, and the receiver phase, φ_{rec}, such that the STE is along the receive axis, shown in Table 2.2. Here we will introduce an additional notation for pulse and receiver phase. We define the 'default' excitation of $\mathbf{B}_1$ along $+x$ (producing transverse magnetization along $+y$) as corresponding to 0 pulse and receiver phase, and then continuing counter-clockwise in steps of $\frac{\pi}{2}$. Note that we write these pulse and receiver phases in radians to avoid confusion with the flip angle, written in degrees. For example, a 180°_y-pulse has phase $\frac{\pi}{2}$, while a receiver phase oriented along $-y$ has phase π. When designing phase cycles, the phase of 90°-pulses are usually alternated on the same axis as the first pulse (i.e., 0, π), whereas 180°-pulses may take any phase value.

Table 2.3: Pathways under a 2-step STE phase cycle.

Pathway	Step 1	Offset	Step 2	Offset
STE	90°_x — 90°_x — 90°_x	0	90°_x — 90°_{-x} — 90°_x	0
SE_1	90°_x — 180°_x — 0°	0	90°_x — 180°_{-x} — 0°	π
SE_2	90°_x — 0° — 180°_x	0	90°_x — 0° — 180°_x	π
SE_3	0° — 90°_x — 180°_x	0	0° — 90°_{-x} — 180°_x	0
SE-SE	90°_x — 180°_x — 180°_x	π	90°_x — 180°_{-x} — 180°_x	0

How do we follow what happens in a pathway? Consider that only transverse magnetization is detected. Thus, any 90°-pulses after the first must be considered in pairs along the same axis: $\pm x$ or $\pm y$. Otherwise, the magnetization is either not stored, or is never brought back into the transverse plane. If the pair of 90°-pulse phases are equal (e.g., π, π), then the magnetization completes a rotation (e.g., from $+y$ to $-y$) and the receiver phase should be shifted by π; if they are opposed (e.g., 0, π), the magnetization is brought back to the same axis. For 180°-pulses, the magnetization is rotated if the pulse and magnetization have orthogonal phase (e.g., a 180°_x pulse rotates magnetization from $+y$ to $-y$) and remains along the same axis otherwise (as is the case for the spin echo illustrated in Fig. 2.3).

We now evaluate the pathways at each step in Table 2.2 with regards to the phase offset between the axis of echo formation and φ_{rec}, shown in Table 2.3. We see that all undesired echoes — excepting the SE_3 pathway, which does not 'see' the first pulse and sees the last pulse as a 180°-pulse — will add destructively, as the offset changes by π between steps. Note that the FIDs from the second and third pulses are also suppressed by this phase cycling scheme. To suppress the SE_3 contribution, the third pulse can be cycled. In order to preserve the effects of cycling the second pulse, the cycles can be 'nested', i.e., looped through iteratively. This produces a 4-step phase cycle, shown in Table 2.4, and which comprises the standard STE phase cycle [28, 36]. In general, the number of steps grows exponentially by 2^n for n pulses being cycled. Given that the number of pathways generated grows by 2×3^n according to Woessner decomposition, phase cycling can become time-consuming and cumbersome for many-pulse sequences.

Table 2.4: 4-step STE phase cycle.

Step	φ_1	φ_2	φ_3	φ_{rec}
1	0	0	0	π
2	0	π	0	0
3	0	0	π	0
4	0	π	π	π

Gradient spoiling

Another, potentially more efficient approach to suppress unwanted pathways is to take advantage of the differing location between pathways (see Table 2.1). Between the second and third pulses (during τ_2), only the STE pathway is stored longitudinally, whilst all other echo-forming pathways remain in the transverse plane. Thus, if we introduce a gradient in the $\mathbf{B}_0$ field during this time interval (using gradient coils, for instance), only the unwanted pathways will experience its effect. Under a gradient $\mathbf{g}(t)$ along a fixed direction, the field becomes a function of position, $\mathbf{r}$:

$$\mathbf{B}_0(\mathbf{r},t) = (B_0 + \mathbf{g}(t)\cdot\mathbf{r})\hat{\mathbf{k}}, \tag{2.1.33}$$

and the precessional frequency offset becomes

$$\Delta\omega(\mathbf{r},t) = \mathbf{G}(t)\cdot\mathbf{r}, \tag{2.1.34}$$

where $\mathbf{G}(t) = \gamma\mathbf{g}(t)$ is the gradient in terms of frequency. From (2.1.27):

$$\phi(t) = \int_0^t \mathbf{G}(t)\cdot\mathbf{r}\,dt. \tag{2.1.35}$$

Spin isochromats will thus acquire phase depending on their position and the ensemble magnetization will rapidly dephase in the presence of a gradient, with the rate depending on the amplitude G. Applying a gradient only during τ_2 of a stimulated echo therefore suppresses unwanted echo-forming pathways by means of dephasing. This technique is called gradient 'spoiling'. Note, however, that spoiling in this manner does not suppress the FID from the third pulse. In practice, several gradient spoiling and phase cycling techniques may need to be employed simultaneously to isolate the desired signal.

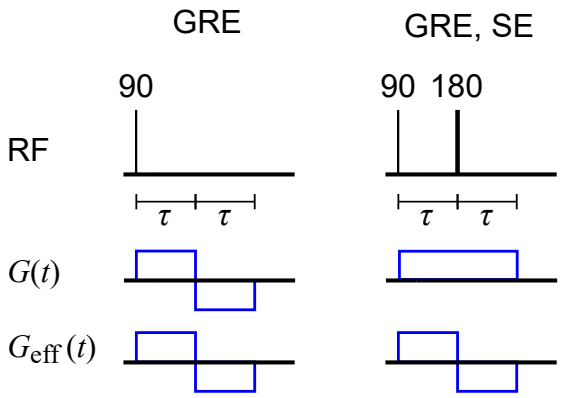

Figure 2.6: Gradient echo (GRE) formation for gradients along the same axis with amplitude $G(t)$. GREs are formed when the gradient integrates to $F(2\tau) = 0$ (2.1.36). (left) A GRE formed by modulating the gradient orientation. (right) A GRE formed by modulating the effective gradient $G_{\text{eff}}(t)$ using a refocusing pulse. In this case, an SE forms at the same time.

Gradient echoes

Consider that gradients are in essence a deliberately applied $\mathbf{B}_0$ field inhomogeneity. Therefore, echoes can be formed in a similar manner. If a pair of gradients of equal amplitude but opposite direction are applied for an equal amount of time, then they will form what is known as a gradient echo (GRE) centered at the termination of the second gradient. Alternatively, a refocusing pulse will flip the phase due to a gradient about some axis, such that application of the same gradient on both sides of a refocusing pulse will produce both a GRE and an SE at the echo time. Thus, we can say that a 180°-pulse reverses the *effective* gradient direction. GRE formation is illustrated in Fig. 2.6. Henceforth, we will not usually distinguish between the gradient and effective gradient. More formally, a GRE is formed when the time integral of the gradient, which we will call $\mathbf{F}(t)$, is equal to 0:

$$\mathbf{F}(t) = \int_0^t \mathbf{G}(t')dt'. \tag{2.1.36}$$

2.1.3 Imaging

Gradients are not only useful for spoiling. Consider that the application of gradients encodes spatial information into the signal vis-à-vis its phase and that gradients can be modulated — spatially by means of gradient coils, or effectively reversed

by refocusing pulses. Taken together, these characteristics enable image formation, discussed below, and the measurement of diffusion, discussed later in Sec. 2.2.

k-space

Upon the application of a gradient, phase develops across an excitation volume according to (2.1.35). This is akin to a spatial frequency across the volume, as the phase wraps around along the direction of the gradient. The ensemble magnetization, or signal, S, at some time t may be written as a function of the phase vector $\mathbf{k}$:

$$S(\mathbf{k}) = \int s(\mathbf{r}) \exp(i\,\mathbf{k}\cdot\mathbf{r})\, d\mathbf{r}, \tag{2.1.37}$$

where $\mathbf{k} = \mathbf{F}(t)$ (2.1.36) and $s(\mathbf{r})$ is the signal at position $\mathbf{r}$, which is proportional to the proton density $\rho(\mathbf{r})$ and other signal evolution mechanisms (relaxation, etc.). There is thus a Fourier relationship between the complex signal $S(\mathbf{k})$ and the signal in space $s(\mathbf{r})$, with inverse relationship:

$$s(\mathbf{r}) = \int S(\mathbf{k}) \exp(-i\,\mathbf{k}\cdot\mathbf{r})\, d\mathbf{k} \tag{2.1.38}$$

By measuring the signal throughout k-space, i.e., at many $\mathbf{k} = \left[k_x, k_y, k_z\right]$, one can reconstruct an image by means of numerical Fourier transform. Note that the inverse relationship between k- and image-space implies the following: (i) the resolution of the image in each direction is determined by the extent of $\mathbf{k}$ in said direction, e.g.,

$$\Delta x = \frac{1}{2|k_x^{\max}|}, \tag{2.1.39}$$

where Δx is the resolution along the x-axis and $|k_x^{\max}|$ is the largest value of $\pm k_x$ that is observed, and (ii) the field-of-view (FOV) is determined by the resolution Δk in k-space, e.g.,

$$\Delta k_x = \frac{1}{\mathrm{FOV}_x}. \tag{2.1.40}$$

Note also that the FOV should be large enough to include all of the excited magnetization so as to avoid aliasing effects.

The k-space domain can be traversed by measuring the signal over various gradient applications and directions over all three spatial dimensions. Typically, however, MR

images are acquired in 2D across several 'slices', as first described by Mansfield [37]. That is, k-space is only traversed in two dimensions, whilst the third is traversed by means of slice selection.

Slice selection

To acquire a series of 2D slices and reconstruct the excitation volume, one can first apply a (linear) gradient perpendicular to the desired slice. The direction of this gradient is conventionally defined to be along the z-axis. This creates spatial variation in the precession frequencies ω_0 along z. An excitation RF pulse with some bandwidth will therefore excite magnetization within a slice of width Δz (e.g., 1 mm) in the sample, where the width of the slice depends on the pulse bandwidth and the gradient amplitude G. For a hard pulse, the pulse duration τ_p is related to the gradient and Δz as

$$\tau_p = \frac{2\pi}{G\Delta z}. \tag{2.1.41}$$

Afterwards, to avoid undesired dephasing, this 'slice-select' gradient may be refocused (i.e., a GRE is formed: $\mathbf{k} = \mathbf{0}$). If further pulses such as refocusing pulses are applied, these are typically also slice-selective, and tuned to apply to a similar slice.

We again stress that the shape of the pulse determines its frequency spectrum and bandwidth. Thus, unless an impractically long sinc pulse is used, regions of the sample at the edge of the slice will experience significantly different pulse powers and thereby flip angles due to side lobes of the pulse spectrum, producing off-resonance effects which must be accounted for. The pulse bandwidth also determines the width of the echo in the time-domain, as different components will come into phase at different times. The echo width is roughly equal to τ_p for hard pulses.

Echo planar imaging

Following slice selection, many techniques have been developed to traverse $\left[k_x, k_y\right]$ and reconstruct a 2D image [22]. The method most frequently used in diffusion MRI — and the method employed in Chapter 5 of this thesis — is single-shot, blipped echo planar imaging (EPI), in which k-space is traversed in a single acquisition

Figure 2.7: Example EPI sequence. After slice selection and rephasing, magnetization is pre-phased to the bottom left corner in k-space. Continuous readout gradients (G_x) and phase blips (G_y) are used to traverse 2D k-space in the trajectory shown to the right.

[37–40]. In this imaging sequence, the magnetization is pre-phased after slice selection, after which 'read' gradients are used to traverse one axis continuously and orthogonal 'phase blips' are used to traverse the other axis, as illustrated in Fig. 2.7. The read and phase encoding directions are conventionally defined as x and y. EPI has the advantage of being very fast and can produce images in a timeframe on the order of $\lesssim 40$ ms [40].

In Fig. 2.7, the EPI sequence is carried out under the influence of T_2^* (GRE). An EPI 'module' can also be attached to echo-forming sequences (SE, STE) by centering the EPI sequence at the point of echo formation (i.e., the echo forms at $k_x = k_y = 0$). In general, any sort of preparation can be placed after slice selection and preceding imaging to sensitize the image to different effects, such as T_2 relaxation or diffusion. Development of EPI-related sequences and image reconstruction methods (e.g., Ref. [41]) is a rich area of study, but we will not dwell on the topic, as most of the work in this thesis was carried out without imaging.

Steady state

Here, we should also point out that multiple images or acquisitions may be carried out successively. The time between these experimental repeats is called the repetition time (TR). Unless TR $\gg T_1$, the longitudinal magnetization M_z at the start of each experiment will decrease over successive TRs due to incomplete T_1 recovery. Thus,

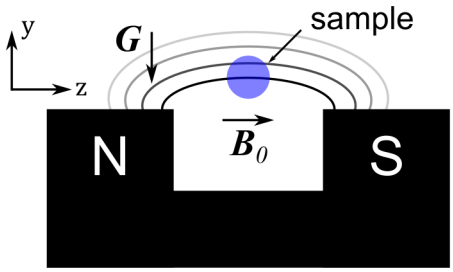

Figure 2.8: Simple schematic of the NMR-MOUSE. Fading lines represent decaying magnetic field lines. In the drawn axis orientation, $\mathbf{B}_0$ is along z ($B_0 = 0.3239$ T), the gradient $\mathbf{G}$ is along y, and $\mathbf{B}_1$, generated in our case using a solenoid RF coil, is along x (not drawn). The field is relatively homogeneous along z at the center of the yoke.

in practice, a series of 'dummy' scans is usually played out to reach a steady state — wherein the loss of signal during the experiment is balanced with the T_1 recovery. Additionally, any remaining transverse magnetization is typically spoiled before the start of each repetition.

2.1.4 Working with permanent magnets

While the use of MR in biomedical applications often involves conventional scanners, most of the experiments in this thesis (Chapters 3, 4, 6) were carried out on a low-field, permanent magnet system: the PM-10 NMR-MOUSE (Magritek, Aachen, Germany) [42, 43]. Given the uniqueness of this system, we discuss here notable differences between it and conventional MRI scanners.

The PM-10 NMR-MOUSE

The PM-10 NMR-MOUSE is an iron yoke magnet with a field strength of $B_0 = 0.3239$ T, diagrammed in Fig. 2.8 [42–44]. The field is roughly homogeneous in the xz-plane in the center of the yoke, forming the $\mathbf{B}_0$ field. The gradient amplitude is approximately $g = 15.3$ T/m (or, equivalently, $G = \gamma g \approx 650$ kHz/mm). In our setup, a solenoid RF coil, oriented along the x-axis (into/out of the page) is used as a transmit-receive coil [45–47]. The most important difference from conventional scanners is that the gradient is not produced by passing current through a set of coils, but rather by the decay of the static magnetic field away from the magnet

along the y-direction, akin to a stray field experiment.

The PM-10's gradient is thus 'always-on' along a fixed axis, which has profound consequences for MR experimentation. Consider that: (i) imaging is not possible, and likewise, directionally-dependent effects (i.e., anisotropy) cannot be interrogated, (ii) all pulses become slice-selective, which, when compounded with the large intrinsic $\mathbf{B}_0$ inhomogeneity, can produce strong off-resonance effects, and (iii) the smaller B_0 (≈ 0.3 T compared to, e.g., 7 T for pre-clinical systems) results in less polarized magnetization and signal; recall, the signal-to-noise ratio (SNR) is (at least) proportional to B_0 (2.1.6). While (i) cannot be remedied, (ii) and (iii) can be ameliorated by experimental design. Careful construction of phase cycles and acquisition timings can mitigate off-resonance effects. A coil with a high filling factor (i.e., that fits the sample snugly) can boost SNR. Furthermore, rather than acquiring a single echo, a CPMG echo train can be acquired as a sum and treated as the signal without any meaningful loss in information [30, 31, 48], since imaging is not (and cannot) performed. This CPMG acquisition-mode mitigates T_2^* effects whilst boosting the number of observed echoes and thereby SNR.

Advantages at low-field

Given these considerable experimental limitations, what do we gain by using such a system? Most importantly, the gradient amplitude *far* exceeds that which is achievable on conventional gradient coil-based systems. For instance, a pre-clinical scanner can achieve, perhaps, $g_{\max} \approx 0.6$ T/m, which is more than 20× smaller than $g = 15.3$ T/m for this system. In addition, gradient coils are limited by slew rates that constrain their ramping speed. On this system, effective gradient switching is limited only by the duration of time between RF refocusing pulses. Thus, when utilizing very short, hard RF pulses ($\tau_p \sim 2\ \mu$s), extremely fast gradient switching is possible, while still attaining appreciable dephasing due to the large gradient amplitude. More specifically, echo times less than one millisecond are possible. As we shall see later in Sec. 2.2.3, these characteristics allow us to probe diffusion over time- and lengthscales that are far smaller than what can be accessed on conventional scanners.

2.2 Diffusion MR signal modelling

Having described the MR phenomenon and relevant experimental details, we turn towards the acquisition and modelling of the diffusion MR signal. During the application of a gradient, spins may diffuse and acquire phase depending on their position *and* their change in position. Adapting (2.1.35) with time-dependent position $\mathbf{r}$, one obtains the phase of an isochromat as a function of time:

$$\phi(t) = \int_0^t \mathbf{G}(t) \cdot \mathbf{r}(t)\, dt. \tag{2.2.1}$$

Thus, when an echo is formed, the phase will not be perfectly reversed due to net displacement(s), and any GRE will exhibit some degree of attenuation due to diffusion. The attenuation of a GRE due to diffusion can be isolated (e.g., from relaxation) by normalizing the signal to an equivalent signal acquisition without the (balanced) gradients, called S_0. We will denote this normalized signal as S/S_0 throughout.

2.2.1 Free diffusion and the *b*-value

Let us first present well-known results regarding the b-value [29, 30, 49–51] and free diffusion. The Bloch equations (2.1.23) were modified by Torrey [51] to include the effects of motion in an inhomogeneous $\mathbf{B}$:

$$\frac{\partial \mathbf{M}}{\partial t} = \gamma \mathbf{M} \times \mathbf{B} - \frac{M_x \hat{\mathbf{i}} + M_y \hat{\mathbf{j}}}{T_2} - \frac{M_z - M_0}{T_1} \hat{\mathbf{k}} + \nabla \cdot D_0 \nabla \mathbf{M}, \tag{2.2.2}$$

where D_0 is the molecular self-diffusion coefficient or diffusivity. While Torrey also included a flow term [51], we will ignore flow here on the basis of mass balance. For free diffusion, wherein the net, mean-squared displacement (MSD) $\langle r^2(t) \rangle$ is given precisely by

$$\langle r^2(t) \rangle = 2 D_0 t, \tag{2.2.3}$$

Stejskal & Tanner [49, 50] showed that the effects of diffusion on the normalized signal (i.e., ignoring precession and relaxation terms) can be captured by what has become known as a 'b-value', used to represent the amount of diffusion weighting:

$$\frac{S}{S_0} = \exp\left(-b D_0\right), \tag{2.2.4}$$

where

$$b = \int_0^{\mathrm{TE}} |F(t)|^2 dt = \int_0^{\mathrm{TE}} \left| \int_0^t G(t')dt' \right|^2 dt, \tag{2.2.5}$$

and $F(\mathrm{TE}) = 0$ (echo condition). This result (2.2.4) is a natural first port of call, and is the most utilized signal model in diffusion MR.

Indeed, many other signal models are merely modifications of the above. For instance, it is common to claim the measurement of an 'apparent' diffusion coefficient (ADC) [11, 12] for a certain b-value or set of b-values. This is, of course, an empirical approach that is not derived from the underlying physical transport properties. Really, there may be a time-dependent diffusivity $D(t)$:

$$D(t) = \frac{\langle r^2(t) \rangle}{2t}. \tag{2.2.6}$$

We stress that signal models which effectively modify the b-value model (2.2.4) (e.g., the stretched exponential [52] or the diffusional kurtosis model [53–55]) are also empirical because they do not begin from a description of the phase arising from time-dependent diffusion (2.2.1). In the following section, we will take a more rigorous, analytical approach and also re-derive the b-value. But first, we demonstrate the calculation of b-values for some typical pulse sequences.

In Fig. 2.9, static gradient (SG) and pulsed gradient (PG) diffusion-weighted sequences are shown: an SG-SE, PG-SE, and PG-STE sequence, all with gradient amplitude $G = \gamma g$. The SG-SE sequence, for example, produces a triangle-shaped $F(t)$, with a peak value of $|F(\tau)| = G\tau$. Integrating $|F(t)|^2$ from $t = [0, \tau]$ and then doubling the result, the b-value is calculated as $b = \frac{2}{3} G^2 \tau^3$ (2.2.4). For the PG sequences, the gradient duration δ and separation Δ parameters determine the b-value, shown in Table 2.5. Consider as well that if $\delta = \Delta$, the PG-SE experiment is identically the SG-SE experiment with $\tau = \delta$.

2.2.2 The Gaussian phase approximation

While the b-value model (2.2.4) is useful, diffusion in tissue is usually influenced by boundaries and may be poorly approximated by a constant diffusivity. Rather, $D(t)$ will decrease over time (i.e., the MSD is sub-linear) due to the confining effect of

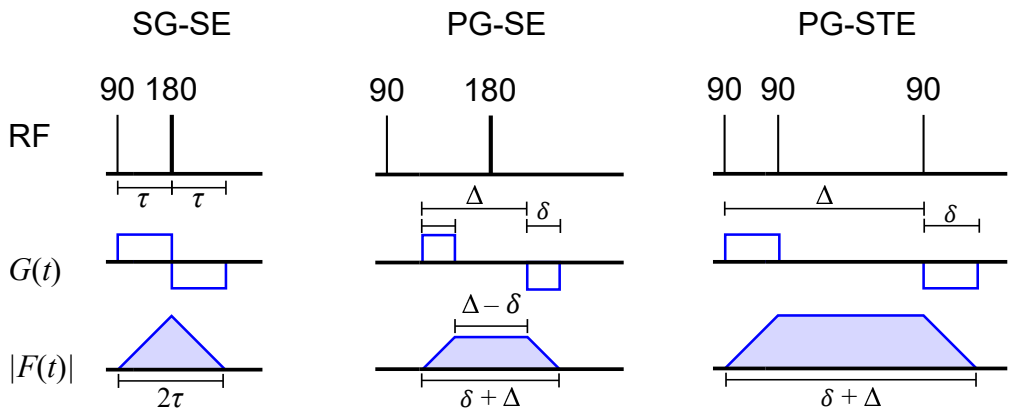

Figure 2.9: Schematic of several diffusion-weighted sequences using pulsed or static gradients (PG, SG) and spin or stimulated echoes (SE, STE). The *effective* gradient $G(t)$ and its integral $|F(t)|$ are illustrated. The integral of $|F(t)|^2$ gives the b-value.

Table 2.5: Parameters and b-values for diffusion-weighted sequences in Fig. 2.9.

Sequence	**Parameters**	b-value
SG-SE	τ	$\frac{2}{3}G^2\tau^3$
PG-SE, PG-STE	δ, Δ	$(G\delta)^2\left(\Delta - \frac{1}{3}\delta\right)$

boundaries. To be able to model this time-dependence, we re-derive the attenuation due to diffusion S/S_0 from more general principles which acknowledge, from the outset, that diffusion can be time-dependent.

The cumulant expansion

We begin by expanding the phase distribution (2.1.27), observed at some time t:

$$\frac{S}{S_0} = \mathbb{E}\left[\exp\left(i\phi\right)\right].$$

The right-hand-side can alternatively be written as the moment-generating function $M_\phi(i)$ via Maclaurin expansion of $\exp(i\phi)$ [56], yielding

$$\frac{S}{S_0} = M_\phi(i) = \sum_{n=0}^{\infty} \frac{i^n}{n!} m_n, \tag{2.2.7}$$

where $m_n = \mathbb{E}[\phi^n]$ are the moments of the phase probability distribution $P(\phi)$ (mean, variance, skewness, kurtosis, etc.). This expansion can be equivalently expressed

in terms of cumulants κ_n,

$$\frac{S}{S_0} = \exp\left(\sum_{n=1}^{\infty} \frac{i^n}{n!}\kappa_n\right). \tag{2.2.8}$$

One might assume that $P(\phi)$ is Gaussian. This is the so-called Gaussian phase approximation (GPA), utilized since the infancy of NMR [29, 30, 57]. Under the GPA, only the first two cumulants are non-zero such that

$$\frac{S}{S_0} = \exp\left(i\mathbb{E}[\phi] - \frac{\mathbb{V}[\phi]}{2}\right) = \exp\left(i\mathbb{E}[\phi] - \frac{\mathbb{E}\left[\phi^2\right] - \mathbb{E}[\phi]^2}{2}\right), \tag{2.2.9}$$

where $\mathbb{V}[\phi] = \mathbb{E}\left[\phi^2\right] - \mathbb{E}[\phi]^2$ is the variance. Thus, to determine S/S_0, one must evaluate how $\mathbb{E}[\phi]$ and $\mathbb{E}\left[\phi^2\right]$ evolve over time.

It is useful to integrate (2.2.1) by parts, yielding an expression in terms of the time-integral of the gradient $\mathbf{F}(t)$ (2.1.36), position $\mathbf{r}(t)$, and velocity $\mathbf{v}(t) = d\mathbf{r}(t)/dt$,

$$\phi(t) = \mathbf{F}(t)\cdot\mathbf{r}(t) - \int_0^t \mathbf{F}(t)\cdot\mathbf{v}(t)\,dt, \tag{2.2.10}$$

The first term on the right-hand-side of (2.2.10) is the position-dependent dephasing. If the gradients are balanced (i.e., at an echo $t = \mathrm{TE}$), then $\mathbf{F}(t = \mathrm{TE}) = \mathbf{0}$ and this term vanishes. The second term accounts for net flow. If there is no net (bulk) flow into or out of the sample (i.e., $\mathbb{E}[\mathbf{v}(t)] = \mathbf{0}\ \forall t$), then

$$\mathbb{E}[\phi(\mathrm{TE})] = \mathbb{E}\left[\int_0^{\mathrm{TE}} \mathbf{F}(t)\cdot\mathbf{v}(t)\,dt\right] = 0. \tag{2.2.11}$$

Note that assuming no net flow is equivalent to an assumption of mass balance. This assumption additionally implies that all odd moments of $P(\phi)$ are 0. This leaves only the phase covariance $\mathbb{E}\left[\phi^2\right]$ term in (2.2.9). Thus, assuming (2.2.11), one obtains for S/S_0 at an echo,

$$\frac{S}{S_0} = \exp\left(-\frac{1}{2}\mathbb{E}\left[\phi^2\right]\right). \tag{2.2.12}$$

Substituting (2.2.10):

$$\frac{S}{S_0} = \exp\left(-\frac{1}{2}\int_0^{\mathrm{TE}}\int_0^{\mathrm{TE}} \mathbf{F}^{\mathrm{T}}(t)\langle\mathbf{v}(t)\mathbf{v}^{\mathrm{T}}(t')\rangle\mathbf{F}(t')\,dt\,dt'\right), \tag{2.2.13}$$

where $\langle\cdot\rangle$ denotes ensemble averaging and $\langle \mathbf{v}(t)\mathbf{v}^{\mathrm{T}}(t')\rangle$ is the velocity autocorrelation function (VACF) in matrix form (outer product), which we note is stationary by (2.2.11). That is, the VACF is time-translation invariant,

$$\langle \mathbf{v}(t)\mathbf{v}^{\mathrm{T}}(t')\rangle = \langle \mathbf{v}(t-t')\mathbf{v}^{\mathrm{T}}(0)\rangle. \tag{2.2.14}$$

As we do not characterize anisotropy anywhere in this thesis, we now simplify (2.2.13) to a single gradient axis and proceed from here onward in 1D,

$$\frac{S}{S_0} = \exp\left(-\frac{1}{2}\int_0^{\mathrm{TE}}\int_0^{\mathrm{TE}} F(t)\langle v(t-t')v(0)\rangle F(t')\,dt\,dt'\right). \tag{2.2.15}$$

This signal representation provides some initial intuition. The emergence of time-dependent diffusion is seen to be tantamount to long-range velocity autocorrelation. Reflecting barriers, for instance, impart a local, negative VACF which increases the echo intensity — i.e., barriers preserve signal.

Revisiting the *b*-value

As an aside, let us re-derive the b-value starting from (2.2.15). The Green-Kubo relations [58, 59] provide a relationship between the VACF and D_0:

$$D_0 = \int_0^{\infty} \langle v(\tau)v(0)\rangle\, d\tau. \tag{2.2.16}$$

A key property of free or Brownian diffusion is that the system has no 'memory' [59, 60]. That is, velocities do not correlate over time. As such, the VACF can be approximated by a normalized delta function $\delta(t)$,

$$\langle v(t-t')v(0)\rangle \approx \left(\int_{-\infty}^{\infty}\langle v(\tau)v(0)\rangle d\tau\right)\delta(t-t') = 2D_0\,\delta(t-t'), \tag{2.2.17}$$

according to (2.2.16). Substituting (2.2.17) into (2.2.15):

$$\frac{S}{S_0} = \exp\left(-D_0\int_0^{\mathrm{TE}}\int_0^{\mathrm{TE}} F(t)F(t')\delta(t-t')\,dt\,dt'\right). \tag{2.2.18}$$

The delta function collapses the double integral into a single integral, and one again retrieves the expression for the b-value (2.2.4):

$$\frac{S}{S_0} = \exp\left(-D_0\int_0^{\mathrm{TE}} |F(t)|^2 dt\right) = \exp(-bD_0). \tag{2.2.19}$$

Frequency-domain representation

The VACF signal representation (2.2.15) is highly flexible and has many equivalent forms [16, 17, 61–65], as summarized by Ning *et al.* [65]. Consider that the integral in (2.2.15) contains a pair: (i) a function produced by the gradient waveform which is twice integrated with (ii) a (stationary) transport property — here, $F(t)$ and the VACF, respectively. The pair can be represented in various ways. For instance, by proceeding from (2.2.1) without integration by parts, (2.2.15) can be re-written in terms of $G(t)$ and the *position* autocorrelation function:

$$\frac{S}{S_0} = \exp\left(-\frac{1}{2}\int_0^{\mathrm{TE}}\int_0^{\mathrm{TE}} G(t)\langle r(t)r(t')\rangle G(t')\,dt\,dt'\right). \tag{2.2.20}$$

To make such representations tractable in practice — i.e., for cases that are not free diffusion — they would ideally simplify into a single integral, such that the first part (i) from the gradient waveform represents a straightforward 'weighting' of the transport property. Such an expression can be obtained by transforming to the frequency domain. Writing the VACF in terms of its spectrum $\widetilde{\mathcal{D}}(\omega)$,

$$\langle v(t-t')v(0)\rangle = \frac{1}{\pi}\int_0^{\infty} \widetilde{\mathcal{D}}(\omega)\exp\left(i\omega\,(t-t')\right)d\omega, \tag{2.2.21}$$

one obtains by substitution into (2.2.15) and some regrouping,

$$\frac{S}{S_0} = \exp\left(-\frac{1}{2\pi}\int_0^{\infty}\left[\int_0^{\mathrm{TE}} F(t)\exp(i\omega t)dt\right]\widetilde{\mathcal{D}}(\omega)\left[\int_0^{\mathrm{TE}} F(t')\exp(-i\omega t')dt'\right]d\omega\right). \tag{2.2.22}$$

The product of the two time-integrals is the (truncated) power spectrum of $F(t)$,

$$|F(\omega)|^2 = \left|\int_0^{\mathrm{TE}} F(t)\exp(i\omega t)dt\right|^2, \tag{2.2.23}$$

such that

$$\frac{S}{S_0} = \exp\left(-\frac{1}{2\pi}\int_0^{\infty}|F(\omega)|^2\widetilde{\mathcal{D}}(\omega)d\omega\right). \tag{2.2.24}$$

This representation (2.2.24), which originates from the work(s) of Stepišnik [16, 17], underlies temporal diffusion spectroscopy (TDS) [15] and related methods (e.g., oscillating gradient spin echo [66, 67]). This representation indicates that using

gradient waveforms which produce a sufficiently sharp power spectrum $|F(\omega)|^2$, such as sine-wave modulation in time, one can effectively probe $\widetilde{\mathcal{D}}(\omega)$ in a point-wise manner and trace out the time- (or frequency-)dependent diffusion over successive experiments. However, this point-wise sampling approach is inherently slow, and furthermore limited by the low slew rate of pulsed field gradients. Typically, maximal frequencies are around $100-200$ Hz, or $\sim 5-10$ ms in the time domain [68]. Higher-frequency (and thus shorter-time) information is not observable in this manner.

Time-domain representations

Single-integral representations in the time domain can also be obtained [65]. These may be more useful, in some sense, because they are intuitive and directly related to the ensemble MSD $\langle r^2(t)\rangle$ as a function of time. In addition, time-domain representations move away from the experimental paradigm of oscillating gradients, and can be applied more generally to arbitrary sequences.

Three such time-domain representations can be written, following Ning *et al.* [65]. Firstly, by Parseval's theorem and (2.2.24):

$$\frac{S}{S_0} = \exp\left(-\frac{1}{2\pi}\int_0^\infty |F(\omega)|^2 \widetilde{\mathcal{D}}(\omega)d\omega\right) = \exp\left(-\int_0^{\mathrm{TE}} \mathcal{F}(t)\langle v(t)v(0)\rangle dt\right), \tag{2.2.25}$$

where

$$\mathcal{F}(t) = \int_0^{\mathrm{TE}} F(s)F(s+t)ds \tag{2.2.26}$$

is the autocorrelation of $F(t)$. One can also derive, starting from (2.2.20), that

$$\frac{S}{S_0} = \exp\left(\frac{1}{2}\int_0^{\mathrm{TE}} \langle r^2(t)\rangle \mathcal{G}(t)dt\right), \tag{2.2.27}$$

where

$$\mathcal{G}(t) = \int_0^{\mathrm{TE}} G(s)G(t+s)ds \tag{2.2.28}$$

is the *gradient* autocorrelation function. Subsequently, integrating (2.2.27) by parts yields an expression in terms of the instantaneous diffusivity $D_{\mathrm{inst}}(t)$,

$$\frac{S}{S_0} = \exp\left(-\int_0^{\mathrm{TE}} D_{\mathrm{inst}}(t)C(t)dt\right), \tag{2.2.29}$$

where $D_{\text{inst}}(t)$ is half the time-derivative of the MSD,

$$D_{\text{inst}}(t) = \frac{1}{2}\frac{\partial}{\partial t}\langle r^2(t)\rangle, \tag{2.2.30}$$

and

$$C(t) = \int_0^{\text{t}} \mathcal{G}(t')dt' \tag{2.2.31}$$

is the cumulative gradient autocorrelation. For completeness, we provide full derivations of (2.2.27) and (2.2.29) in Appendix A.

This final signal representation (2.2.29) is particularly useful because it measures a transport property $D_{\text{inst}}(t)$ which hones in on the anomalous diffusion behavior. Consider, if the MSD is linear in time, as in free diffusion, then $D_{\text{inst}}(t)$ is simply D_0. Barriers will cause sub-diffusion, or a less than linear change in the MSD such that $D_{\text{inst}}(t)$ decreases over time. It is precisely this decay of $D_{\text{inst}}(t)$ — and the resulting preservation of signal, weighted by $C(t)$ — which characterizes the deviation from free diffusion or Brownian motion within the spin ensemble.

To illustrate how these representations may be applied to experiments, we calculate $\mathcal{G}(t)$ and $C(t)$ for the SG-SE sequence, first shown in Fig. 2.9. In calculating $\mathcal{G}(t)$, we shift $G(t)$ over all time-shifts from $[0, \text{TE}]$ and then evaluate the area of the product of the un-shifted and shifted $G(t)$ under that same interval. We have that:

$$G(t) = G\begin{cases} 1 & 0 \le t \le \tau \\ -1 & \tau \le t \le 2\tau \end{cases}. \tag{2.2.32}$$

There is a maximum at $\mathcal{G}(0) = 2G^2\tau$, a minimum at $\mathcal{G}(\tau) = -G^2\tau$ (when the positive part and negative part overlap), and $\mathcal{G}(2\tau) = 0$. Because $\mathcal{G}(t)$ is linear:

$$\mathcal{G}(t) = G^2\begin{cases} 2(\tau - 3t) & 0 \le t \le \tau \\ t - 2\tau & \tau \le t \le 2\tau \end{cases}. \tag{2.2.33}$$

Finally, we integrate piece-wise whilst adding terms to the intervals after the first as necessary to make $C(t)$ continuous:

$$C(t) = \begin{cases} t\left(-\frac{3}{2}t + 2\tau\right) & 0 \le t \le \tau \\ t\left(\frac{1}{2}t - \tau\right) + 2\tau^2 & \tau \le t \le 2\tau \end{cases}. \tag{2.2.34}$$

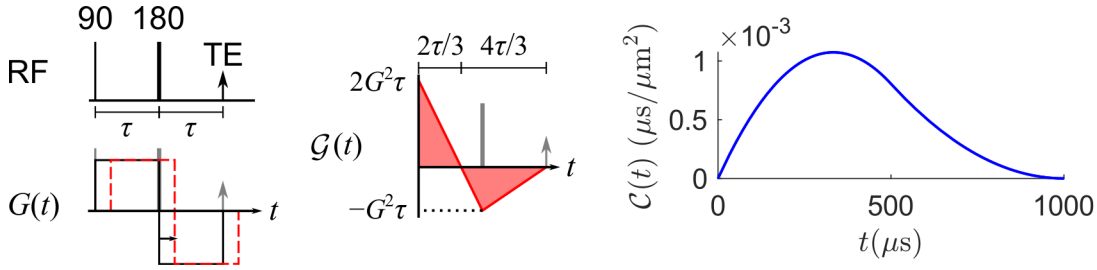

Figure 2.10: Visualization of the calculation of $\mathcal{G}(t)$ and $C(t)$ for the SG-SE sequence (left). The integral of the product of $G(t)$ and its shifted counterpart (red dashed lines) yield $\mathcal{G}(t)$ (middle), which is then integrated to yield $C(t)$ (right). An exemplar $C(t)$ is plotted for $\tau = 500\ \mu$s (TE $= 2\tau = 1$ ms) and $G = 15.3$ T/m, corresponding to the PM-10 system.

Table 2.6: Single-integral representations of the diffusion attenuation S/S_0 at a gradient echo formed at $t =$ TE, assuming mass balance and a Gaussian phase distribution.

Transport property	**Weighting function**	**Signal**: $\ln(S/S_0)$
$\langle r^2(t)\rangle$	$\mathcal{G}(t) = \int_0^{\mathrm{TE}} G(s)G(s+t)ds$	$\frac{1}{2}\int_0^{\mathrm{TE}} \langle r^2(t)\rangle \mathcal{G}(t)dt$
$D_{\mathrm{inst}}(t)$	$C(t) = \int_0^{\mathrm{t}} \mathcal{G}(t')dt'$	$-\int_0^{\mathrm{TE}} D_{\mathrm{inst}}(t)C(t)dt$
$\langle v(t)v(0)\rangle$	$\mathcal{F}(t) = \int_0^{\mathrm{TE}} F(s)F(s+t)ds$	$-\int_0^{\mathrm{TE}} \mathcal{F}(t)\langle v(t)v(0)\rangle dt$
$\widetilde{\mathcal{D}}(\omega)$	$\lvert F(\omega)\rvert^2 = \left\lvert\int_0^{\mathrm{TE}} F(t)\exp(i\omega t)dt\right\rvert^2$	$-\frac{1}{2\pi}\int_0^{\infty} \lvert F(\omega)\rvert^2 \widetilde{\mathcal{D}}(\omega)d\omega$

The calculation of $C(t)$ for the SG-SE sequence is visualized in Fig. 2.10. Consider that the shape of $C(t)$ defines the time-domain weighting of a sequence. For an SG-SE sequence, $C(t)$ spans $t = [0, \mathrm{TE} = 2\tau]$ and is rather broad — as expected for a gradient that is not oscillated over many cycles – with a peak at $t = \frac{2}{3}\tau$.

In summary, the GPA under the additional assumption of mass balance yields a family of time- and frequency-dependent signal representations in terms of equivalent (stationary) transport properties that are inter-convertible:

$$D_{\mathrm{inst}}(t) \underset{\partial_t/2}{\overset{2\int_0^t dt}{\rightleftharpoons}} \langle r^2(t)\rangle = 2tD(t) \underset{2\int_0^t (t-t')\,dt'}{\overset{\partial_t^2/2}{\rightleftharpoons}} \langle v(t')v(0)\rangle \overset{\mathscr{F}}{\longleftrightarrow} \widetilde{\mathcal{D}}(\omega), \tag{2.2.35}$$

where $\mathscr{F}$ denotes Fourier transformation. The various single-integral representations are summarized in Table 2.6 [64, 65].

2.2.3 Limiting regimes of signal behavior

We should also investigate when these results are valid, that is, when the GPA holds. To do so, we will look at several limiting regimes of signal behavior.

Characteristic lengthscales

According to Hürlimann *et al.* [69] and others [70–73], the signal decay due to diffusion can be separated, roughly speaking, into three regimes (c.f. Grebenkov [74], Yablonskiy & Sukstanskii [75]). For simplicity, we will consider only the SG-SE sequence with gradient amplitude g and echo time 2τ or, equivalently, the PG-SE sequence where $\delta = \Delta = \tau$ (see Fig. 2.9). The three regimes are associated with three lengthscales: (i) the diffusion length,

$$\ell_d = \sqrt{D_0 \tau}, \tag{2.2.36}$$

which is the typical distance travelled by a spin isochromat during each application of the gradient; (ii) the gradient dephasing length,

$$\ell_g = (D_0/G)^{1/3}, \tag{2.2.37}$$

which is the distance that two isochromats with the same initial position must travel to de-correlate their phase (i.e., such that $\phi_1 - \phi_2 = 2\pi$); and (iii) the structural length, ℓ_s, which is the lengthscale over which spins are restricted along the gradient direction, e.g., $\ell_s = 2R$ for spherical pores, where R is the radius.

The smallest of the three lengthscales determines the regime of signal behavior [69]. The simplest case is when $\ell_d \ll \ell_s$. Spins do not encounter barriers on the experimental timescale, the GPA holds, free diffusion is observed, and the b-value representation may be used (2.2.4). Note that the attenuation due to diffusion can be expressed in terms of the lengthscales as

$$bD_0 = \frac{2}{3}\left(\frac{\ell_d}{\ell_g}\right)^6. \tag{2.2.38}$$

Motional averaging

When ℓ_s is smallest, spins can diffuse across the restricted (i.e., bounded) volume without significant dephasing. In this regime, spins are confined within a space that is much smaller than a turn of the phase winding helix imposed by a diffusion-weighting gradient. Spins thus experience a limited range of frequency offsets $\Delta\omega$, resulting in the 'motional averaging' or narrowing regime [76–78]. Does the GPA break down in this case?

Consider that if $\ell_s \ll \ell_d, \ell_g$, then spins will fully sample the structure during the measurement (we stress, again, without significant dephasing). This means that observing a spin isochromat at the echo time amounts to taking an individual sample of the phase distribution $P(\phi, \mathbf{r})$ associated with the structure, which is not necessarily Gaussian. By the central limit theorem, observing the spin *ensemble* will produce a Gaussian distribution. Hence, the GPA holds for the motional averaging regime. Put another way, the GPA holds when the initial position of spins does not matter.

Localization

When ℓ_g is smallest, signal localized near barriers perpendicular to the gradient (within a distance of roughly ℓ_g) dephases much more slowly than signal from spins that are farther from barriers. This localized signal dominates, producing the so-called 'localization' regime [70, 79–81]. In the long τ limit (i.e., large ℓ_d), signal at a distance greater than ℓ_g from barriers has completely dephased and the decay of the persistent localized signal, assuming no exchange across barriers, is, to a first-order approximation [70],

$$\frac{S}{S_0} \simeq a_0 \cdot \frac{\ell_g}{\ell_s} \exp\left(-a_1 \left[\frac{\ell_d}{\ell_g}\right]^2\right), \;\; \ell_g \ll \ell_d, \ell_s \tag{2.2.39}$$

where a_0 is a geometry-dependent prefactor (e.g., $a_0 = 5.8841$ in the case of parallel plates [69]) and $a_1 = 1.0188$ is a universal prefactor. Compared to the other regimes, the signal behavior in the localization regime is complicated, however, and higher order terms may be significant [70, 82].

In the localization regime, the initial position of spins *does* matter, and the GPA breaks down. Higher order, even moments of the phase distribution $P(\phi)$ may need to be considered, and the signal representations developed in Sec. 2.2.2 may not apply. We can say that in general, the GPA approximately holds when $\ell_d \lesssim \ell_g$, or for small to intermediate b-values (2.2.38), i.e., $-bD_0 \lesssim \frac{2}{3}$, irrespective of structure. At larger b-values, the possibility of localized signal behavior must be acknowledged, and the range of relevant structure sizes ℓ_s becomes important.

Accessible diffusion times

Framing the diffusion MR experiment in terms of these lengthscales allows us to assess what sort of time- and lengthscale regimes are practically accessible. Setting $\ell_d = \ell_g$ is a reasonable heuristic which produces appreciable, but not excessive attenuation, and avoids the localization regime. Solving for τ when $\ell_d = \ell_g$:

$$\tau = (\gamma g)^{-2/3} D_0^{-1/3}. \tag{2.2.40}$$

For the PM-10 NMR-MOUSE with $g = 15.3$ T/m, we have approximately that $\tau = 0.3$ ms for $D_0 = 3\ \mu\text{m}^2/\text{ms}$. For a more typical gradient of, say, $g = 0.3$ T/m, we have that $\tau = 4$ ms. These correspond to ℓ_d of around 1 vs. 3.5 μm, respectively. The advantages of the extremely strong gradients provided by PM-10 NMR-MOUSE are made clear; the large gradient allow us to measure diffusion at short, sub-millisecond timescales as well as sub- to single-micron lengthscales.

2.2.4 Time-dependent diffusion

We now possess the signal models to characterize $D(t)$ (i.e., from its equivalent transport properties (2.2.35), e.g., $D_{\text{inst}}(t) = \partial_t [2tD(t)]$), provided that the GPA and mass balance are valid assumptions. But what form might $D(t)$ actually take? And how might $D(t)$ relate to the microstructure? Analytical models of $D(t)$ and the resulting signal generally do not exist [83], and must be simulated (e.g., by Monte Carlo methods). Let us consider several special cases where such solutions do exist.

Restricted diffusion in simple geometries

In simple, impermeable geometries such as spheres, it is possible to obtain exact solutions for the phase covariance $\langle \phi^2(t) \rangle$. These solutions were provided by Neuman [77] for the SG-SE sequence. Briefly, beginning from (2.2.20):

$$\frac{S}{S_0} = \exp\left(-\frac{1}{2} \int_0^{\mathrm{TE}} \int_0^{\mathrm{TE}} G(t) \langle r(t) r(t') \rangle G(t') dt\, dt' \right),$$

under the GPA. The position autocorrelation can then be re-written in terms of position and displacement probabilities

$$\langle r(t) r(t') \rangle = \int_{V_0} \int_V \int_{V'} (r - r_0)(r' - r_0)\ P(r_0) P(r, r_0; t) P(r, r'; t' - t)\ dV_0 dV dV', \quad (2.2.41)$$

where V denotes the considered volume, $P(r_0)$ is the initial distribution, $P(r, r_0; t)$ is the probability of displacement from r to r_0 over t, and $P(r, r'; t' - t)$ is the probability of displacement from r to r' over t to t'. One can solve for P using the diffusion equation,

$$\frac{\partial P}{\partial t} = D_0 \nabla^2 P, \quad (2.2.42)$$

and by applying the initial condition $P(t = 0) = \delta(r - r_0)$ and the Neumann boundary condition ($\nabla^2 P = 0$ at the boundary), which amounts to impermeability or 'hard' boundaries, also called restricted diffusion or simply restriction.

Solving for P is analogous to the treatment of heat conduction and other transport phenomena and solutions are known for simple geometries [84]. For example, for spheres of radius R [77, 85, 86], one obtains

$$\frac{S}{S_0} = \exp\left(-\frac{2G^2}{D_0} \sum_{m=1}^{\infty} \frac{\alpha_m^{-4}}{(\alpha_m R)^2 - 2} \left[2\tau - \frac{3 - 4\exp\left(-\alpha_m^2 D_0 \tau\right) + \exp\left(2\alpha_m^2 D_0 \tau\right)}{\alpha_m^2 D_0} \right] \right), \quad (2.2.43)$$

where α_m is mth root of

$$\alpha_m R J'_{3/2}(\alpha_m R) - \frac{1}{2} J_{3/2}(\alpha_m R) = 0, \quad (2.2.44)$$

and J is a Bessel function of the first kind, for which the first five roots are given by $\alpha_m R = 2.0815, 5.940, 9.206, 12.405, 15.579$, and $G = \gamma g$ is the static gradient amplitude.

When τ is much longer than the time needed to diffuse to the boundary R^2/D_0 — i.e., $\ell_d \gg \ell_s$, or the motional averaging regime — one obtains the approximation,

$$\frac{S}{S_0} \approx \exp\left(-\frac{8}{175}\frac{R^4\gamma^2 g^2}{D_0}\left[2\tau - \frac{581}{840}\frac{R^2}{D_0}\right]\right), \tag{2.2.45}$$

and generally for motional averaging, the long-ℓ_d, ℓ_g signal behavior takes the form

$$\frac{S}{S_0} \simeq \exp\left(-a \cdot \frac{\ell_s^4 \ell_d^2}{\ell_g^6}\right), \ \ell_s \ll \ell_d, \ell_g \tag{2.2.46}$$

where $\ell_s = 2R$ for spheres and we drop the trailing term $R^2/D_0 \propto (\ell_s/\ell_d)^2$ as being small compared to $2\tau \propto \ell_d^2$. The prefactor a (e.g., $a = 2/175$ for spheres [77]) depends on the geometry.

Hindered or tortuous diffusion

On the other extreme, what if the structures are fully-connected — whether by high permeability or an open pore structure? Diffusion in a medium consisting of fully-connected pores (i.e., the MSD remains unbounded) is said to be hindered. The actual path length $\Delta l(t) = \int_0^t r(t')dt'$ travelled by a spin isochromat is longer than the net displacement $\Delta r(t) = r(t) - r(0)$, where the ratio $\Delta l/\Delta r$ depends on the tortuosity of the medium and the time over which diffusion is observed. The diffusivity is modified by a tortuosity factor [87]:

$$D(t) = D_0\left(\frac{\langle \Delta r(t)\rangle}{\langle \Delta l(t)\rangle}\right)^2. \tag{2.2.47}$$

In the long-time limit when the medium is fully explored by the diffusing species, the tortuosity factor becomes a constant $\mathcal{T}$, at which point the b-value signal model (2.2.4) may be applied with an effective Gaussian diffusivity

$$D_\infty = \lim_{t\to\infty} D(t) = \frac{D_0}{\mathcal{T}}, \ \mathcal{T} = \lim_{t\to\infty}\left(\frac{\langle \Delta r(t)\rangle}{\langle \Delta l(t)\rangle}\right)^2 \tag{2.2.48}$$

in place of D_0. This is called the tortuosity limit. Novikov *et al.* [83, 88–90] found that the asymptotic decrease of $D_{\text{inst}}(t)$ from D_0 to D_∞ generally takes the form of some power law,

$$D_{\text{inst}}(t) \simeq D_\infty + \text{const.} \cdot t^{(d+p)/2}, \ t \to \infty \tag{2.2.49}$$

where d is the dimensionality and p is a structural exponent characterizing the disorder of the medium. Hindered and free diffusion are often collectively referred to as Gaussian diffusion, contrasted with non-Gaussian diffusion (all other cases).

The short-time limit

Finally, Mitra *et al.* [2, 4] found that in the short-time limit when few collisions with barriers have occurred $\ell_d \lesssim \ell_s$, $D(t)$ exhibits universal behavior which depends on the barrier's surface-to-volume ratio (SVR, S/V),

$$D(t) \simeq D_0 \left[1 - \frac{S}{V}\left(\frac{4\ell_d}{9\sqrt{\pi}}\right)\right], \quad t \to 0. \tag{2.2.50}$$

This result extends the signal model for free diffusion to account for the effects of initial encounters with a barrier.

2.3 Diffusion in neural tissue

How can these signal models be applied to tissue? There are two major types of tissue in the central nervous system: white matter (WM) and gray matter (GM). WM is mainly composed of myelinated axons and oligodendrocytes, whereas GM includes a variety of components: soma, unmyelinated axons, dendrites, glia (astrocytes, microglia), and glial processes. More generally, there is an extracellular space (ECS) outside the plasma membranes of cells, contrasted with the intracellcular space (ICS). Blood vessels and cerebrospinal fluid (CSF) compartments may also be present.

2.3.1 Compartment models

The size of an imaging voxel (on the order of mm) is much larger than the size of individual cells or cellular processes (on the order of μm). Thus, any diffusion MR measurement probes a block of tissue which may contain many cellular structures of varying sizes (i.e., ℓ_s), along with the ECS and blood vessels. That is, the signal behavior arises from a heterogeneous mixture of components.

Multi-exponential representation

One approach to model the heterogeneous signal arising from tissue is to extend the b-value representation to account for a distribution of diffusivities $P(D)$ [91]:

$$\frac{S}{S_0} = \int_0^\infty P(D) \exp(-bD)\, dD. \tag{2.3.1}$$

By measuring the signal over a range of b-values, one can obtain, by a numerical inverse Laplace transform (ILT), the apparent $P(D)$. This is a well-known ill-posed mathematical problem, however, and care must be taken in implementing the numerical techniques (e.g., see CONTIN [92] and Refs. [93, 94]) and in acquiring a sufficient coverage of b-values. Simpler, related approaches may be taken. For example, one may assume a biexponential representation [95] with two diffusivities denoted D_I and D_E (e.g., for the ICS and ECS) with relative signal fractions f_I and f_E ($f_I + f_E = 1$):

$$\frac{S}{S_0} = f_I \exp(-bD_I) + f_E \exp(-bD_E). \tag{2.3.2}$$

Such multiexponential approaches, however, are empirical, and do not reflect the actual signal behavior. For instance, consider that in the motional averaging regime (2.2.46), the decay scales with ℓ_d^2/ℓ_g^6 at long times, as compared to $bD_0 \propto (\ell_d/\ell_g)^6$ (2.2.38). If we hold G constant and vary τ to achieve different b-values as in an SG-SE experiment, then only ℓ_d varies, and the signal decay actually scales with $(bD_0)^{1/3}$. Thus, a homogeneous distribution of spheres with equal radii would produce a broad spectrum $P(D)$ by this method, erroneously suggesting size heterogeneity when none is present, as we will later show in Chapter 3 (Sec. 3.4.3).

The 'standard model' of white matter

More rigorous tissue models take the approach of adapting one or more of the signal models presented in Sec. 2.2.4 [96]. For example, the Combined Hindered and Restricted Model of Diffusion (CHARMED) [97] models WM as restricted signal arising from myelinated axons and neurites, using (2.2.46) with a cylindrical pre-factor, and hindered signal arising from the ECS, using (2.2.48). CHARMED

and similar models have come to be known as part of a 'standard model' of WM [96], though such models usually also include an impermeable, zero-radius 'stick' component [98], representing small axons or neurites.

While the 'standard model' has been effective for describing the signal behavior due to diffusion in WM, it has failed to translate to GM [89, 96, 99], perhaps due to the high permeability of GM components, such as astrocytes which highly express aquaporin-4 (AQP4), a transmembrane water channel [100].

Gray matter: The exchange problem

Many recent signal models, summarized by Olesen *et al.* [101] (e.g., SANDI [102] and NEXI [103]), have attempted to extend the 'standard model' to apply to GM. These models variously include: soma modelled as restricted spheres, exchange between neurites (restricted cylinders) and soma, exchange between neurites and the hindered ECS, a fraction of impermeable neurites, and a dot compartment (having no visible signal decay). The key difference between GM and WM, therefore, is the need to account for exchange between two or more compartments on the timescale of the measurement. We will now discuss permeability to indirectly address GM signal modelling.

2.3.2 Permeability and exchange

The permeability of a barrier is described by a permeability coefficient κ, which has units of length per time and can be thought of as a velocity through the membrane.

The high-permeability regime

Following Novikov [88] and Grebenkov [104], we define an additional characteristic lengthscale: the permeability length

$$\ell_\kappa = \frac{D_0}{\kappa}, \tag{2.3.3}$$

which is the effective length of the membrane — that is, the distance the spin density profile $\rho(\mathbf{r})$ would need to be shifted to heal the jump discontinuity imposed by the

membrane [88]. This ratio can also be seen as a competition between the diffusive kinetics and the barrier. When $\ell_\kappa \ll \ell_s, \ell_d$ (i.e., κ is large), the barrier acts merely as a hindrance and the hindered model of diffusion is recovered [64] with

$$D_\infty = \frac{D_0}{1+\zeta}, \tag{2.3.4}$$

where

$$\zeta = \frac{1}{2d}\left(\frac{S}{V}\right)\ell_\kappa \tag{2.3.5}$$

characterizes the ability of the membranes to hinder diffusion, S/V is the SVR and d is the dimensionality. The kinetics are diffusion-limited in this case and indicate that compartments with highly permeable membranes can be lumped into a hindered component of the signal model when $\ell_\kappa \ll \ell_s, \ell_d$.

The low-permeability regime

When $\ell_\kappa \gg \ell_s$ (small κ) as well as $\ell_d \gg \ell_s$, the kinetics become barrier-limited. Making a similar argument to that which was made when discussing motional averaging, spins will diffuse between the barriers many times during the observation time (i.e., they are well-mixed) such that exchange across the barrier is homogeneous along the surface area of the structure and the spin density ρ within the structure is uniform for all times. We will ignore, for the time being, spins outside the structure and re-entry after exchange, focusing on the efflux rate of spins. In this case, the leakage flux may be written as

$$\frac{\partial \rho}{\partial t} = -\rho\kappa\left(\frac{S}{V}\right), \quad \ell_\kappa, \ell_d \gg \ell_s \tag{2.3.6}$$

which gives

$$\rho(t) = \rho_0 \exp\left(-k_{\text{out}} t\right), \tag{2.3.7}$$

where

$$k_{\text{out}} = \frac{\kappa S}{V}, \tag{2.3.8}$$

is the exchange rate out of the structure. Barrier-limited exchange is seen to be an inherently first-order rate process, wherein the exchange rate is proportional to

Table 2.7: Characteristic lengthscales which define the signal behavior due to diffusion in an SG-SE experiment with gradient $G = \gamma g$ and echo time 2τ.

Lengthscale	**Formula**	**Description**
Diffusion length	$\ell_d = \sqrt{D_0 \tau}$	Typical distance travelled by a spin during each gradient application
Structural length	ℓ_s	Length scale over which spins are restricted (e.g., diameter $\ell_s = 2R$ for spheres)
Gradient dephasing length	$\ell_g = (D_0/G)^{1/3}$	Distance two spin isochromats at the same initial position must travel to de-correlate their phase by 2π
Permeability length	$\ell_\kappa = D_0/\kappa$	Ratio of diffusivity and permeability; competition between diffusive and barrier-limited kinetics

the SVR and the permeability of the membrane. One can also define the typical residence time or exchange time under these conditions,

$$\tau_k = \frac{1}{k} = \frac{V}{\kappa S}. \tag{2.3.9}$$

We have now presented a full picture of the various diffusion signal models and their associated regimes, characterized by different lengthscales, given in Table 2.7. These regimes are summarized in Fig. 2.11.

The Kärger model

Incorporating exchange into diffusion signal models is non-trivial. The most common approach [101] is to use some variation of the Kärger model [105, 106]. This model assumes the presence of two compartments denoted I and E (to represent, for instance, the ICS and ECS) and their respective normalized signal:

$$\frac{S}{S_0} = S_I + S_E. \tag{2.3.10}$$

The following coupled differential equations are solved,

$$\begin{cases} dS_I/dt = S_E k_{E\to I} - S_I(R_I + k_{I\to E}) \\ dS_E/dt = S_I k_{I\to E} - S_E(R_E + k_{E\to I}) \end{cases}, \tag{2.3.11}$$

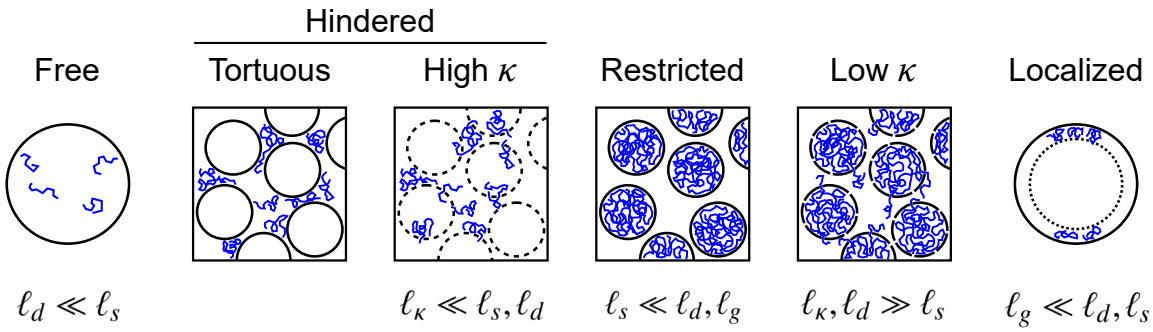

Figure 2.11: Summary of the regimes of signal behavior due to diffusion in order of increasing complexity, left to right. Note that these lengthscales are defined for the extended gradient experiment (SG, or PG with $\delta = \Delta$). For short diffusion times $\ell_d \gg \ell_s$, diffusion is effectively free. The b-value representation (2.2.4) and the short-time limit (2.2.50) apply. For tortuous diffusion in a fully-connected space, or for highly permeable boundaries $\ell_\kappa \ll \ell_s, \ell_d$, the hindered diffusion model (2.2.48) applies with some effective diffusivity D_∞ at long ℓ_d (2.3.4). For restricted diffusion in the motional averaging regime $\ell_s \ll \ell_d, \ell_g$, Neuman's [77] solutions apply (2.2.46). In the low-permeability regime $\ell_\kappa, \ell_d \gg \ell_s$, exchange is barrier-limited and obeys first-order rate kinetics. The Kärger model (2.3.11) may be used. Finally, when $\ell_g \ll \ell_d, \ell_s$, the localization regime appears and signal behavior is complicated, with a persistent annulus of signal of width $\approx \ell_g$ perpendicular to the gradient. The GPA breaks down. For the low-permeability case, the limiting behavior in (2.2.39) applies.

where $k_{I\to E}$, $k_{E\to I}$ are directional exchange rates and R_I, R_E are decay rates. Usually, Gaussian diffusion and an infinitely narrow gradient pulse ($\delta \approx 0$) are assumed such that the signal decay rate (for a PG-SE experiment) may be written as $R = F^2 \Delta D$ [106, 107]. We will, however, provide the more general solution, acknowledging that the decay may also contain relaxation terms or may arise from non-Gaussian diffusion. Such solutions were given in Refs. [108, 109]. The initial conditions used to solve (2.3.11) are the signal fractions at equilibrium, f_I and f_E:

$$S_I(t=0) = f_I = 1 - f_E, \;\; S_E(t=0) = f_E. \tag{2.3.12}$$

Solving,

$$S_I = (1 - f_E)\left[X_2 + \frac{k_3 + k' + 2r_S k_{E\to I}}{2k'}(X_1 - X_2)\right] \tag{2.3.13a}$$

$$S_E = f_E\left[X_1 - \frac{k_3 + k' + 2r_S^{-1} k_{I\to E}}{2k'}(X_1 - X_2)\right] \tag{2.3.13b}$$

where k_1, k_2, and k_3 are linear combinations of the decay and exchange rates,

$$\begin{aligned} k_1 &= (R_E + k_{E\to I}) + (R_I + k_{I\to E}), \\ k_2 &= (R_E - k_{E\to I}) - (R_I - k_{I\to E}), \\ k_3 &= (R_E + k_{E\to I}) - (R_I + k_{I\to E}), \end{aligned} \tag{2.3.14}$$

$X_{1,2}, k'$ are defined as,

$$\begin{aligned} X_{1,2} &= \exp\left(-\tau\left[k_1 \mp k'\right]\right), \\ k' &= \sqrt{k_2^2 + 4k_{I\to E}k_{E\to I}}, \end{aligned} \tag{2.3.15}$$

and r_S is the signal ratio at equilibrium,

$$r_S = \frac{f_b}{1 - f_b}. \tag{2.3.16}$$

Note that one parameter may be eliminated by mass balance, which implies equal bi-directional flux:

$$f_E k_{E\to I} = f_I k_{I\to E}. \tag{2.3.17}$$

Another possible simplification is to assume that the decay in the ICS compartment is negligible and set the decay rate to 0 [107].

Concluding remarks

While the Kärger model can be simplified, it remains evidently unwieldy, and highlights the principal problem regarding the conventional measurement of exchange using diffusion MR. That is, the number of parameters that must be included in the signal model increases when exchange is considered, which can make attaining fit stability difficult. The increase in parameters also results in degeneracy [101, 110]. These issues are further compounded by the number of compartments that are considered to be exchanging. For these reasons, the study of GM has been called a 'terra incognita' [83] for diffusion MR, with exchange greatly complicating the characterization of GM tissue.

That being said, we now turn towards the novel results of this thesis. In the following chapter, we develop and demonstrate a method to isolate exchange from

other signal evolution mechanisms using double pulsed-field gradient or double diffusion encoding methods, overcoming the issue of parameter degeneracy and reducing the data requirement in the process.

3
Rapid Isolation of Exchange

3.1 Introduction 50
3.1.1 Chapter outline and related works 51
3.2 Diffusion Exchange Spectroscopy (DEXSY) 53
3.2.1 The DEXSY pulse sequence 54
3.2.2 Conventional DEXSY analysis 56
3.3 The 'curvature' method 58
3.3.1 The bi-exponential signal model 58
3.3.2 Validation on a tissue phantom 62
3.3.3 Correspondence in fixed spinal cord 66
3.3.4 Normalization approaches 76
3.4 Disentangling restriction and exchange 81
3.4.1 Signal scaling for non-Gaussian diffusion 81
3.4.2 Two-compartment model with restriction 85
3.4.3 Artifacts in diffusion-diffusion spectra due to restriction . . 87
3.4.4 Measuring restriction from curvature 90
3.5 Comparison to 'Filter Exchange' methods 92

3.1 Introduction

Given that exchange introduces additional parameters into the modelling of the diffusion MR signal (leading to fitting issues), a natural remedy is to increase the number of *experimental* parameters or dimensions. One way to do so is to utilize double pulsed-field gradient (dPFG) or double diffusion encoding (DDE),

wherein two GREs of potentially different b-values are formed and the second is measured. Coelho *et al.* [111] and others [112–114] have shown that DDE-based methods provide additional information that is largely inaccessible to conventional, single diffusion encoding (SDE) methods. Of course, an increase in experimental dimensions can lead to longer experiment times. Thus, the challenge of optimizing such methods is the balancing act between experiment time and information. Here, we address a sub-problem within the broader challenge of optimizing DDEs: What is the minimum number of DDE acquisitions needed to robustly measure exchange as an isolated effect?

3.1.1 Chapter outline and related works

We begin from the DDE method, Diffusion Exchange Spectroscopy (DEXSY), proposed by Callaghan and Furó [14]. In DEXSY, two diffusion encodings along the same direction $[b_1, b_2]$ are separated by a longitudinal storage time, called the mixing time t_m. Data is acquired across a grid of $[b_1, b_2]$ to determine the diffusion-diffusion correlation at multiple t_m and quantify exchange.

We first show that the signal variation due to exchange can be isolated by sub-sampling DEXSY data following a rotation of axes in the $[b_1, b_2]$ domain. We call this sampling scheme the 'curvature' method for reasons made clear in Sec. 3.3. We validate the method on a tissue phantom using a pre-clinical imaging system. This work was first described in [115]:

- †**Cai, T. X.**, Benjamini, D., Komlosh, M. E., Basser, P. J., & Williamson, N. H. (2018). Rapid detection of the presence of diffusion exchange. *Journal of Magnetic Resonance*, *297*, 17–22.

Rather than a whole grid of $[b_1, b_2]$-values (e.g., 32×32 [14]), a minimum of 4 points per mixing time is shown to be sufficient to measure the exchanging signal fraction, representing an orders-of-magnitude reduction in experiment time compared to fully-sampled DEXSY. †We stress that this work was published before the start of the degree and is included here only insofar as is necessary to understand the follow-up works. We do, however, expand significantly upon the work, providing

previously unpublished analyses to support the optimality of the method and which merit inclusion here.

We next demonstrate the curvature method on *ex vivo* neonatal mouse spinal cord using the PM-10 NMR-MOUSE (Fig. 2.8, Sec. 2.1.4) and further develop the experimental details in collaborative works that were led by Dr. Williamson, with input on the theory from myself, along with new analyses for this thesis:

- Williamson, N. H., Ravin, R., **Cai, T. X.**, Benjamini, D., Falgairolle, M., O'Donovan, M. J., & Basser, P. J. (2020) Real-time measurement of diffusion exchange rate in biological tissue. *Journal of Magnetic Resonance*, *317*, 106782.

- Williamson, N. H., Ravin, R., Benjamini, D., Merkle, H., Falgairolle, M., O'Donovan, M. J., Blivis, D., Ide, D., **Cai, T. X.**, Ghorashi, N. S., Bai, R., & Basser, P. J. (2019). Magnetic resonance measurements of cellular and sub-cellular membrane structures in live and fixed neural tissue. *eLife*, *8*, e51101.

Importantly, correspondence to full DEXSY experiments is shown. Normalization schemes (i.e., to remove the effects of relaxation) are also compared and the data requirement is reduced even further to just 1 or 2 points per mixing time, yielding an optimal 5-point measurement (in terms of SNR and rapidity) of the apparent exchange rate (AXR).

In the main first-authored work(s) described in this chapter we extend the theory underlying the curvature method to be more physically accurate by incorporating restriction, represented as an exchanging, motionally averaged compartment [77] (see Fig. 2.11 and Sec. 2.2.4), thereby bringing the theoretical framework more in line with other tissue compartmentalization models (see Sec. 2.3.1):

- **Cai, T. X.**, Williamson, N. H., Ravin, R., & Basser, P. J. (2022). Disentangling the effects of restriction and exchange with diffusion exchange spectroscopy. *Frontiers in Physics*, *10*, 805793.

- **Cai, T. X.**, Williamson, N. H., Ravin, R., & Basser, P. J. Isolating restriction and exchange in gray matter using double and single diffusion encodings with equal

diffusion weighting. (2022, June). [Oral Presentation]. *Proceedings of the 31st Annual Meeting of the ISMRM*, London, England, U.K., Abstract #252.

We show that the curvature method can also be used to quantify restriction in a manner isolated from exchange, overcoming the inherent degeneracy of these two effects. We highlight as well that restriction can lead to artifacts in the conventional analysis of DEXSY data, and caution against literal interpretation of DEXSY spectra in the presence of non-Gaussian diffusion. We again use the *ex vivo* tissue model and the PM-10 to validate this extended theoretical framework, along with synthetic data.

Finally, we conclude the chapter with a comparison of the curvature method to Filter Exchange Spectroscopy (FEXSY) [116], which is another way to efficiently sub-sample the $[b_1, b_2]$-domain based on using a fixed b_1 to 'filter' the signal from the more mobile compartment. While the methods are potentially similar in time-efficiency and SNR characteristics, the modelling approaches are fundamentally different. We argue that the curvature method can more easily be applied in a model-free manner, which readily permits follow-on analyses such as the analysis of distributed exchange times in Chapter 4.

3.2 Diffusion Exchange Spectroscopy (DEXSY)

Compared to SDE methods, DEXSY can better reveal the exchange dynamics between different diffusive microenvironments [14, 117], i.e., environments which show different degrees of signal attenuation due to diffusion. DEXSY also has distinct advantages over other MR/MRI methods that measure some form of exchange. Unlike arterial spin labelling or the related dynamic contrast enhanced (DCE) methods [118, 119], DEXSY can probe steady-state, *cellular* water exchange, and *without the use of exogenous contrast agents*. As such, DEXSY-based methods are ideally suited for studying trans-membrane water exchange of the cell and have begun to see wider use in biomedical applications in the past decade — either in its originally proposed form [117, 120, 121], or in a modified form [18, 19, 45, 46, 116, 122–131].

3.2.1 The DEXSY pulse sequence

The DEXSY experiment is composed of two diffusion encodings $[b_1, b_2]$ separated by a longitudinal mixing time t_m. Storing the signal longitudinally allows more time for exchange to occur ($T_1 > T_2$) and longer exchange processes can be observed. Indeed, longitudinal storage is the major difference between DEXSY and SDEs. While one can vary Δ in a PG-SE measurement as a pseudo-mixing time [101, 102, 132, 133], the range of accessible times is limited by T_2 rather than T_1. Furthermore, the magnetization continues to dephase during mixing (i.e., during Δ) for an SDE experiment such that there is limited decoupling of exchange from the effects of diffusion [111, 114]. This lack of decoupling is part of what makes the modelling and fitting of exchange difficult using SDEs. While DEXSY sequences have their own challenges, such as the loss of signal from multiple pulses, the decoupling of exchange and diffusion is a major advantage.

In general, a DEXSY sequence is sensitive to exchange with residence times τ_k that lie approximately between the diffusion encoding time (i.e., before rephasing: Δ for PG, and τ for SG) and $\approx 2T_1$. If $\tau_k \ll \tau$, we have the high-permeability case of $\ell_\kappa \ll \ell_s, \ell_d$ (see (2.3.4) and Fig. 2.11), and the signal behavior will resemble hindered diffusion (2.3.4) with limited ability to distinguish between compartments, which have nearly fully mixed during the encoding. This brings to light another advantage of the SG, PM-10 system; its capacity for extremely short diffusion encodings permits the observation of exchange as fast as $\tau_k \lesssim 1$ ms.

There are, of course, multiple ways to construct a DEXSY sequence. The PG- and SG-DEXSY sequences used in this chapter are shown in Fig. 3.1. Note that in the SG-DEXSY sequence, the b-value is modified by changing the diffusion encoding time τ (varying ℓ_d), whereas in PG-DEXSY, the timing parameters δ, Δ are usually held constant while G is varied (varying ℓ_g).

Coherence selection

The DEXSY sequences in Fig. 3.1 contain 5 (slice-selective) pulses before signal measurement and thus many coherences may be generated (indeed, up to 40

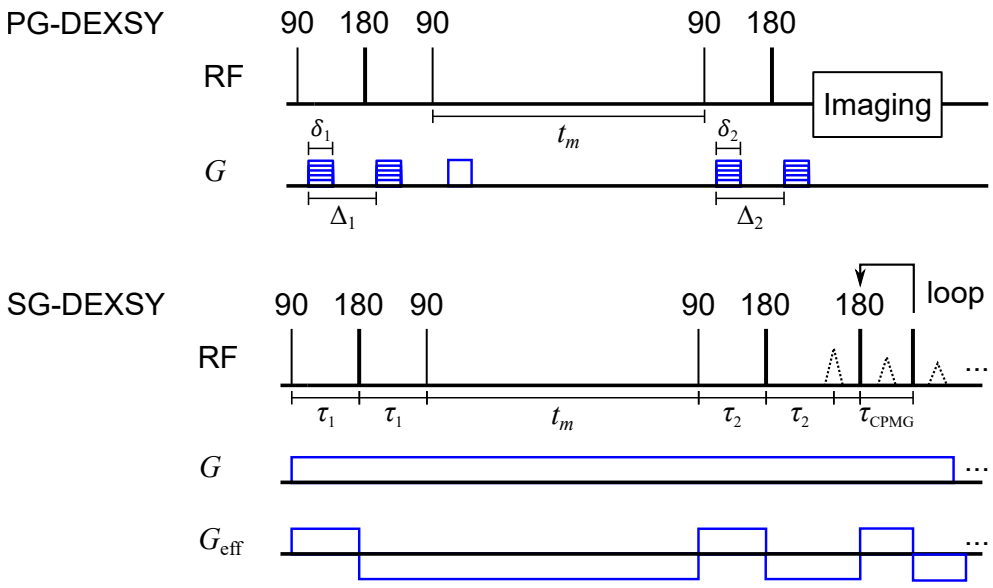

Figure 3.1: Pulsed and static gradient (PG, SG) forms of the DEXSY pulse sequence. In the PG-DEXSY sequence, slice-select gradients and between-repetition spoilers are present but not shown. Note the spoiler during t_m. In the SG-DEXSY sequence, a CPMG loop is played out at the end and the echoes are summed. This sum is treated as the signal, boosting SNR.

echoes [33]). Proper phase cycling and/or spoiling is therefore essential. Perhaps surprisingly, the optimal method(s) to suppress unwanted coherences in DEXSY sequences remains an area of ongoing development, with various methods extant in the literature. Compare, for instance, Refs. [129] and [134], which utilize different spoiling and phase cycling schemes.

In this chapter, we use a simple 2-step phase cycle for the PG-DEXSY experiment [115], cycling the storage 90°-pulses together to $\pm x$ (0 and π), along with a spoiler gradient during t_m (Fig. 3.1, top). For the SG-DEXSY experiment, we use a more considered 8-step phase cycle [45, 46], developed in-house, along with unequal diffusion-weightings ($\tau_1 \neq \tau_2$) to spoil certain pathways. In fact, however, neither of these approaches is optimal. The 2-step phase cycle fails to suppress all unwanted coherences and the 8-step phase cycle is redundant. Recently, we developed a more optimal DEXSY phase cycling scheme — a comprehensive, 4-step cycle — which is presented as a result in Chapter 4 (Sec. 4.3.2). We will return to the topic then. For now, we shall proceed with the caveat that some off-resonance effects may affect the presented PG-DEXSY results.

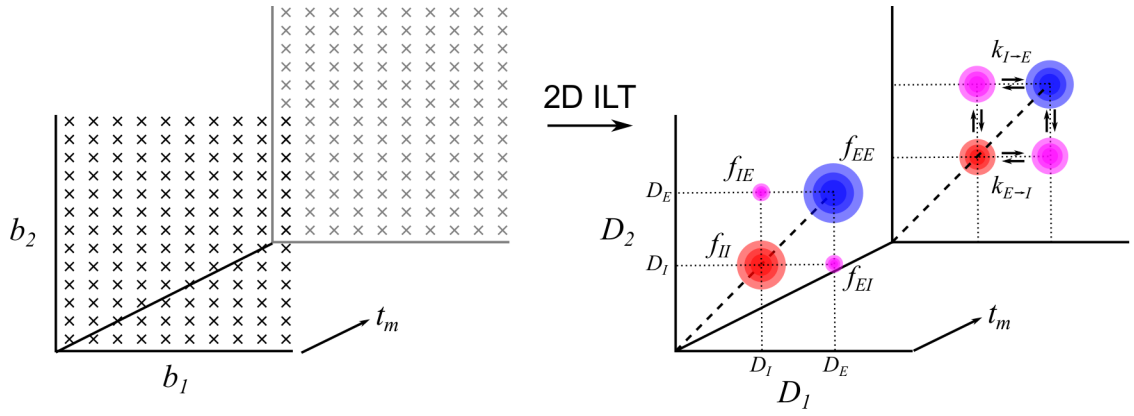

Figure 3.2: Schematic representation of DEXSY data analysis assuming two Gaussian compartments with diffusivities D_I and D_E. Off-diagonal peaks in the spectrum $P(D_1, D_2)$, labelled f_{IE} and f_{EI}, grow with increasing mixing time according to first-order rate kinetics.

3.2.2 Conventional DEXSY analysis

DEXSY is so-named because the data analysis is based on a 2D ILT, much like 2D relaxometry experiments [14, 117, 135]. DEXSY extends the representation in (2.3.1) to account for two diffusion encodings:

$$\frac{S(b_1, b_2, t_m)}{S_0} = \int_0^\infty \int_0^\infty P(D_1, D_2, t_m) \exp\left(-b_1 D_1 - b_2 D_2\right) dD_1 dD_2. \tag{3.2.1}$$

The use of an ILT, as mentioned previously, means that Gaussian diffusion is assumed and that the data must be well-sampled in the $[b_1, b_2]$ domain, with care given to how the numerical techniques (regularization, etc.) are employed. The joint probability distributions or spectra $P(D_1, D_2)$ measured at different t_m are then analyzed to quantify exchange. On-diagonal peaks, lying along $D_1 = D_2$, correspond to non-exchanging signal fractions, whereas off-diagonal peaks indicate exchanging signal fractions between diffusive microenvironments. The growth in these off-diagonal peaks with t_m can be fit to a first-order rate equation to yield an exchange rate. A representative diagram of this pipeline is shown in Fig. 3.2.

Two-site exchange modelling

To be more precise about how an exchange rate is measured, let us consider the simplest case of two microenvironments at steady state with equilibrium fractions

f_I, f_E. By mass balance, $f_{EI} = f_{IE}$, and we need only solve the following system [117, 135] (see Fig. 3.2):

$$\begin{bmatrix} df_{II}/dt \\ df_{IE}/dt \end{bmatrix} = \begin{bmatrix} -k_{I\to E} & k_{E\to I} \\ k_{I\to E} & -k_{E\to I} \end{bmatrix} \begin{bmatrix} f_{II} \\ f_{IE} \end{bmatrix}, \tag{3.2.2}$$

with initial conditions

$$f_{II}(0) = f_I, \;\; f_{IE}(0) = 0, \tag{3.2.3}$$

yielding

$$f_{IE}(t_m) = \frac{f_I\, k_{I\to E}}{k_{I\to E} + k_{E\to I}} \left[1 - \exp\left(-\left[k_{I\to E} + k_{E\to I}\right] t_m\right)\right]. \tag{3.2.4}$$

The numerator is the rate of signal turnover and is equal in both directions by mass balance: $f_I k_{I\to E} = f_E k_{E\to I}$ (2.3.17). Swapping the numerator gives the expression for f_{EI}. In practice, the *total* exchanging fraction f_{exch} is usually measured,

$$f_{\text{exch}}(t_m) = f_{IE} + f_{EI} = f_{\text{SS}}\left[1 - \exp\left(-k t_m\right)\right], \tag{3.2.5}$$

where

$$f_{\text{SS}} = \lim_{t_m\to\infty} f_{\text{exch}}(t_m) = \frac{2 f_I k_{I\to E}}{k} \tag{3.2.6}$$

is the exchanging fraction at steady state (long t_m) and

$$k = k_{I\to E} + k_{E\to I} \tag{3.2.7}$$

is the sum of exchange rates. Mass balance additionally implies that the proportion of exchange rates must be inversely related to the equilibrium signal fractions,

$$\frac{f_E}{f_I + f_E} = \frac{k_{I\to E}}{k}, \tag{3.2.8}$$

which allows the simplification

$$f_{\text{SS}} = 2 f_I f_E = 2 f_I (1 - f_I) \tag{3.2.9}$$

by $f_I + f_E = 1$. Finally, we amend (3.2.5) to have an intercept term $f_0 = f_{\text{exch}}(0)$ to capture extraneous effects such as exchange during the diffusion encoding and potential T_2 effects, among others. This leads to a 3-parameter model for exchange:

$$f_{\text{exch}}(t_m) = (f_{\text{SS}} - f_0)\left[1 - \exp\left(-k t_m\right)\right] + f_0, \tag{3.2.10}$$

composed of an (i) intercept (f_0) a (ii) limit (f_{SS}) and (iii) the exchange rate k. Thus, at least three values of t_m are needed to determine all three parameters, or two if the intercept $f_0 = 0$. We stress, however, that this is a simplified model. In reality, there may be multiple (> 2) exchanging sites and the detailed balance may break down while overall mass is still conserved [136]. Furthermore, differences in relaxation rates between compartments are not accounted for. Accordingly, we refer to k as an *apparent* exchange rate (AXR) [122], used interchangeably throughout.

3.3 The 'curvature' method

While DEXSY can provide a detailed view of the exchanging microenvironments (as in Fig. 3.2), the method is hampered by its extremely high data requirement. For a 32×32 grid of b-values, the experiment time is in excess of 10 hours, rendering its biological or clinical use infeasible.

Efforts have been made to accelerate the ILT, e.g., by compressed sensing [137] and more recently by constraints using the marginal 1D distribution [138–140]. These advances have greatly reduced the necessary amount of data to about 24 points per mixing time [140], bringing the total experiment time to 20 – 30 minutes. Much of that time, however, is actually spent on acquiring marginal distributions (where b_1 or $b_2 = 0$), which indicates that the exchange information can be acquired in even fewer points if one is willing to discard the information provided by the spectrum. Given the issues inherent to ILTs (numerical challenges, Gaussian diffusion assumption), it may be prudent to dispense with the ILT formalism altogether. We take this ILT-free approach here, and show that by careful sub-sampling of DEXSY data, one can measure an exchange rate in as few as 5 *total* points [45, 46, 115]. This is, to our knowledge, the fastest such measurement in the literature.

3.3.1 The bi-exponential signal model

We first develop the theory for our method using a biexponential signal model before later refining the model in Sec. 3.4. Following the schematic in Fig. 3.2, we may

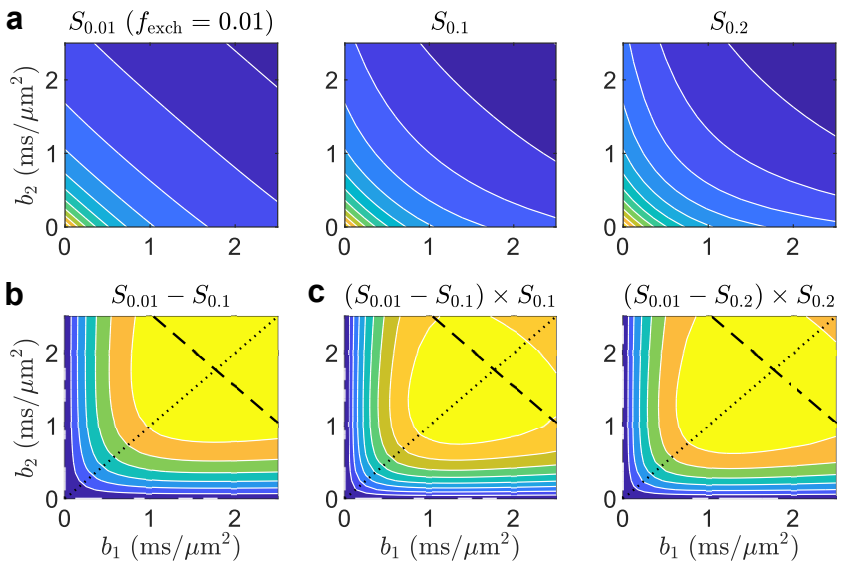

Figure 3.3: Contour maps of the signal and signal difference for a biexponential signal model of exchange (3.3.1). We set $D_I = 5.8 \times 10^{-2}, D_E = 2.1$ μm^2/ms and $f_I = 0.65, f_E = 0.35$. The exchanging signal fraction $f_{\text{exch}} = 2f_{IE} = 2f_{EI}$ is set to $[0.01, 0.1, 0.2]$ from left-to-right. (a) The generated signal maps $S_{0.01}, S_{0.1}, S_{0.2}$ are denoted by the given value of f_{exch}. (b – c) Difference maps from part (a), illustrating that the maximal exchange-weighted difference lies on the forward diagonal axis $b_1 = b_2$ or $b_d = 0$ (dotted line). The predicted optimum value of $b_s = b_1 + b_2 \approx 3.5$ ms/μm^2, where the curvature is deepest, is drawn (dashed line). (c) Scaling by the signal level shifts the optimum slightly towards smaller b_s.

write the signal as arising from four fractions:

$$\frac{S(b_1, b_2, t_m)}{S_0} = f_{II} e^{-b_1 D_I - b_2 D_I} + f_{IE} e^{-b_1 D_I - b_2 D_E} + f_{EI} e^{-b_1 D_E - b_2 D_I} + f_{EE} e^{-b_1 D_E - b_2 D_E}, \tag{3.3.1}$$

where we note that $f_{\text{exch}} = 2f_{IE} = 2f_{EI}$, $f_{II} = f_I - f_{IE}$, $f_{EE} = f_E - f_{EI}$, and the sum of all fractions is 1. In Fig. 3.3 we generate synthetic data using this signal model and plot the contour maps. As the exchanging signal fraction increases (left-to-right), the contours are seen to develop a symmetric curvature, centered around the forward-diagonal axis where $b_1 = b_2$. Looking at the contours of the *difference* map between the exchanging and non-exchanging cases, it becomes clear that the point with maximal difference (i.e., highest exchange weighting) lies along this diagonal axis, with little difference along the vertical/horizontal axes. A similar result was found by Lampinen *et al.* [125], wherein $b_1 \approx b_2$ was found to produce the most robust AXR measurements in a FEXSY protocol.

Rotating the domain

The shape of the contours in Fig. 3.3 suggest that a rotation to the forward- and anti-diagonal axes isolates the signal variation due to exchange. This property was first noticed Song *et al.* in the context of T_2–T_2 relaxometry data. Such a rotation amounts to rewriting (3.3.1) in terms of the sum b_s and difference b_d in b-values:

$$b_s = b_1 + b_2, \;\; b_d = b_1 - b_2, \tag{3.3.2}$$

(n.b., we defined b_d as $b_d = b_2 - b_1$ in previous work [115], but this makes no practical difference in the following theory or results) yielding

$$\frac{S(b_s, b_d, t_m)}{S_0} = f_{II} e^{-b_s D_I} + f_{EE} e^{-b_s D_E} + e^{-b_s D_s} \left[f_{IE} e^{b_d D_d} + f_{EI} e^{-b_d D_d} \right], \tag{3.3.3}$$

where

$$D_s = \frac{1}{2}(D_I + D_E), \;\; D_d = \frac{1}{2}(D_E - D_I). \tag{3.3.4}$$

In particular, the *curvature* along the anti-diagonal $b_d \in [-b_s, b_s]$ axis (holding b_s constant) increases with increasing f_{exch} (see Fig. 3.3a). Thus, in the interest of isolating exchange, we can evaluate the curvature with respect to b_d,

$$\frac{\partial^2}{\partial b_d^2}\left(\frac{S}{S_0}\right) = D_d^2 e^{-b_s D_s} \left[f_{IE} e^{b_d D_d} + f_{EI} e^{-b_d D_d} \right]. \tag{3.3.5}$$

Finally, we substitute $f_{IE} = f_{EI} = f_{\text{exch}}/2$, yielding

$$\frac{\partial^2}{\partial b_d^2}\left(\frac{S}{S_0}\right) = f_{\text{exch}} \cdot \frac{D_d^2}{\exp(b_s D_s)} \cosh(b_d D_d). \tag{3.3.6}$$

The contributions from non-exchanging fractions (f_{II}, f_{EE}) disappear upon evaluating the curvature, leaving an expression that is proportional to the exchanging signal fraction f_{exch}. This is an intuitive result. If the total b-value is held constant, then non-exchanging, Gaussian signal fractions will show exactly the same signal attenuation, regardless of how b_1 and b_2 are split up. Any signal variation along the b_d axis is thus due only to exchange (for this signal model). This is the key advantage of the curvature method — isolating exchange — and the origin of its namesake.

Measuring the exchanging signal fraction

The curvature along some constant b_s can be estimated by finite differencing in order to measure f_{exch}. The most straightforward approach is to take a central, second-order finite difference centered at $b_d = 0$ such that the cosh term in (3.3.6) is equal to 1, with some differencing step Δb_d. This finite difference is given by [141]

$$\left(\frac{\partial^2 S}{\partial b_d^2}\right)_{b_d=0} \approx \left[\frac{S(b_d = -\Delta b_d) - 2S(b_d = 0) + S(b_d = \Delta b_d)}{\Delta b_d^2} - \frac{\Delta b_d^2}{12}\frac{\partial^4 S}{\partial b_d^4} + \ldots\right]. \tag{3.3.7}$$

Truncating (3.3.7) at the first term and using the maximum differencing step of $\Delta b_d = b_s$ yields the following approximation:

$$\left(\frac{\partial^2 S}{\partial b_d^2}\right)_{b_d=0} \approx \left[\frac{S(0, b_s) - 2S\left(\frac{b_s}{2}, \frac{b_s}{2}\right) + S(b_s, 0)}{b_s^2}\right], \tag{3.3.8}$$

where we have written S as a function of (b_1, b_2) for clarity. Note that $b_d = b_s$ corresponds to $(b_1, b_2) = (b_s, 0)$, $b_d = 0$ corresponds to $b_1 = b_2 = \frac{1}{2}b_s$ and so forth. From (3.3.6), f_{exch} can then be measured as

$$f_{\text{exch}} = \frac{1}{S_0} \cdot \frac{\exp(b_s D_s)}{D_d^2} \cdot \left(\frac{\partial^2 S}{\partial b_d^2}\right)_{b_d=0}. \tag{3.3.9}$$

Substituting (3.3.8) yields an experimental measurement of f_{exch}. Thus, provided that the biexponential signal model (3.3.1) is a good approximation, f_{exch} can be measured with 4 points (3 to estimate the curvature, along with S_0) provided *a priori* knowledge of the compartmental diffusivities D_I and D_E, which can in turn be estimated by conventional SDE methods. We should point out, however, that such diffusivity estimates can be difficult to achieve in practice due to differences in relaxation rates between compartments, the presence of potentially more than 2 compartments, non-Gaussian diffusion, among other issues [142]. Values of f_{exch} measured at (at least) 3 values of t_m can then be fit to yield an AXR from (3.2.10).

Note that the choice of b_s at which to measure the curvature is also important, and low values will result in little to no exchange contrast (see Fig. 3.3b). The

maximum depth of curvature is achieved at b_s equal to:

$$\begin{aligned}\underset{b_s}{\operatorname{argmax}}\, S(b_s,0) - S\left(\frac{b_s}{2},\frac{b_s}{2}\right) &= \underset{b_s}{\operatorname{argmax}}\, \frac{f_{\text{exch}}}{\exp(b_s D_s)}\left[\cosh(b_s D_d) - 1\right] \\ &= \frac{1}{D_d}\ln\left(\frac{D_s}{D_I} + \sqrt{\left(\frac{D_s}{D_I}\right)^2 - 1}\right).\end{aligned} \tag{3.3.10}$$

This optimal value of b_s is drawn in the difference maps in Fig. 3.3b. In practice, the signal level is also important (i.e., SNR), not just the curvature depth. Scaling by the signal level shifts the optimum towards somewhat smaller b_s, but (3.3.10) nonetheless remains a good heuristic for selecting experimental parameters. In general, provided that D_E and D_I are well-separated, the optimal value of b_s should fully attenuate ECS signal while minimally attenuating the ICS signal, similar to the notion of an efficient 'filtering' value of b_1 in FEXSY [116].

In the following, we apply the curvature method to measure the exchanging signal fraction in a WM tissue phantom. Before proceeding, we make the (perhaps obvious) point that for a single compartment or diffusivity, such as a simple liquid, no curvature is expected, and the signal difference between mixing times arises only from T_1 relaxation.

3.3.2 Validation on a tissue phantom

Materials and methods

To validate the curvature method, we studied a DEXSY phantom for which the biexponential signal model roughly applies and f_{exch} can be exactly predicted: a glass capillary array with capillary diameter (ℓ_s) of 5 μm and an open-area-ratio of 0.55, first described by Benjamini *et al.* [140]. The array is open to a bulk water compartment and the signal at the interface is designed to mimic the exchange between an intra-axonal space (WM) and the ECS. The phantom was studied using a 7 T vertical, wide-bore magnet (Bruker BioSpin, Germany) with an AVANCE III spectrometer, Micro2.5 microimaging probe and gradient set, GREAT 60 gradient amplifiers, and 20 mm RF coil.

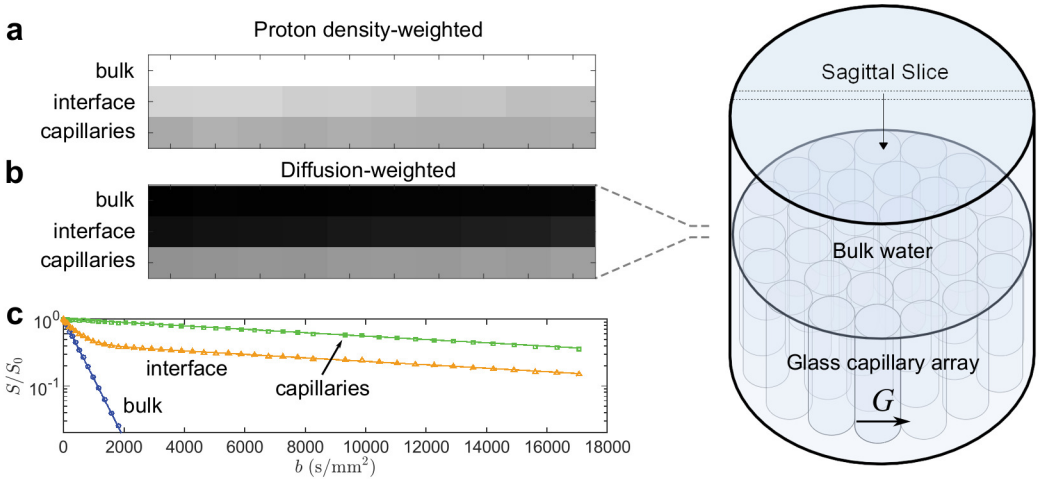

Figure 3.4: Diagram of glass capillary array tissue phantom (5 μm diameter, open-air-ratio of 0.55), along with images taken from an ROI at the interface, as well as diffusion data. (a) A proton density-weighted image shows less signal for capillaries due to the space occupied by the glass walls. (b) A diffusion-weighted image (same color scale) with $b_1 = b_2 = 1.5$ ms/μm^2, same parameters as (c), shows complete attenuation of bulk water. (c) Diffusion data acquired with the PG-DEXSY sequence ($\delta = 3$, $\Delta = 15$ ms, $b_s = b_1 + b_2$, $b_1 = b_2$) and averaged row-wise across the ROI are fit to yield $D_I = 5.8 \times 10^{-2}$ (capillaries, green squares) and $D_E = 2.1$ μm^2/ms (bulk, blue circles). The interface (yellow triangles) is well-fit by a biexponential decaying with D_E, D_I and a capillary fraction of $f_I \approx 0.25$. (Adapted from Ref. [115].)

The PG-DEXSY sequence as described in Fig. 3.1 was used with $\delta = 3$ and $\Delta = 15$ ms, b-values up to 1.7 ms/μm^2, with the gradient oriented perpendicular to the capillaries, and 50 μs RF pulses. Gradient pulses were trapezoidal in shape (but assumed to be rectangular for the purpose of calculating b-values). A standard multi-slice, multi-echo sequence was used for the imaging block, with slice thickness $\Delta z = 4$ mm and an in-plane resolution of 350×350 μm.

In Fig. 3.4, we diagram the phantom, show proton density (no diffusion gradients, Fig. 3.4a) and diffusion-weighted images at $b_1 = b_2 = 1.5$ ms/μm^2 for an ROI taken at the interface (Fig. 3.4b), and plot diffusion attenuation data for the (row-averaged) ROI (Fig. 3.4c). All data is magnitude data. These data confirm that the interface contains a partial volume of water from capillaries and free water. An inversion recovery sequence was used to measure T_1, yielding $T_1 = 2.5$ s^{-1} for the bulk and a reduced $T_1 = 1.7$ s^{-1} (likely due to surface relaxation effects) for the capillaries. We are thus sensitive to exchange times as long as 2 s.

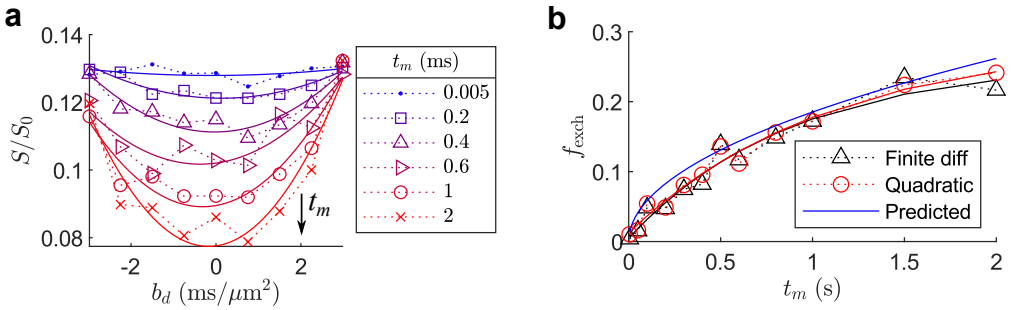

Figure 3.5: Curvature along b_d and corresponding f_{exch} values for a row-averaged ROI at the interface of the phantom described in Fig. 3.4. (a) Increasing curvature along b_d with increasing t_m is shown for a fixed $b_s = 3$ ms/μm^2. To estimate the curvature, we use either a 3-point finite difference (3.3.9) (using the endpoints and midpoint in b_d), or a quadratic fit using all points (solid lines), which is a good approximation for the curvature about $b_d = 0$. (b) Fits to the 3-parameter model of two-site exchange (3.2.10) are shown using the finite difference or quadratic fitting methods (solid lines) and compared to the predicted exchange for Gaussian diffusion (blue line) given by $f_{\text{exch}} = \sqrt{2D_E t_m}/\Delta x$, where $\Delta x = 350$ μm.

We note that for $D_0 = 2.1$ μm^2/ms, the diffusion length is $\ell_d = \sqrt{2D_0\Delta} \approx 8$ μm, which is slightly longer than $\ell_s = 5$ μm. Spins thus feel the effect of the barrier, reducing their mobility. We also note that because the interface is effectively a fully-connected space and $\ell_d \gtrsim \ell_s$ is near the short-time limit (2.2.50), the hindered diffusion model (2.2.48), and thus the biexponential signal model with steady-state, two-site exchange (3.2.10), may be applied without reservation. To confirm that this model applies, the diffusion data at the interfacial voxels is well-fit by a biexponential signal model (2.3.2) using the fitted capillary and bulk diffusivities ($D_I = 5.8 \times 10^{-2}, D_E = 2.1$ μm^2/ms, respectively), shown in Fig. 3.4c. The capillary fraction is estimated as $f_I \approx 0.25$.

For the diffusivities measured, the predicted optimum with deepest curvature (3.3.10) lies at about $b_s = 3.5$ ms/μm^2. Acknowledging the discussion in the previous section, we chose a slightly smaller $b_s = 3$ ms/μm^2 to measure f_{exch}, as the bulk water is still fully attenuated at this b-value (see Fig. 3.4c). To measure exchange, mixing times spaced between $t_m = 0.005 - 2$ s were used.

Curvature and exchange

In Fig. 3.5a, we show the signal variation along b_d at a fixed $b_s = 3$ ms/μm^2 and find the expected behavior of increasing curvature with t_m. We note, however, that the

curves are somewhat asymmetric, with the $b_d = -b_s$ (i.e., $b_1 = 0$, $b_2 = b_s$) endpoint (leftmost) being reduced compared to the $b_d = b_s$ (rightmost) point. This difference is not expected for steady-state, two-site exchange, and can be attributed to failing to suppress a pathway which misses the first 180°-pulse but goes through the rest of the sequence. As a result, when $b_1 = 0$, this pathways is not dephased/spoiled by the first diffusion encoding and will exhibit T_2^* dephasing during the encoding, T_1 relaxation during t_m, followed by attenuation due to b_2. Thus, less (normalized) signal is expected at the left endpoint, with the effect increasing with t_m, as seen in the plot (Fig. 3.5a). We point out that this asymmetry will reduce the curvature about $b_d = 0$ and lead to slight underestimation of exchange parameters. This bias highlights the importance of comprehensive coherence selection. We will give a full treatment of coherence selection in DEXSY sequences in Chapter 4 (Sec. 4.3.2), as previously mentioned. Further details are also given in Appendix B.

Values of f_{exch} were calculated using (3.3.9) and fit to (3.2.10), yielding an AXR of $k = 1.12\ \text{s}^{-1}$ for the 3-point finite difference method, and $k = 0.93\ \text{s}^{-1}$ for a quadratic fit using all points (Fig. 3.5b). Although the form of the signal with respect to b_d is complicated (3.3.3), a quadratic fit nonetheless provides a good approximation of the curvature about $b_d = 0$ (see Fig. 3.5a). Steady-state exchange fractions were fit as $f_{\text{SS}} \approx 0.26,\ 0.29$, respectively. Thus, sub-sampling to 3 points produces similar parameters to using all points, supporting the feasibility of finite differencing as a data reduction method, though some truncation error (3.3.9) may remain.

We also compare the fits to what would be expected for a simple Gaussian diffusion model. Presuming that the interface lies within a voxel of size Δx (here, 350 μm), where x is orthogonal to the gradient direction and $\ell_d \ll \Delta x$, the expected exchanging signal fraction is given simply by $f_{\text{exch}} = \sqrt{2D_E t_m}/\Delta x$ (blue line, Fig. 3.5b) — i.e., the ratio of the mean displacement and the voxel size. The fits are in close agreement with this prediction, supporting the validity of the exchange rate measurement. However, the values of f_{exch} are slightly underestimated compared with this prediction (see Fig. 3.5b), likely due to the coherence selection issue and asymmetry in b_d.

Finally, we point out that the curvature method can also yield a map of f_{exch} at each t_m, as shown in Fig. 3.6. Thus, if exchange-*weighted* contrast is sufficient, then

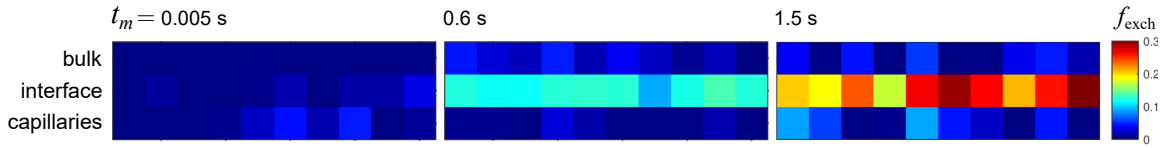

Figure 3.6: Exchanging signal fraction f_{exch} maps at three different t_m = [0.005, 0.6, 1.5] s for the ROI shown in Fig. 3.4. (Adapted from Ref. [115].)

one can simply look at f_{exch} or curvature maps without fitting to the 3-parameter model of exchange (3.2.10), reducing the data requirement, truly, to 4 points. Indeed, even the calculation of f_{exch} (which requires an assumption of Gaussian diffusivities and *a priori* knowledge of said diffusivities) is not strictly necessary, and one may simply look at the difference between the mid- and endpoints along b_d to generate exchange-weighted contrast, which we will explore further in Chapter 5.

3.3.3 Correspondence in fixed spinal cord

With confidence in the validity of the method based on studies of a tissue phantom, we proceed to study fixed, *ex vivo* neonatal mouse spinal cord dissected at post-natal days 1 – 4 (P1 – P4) using the PM-10 magnet (Fig. 2.8). At this stage of development, mouse spinal cords consist primarily of GM [143, 144] and thus represent a good model for the study of heterogeneous tissue with exchanging compartments. We also study live (viable) spinal cords under normal and abnormal conditions later in Chapter 4. Here we show that, in fixed tissue, the curvature method agrees with exchange rates measured using full DEXSY spectra $P(D_1, D_2)$, thus demonstrating correspondence between the methods and that little to no bias is introduced by the heavy sub-sampling approach.

Materials

The PM-10 system first described in Fig. 2.8 was outfitted with a test chamber to accommodate these spinal cord specimen [45, 46, 145], shown in Fig. 3.7. The chamber has two environments: an artificial cerebrospinal fluid (aCSF) bath and a gas chamber above kept at 95% O_2/5% CO_2 (Fig. 3.7a). The aluminum test chamber is surrounded by a water bath used to maintain temperature. All experiments were

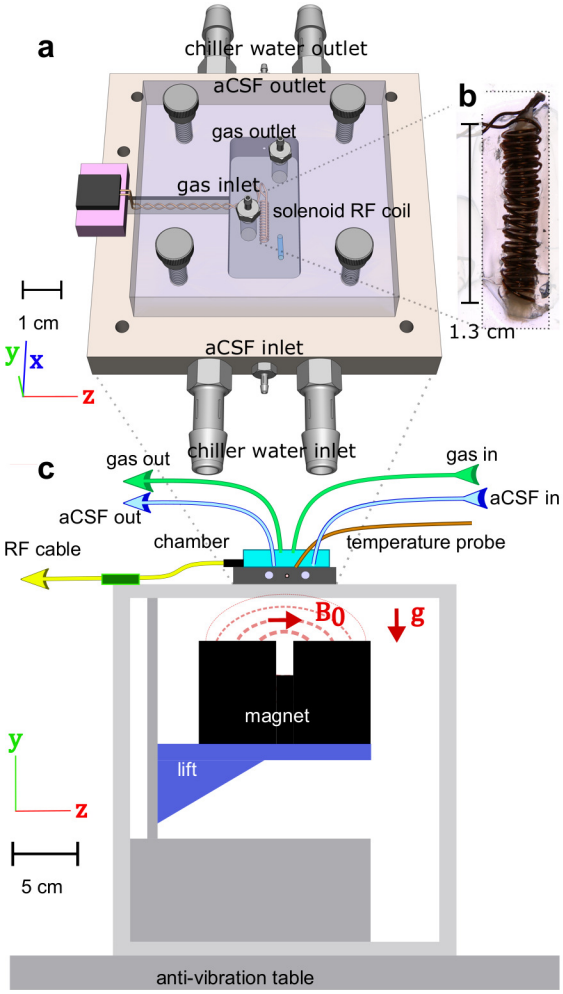

Figure 3.7: Technical drawing of a PM-10 NMR-MOUSE with spinal cord sample. (a) Gas chamber kept at 95% O_2/5% CO_2 and aCSF bath, as well as inlets to external water baths used to control temperature. (b) Solenoid RF coil with 13×2 mm (inner diameter) and spinal cord sample, demonstrating a snug fit and high filling factor. The coil is oriented to produce a $\mathbf{B}_1$ field in the x-direction. (c) Orientation of the $\mathbf{B}_0$ field ($B_0 = 0.3239$ T) and gradient $g = 15.3$ T/m ($G = 650$ kHz/mm). Positioning of the magnet is controlled precisely using a lift. Temperature control and monitoring using a heated/chilled water bath and fiber optic probe are also shown. (Adapted from Refs. [45, 46])

performed at 25 °C, monitored and controlled using the water bath and a fiber optic temperature probe (Fig. 3.7c). The magnet is adjusted by a lift, centering the sample where the field in the xz-plane is roughly homogeneous with amplitude $B_0 = 0.3239$ T, $\omega_0 = 13.79$ MHz, and gradient along y of 15.3 T/m due to the decay of the field with distance (Fig. 3.7c).

Spinal cords were extracted from Swiss Webster wild type (Taconic Biosciences, Rensselaer, NY, USA) via a ventral laminectomy while bathed in low-calcium, high-magnesium aCSF (concentrations in mM: 128.35 NaCl, 4 KCl, 0.5 $CaCl_2 \cdot 2H_2O$, 6 $MgSO_4 \cdot 7H_2O$, 0.58 $NaH_2PO_4 \cdot H_2O$, 21 $NaHCO_3$, 30 D-glucose). Spinal cords were subsequently isolated together with the ventral roots and ganglia. In terms of size, spinal cords were roughly $15 \times 1 \times 1.5$ mm (anterior–posterior length × lateral width × ventral–dorsal height), increasing with days postnatal. Spinal cords were fixed immediately after dissection in 4% paraformaldehyde and left overnight at 4 °C. Fixative was then replaced with normal aCSF (same as before, but with 1.5 mM $CaCl_2 \cdot 2H_2O$, 1 mM $MgSO_4 \cdot 7H_2O$) three times over 2 days to remove residual paraformaldehyde before NMR measurements.

The solenoid RF coil has dimensions of 13×2 mm and is designed to snugly fit the spinal cord specimen, resulting in a high filling factor (Fig. 3.7b), and increasing the SNR by a factor of about 10 compared to flat coil designs [145]. Indeed, only $\approx 5\%$ of the measured signal is attributable to aCSF according to SDE data [45]. The orientation of the spinal cord leads to sagittal slices.

NMR Methods

For the NMR measurements, hard RF pulses with pulse powers of $-16/22$ dB for $90°/180°$-pulses were used, leading to a slice thickness of $\Delta z = 400$ μm through the center of the specimen. Pulses were driven with a 100 W amplifier (Tomco, Adelaide, Australia). Measurements were performed using a Kea2 spectrometer (Magritek, Wellington, New Zealand) and all data were acquired as signal from the real channel, summing over all echoes in a CPMG echo train with 2000 echoes and $\tau_{\mathrm{CPMG}} = 12.5$ μs (see Fig. 3.1).

The SG-DEXSY sequence was developed in Prospa (V3.22) and used an 8-step phase cycle, given in Table B.4. When combined with unequal b-values for spoiling ($\tau_1 \neq \tau_2$ or $b_d \neq 0$) this approach comprehensively suppresses unwanted coherences, as we show in Appendix B. For full DEXSY data, a 21×21 grid of $[b_1, b_2]$ values was acquired, with b-values up to $b \approx 400\ \mathrm{ms}/\mu\mathrm{m}^2$. Unequal b-values were achieved by incrementing τ_1 linearly from $0.2 - 3.3$ ms and incrementing τ_2 from a slightly shifted $0.213 - 3.313$ ms. A total of 4 mixing time were acquired: $t_m = [0.2, 4, 20, 160]$ ms.

Relaxation rates T_1, T_2 in the fixed spinal cord specimen were measured using saturation recovery and CPMG experiments, and were estimated as ≈ 1 s and ≈ 55 ms, respectively [45]. The fits for T_1 and T_2 were both approximately monoexponential, suggesting that differences in relaxation rates between compartments may, to a first approximation, be ignored. Furthermore, for the values of τ_1 and τ_2 used (≤ 3.313 ms), T_2 relaxation during the encodings should be negligible. Similarly, the t_m values (up to 160 ms) are much less than T_1 such that sufficient signal remains. For all measurements, the TR was 2 s.

For the curvature method (4-point measurement) S_0 was measured at $b_s \approx 0.2$, $b_d \approx -0.02\ \mathrm{ms}/\mu\mathrm{m}^2$ ($b_1 \approx 0.09$, $b_2 \approx 0.11$) and 3 points were measured along an axis of constant $b_s \approx 4.5$ at $b_d \approx [-4.3, 0.15, 4.3]\ \mathrm{ms}/\mu\mathrm{m}^2$ over a more finely sampled set of 11 mixing times: $t_m = [0.2, 1, 2, 4, 7, 10, 20, 40, 80, 160, 300]$ ms. Note that we do not measure the exact endpoints of $b_d = \pm b_s$ because b_1 and b_2 cannot be set to 0 on an SG system — any time between pulses results in diffusion weighting — and we also want $b_d \neq 0$ ($\tau_1 \neq \tau_2$) for spoiling purposes. For further details on the NMR and biological methods, see Refs. [45, 146].

Signal and difference maps

As a first result, we plot contour maps of the normalized signal S/S_0 from the full DEXSY measurement over increasing values of t_m, as well as difference maps between exchange-weighted and relatively non-exchange-weighted (long vs. short t_m) signals, shown in Fig. 3.8. Within the contour maps (Fig. 3.8a), the characteristic increase of (symmetric) curvature with t_m is seen, indicative of exchange over the mixing

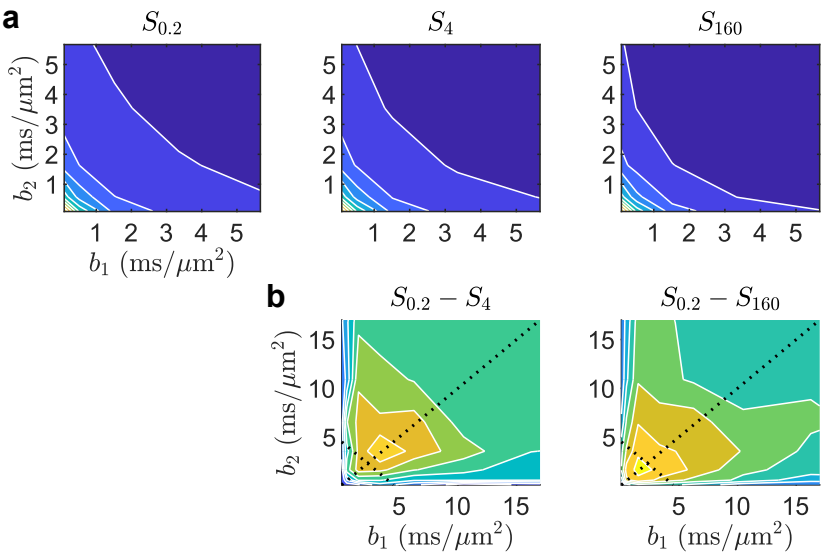

Figure 3.8: Contour maps of the signal and signal difference from SG-DEXSY experiments on fixed spinal cord using the system described in Fig. 3.7. Data is shown for one spinal cord, averaging three experimental repeats. A subset of the acquired 21×21 grid of $[b_1, b_2]$-values is shown to highlight regions of large signal decay. (a) Signal maps are denoted by the mixing time t_m (ms), increasing left-to-right. (b) Difference maps confirm that the maximal exchange-weighted signal difference lies along $b_d = 0$. The selected $b_s = 4.5 =$ ms/μm^2 for the curvature method is also drawn, indicating that this choice is near optimal and corresponds with the greatest exchange-weighted difference.

time. The difference maps (Fig. 3.8b) show a maximum along the forward diagonal where $b_d = 0$, resembling those shown for the biexponential signal model (see Fig. 3.3b), and the maximum is observed at around $b_s \approx 3-6$ ms/μm^2. Thus, our choice of $b_s \approx 4.5$ ms/μm^2 for the curvature method is appropriate from the perspective of maximal exchange weighting.

In these data, however, we note that even at the shortest mixing time of $t_m = 0.2$ ms, curvature is present, in contrast to the flat contours predicted for the biexponential signal model (Fig. 3.3b). Given the extremely short encoding and mixing time — for the exchange-weighted point with $b_d \approx 0$, $b_s = 4.5$ ms/μm^2, we have that $\tau_1 \approx \tau_2 \approx 0.7$ ms, for a total of ~ 1 ms encoding plus minimum mixing time $t_m = 0.2$ ms — we do not expect a large amount of exchange in this time-frame and the curvature at short t_m cannot be attributed solely to exchange. Indeed, we will show in Sec. 3.4 that much of the short-t_m curvature can be explained by non-Gaussian diffusion.

Relevant lengthscales

On a related note, let us consider the relevant lengthscales for this experiment. For $\tau \approx 0.7$ ms corresponding to the $b_d \approx 0$, exchange-weighted point, we have that $\ell_d \approx \sqrt{2D_0\tau} \approx 1.7\ \mu$m, using the experimentally measured diffusivity of pure aCSF at 25 °C: $D_0 = 2.15\ \mu$m/ms. For $g = 15.3$ T/m, we have that $\ell_g \approx 0.8\ \mu$m. The measurement therefore lies in a potentially complicated intermediate regime of $\ell_d \approx 2\ell_g$, where for $\ell_g < \ell_s < \ell_d$, some degree of localized signal behavior may be present, and for $\ell_s \ll \ell_g < \ell_d$, motional averaging is expected (see Fig. 2.11). Without *a priori* knowledge of the structure (i.e., values of ℓ_s), nor the ability to change the gradient amplitude g, these cases cannot be distinguished. Of course, for $\ell_s > \ell_d$, diffusion is approximately free or in the short-time limit (2.2.50) and this signal component will strongly attenuate.

Despite the potentially complicated signal behavior, the general picture of two-site exchange applies because both the motional averaging and localized signal regimes will exhibit much less signal attenuation compared to a free compartment, with $\ell_s = \ell_d$ (equivalently, $bD_0 = 1$) being the approximate dividing line between these two cases. Thus, provided that $\ell_\kappa \gg \ell_s$, barrier-limited exchange can be experimentally observed. Put another way, exchange during t_m will produce contrast in the signal, regardless of the particular signal behavior in the less attenuated compartment(s). Note that the relationship between the structure (SVR) and the measured AXR, however, will break down in the localized signal regime. In this regime, the persistent annulus of signal (perpendicular to the gradient) with width ℓ_g increases the effective SVR, and the AXR cannot be interpreted directly in terms of the structure as $k = \kappa S/V$ (2.3.8). For this reason, we caution against such an interpretation of the exchange rate and do not attempt to estimate κ here, nor throughout this thesis.

These lengthscales also indicate what exchange process is being probed. As we noted above, $\ell_s = \ell_d$ acts as a dividing line between strongly and weakly attenuating signal, whether it be motionally averaged or localized. Thus, we can say that our measurement probes exchange of signal into/out of structures corresponding to confinement within $\ell_s = \ell_d \approx 1.7\ \mu$m or less, and for which the permeability is small enough such that $\ell_\kappa \gg \ell_s$ and barrier-limited exchange is expected. We note that

reported AXRs in neural tissue vary widely within the literature. For instance, see Refs. [103, 147, 148] for reports ranging from $\tau_k = 25 - 620$ ms or even longer in GM and WM, and as short as $\tau_k = 15$ ms in GM [103]. Some of this variability may be due to the experimentally probed lengthscales, rather than actual differences in the tissue being measured. Given the GM tissue model and the micron-level structures probed here, along with the sub-millisecond diffusion encoding time, we might expect to measure fast exchange rates in line with or greater than the fastest reports in the literature ($\tau_k \lesssim 15$ ms, or $k \gtrsim 70$ s^{-1}).

Full DEXSY spectra

We next show the full DEXSY spectra $P(D_1, D_2)$ obtained by a 2D ILT. The 2D ILT was performed with L_2 regularization and singular value decomposition, following the method described in Refs. [93, 149]. The dimension of the inverted space $[D_1, D_2]$ was 21×21, spaced log-linearly spaced from $10^{-13} - 10^{-8}$, and was chosen to match the dimension of the experimental data in $[b_1, b_2]$. The regularization parameter was chosen by the L-curve method [150, 151] for the $t_m = 0.2$ ms case and held constant for the longer t_m values in order to keep a consistent amount of regularization throughout t_m. In Fig. 3.9, we show the $P(D_1, D_2)$ spectra obtained from one specimen measured three times, along with the marginal distributions $P(D_1)$ and $P(D_2)$. The spectra are normalized by $D_0 = 2.15$ μm/ms, measured in aCSF.

We bin the diffusivities into three regions A, B, C in order of increasing diffusivity, where A, B correspond to water in small tissue compartments (perhaps restricted or localized) and C is a roughly free component, corresponding, perhaps, to the ECS (Fig. 3.9a). We note that the marginal distributions $P(D_1)$ and $P(D_2)$ do not show two well-separated diffusivities, but rather a long tail of smaller diffusivities. We will show in Sec. 3.4 that this, like the curvature at short-t_m, may be an effect of non-Gaussian diffusion. In a stacked view across mixing times (Fig. 3.9b), a symmetric increase in the off-diagonal components AC/CA and BC/CB is observed, while AB/BA is largely unchanged, indicating no exchange between the lower diffusivity bins A, B. Integrating the peaks, AXRs of $k \approx 140$ s^{-1} ($\tau_k \approx 7$ ms) were obtained by fitting the

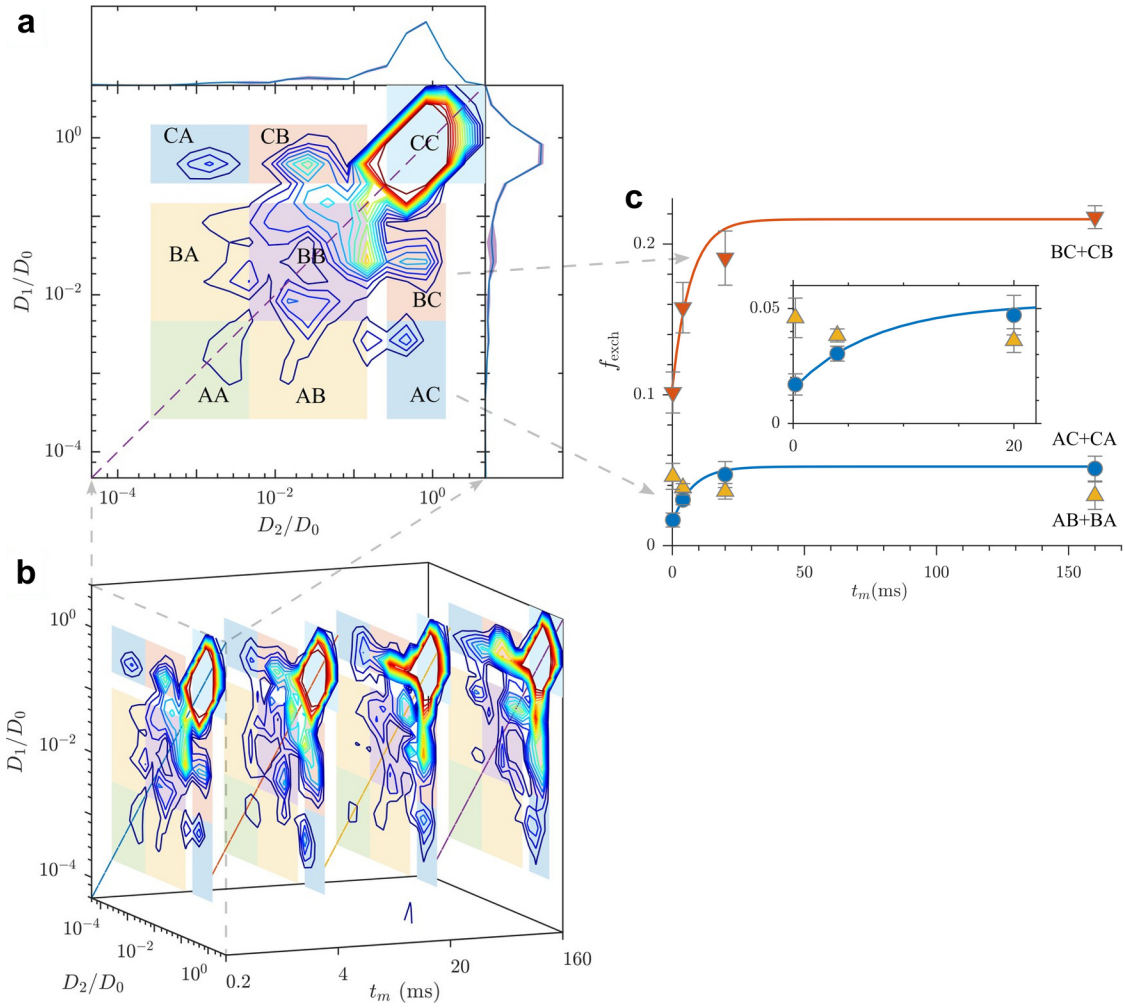

Figure 3.9: Spectra derived from 2D ILTs of full DEXSY data (21×21 in $[b_1, b_2]$) acquired in a fixed spinal cord measured three times. (a) Spectrum $P(D_1, D_2)$ obtained at the shortest mixing time $t_m = 0.2$ ms. Components are binned into three regions A, B, C, in order of increasing diffusivity, where C roughly corresponds to the measured free diffusivity of aCSF $D_0 = 2.15\ \mu\text{m}^2/\text{ms}$, $D/D_0 = 1$. Components are shaded and labelled in a 3×3 grid of non-exchanging signal fractions on the 45°-diagonal and exchanging fractions off the diagonal. Marginal distributions $P(D_1)$, $P(D_2)$ are also shown, with mean (blue line) and standard deviation SD (shaded region) from three repeats. Note that the range of $P(D_1, D_2)$ is set to add detail to components A, B, cutting off the top of the peak in CC. (b) Stacked view of the spectra for all mixing times $t_m = [0.2, 4, 20, 160]$ ms, showing roughly symmetric growth in the off-diagonal peaks, specifically of AC/CA and BC/CB. (c) Exchanging signal fractions obtained by numerically integrating the peaks in (b). Error bars = mean ± SD from three repeats. The means were fit to the 3-parameter model of exchange (3.2.10), yielding AXRs of $k \approx 140\ \text{s}^{-1}$ for both AC+CA and BC+CB. No exchange (and even a slight negative trend) is observed between A, B. (Adapted from Ref. [45].)

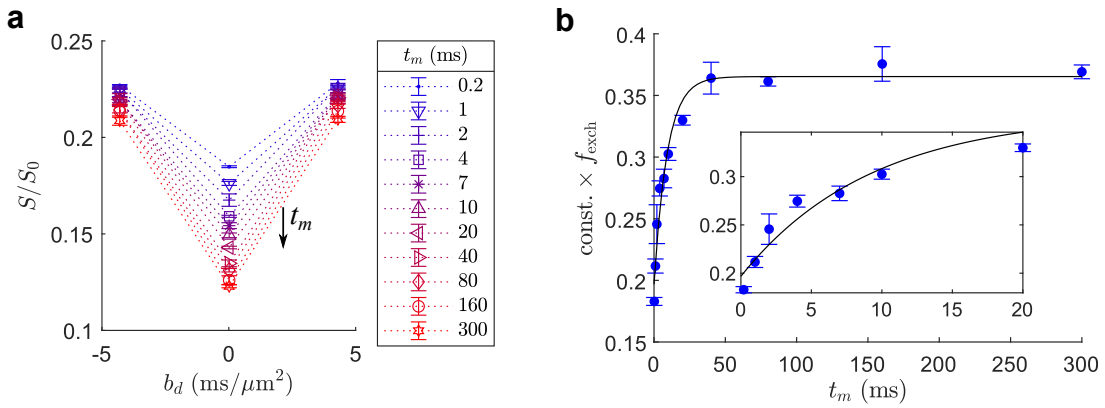

Figure 3.10: Curvature along b_d and corresponding (apparent) f_{exch} values for a fixed spinal cord measured three times. Error bars = mean ± SD. (a) Increasing curvature is observed with increasing t_m from $0.2-300$ ms, indicative of exchange. The endpoints at $b_d = \pm 4.3$ are smaller than $b_s = 4.5$ ms/μm^2 such that these points are slightly exchange-weighted and exhibit some decrease with t_m. (b) Values of f_{exch} calculated by finite differencing and using (3.3.9) with $D_I = 0.01$, $D_E = 1$ ms/μm^2, chosen arbitrarily. As such, f_{exch} is scaled by an unknown constant. A fit of the 3-parameter model of exchange (3.2.10) to the mean is shown (solid black line). The AXR was measured as $k = 110 \pm 30$ s^{-1} ($\tau_k = 9.4 \pm 3$ ms).

3-parameter exchange model (3.2.10) (i.e., including an intercept) to the means (Fig. 3.9c). This indicates extremely rapid exchange, approximately in line with other reports in GM [101, 103], though these studies were performed with PG-SE sequences, complicating direct comparisons between studies.

Applying the curvature method

We now compare the AXRs obtained using full DEXSY data to AXRs obtained using the curvature method, following the 4-point sampling method described in the previous section. In Fig. 3.10a, we plot the three points $b_d = [-4.3, -0.15, 4.3]$ at a fixed $b_s = 4.5$ ms/μm^2 normalized to S_0 ($b_s = 0.2, b_d = -0.02$ ms/μm^2) over 11 values of t_m from $0.2-300$ ms. Again, the data is presented for one specimen measured three times. We find the expected trend of increasing curvature depth with increasing t_m, indicative of exchange. Note that because we do not measure exactly at $b_d = \pm b_s$, the endpoints are also slightly exchange-weighted, and decrease slightly with t_m. That is, the differencing step was chosen as $\Delta b_d \approx 4.3 < b_s = 4.5$ ms/μm^2. In these data, unlike for the glass capillary array phantom, the endpoints along b_d

are symmetric, demonstrating comprehensive coherence selection by the 8-step phase cycle and setting $\tau_1 \neq \tau_2$.

In calculating f_{exch} from the finite difference using (3.3.9), we point out that the biexponential signal model cannot be meaningfully applied due to the distributed diffusivities in the marginal distributions (see Fig. 3.9a), in addition to issues such as differences in relaxation rates between compartments and non-Gaussian diffusion, mentioned previously in Sec. 3.3.2. We chose, somewhat arbitrarily, $D_I = 0.01$ and $D_E = 1\ \text{ms}/\mu\text{m}^2$ to calculate f_{exch} (Fig. 3.10b) and values of f_{exch} should therefore be regarded as non-quantitative. We acknowledge that in using this exchange model, there may be some unknown scaling between the apparent f_{exch} shown in Fig. 3.10b and the 'true' f_{exch}. In this case, one might consider the sum total of the off-diagonal components in $P(D_1, D_2)$ (Fig. 3.9) as the ground truth, in which case these values roughly agree; summing AC+CA and BC+CB yields a total $f_{\text{exch}} \approx 0.3$ at long t_m as compared to ≈ 0.37 in Fig. 3.10b. Despite this shortcoming (i.e., needing *a priori* estimates of D_E, D_I), consider that the 3-parameter model of exchange (3.2.10) needs only an intercept (f_0), a limit (f_{SS}), and a rate (k). Thus, the rate can still be measured accurately *whether or not* the bounding intercept and limit are 'correctly' scaled using estimates of D_I, D_E. Note as well that any effects which are not t_m-dependent, such as the minor T_2-weighting difference between the $b_d \approx 0$ and $b_d \approx \pm b_s$ points, will be captured in the intercept f_0 and are not expected to affect or confound the AXR measurement.

The AXR was measured as $k = 170 \pm 90\ \text{s}^{-1}$ (equivalently, $\tau_k = 8.0 \pm 6\ \text{ms}$) when using the same set of $t_m = [0.2, 4, 20, 160]$ as the full DEXSY experiment and $k = 110 \pm 30\ \text{s}^{-1}$ ($\tau_k = 9.4 \pm 3\ \text{ms}$) when using all 11 t_m values (mean ± SD from three repeats). A fit to the means is shown in Fig. 3.10b. In either case, the AXR is not statistically different from the value obtained from full DEXSY data ($k \approx 140\ \text{s}^{-1}$), demonstrating correspondence between the methods. Though this data is not shown, averaging over all fitted exchange rates from 5 samples (5 fixed spinal cords × 3 repeats), yields $k = 110 \pm 20\ \text{s}^{-1}$, indicating high repeatability between samples and some degree of coherent averaging.

3.3.4 Normalization approaches

Thus far, we have applied the curvature method to measure exchange in a WM phantom where the exchange characteristics could be precisely predicted, and a GM tissue model (fixed, *ex vivo* neonatal mouse spinal cord), where the fitted exchange rates were found to agree with those produced by 2D ILTs of fully-sampled data. We noted in the spinal cord model, however, that the curvature itself no longer measures a true f_{exch} if the biexponential signal model does not apply. This calls into question the need for 4 points per t_m if ultimately, the intercept and limit parameters are scaled by some arbitrary factor. Furthermore, f_0 may not represent exchange at all, and may include effects such as non-Gaussian diffusion. If we are interested only in the AXR, then we need only measure the change in the exchange-weighted $b_d = 0$ ($b_1 = b_2$) point with t_m, whilst normalizing the effect of T_1 relaxation during t_m. That being said, we investigate here further data reduction and normalization approaches within the curvature method.

In Fig. 3.11a, we plot each of the 4 points used to generate Fig. 3.10 separately, labelled as S_0, S_{mid}, $S_{\text{end,left}}$, and $S_{\text{end,right}}$, corresponding to the (weakly diffusion-weighted) S_0, the midpoint near $b_d = 0$, and the left/right endpoints at $b_d \approx \pm b_s$, respectively. We then normalize (i.e., divide) all points by the first S_0 point at $t_m = 0.2$ ms to obtain decays between 0 and 1. We find that $S_{\text{end,left}}$ and $S_{\text{end,right}}$ are indistinguishable from one another and thus one point is redundant, reducing the data requirement to 3 points. Going forward, we use only the $b_1 \approx b_s$ (right) endpoint and call it S_{end}.

To reduce the data requirement further, consider that there are three signal evolution mechanisms present: diffusion, exchange, and T_1 relaxation. The only point with significant exchange weighting is S_{mid}. Both S_{mid} and S_{end} contain equal diffusion and T_1 weighting. The diffusion weighting appears merely as a shift in the signal amplitude and does not vary with t_m (see Fig. 3.11a). Thus, the only remaining signal evolution mechanism in S_{mid} other than exchange is the *diffusion-weighted* T_1. Thus, if we can remove the effect of T_1 from S_{mid}, we isolate the signal variation due to exchange, and S_0 is also not necessary. Indeed, the fitted T_1 of S_0 is actually

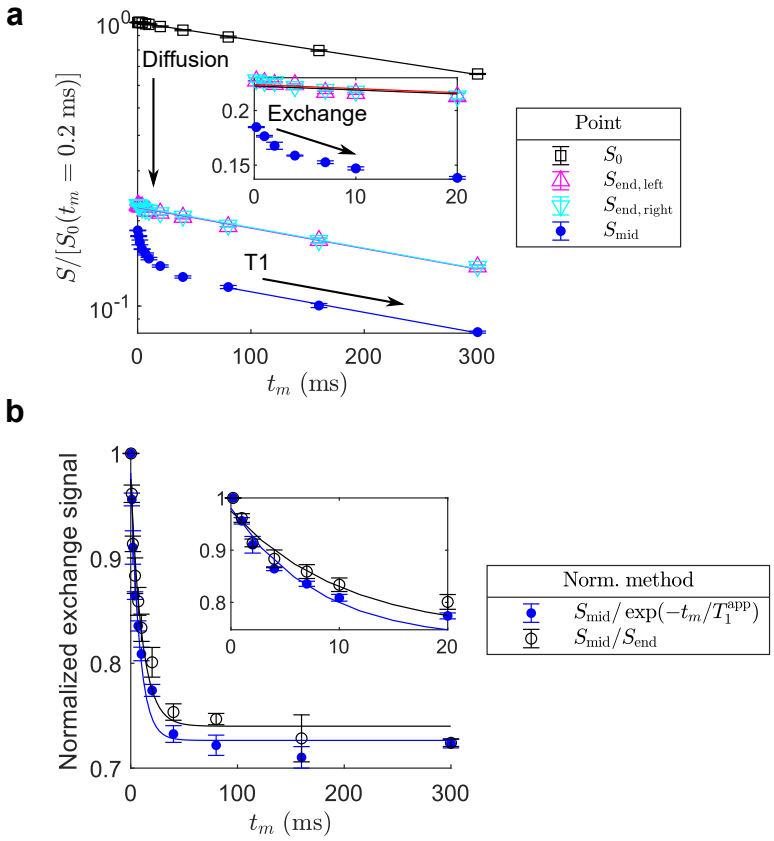

Figure 3.11: Normalization and further data reduction approaches in the curvature method. (a) The 4 individual points — S_0 and the three points along the b_d axis: S_{mid}, $S_{\mathrm{end,\,left}}$, and $S_{\mathrm{end,\,right}}$ — used to generate Fig. 3.10 are plotted. Error bars = mean ± SD from three repeats. Monoexponential fits to the mean (solid lines) are shown. S_0 evolves by T_1 ($= 710 \pm 10$ ms), S_{mid} evolves by exchange and a diffusion-weighted T_1 ($= 600 \pm 20$ ms from fitting the tail over $t_m \geq 80$ ms). $S_{\mathrm{end,\,left}}$, and $S_{\mathrm{end,\,right}}$ are identical and evolve by T_1^{app} ($= 600 \pm 30$ ms for both) with a small amount of exchange weighting. (b) Two normalization approaches are compared for removing the diffusion-weighted T_1 from S_{mid}. Data are plotted relative to the first S_0 point at $t_m = 0.2$ ms. In the division approach ($k = 100 \pm 30\ \mathrm{s}^{-1}$), some exchange weighting is divided out, leading to less total signal variation and underestimation of the AXR, along with error propagation. In the T_1^{app} approach ($k = 125 \pm 9\ \mathrm{s}^{-1}$), the diffusion-weighted T_1 may be slightly underestimated, leading to a non-monotonic rise in signal at $t_m = 300$ ms. Fits to the mean (solid lines) are shown.

different (longer) than the T_1 observed in the diffusion-weighted points due to these signals being weighted towards smaller compartments. The question becomes, how exactly do we estimate and remove the diffusion-weighted T_1?

Removing the diffusion-weighted T_1

Several approaches are feasible. An obvious approach is to fit a monoexponential of the form $C\exp(-t_m/T_1)$ to the long-t_m tail of S_{mid} after exchange has presumably reached its steady state, as we show in Fig. 3.11a. However, this is not accurate if long-time exchange processes are present and may extend the experiment time by requiring long t_m. Another approach is to divide S_{mid} by the non-exchange-weighted point, S_{end}. This, too has disadvantages. Firstly, the division of data leads to error propagation, roughly doubling the proportional error. Note that error propagation is also an issue in the 4-point curvature method to an even greater extent. Indeed, if we approximate the SNR of each point to be equal, then evaluating the quotient reduces SNR by a factor of $1/\sqrt{2}$ while the 4-point method reduces SNR by a factor of $1/2$ (along with some truncation error). This can be seen by comparing the size of the error bars in Figs. 3.10a and 3.10b. Secondly, because S_{end} is slightly exchange-weighted, dividing by it removes some exchange weighting, decreasing the sensitivity to exchange and reducing the AXR somewhat. These effects can be seen in Fig. 3.11b.

Yet another approach is to fit a monoexponential to S_{end} in order to estimate the diffusion-weighted T_1, which should be the same between S_{mid} and S_{end}. This will smooth out the small signal variation due to exchange weighting (see Fig. 3.10a) and results in an *apparent* relaxation rate T_1^{app} comparable to the tail of S_{mid}. We obtain, using either endpoint, $T_1^{\text{app}} = 600 \pm 20$ ms over all 11 t_m, which is statistically indistinguishable from the T_1 obtained by fitting the tail of S_{mid} over just the longer mixing times $t_m = [80, 160, 300]$ ms: $T_1 = 600 \pm 30$ ms. Compare this to the T_1 obtained by fitting S_0, which is larger at $T_1 = 710 \pm 10$ ms, as expected due to the difference in diffusion weighting.

The remaining effect of the (slight) exchange weighting in S_{end} must be carefully considered, however. The exchange weighting may lead to T_1^{app} being slightly

underestimated compared to the actual diffusion-weighted T_1, as might be measured in the absence of exchange weighting (i.e., if $b_d = b_s$). This issue also applies to fitting the tail of S_{mid} if long-time exchange is present. If the diffusion-weighted T_1 is underestimated, then we expect that normalization of S_{mid} using the fitted T_1^{app} will over-correct the signal at long t_m and the expected monotonicity for an exchange-weighted decay may not be preserved. Such an effect can be seen in Fig. 3.11b, where the exchange signal from the normalized S_{mid} data rises up at the longest $t_m = 300$ ms compared to the previous point at $t_m = 160$ ms. This, like the division approach, can potentially lead to underestimation of the AXR.

Finally, after the effect of relaxation has been divided out of S_{mid}, the decay of S_{mid} (see Fig. 3.11b) can be attributed solely to exchange and thus be fit to yield an AXR,

$$\frac{S_{\text{mid}}}{\exp\left(-t_m/T_1^{\text{app}}\right)} = C_1 \exp(-t_m k) + C_0, \tag{3.3.11}$$

which is again a 3-parameter exchange model like (3.2.10) consisting of a rate and terms comprising an intercept ($C_0 + C_1$), and limit (C_0). Note that exchange is modelled as a decay here, rather than as a recovery. Furthermore, we now acknowledge that parameters other than k are fitting constants without, necessarily, any (bio-)physical meaning. We compare the two approaches of taking the quotient $S_{\text{mid}}/S_{\text{end}}$ or fitting for T_1^{app} using S_{end} in Fig. 3.11b, normalizing to the first point at $t_m = 0.2$ ms to obtain decays from 1.

Comparing approaches

The fitted AXRs and variability (mean ± SD) using all the described methods to this point are summarized in Table 3.1. Both normalization approaches produce AXR values similar to those obtained for the 4-point curvature method (Fig. 3.10), but slightly smaller for the division approach, likely due to the removal of some exchange weighting. All methods are roughly in agreement with the fully-sampled DEXSY result (see Table 3.1) and with previous reports of fast exchange ($\tau_k \lesssim 15$ ms, $k \gtrsim 70\ \text{s}^{-1}$) in GM [101, 103]. See Ref. [46] for a more thorough examination of the various normalization approaches and Ref. [148] for a review of AXRs reported

Table 3.1: AXRs measured in a fixed spinal cord over 3 repeats using different methods

Method	**Number of points used** × **Number of** t_m (ms)	k (s^{-1})
Fully-sampled DEXSY	$[21\times21]\times4$ $t_m = [0.2, 4, 20, 160]$	≈ 140
4-point curvature	4×11; $t_m = 0.2-300$	110 ± 30
	4×4; $t_m = [0.2, 4, 20, 160]$	170 ± 90
$S_{\text{mid}}/S_{\text{end}}$	2×11; $t_m = 0.2-300$	100 ± 30
	2×3; $t_m = [0.2, 10, 160]$	100 ± 20
$S_{\text{mid}}/\exp\left(-t_m/T_1^{\text{app}}\right)$	2×11; $t_m = 0.2-300$	125 ± 9
	2×3; $t_m = [0.2, 10, 160]$	110 ± 10

in the literature. Similar AXRs and variability were obtained whether using all 11 t_m or a minimal subset of just 3 points at t_m = [0.2, 10, 160] ms, demonstrating the potential speed of these approaches. The T_1^{app} approach has the least variability and best SNR characteristics due to the lack of error propagation, while the 4-point method has the highest variability due to the combination of 4 points. We stress again, however, that the T_1^{app} approach can lead to non-monotonic tail behavior, as seen in Fig. 3.11, and thus, in some cases, the division approach may be preferable, despite its apparent shortcomings.

We now have several approaches to measure an AXR. If the curvature itself has biophysical meaning — i.e, when a simplified model like the biexponential signal model may be applied — then it may be worthwhile to estimate the diffusivities D_I, D_E and calculate f_{exch} from (3.3.6), in which case 3 points (S_0, S_{mid}, and S_{end}) per t_m are needed, for a minimum of 9 points to fit a 3-parameter model. If only the AXR is of interest, then as few as 5 total points (S_{mid} at 3 t_m, S_{end} at 2 t_m to fit T_1^{app}) are needed. This minimal 5-point protocol has, perhaps counter-intuitively, better SNR characteristics due to the avoidance of data combination. With this protocol, we showed that exchange rates could be measured in fixed spinal cord on the PM-10 system in just 80 s [46] (2 s TR × 5 points × 8 phase cycle steps). Finally, if exchange-weighted *contrast* is sufficient, then such contrast can be generated (as in Fig. 3.6) with just 2 or 3 points acquired at a single t_m. That is, the difference S_{mid} and S_{end} at long-t_m would be sufficient as a measurement of exchange-weighted contrast.

We have therefore accomplished what we set out to do at the beginning of this chapter and have described a rapid, minimally sampled experiment to robustly measure exchange. Yet, the signal modelling (bi- or multiexponential to this point, i.e., multiple Gaussian compartments) remains simple and unrepresentative of what is most likely a restricted environment in tissue. In the following section, we will amend the signal model(s) and methods to incorporate both exchange *and restriction* in order to account for non-Gaussian diffusion.

3.4 Disentangling restriction and exchange

In our investigation of exchange in fixed spinal cord, we noted several findings that seemed to be inconsistent with a two-compartment, Gaussian model. In the full DEXSY spectra, the marginal distributions $P(D_1)$, $P(D_2)$ were found to have a long tail of small, distributed diffusivities (Fig. 3.9a). In the curvature measurements, a large intercept at the shortest t_m was observed (Fig. 3.10), inconsistent with the short encodings and mixing times used. Here, we revisit these findings and show that the data acquired in fixed spinal cord are more accurately modelled by a restricted compartment exchanging with a freer compartment. This model is capable of reproducing the tail within the ILT-derived spectra and explaining, in part, the intercept in the curvature. We also show that by varying b_s rather than t_m, we can leverage the curvature method to probe restriction rather than exchange. We thus fully disentangle the measurement of exchange and restriction.

3.4.1 Signal scaling for non-Gaussian diffusion

Let us first argue that there is evidence of restriction in fixed spinal cord by analyzing the high-b scaling in SDE data. For Gaussian diffusion, we have that the (log) signal decay scales with $bD_0 = (\ell_d/\ell_g)^6$ (2.2.38) or with some reduced, hindered diffusivity bD_∞. On a scale with b, we expect that the signal decay in this case will be linear. This is not the case for non-Gaussian diffusion.

Shared scaling in motional averaging and localization

Recall that for motional averaging, the long-time behavior is given by (2.2.46)

$$\frac{S}{S_0} \simeq \exp\left(-a \cdot \frac{\ell_s^4 \ell_d^2}{\ell_g^6}\right), \ \ell_s \ll \ell_d, \ell_g$$

and for localization (2.2.39),

$$\frac{S}{S_0} \simeq a_0 \cdot \frac{\ell_g}{\ell_s} \exp\left(-a_1 \left[\frac{\ell_d}{\ell_g}\right]^2\right), \ \ell_g \ll \ell_d, \ell_s.$$

Usually (in PG experiments), the relevant scaling difference is in ℓ_g because the gradient amplitude is varied. In this case, we note that the Gaussian diffusion and motional averaging regimes (in both of which the GPA holds) scale with $1/\ell_g^6 \propto g^2$, while the localization regime instead scales with $1/\ell_g^2 \propto g^{2/3}$ (and the GPA is violated) [69, 74]. In SG experiments, however, g is not varied. Instead, the encoding time $\tau \propto \ell_d^2$ is varied. Thus, the relevant scaling difference is between Gaussian diffusion, which scales with $\ell_d^6 \propto \tau^3$, and motional averaging *or* localization, which both scale with $\ell_d^2 \propto \tau$. Put another way, for SG experiments, Gaussian diffusion scales with $b = \frac{2}{3}\gamma^2 g^2 \tau^3$, while the non-Gaussian cases scale with $b^{1/3}$, as was pointed out by Grebenkov [74, 152]. To make this clear, we rewrite the above in terms of

$$(bD_0)^{1/3} = \left(\frac{\ell_d}{\ell_g}\right)^2, \tag{3.4.1}$$

yielding for motional averaging (i.e., restriction in the long-ℓ_d limit)

$$\ln\left(\frac{S}{S_0}\right) \simeq -a \cdot \left(\frac{\ell_s}{\ell_g}\right)^4 (bD_0)^{1/3}, \ \ell_s \ll \ell_d, \ell_g, \tag{3.4.2}$$

and for localization,

$$\ln\left(\frac{S}{S_0}\right) \simeq -\ln\left(a_0 \cdot \frac{\ell_g}{\ell_s}\right) a_1 \cdot (bD_0)^{1/3}, \ \ell_g \ll \ell_d, \ell_s. \tag{3.4.3}$$

Scaling in fixed spinal cord

In Fig. 3.12, we compare the predicted signal for all three regimes: (i) free diffusion with the diffusivity of aCSF measured to be $D_0 = 2.15\ \mu\text{m}^2/\text{s}$, (ii) restricted spheres

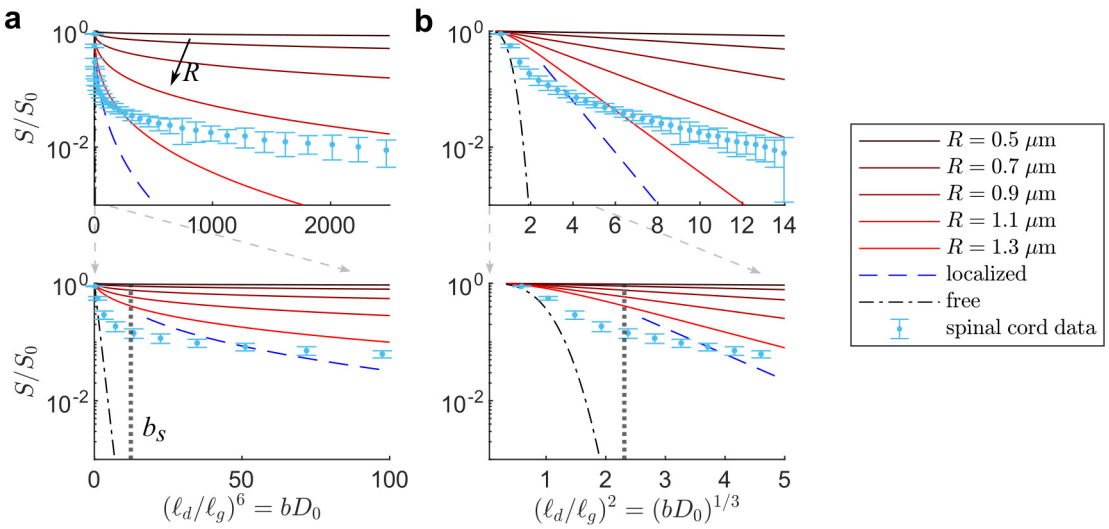

Figure 3.12: Predicted signal decays for free diffusion using $D_0 = 2.15\ \mu\text{m}^2/\text{s}$ (black dash-dot line), restriction in spheres of radii from $0.5-1.3\ \mu$m (solid black to red lines), and the tail of the localization regime, plotted only for $\ell_d > 1.5\ell_g$ with pre-factor $a_0 = 5.8841$, $\ell_s = 1.3\ \mu$m (dashed blue line), compared to SG-SE data on fixed spinal cord (cyan). Error bars = mean ± SD from 174 repeats. (a) Predictions and data plotted on an axis of bD_0. Free diffusion decays linearly, as seen in the zoomed plot below, while all other cases do not. The spinal cord data has a small component of aCSF ($\approx 5\%$) which rapidly decays, leaving restricted or localized signal. The value of $b_s = 4.5\ \text{ms}/\mu\text{m}^2$ is also shown to indicate where the SG-DEXSY data lie. Bottom row shows a zoomed range on the x-axis. (b) Predictions and data plotted on an axis of $(bD_0)^{1/3}$. The tails of the restricted and localized signal become linear. The spinal cord data also decays linearly, supporting the presence of non-Gaussian signal behavior.

with radii $R = 0.5-1.3\ \mu$m using Neuman's expression [77] summed up to the fifth root (2.2.43), and (iii) the tail of the localization regime (3.4.3) (plotted for $\ell_d > 1.5\ell_g$, using the prefactor $a_0 = 5.8841$ for parallel plates [70] and $\ell_s = 1.3\ \mu$m). Overlaid on these predictions, we present data acquired using an SG-SE sequence on a fixed spinal cord. The NMR methods were the same as previously described and used a standard 4-step phase cycle (see Table 2.2 in Ref. [48]) with values of τ incremented linearly in 43 steps from 0.05 to 6.55 ms, corresponding to b-values between 5×10^{-4} and $3\times10^3\ \text{ms}/\mu\text{m}^2$, though only up to $\tau = 5.5$ ms, $b \approx 1.8\times10^3\ \text{ms}/\mu\text{m}^2$ are plotted. The measurement was repeated 174 times. Along an axis of bD_0 (Fig. 3.12a), the free diffusion decay is linear, while the others are not. A small component of the spinal cord signal ($\approx 5\%$) follows the free decay, representing an aCSF component.

In contrast, along an axis of $(bD_0)^{1/3}$ (Fig. 3.12b), the restricted and localized signal as well as the tail of the spinal cord data decay linearly. Note that we have plotted these regimes with parameters in concordance with the SG-DEXSY experiment. For restriction, $\ell_s \leq 1.3\ \mu$m values are kept below $\ell_d \approx 1.7\ \mu$m (corresponding to the $b_d \approx 0$ point). For localization, we set $\ell_s = 1.3 > \ell_g \approx 0.8\ \mu$m, and plot this regime only once $\ell_d > 1.5\ell_g$, representing the change-over from restriction to localization as ℓ_d grows. While the pre-factors chosen may not be appropriate, we note that the prefactor for the restricted case would merely shift the slopes (3.4.2), and the pre-factor for the localization case would shift the line up or down without affecting the slope (3.4.3), which is universal [70, 81]. Regardless, the general scaling behavior of the spinal cord data with $b^{1/3}$ is the primary observation. As an aside, the value of $b_s = 4.5$ ms/μm^2 used in the SG-DEXSY data is also shown, indicating that this choice of b_s fully decays the aCSF signal and maximally separates free vs. weakly attenuating signal.

There is therefore clear evidence of non-Gaussian signal behavior in fixed spinal cord which appears to be consistent, according to a cursory analysis, with restriction (the scaling is roughly parallel to $R = 0.9\ \mu$m, see Fig. 3.12b, though this would also depend on the pre-factor/geometry) rather than localization, because the slope is smaller than the universal scaling in the localization regime. In actuality, however, some combination of the regimes may be present if ℓ_s is broadly distributed, yielding some overall, effective scaling or slope in $(bD_0)^{1/3}$.

Degeneracy in single diffusion encodings

We should also clarify the effect of exchange. Exchange (during the encoding) should increase linearly with $\tau \propto (bD_0)^{1/3}$ and thus, if we approximate that any signal which exchanges would immediately dephase at such high b-values, exchange would have the effect of increasing the slope in the tail by a factor proportional to the exchange time τ_k. This approximation of the effect of exchange in SDEs has been described previously, e.g., in Refs. [126, 153, 154]. In short, exchange is expected to produce an additive effect on the signal scaling at high b-values. Consider that

SDEs are incapable of disentangling these effects. Decreased restriction and increased exchange or vice versa are both compatible explanations of changes in the SDE scaling and cannot be distinguished without additional experimental parameters such as with DDEs or by changing Δ in PG experiments. That is, the parameters that characterize restriction or exchange are degenerate.

Ignoring one or the other effect, as is common in signal models of tissue (e.g., CHARMED assumes negligible exchange between the intra-axonal and hindered compartments [97], and implementations of the Kärger model often either ignore restriction or set the restricted signal decay to 0 [101]) may significantly bias parameter estimates. If exchange is ignored, restriction parameters (ℓ_s) may be overestimated as the decay due to exchange will be attributed to increased ℓ_s; similarly, if the restricted signal is presumed not to decay, then the AXR may be overestimated as the restricted signal decay is attributed to increased exchange. If both effects are jointly modelled in SDE data, then fitting will be difficult due to the degeneracy of these effects and parameter estimates may end up being strongly dependent on the given initial values for the fit [111]. That being said, we now incorporate restriction into the curvature method and show how it can potentially be leveraged to disentangle these effects by individually varying the experimental parameters in the curvature method: b_s and t_m.

3.4.2 Two-compartment model with restriction

We begin by writing 4 signal fractions as we did for the biexponential signal model (3.3.1), but with the f_I signal fraction being motionally averaged and setting $D_E = D_0$. We denote the motionally averaged signal fraction as f_M:

$$\frac{S(b_1, b_2, t_m)}{S_0} = f_{MM} e^{-r_M \left(b_1^{1/3} + b_2^{1/3}\right)} + f_{ME} e^{-b_1^{1/3} r_M - b_2 D_0} + f_{EI} e^{-b_1 D_0 - b_2^{1/3} r_M} + f_{EE} e^{-D_0 (b_1 + b_2)}, \tag{3.4.4}$$

where

$$r_M = a \cdot \left(\frac{\ell_s}{\ell_g}\right)^4 D_0^{1/3} \tag{3.4.5}$$

is the approximate rate of signal decay with $b^{1/3}$ in the restricted compartment (which has units of $\mathrm{m}^{2/3}/\mathrm{s}^{1/3}$). Alternatively, we can write r_M in terms of an *apparent*

spherical radius R_{app} (apparent because we do not know the exact geometry and a localized signal component may contribute):

$$r_M = \frac{16}{175}\frac{(\gamma g)^{4/3}}{(2/3)^{1/3}D_0}\cdot R_{\text{app}}^4. \tag{3.4.6}$$

Again, we perform the rotation of the domain to b_s and b_d, evaluate the curvature along b_d about $b_d = 0$, and replace $f_{ME} = f_{EM} = \frac{1}{2}f_{\text{exch}}$, yielding [155]

$$\begin{aligned}\left(\frac{\partial^2 S}{\partial b_d^2}\right)_{b_d=0} =& \left(f_M - \frac{f_{\text{exch}}}{2}\right)\frac{r_M}{9}\left(\frac{2}{b_s}\right)^{5/3}\exp\left(-2\left[\frac{b_s}{2}\right]^{1/3} r_M\right) \\ &+ f_{\text{exch}}\left[\left(\frac{1}{3}\frac{r_M}{2^{1/3}b_s^{2/3}} - \frac{D_0}{2}\right)^2 + \frac{2^{2/3}r_M}{9b_s^{5/3}}\right]\exp\left(-\left[\frac{b_s}{2}\right]^{1/3} r_M - \frac{b_s}{2}D_0\right),\end{aligned} \tag{3.4.7}$$

As expected, the non-exchanging, Gaussian signal fraction f_{EE} disappears. We can approximate the curvature as before with a finite difference (3.3.8), but using just 3 points now in acknowledgement of our previous discussion about the redundancy of the left/right endpoints in b_d,

$$\left(\frac{\partial^2 S}{\partial b_d^2}\right)_{b_d=0} \approx \frac{2\Delta S}{\Delta b_d^2}, \tag{3.4.8}$$

where

$$\Delta S = \frac{1}{S_0}\left(S_{\text{end}} - S_{\text{mid}}\right) \tag{3.4.9}$$

is the difference between the normalized mid and endpoints along b_d and Δb_d is the differencing step. We can thus rewrite (3.4.7) in terms of f_{exch} as

$$f_{\text{exch}} = \frac{2\left(\Delta S - f_M c_1 b_s^2\right)}{\Delta b_d^2\left(c_0\exp\left(-\left[\frac{b_s}{2}\right]^{1/3} r_M - \frac{b_s}{2}D_0\right) - c_1\right)}, \tag{3.4.10}$$

where we define

$$c_0 = \left(\frac{1}{3}\frac{r_M}{2^{1/3}b_s^{2/3}} - \frac{D_0}{2}\right)^2 + \frac{2^{2/3}r_M}{9b_s^{5/3}},\ \ c_1 = \frac{r_M}{18}\left(\frac{2}{b_s}\right)^{5/3}\exp\left(-2\left[\frac{b_s}{2}\right]^{1/3} r_M\right). \tag{3.4.11}$$

Unlike for the biexponential signal model, the signal contribution from the non-exchanging, less mobile compartment $f_{MM} = f_M - f_{\text{exch}}$ *does not disappear*, and

contributes to the experimentally measured curvature. This contribution is captured by the first term in (3.4.7) and results in an f_M term that must be subtracted in the numerator of (3.4.10) to obtain the exchanging signal fraction. Therefore, non-Gaussian diffusion may account, in part, for the large intercept in the curvature observed in the fixed spinal cord data (see Fig. 3.8).

Note that the additional parameters introduced by restriction (f_M, r_M) do not confound the measurement of the AXR because the effects of restriction do not vary with t_m and will remain as an intercept and scaling constant that are ultimately fitted out by the 3-parameter exchange model (3.2.10). Indeed, we can exploit the 'orthogonality' of the experimental dimensions b_s and t_m to separately measure restriction and exchange. This property of DEXSY and similar sequences, wherein the restriction weighting is held constant whilst varying t_m, was recently pointed out by Chakwizira *et al.* [114] (c.f. Ning *et al.* [113]).

3.4.3 Artifacts in diffusion-diffusion spectra due to restriction

Before measuring these restriction parameters, let us investigate the effect of such non-Gaussian diffusion on ILTs. The tail of small diffusivities seen in the marginal distributions of $P(D_1, D_2)$ from full DEXSY data (Fig. 3.9a) can also be explained by restriction and may thus be artefactual or at least misleading in nature.

Simulated data

In Fig. 3.13, we plot signal contour maps and ILT-derived spectra for data simulated using the model in (3.4.4). We set the following parameters: $f_M = f_E = 0.5$, $r_M = 1.2\,\mu\text{m}^{2/3}/\text{ms}^{1/3}$, $D_0 = 2.15\,\mu\text{m}^2/\text{ms}$, and $t_m = [0,\, 1/(2k),\, 1/k]$ (corresponding to $f_{\text{exch}} \approx 0, 39, 63\%$ of f_{SS}). Note that the chosen value of r_M is large and corresponds to $R^{\text{app}} \approx 40\,\mu\text{m}$, which is not very realistic. In actuality, r_M may be much smaller, on the order of $\sim 0.1\,\mu\text{m}^{2/3}/\text{ms}^{1/3}$ for $R \lesssim 1\,\mu\text{m}$. We set a large value here to bring the range of b-values needed to fully attenuate the signal more in line with b-values that are attainable for conventional, PG-based experiments, and to show that ILT artifacts may appear even with these parameters, for which the effects of non-Gaussian diffusion

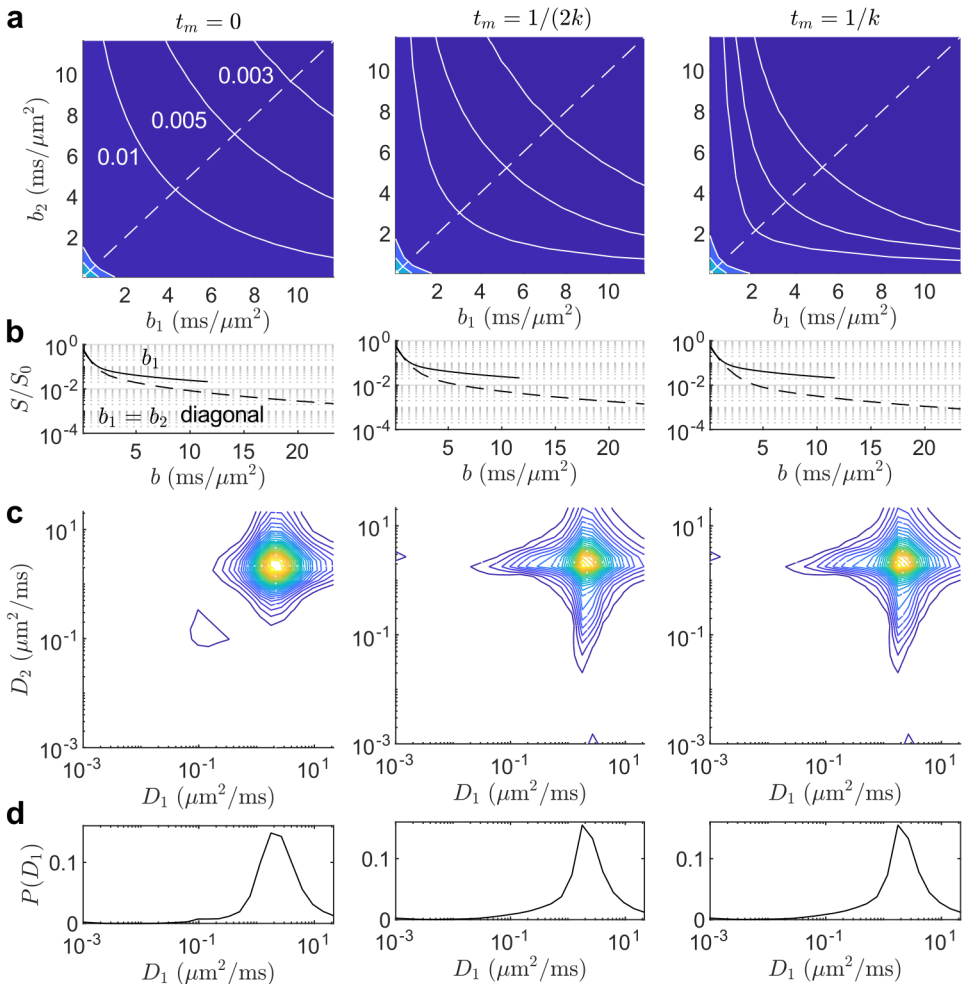

Figure 3.13: Simulated data and diffusion-diffusion spectra $P(D_1, D_2)$ for the presented two-compartment signal model with restriction (3.4.4). (a) Simulated DEXSY signal for three cases of increasing exchange left-to-right: $t_m = [0,\ 1/(2k),\ 1/k]$. Gaussian noise with SNR = 100 was added. Iso-signal contours at $S/S_0 = [0.01, 0.005, 0.003]$ are shown. (b) Signal decay from (a) along $b_2 = 0$ (solid line) and the $b_1 = b_2$ or $b_d = 0$ diagonal (dashed line). Increased exchange results in increased decay along the diagonal, and thus increasing symmetric curvature in (a), as expected. (c) ILT-derived diffusion-diffusion spectra $P(D_1, D_2)$. The range of diffusivities given for the inversion was $(D_1, D_2) \in [1\times10^{-3}, 22.5]$ μm^2/ms. The L_2 regularization parameter was chosen to produce a residual sum of squares RSS $\approx 1/\text{SNR}$ for the $t_m = 0$ case and held constant for the other cases. Broadening of the (D_0, D_0) component into a star-like shape is observed. In exchanging cases, distributed exchanging (off-diagonal) components are observed. (d) Marginal $P(D_1)$ distribution from (c). Note the long tail of distributed, small diffusivities. (Adapted from Ref. [155])

are exceedingly weak. Nonetheless, the simulations presented here are informative, and the observations should apply to any system in which $b^{1/3}$ scaling is present. Prior to inversion, Gaussian noise was added with SNR = 100, and the regularization parameter was chosen to produce a residual sum of squares approximately equal to 1/SNR for the $t_m = 0$ case and kept the same for the other cases.

Artifacts and spurious components

In Fig. 3.13a, the increasing curvature with t_m characteristic of exchange, as well as the curvature associated with restriction (when no exchange is present, $t_m = 0$) can be seen. These signal maps are similar to those presented in Fig. 3.8 for fixed spinal cord, wherein curvature was observed even at the shortest measured $t_m = 0.2$ ms. In the spectra (Fig. 3.13c), restriction leads to a star-like broadening of the (D_0, D_0) component. As a result, the exchanging 'peaks' are broadly distributed. The marginal distributions (Fig. 3.13d) bear striking similarity to those presented in Fig. 3.9a, and contain a long tail of small, distributed diffusivities. This tail, of course, is inconsistent with the two-compartment model used to simulate the data, and appears because a Gaussian diffusion model attempts to reproduce or fit the $b^{1/3}$ scaling as a series approximation spanning many values of D. Furthermore, we note that spurious off-diagonal components may be detected even in the absence of exchange due to the broadening of the (D_0, D_0) component.

With less regularization (data not shown), this tail can split into multiple peaks, in an effect known as 'pearling' [156]. Indeed, this may explain the multiple low diffusivity compartments seen in Fig. 3.9a (labelled A, B). Consider that if these were truly different compartments corresponding to different radii of restriction, then the observed exchange rates should be different due to the SVR scaling of k. This was not observed, and both components yielded $k \approx 140\ \mathrm{s}^{-1}$ upon fitting to the exchange model (3.2.10). Thus, we conclude that while ILTs may be able to detect exchange in a general sense, via an increase in the sum total of the off-diagonal components in the spectrum, the location and shape of these components cannot be meaningfully interpreted in the presence of non-Gaussian signal behavior that leads to non-b

scaling. Note that in SG experiments, this scaling appears with either restriction or localization, whereas in typical PG experiments (fixing ℓ_d and varying ℓ_g), the change in scaling appears only for localization. These findings suggest that care must be taken when interpreting spectra in ILT-based studies of diffusion, particularly when some degree of localization ($\ell_d \gg \ell_g$) is expected (see, for instance, the tail of small diffusivities reported in Ref. [157]).

3.4.4 Measuring restriction from curvature

Signal model

Going further, we can potentially estimate f_M and r_M by measuring the curvature at short t_m and varying b_s, where we may approximate $f_{\text{exch}} \approx 0$. Setting $f_{\text{exch}} = 0$ in (3.4.7) and evaluating ΔS (3.4.8) yields

$$\Delta S(b_s) = f_M \left[\exp\left(-b_s^{1/3} r_M\right) - \exp\left(-2^{2/3} b_s^{1/3} r_M\right)\right], \quad f_{\text{exch}} \to 0,\ \ell_d \gg \ell_s, \tag{3.4.12}$$

where the value of ΔS is half the curvature times the square of the differencing step Δb_d^2 (3.4.8). As few as two values of b_s are needed to determine f_M and r_M. Note, however, that this expression was obtained using the limiting long-ℓ_d behavior of the motional averaging regime, and not the full series expression for restriction in spheres (2.2.43). We have also dropped the R^2/D_0 term (2.2.46) as being small. These biases can be minimized by measuring in the regime where $\ell_d > \ell_g \gtrsim \ell_s$. As ℓ_d greatly exceeds ℓ_g, however, localized signal may appear. Furthermore, as $\tau \propto \ell_d^2$ increases, so will exchange during the encoding, violating the approximation $f_{\text{exch}} \approx 0$. These are competing constraints on the validity or applicability of (3.4.12). To try and balance these constraints, we choose to fit the model only over the range of $1.23\,\ell_g \leq \ell_d < 1.6\,\ell_g$, corresponding to $b_s = 2-5$ ms/μm^2. Another issue is that $f_{\text{exch}} \approx 0$ is not valid for rapid exchange even with exceedingly short encodings. In our case, where we found that $k \gtrsim 100$ s^{-1}, we actually expect about 10% of the signal to exchange over the encoding and $t_m = 0.2$ ms (≈ 1 ms total).

Therefore, we stress that r_M, f_M measured in this way are apparent, and do so here merely as a demonstration of the flexibility of the curvature method. More generally,

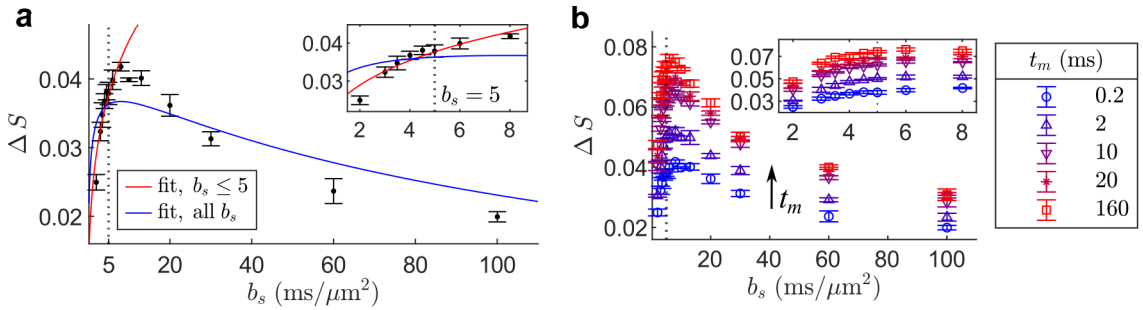

Figure 3.14: Measurement of restriction from curvature in a fixed spinal cord. (a) The difference between the normalized mid and endpoints in b_d, $\Delta S = (S_{\text{end}} - S_{\text{mid}})/S_0$, is plotted for $b_s = 2-100$ ms/μm^2 and $t_m = 0.2$ ms. Error bars = mean ± SD from three repeats. Fitting the model in (3.4.12) to a truncated range $b_s = 2-5$ ms/μm^2 produces a good fit (red line), as shown in the inset, yielding $r_M = 0.12 \pm 0.03$ μm$^{2/3}$/ms$^{1/3}$ and $f_M = 0.43 \pm 0.08$. The model is incapable of fitting over the entire range (blue line) due, perhaps, to the effects of localization and increased exchange during the encoding as ℓ_d (and b_s) increases. (b) Plots of ΔS vs. b_s for $t_m = [0.2, 2, 10, 20, 160]$ ms. The shape of the variation in ΔS is preserved over increasing t_m, though a slight decrease is seen at high b_s values, likely due to increased exchange during the encoding. This supports that the effects of non-Gaussian diffusion are fixed whilst varying t_m. Also shown in both plots is the choice of maximum $b_s = 5$ ms/μm^2 (dotted line) for the truncated fit. (Adapted from Ref. [155].)

we can say that measuring the curvature removes the effects of non-exchanging, Gaussian diffusion, leaving (i) non-Gaussian diffusion and (ii) exchange. These effects can then be disentangled to some degree by choosing experimental parameters that fix the weighting for one or the other effect. Fixing t_m and varying b_s probes (i) non-Gaussian diffusion. Fixing b_s and varying t_m probes (ii) exchange. Although the simplified signal model presented here may not be ideal for rigorously probing restriction, the notion that different parameter axes yield different contrast remains evident.

Results

In Fig. 3.14a, we show ΔS acquired over a range of $b_s = 2-100$ ms/μm^2 using the minimum $t_m = 0.2$ ms from three repeats on a fixed spinal cord. Fitting to the truncated range $b_s = 2-5$ ms/μm^2 yields a good fit to the model (3.4.12) with parameter estimates of $r_M = 0.12 \pm 0.03$ μm$^{2/3}$/ms$^{1/3}$ and $f_M = 0.43 \pm 0.08$ (mean ± SD). These parameters correspond to about $40-50\%$ of the signal being restricted within structures for which $R^{\text{app}} \approx 0.8$ μm or $\ell_s \approx 1.6$ μm. This is slightly less than the

diffusion length $\ell_d \approx 1.7\ \mu$m for the S_{mid} point, and confirms our previous discussion about how the lengthscales of the SG-DEXSY experiment determine the exchange process being measured, with $\ell_d = \ell_s$ as the rough dividing line between strongly and weakly attenuating signal. We see that the model cannot be fit over the whole range of b_s, likely due to the effects of localization and/or increasing exchange during the encoding. With these estimates of r_M and f_M, the approximate proportion of the short-t_m curvature due to restriction can be estimated by evaluating the ratio of the terms in the numerator of (3.4.10): $f_M c_1 b_s^2 / \Delta S(t_m = 0.2\text{ ms}) \approx 0.5$. Thus, as much as half of the short-t_m curvature can be explained by restriction, with the rest being due, perhaps, to exchange during the encoding, minor T_2 effects, or T_2–T_2 exchange.

We also show these data over several mixing times $t_m = [0.2, 2, 10, 20, 160]$ ms (Fig. 3.14b) to illustrate that the shape of the variation in ΔS with respect to b_s does not change much with t_m, consistent with the effect of restriction (or localization) being constant across t_m. The plot also highlights, once again, that our choice of $b_s = 4.5\ \text{ms}/\mu\text{m}^2$ is nearly optimal and produces the greatest contrast ΔS due to exchange. For more details on the separation of exchange and restriction using the curvature method and double SE experiments (i.e., truly $t_m = 0$), see Ref. [155].

3.5 Comparison to 'Filter Exchange' methods

Before continuing on to further results with the curvature method, we briefly discuss how the curvature method fits into the broader literature on approaches to sub-sampling DEXSY data. The most relevant comparison is to FEXSY, a method proposed by Åslund *et al.* [116] and refined by Lasič *et al.* [122], which also eschews the use of an ILT. In FEXSY, b_1 is held constant in order to filter the signal from the freer compartment. As described by Lasič *et al.* [122], the value of b_2 is then varied to measure a filtered ADC that recovers to a baseline value as t_m increases due to equilibration of the signal via exchange. Thus, FEXSY measures a recovery in the ADC and the rate of this recovery is fit as an AXR. Seen a different way, FEXSY 'slices' the $[b_1, b_2]$ domain vertically (for b_1 along the horizontal axis) while the curvature method slices the domain (anti-) diagonally, as diagrammed in Fig. 3.15, in which

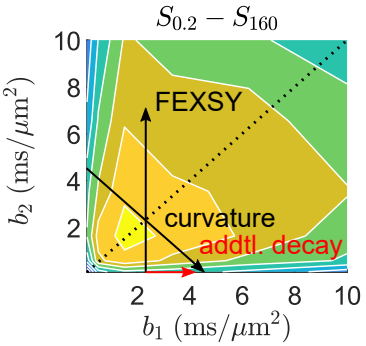

Figure 3.15: Comparison of the FEXSY and curvature methods and how each sub-samples DEXSY data. The sampling methods are overlaid on a difference map of the signal from fixed spinal cord at t_m = 160 vs. 0.2 ms averaged over three repeats, re-used from Fig. 3.8. FEXSY slices the data vertically (holding b_1 constant), while the curvature approach slices (anti-)diagonally along constant b_s. If the filtering b_1 value is smaller than b_s, the curvature approach will show less signal contrast due to decay along b_1 (red arrow).

the two sampling schemes are overlaid on the difference map presented in Fig. 3.8b.

If we consider that 2 points are needed to measure an ADC, and that the baseline ADC can be used as an *a priori* limit in the 3-parameter model of exchange, then FEXSY can use also as few as 5 total points (2 points to measure the baseline ADC and 2 ADC measurements at 2 t_m, recycling the normalization point $S(b_1, b_2 \approx 0)$ for the filtered signal), which is just as fast as our minimal, 5-point measurement. Furthermore, if the filtering b_1 value is smaller than b_s, then the curvature method will potentially produce less signal contrast when evaluating ΔS due to the additional signal decay along b_1 (see Fig. 3.15) and FEXSY may have better SNR characteristics. The curvature method also does not provide information about the diffusion characteristics of the compartments, whereas FEXSY, by the nature of measuring ADCs, can. This specificity to exchange could be considered a disadvantage that leads to poor fitting of multi-parametric models (i.e., that include diffusion parameters) when compared to other sampling schemes, as noted recently by Ordinola *et al.* [158] and Cheng *et al.* [159]. On the other hand, by isolating exchange — rather than measuring it in a proximate manner such as via an ADC — the curvature method can produce f_{exch} or exchange-weighted contrast maps at a single t_m, as shown previously (Fig. 3.6). Indeed, we emphasize that the lack of information about diffusion in the curvature

method is by intentional design and should not be considered a disadvantage *per se*, given that we are interested principally in exchange.

Furthermore, we stress that the difference map (Fig. 3.15) unambiguously indicates that a *single* point in the domain (along $b_1 = b_2,\ b_d = 0$) contains the most exchange weighting. If we take into consideration the normalization approaches described in Sec. 3.3.4, the optimal approach to measure an AXR (from both an SNR and rapidity perspective) is evidently to measure the variation in this single point whilst removing the effect of diffusion-weighted T_1 relaxation (see Sec. 3.3.4). In doing so, we dispense with any modelling of the intercept/limit in the 3-parameter model of exchange (3.2.10) and measure the AXR in an essentially model-free manner, which can be performed directly in the signal domain and without needing S_0 (see Fig. 3.11b). From this perspective, there is no functional difference between FEXSY performed with $b_1 = \frac{b_s}{2}$, where b_s is chosen to intersect with this maximally exchange-weighted point, and the curvature method, besides the T_1 normalization approach. Scher *et al.* [128] recently developed just such a variation of FEXSY where ADC modelling was not performed and the decay of a single point along t_m was fit to produce an AXR. Note, however, that because FEXSY does not hold the total b-value constant, the diffusion-weighted T_1 may differ between points, introducing bias that is not present for the curvature method [46]. That being said, we argue that the approaches in Sec. 3.3.4 are optimal for measuring the AXR (relatively speaking).

Remaining limitations

That is not to say that the curvature method and FEXSY come without significant methodological limitations. As we alluded to in Sec. 3.4, the effects of non-Gaussian diffusion (modelled here as restriction), remain as an effect in DDEs in general. Indeed, the measurement of restriction using DDEs is another sub-field in its own right [112], though typically employs different orientations between the two diffusion encodings [14, 117]. DDEs have been applied to estimate pore sizes [160, 161] or, more empirically, a time-dependent kurtosis [162, 163]. The degree to which such effects bias estimates of the AXR using FEXSY remains a subject of debate [131, 164,

165]. In the curvature method, variable restriction-weighting between S_{mid} and S_{end} is present due to the varying τ, though we expect that this effect is not t_m-dependent, as discussed, leaving the AXR estimation unaffected (see Chapter 7, Fig. 7.1 for a calculation of $C(t)$ of both acquisitions). Nonetheless, some effect of non-Gaussian diffusion may remain, particularly if the GPA does not hold (i.e., due to localization).

Another issue arises if multiple exchanging sites are present, such as vascular exchange or exchange [134, 166] between neurites/soma and the ECS, complicating the notion of a singular AXR. For the spinal cord specimen, no vasculature is present, but this could be an issue in the *in vivo* studies in Chapter 5. We will explore methods to probe multiple exchange rates in Chapter 4, concluding that, a single AXR may in fact be insufficient to describe exchange in tissue.

Concluding remarks

We have developed a sub-sampling method for DEXSY data wherein we hold the total b-value (b_s) constant and vary the ratio of b_1 and b_2 in order to rapidly measure exchange. The curvature along an axis of $b_d = b_1 - b_2$ is seen to be proportional to the exchanging signal fraction, as validated on a WM tissue phantom. By measuring the increase in this curvature, an AXR can be fit using as few as 5 total data points (Sec. 3.3.4) as demonstrated in fixed neonatal mouse spinal cord — a GM tissue model — using the PM-10 system. We find that exchange is extremely rapid in this specimen, with an AXR of $k \approx 140\ \text{s}^{-1}$ ($\tau_k \approx 7$ ms). This is approximately in line with the fastest reports for GM exchange in the literature of $\tau_k \approx 15$ ms or smaller (e.g., Refs. [103], [101]). We point out that our PM-10 system, capable of sub-millisecond diffusion encoding times, is uniquely sensitive to such fast exchange, and thus the high AXR is not necessarily surprising given the parameters and specimen in question.

We further showed that by incorporating non-Gaussian diffusion (i.e., restriction) into our signal model — motivated by SDE data indicating $b^{1/3}$ signal scaling — we can reproduce certain characteristics of the data acquired in fixed tissue, such as a long tail of small diffusivities in the marginal diffusion spectra $P(D)$ and a large intercept in the curvature. These findings expose pitfalls in the conventional analysis

of DEXSY data and make the case for ILT-free approaches such as the curvature method, which are both faster and not susceptible to these artifacts. The flexibility of the curvature method in its ability to somewhat separate exchange-weighting from restriction-weighting (or non-Gaussian diffusion) was also demonstrated.

While FEXSY is another method to rapidly sub-sample DEXSY data, potentially with advantages compared to variants of the curvature method that use 3 points per t_m, we argue that the rapid, 5-point method is an optimal method for measuring the AXR that can be applied in a model-free manner. In the following Chapters 4, 5, we move on to the study of live *ex vivo* neonatal mouse spinal cord and *in vivo* mouse brain.

4

Distributed Exchange Times and Activity

4.1 Introduction 97
4.1.1 Chapter outline and related works 99
4.2 Evidence for active exchange in live tissue 101
4.2.1 Activation energies in live vs. fixed tissue 101
4.2.2 Suppression of the sodium-potassium pump 105
4.2.3 Oxygen-glucose deprivation model 106
4.3 Measuring a distribution of exchange times 109
4.3.1 Signal modelling 110
4.3.2 Phase cycling in DEXSY experiments 111
4.3.3 Distributions in live tissue 116
4.4 Effects on the distribution under perturbations 124
4.4.1 Temperature variation 124
4.4.2 Suppression of the sodium-potassium pump 126
4.4.3 Tissue 'rundown' 128
4.4.4 Fixation 130
4.4.5 Osmolarity perturbation after ouabain 132
4.5 Discussion 136

4.1 Introduction

Having validated and thoroughly investigated a rapid measurement of exchange, we now study what information the AXR contains in living tissue. The AXR is generally thought to be a probe of structure and permeability ($k = \kappa S/V$), i.e., of passive

exchange. The historical perspective is that water exchanges *only* passively (along its osmotic gradient), with the permeability of the membrane being mediated by aquaporin expression. In the brain parenchyma, the isoform aquaporin-4 (AQP4) is most important, and is localized to the endfeet of astrocytes [100, 167]. A growing body of evidence, however, suggests that water transport also occurs via active (i.e., energy- or ATP-dependent) processes. More specifically, certain membrane transport proteins such as the Na^+/glucose transporter have been found to co-transport up to hundreds of molecules of water per ion [168–174]. Ion transport may also create transient, local osmotic gradients that drive water transport in the vicinity of ion transporters [171]. Thus, the water exchange rate may amplify the ion exchange rate. Paraphrasing a recent review by MacAulay [174]: "[A]quaporins ... do not suffice to explain the overall brain water movement ... brain fluid can be secreted against an osmotic gradient, suggesting that conventional osmotic water flow may not describe all transmembrane fluid transport in the brain." Therefore, one may posit that transmembrane water exchange is linked, in part, to activity and metabolism. More specifically, one may posit that passive exchange, characterized by $k = \kappa S/V$, occurs in tandem with active exchange, characterized by electrochemical potentials.

Indeed, several MR studies of exchange suggest that a component of the AXR in neural tissue is linked to metabolism and particularly the activity of the Na^+/K^+–ATPase [175–181]. While most of these findings were based on DCE MRI methods [175–178], recent work by Springer *et al.* [180, 181] found that the AXR measured by diffusion-based methods can also probe Na^+/K^+–ATPase activity whilst avoiding the use of contrast agents and sidestepping the experimental challenges associated with DCE methods, such as the issue of blood-brain barrier permeability to contrast agents [176]. We aim to further these investigations here by studying exchange in viable, *ex vivo* neonatal mouse spinal cord using the PM-10 system under various conditions consistent with energetic failure [146].

This investigation forms part of a broader debate about the feasibility of measuring activity using diffusion MR methods [182–185]. Such methods aim to assess neuronal activity directly via their associated neuronal or astrocytic swelling [184, 186, 187], rather than indirectly via hemodynamic couping as in conventional blood-oxygen-

level-dependent (BOLD) functional MRI (fMRI) [188]. However, the sensitivity of diffusion to function [189] and the nature of the observed signal differences [190] (whether they be cell-related or vascular in nature) remains controversial.

Despite the continued reservations concerning diffusion fMRI, we note that the signal contrast generated by DEXSY-based methods such as the curvature method is fundamentally different from SDEs [111] and may therefore show unique sensitivity to activity. Moreover, as we have pointed out, the length- and timescales probed on the PM-10 are unique and generally unattainable on more conventional systems. Thus, our method(s) may be able to detect activity-based contrast whereas conventional SDE methods have not (yet) clearly done so. Finally, we stress that we do not make the much stronger claim that the AXR can measure the transient activity of cells — nor can we measure the AXR on such a timescale — but instead limit our study to *steady state* metabolic activity. That is, we compare 'normal', baseline function to states associated with energetic failure.

4.1.1 Chapter outline and related works

We first build the case that the AXR has active and passive components. Using temperature variation to measure activation energies, suppression of the Na^+/K^+–ATPase using ouabain, and an oxygen-glucose deprivation (OGD) perturbation, we present evidence for active exchange in live spinal cord. This work [146] was led jointly by Drs. Williamson and Ravin with input on the theory and data analysis from myself:

- Williamson, N. H.*, Ravin, R.*, **Cai, T. X.**, Falgairolle, M., O'Donovan, M. J., & Basser, P. J. (2023) Magnetic Resonance measurements of steady-state transmembrane water exchange detect cellular activity and homeostasis in central nervous system tissue. *PNAS Nexus*, *2*(3), pgad056.

We also find that values of k under conditions of energetic failure are similar (i.e., both ouabain and OGD produce similar decreases in k) and are highly repeatable across samples, indicating that the exchange rate is an absolute, intrinsic measurement that may serve as a useful biomarker of steady state activity.

If there are, in fact, passive and active contributions to exchange, these may represent exchange processes with different rates. To test this hypothesis, we investigate the *distribution* of exchange times using ILT analysis of data acquired using the curvature method across many mixing times. We find that there is a bimodal distribution of exchange times in live tissue, and that only the faster of these peaks is suppressed upon the introduction of ouabain. These findings suggest that active exchange is linked, specifically, to fast exchange processes. Some of this data was recently presented at:

- **Cai, T. X.**, Williamson, N. H., Ravin, R., & Basser, P. J. Multiexponential analysis of diffusion exchange times reveals a distinct exchange process associated with metabolic activity. (2023, June). *Proceedings of the 32nd Annual Meeting of the ISMRM*, Toronto, Canada, Abstract #5017.

Importantly, we observe high repeatability of the distributions within- and between-samples, indicating that the experimental and analysis method(s) are robust.

Expanding upon this work, we present exchange time distributions under various conditions: temperature variation, the loss of tissue viability or 'death' — which we call tissue 'rundown' — fixation, and upon the introduction of an osmolyte. These results provide further mechanistic insight into the nature of active exchange and form part of a first-authored publication in preparation:

- **Cai, T. X.**, Williamson, N. H., Ravin, R., & Basser, P. J. Multiexponential analysis of exchange times in neural tissue reveals a bimodal distribution of distinct exchange processes. In preparation.

Findings in fixed tissue and under osmolarity perturbations suggest that the observed bimodality in the exchange time distributions arises from different structures, rather than parallel exchange processes. We also take the opportunity to present an optimal 4-step phase cycle of the SG-DEXSY experiment, implemented here in order to reduce the time required for each acquisition and to free up experiment time to acquire more mixing times. Compared to existing coherence selection schemes, this 4-step phase cycle is both shorter and more comprehensive, and represents a significant advance in DEXSY methodology.

In summary, these results support that exchange in (GM) tissue contains both passive and active components. Further ILT analyses reveal a bimodal distribution of exchange times in live tissue. Perturbations to disrupt activity suggest that the faster of the two exchange peaks, specifically, is associated with activity.

4.2 Evidence for active exchange in live tissue

In this section, we present a compendium of evidence supporting the existence of active exchange.

4.2.1 Activation energies in live vs. fixed tissue

Passive and active processes should have different temperature dependence. The activation energy E_a for the passive self-diffusion of water is about $18 - 20\,\mathrm{kJ/mol}$ [191]. In contrast, E_a for active processes is much higher due to the compounded temperature-dependence of substrate diffusion and different enzymatic reaction steps [192]. The Na^+/K^+–ATPase or sodium-potassium pump, for example, has an E_a of around $100\,\mathrm{kJ/mol}$ [192, 193]. As a first step in studying the presence of active exchange, we measured the E_a of the exchange rate k in live — or, more accurately, viable — *ex vivo* neonatal mouse spinal cord as compared to fixed spinal cord, again using the PM-10 and the curvature method.

Methods

The NMR and tissue preparation methods were largely the same as previously described (Secs. 3.3.3, 3.3.4) except that viable spinal cords were studied immediately after dissection and their viability was confirmed by the recording of action potentials via electrophysiological methods. Specifically, motoneuronal electrical activity was observed after stimulation of a dorsal root, and mono- and polysynaptic reflexes were recorded in $n = 4$ specimen at up to 7 hrs after dissection and following 2 hrs of NMR measurements (see Ref. [45]). Thus, loss of viability is not expected in any experiments except where noted otherwise.

To look at the effects of temperature, the temperature of the test chamber was varied in a step-wise manner to 7, 25, or 35 °C by varying the temperature of chiller/heaters which pump water through holes in the aluminum chamber (see Fig. 3.7). Rapid temperature switching was achieved by having external water baths pre-chilled or -warmed to the desired temperature and using valves to switch the water source. The temperature was varied in sequence from $25 \rightarrow 7 \rightarrow 25 \rightarrow 35 \rightarrow 25$ °C, wherein the 25 °C condition was repeated in a 'test-retest' manner to ensure that the samples recovered from being subjected to colder/warmer temperatures. A total of $n = 6$ fixed samples and $n = 3$ live samples were studied in this manner. Additionally, $n = 4$ live spinal cords underwent just the first $25 \rightarrow 7 \rightarrow 25$ °C conditions. Fewer live samples underwent the full experiment due to the difficulty of maintaining high temperatures without loss of viability, observed qualitatively as an irreversible decrease in k (data not shown). NMR measurements were carried out over 40 minutes at each temperature, after first allowing 10 minutes for temperatures to stabilize.

Exchange and ADC measurements were performed. Here, the 4-point method was used with an 8-step phase cycle (Table B.4) and the same SG-DEXSY parameters as given in the previous chapter: $b_d = [-4.3, -0.15, 4.3]$ at a fixed $b_s = 4.5$ ms/μm^2 normalized to S_0 ($b_s = 0.2, b_d = -0.02$ ms/μm^2) and using 11 mixing times, $t_m =$ [0.2, 1, 2, 4, 7, 10, 20, 40, 80, 160, 300] ms. For ADC measurement, an SG-SE sequence with a 4-step phase cycle [48] was used. For this measurement, the normalization point S_0 was measured at $b \approx 0.1$ ms/μm^2 (recall that no diffusion weighting is not possible) and diffusion-weighted signals S were measured at equally-spaced τ up to a maximum $b = 1.5$ ms/μm^2, corresponding to $\tau \approx 0.2$, 0.35, and 0.5 ms. We note that this ADC is measured perpendicular to the spinal cord (i.e., along the y-axis, see Fig. 3.7), and denote it as ADC$_y$. Finally, activation energies E_a were fit using an Arrhenius model

$$f(T^{-1}) = A \exp\left(-\frac{E_a}{RT}\right), \tag{4.2.1}$$

where T is the absolute temperature in Kelvins and $R = 8.3145 \times 10^{-3}$ kJ/(mol K) is the ideal gas constant. See Ref. [146] for further details on the methods.

Results

In Fig. 4.1 fits of E_a to (4.2.1) for k and ADC_y in live and fixed spinal cord(s) are shown. For exchange k (Figs. 4.1a, b), the measured activation energies were found to be significantly different ($p < 0.005$) between live ($E_a = 36 \pm 7$ kJ/mol, mean ± SD across samples) and fixed specimen ($E_a = 21 \pm 8$ kJ/mol). Note that the E_a measured in fixed spinal cord resembles that of free diffusion ($E_a = 18$ kJ/mol), as measured in pure aCSF and consistent with previous reports [191]. On the other hand, the E_a measured for ADC_y (Figs. 4.1c, d), was not significantly different ($p = 0.21$) between fixed ($E_a = 7.0 \pm 2.1$ kJ/mol) and live ($E_a = 8.3 \pm 1.5$ kJ/mol) specimen. These results suggest that active exchange exists and that k is sensitive to steady-state, metabolic activity whereas ADC_y is not.

Effects of fixation

The effect(s) of fixation and whether they impact this conclusion must also be considered, however. Notably, we found that ADC_y values were reduced by about 20% in fixed specimen (see the downward shift in Fig. 4.1c). This is consistent with the reported reduction in the ECS (from ≈ 20 to 5%) [194] caused by fixation. Fixation therefore reduces the fraction of mobile, extracellular water, and this reduction can sufficiently explain the observed reduction in ADC_y. Fixation is also known to cause some degree of permeation in membranes [194, 195]. Do these structural changes significantly impact the conclusion? We point out that at 7 °C, for which no enzymatic activity is expected [193], the values of k for fixed and live specimen begin to converge (see Fig. 4.1a), indicating similar, though not quite equal, structural characteristics for the exchanging (i.e., enclosed or restricted, ICS) compartment at this temperature — recall that $k = \kappa S/V$ is proportional to the SVR (apparent SVR, due to the possibility of localization) assuming passive exchange. Thus, most of the additional temperature-dependence of k in live tissue can likely be attributed to activity, rather than structural or permeability differences, and we interpret these results as evidence of active exchange.

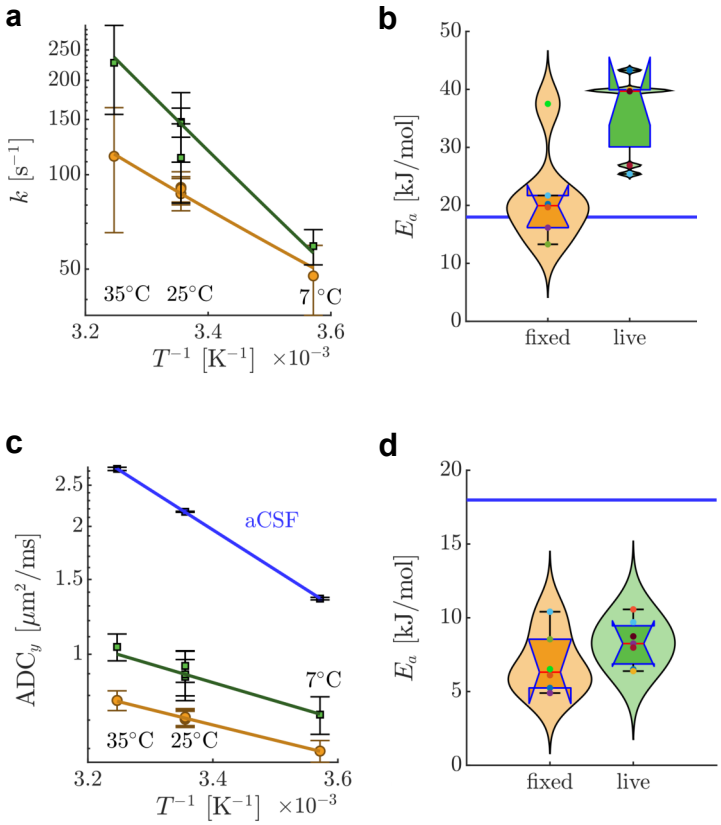

Figure 4.1: Activation energies E_a for the exchange rate k and ADC$_y$ in live and fixed spinal cords. (a) Measurements of k using the 4-point curvature method over several temperatures 7, 25, and 35 °C, varied step-wise as 25 → 7 → 25 → 35 → 25 °C. Thus, 25 °C appears 3 times. Error bars = mean ± SD from 3 measurements each on $n = 6$ fixed spinal cords (orange), and $n = 7$ live spinal cords (green), pooling all measurements. Note that, of the live specimen, $n = 3$ went through all temperatures and $n = 4$ went through just 25 → 7 → 25 °C. Solid lines show a fit of the Arrhenius model (4.2.1) to the means. (b) Box and violin plots of the E_a obtained by fitting (4.2.1) to each sample (3 measurements). Each dot represents a different specimen. The E_a for live spinal cords, or the slope in (a), is measured as $E_a = 36 \pm 7$ kJ/mol, which is significantly different ($p < 0.005$) from that of fixed spinal cords $E_a = 21 \pm 8$ kJ/mol (mean ± SD across samples). Also shown for comparison is the $E_a = 18$ kJ/mol measured in pure aCSF (blue line) — see part (c) — similar to that reported for the self-diffusion of water 18 – 20 kJ/mol [191]. (c) Measurements of ADC$_y$ over the same temperatures. Pure aCSF is also shown (blue). (d) Fitted E_a for ADC$_y$. Here, the values of E_a are not significantly different ($p = 0.21$) between live ($E_a = 8.3 \pm 1.5$ kJ/mol), and fixed spinal cords ($E_a = 7.0 \pm 2.1$ kJ/mol), indicating that exchange shows different sensitivty than diffusion. Note as well that in (a) and (c), k and ADC$_y$ are reduced for fixed tissue due to the net effects of fixation. (Adapted from Ref. [146].)

4.2.2 Suppression of the sodium-potassium pump

To further investigate the activity-dependence of exchange, and particularly whether this dependence is mediated by certain enzymes, we measured k in live specimen under the influence of ouabain, an Na^+/K^+–ATPase inhibitor. Considering that continual activity of the Na^+/K^+–ATPase accounts for as much as 50% of the total energy budget in central nervous system tissue [196], the Na^+/K^+–ATPase is a prime candidate for mediating the activity-dependence of exchange.

Methods

A 100 μM dose of ouabain was used, which is sufficient to completely inhibit the various isoforms of the Na^+/K^+–ATPase in the specimen [197]. That is, dose-response experiments indicate that this is a saturating dose. To measure the response to ouabain in real-time, we used the T_1^{app} approach but modified to measure a biexponential T_1^{app} and thus capture some of the exchange weighting (see Sec. 3.3.4). This halves the data needed (by omitting S_0 and one of the endpoints in b_d), such that k can be measured in roughly 6 minutes (2 s TR $\times$ 2 points $\times$ 11 t_m $\times$ 8 phase cycles). Measurements of k were interleaved with measurements of ADC_y. Specimen were monitored for 40 min before and for 40 min after the introduction of 100 μM ouabain in order to observe both the baseline and the limiting effect of ouabain.

Results

In Fig. 4.2, results are presented for $n = 3$ live specimen. Exchange rates k were found to drop from $k \approx 140\ \text{s}^{-1}$ and stabilize at a plateau of around $k = 36 \pm 11\ \text{s}^{-1}$, representing a large $71 \pm 8\%$ decrease (mean ± SD from three samples, averaged after the plateau in Fig. 4.2a). In contrast, the measured ADC_y decreased more modestly by $9 \pm 1\%$ (Fig. 4.2b), indicating that exchange is highly sensitive to the effect(s) of ouabain and exhibits contrast (i.e., an effect size) different from ADC_y.

Note that the effect of ouabain is a loss of resting membrane potential, which results in a net influx of ions (i.e., the loss of ionic gradients) and subsequent cytotoxic swelling or edema [198]. This is consistent with the effects of energetic

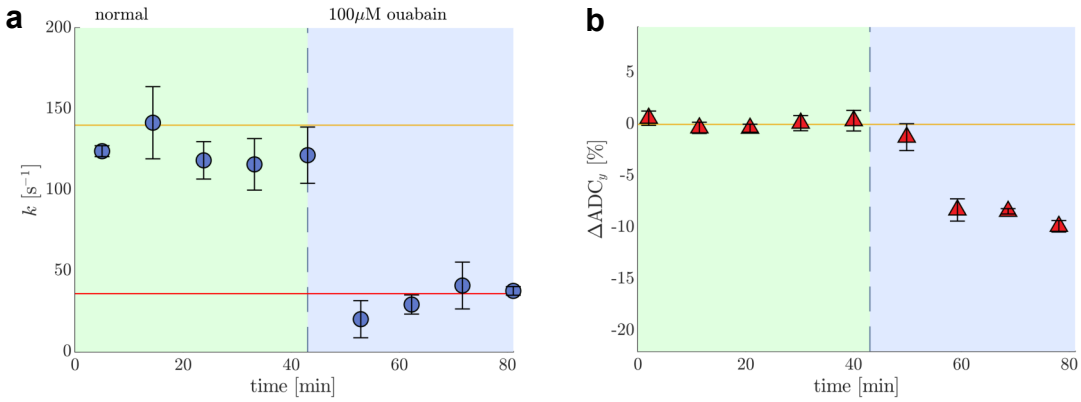

Figure 4.2: Measurements of k and ADC_y in live spinal cord during the addition of 100 μM ouabain at 25°C. (a) Change in k over time as the specimen goes from normal conditions (green shading) to after the addition of ouabain (light blue shading). Error bars = mean ± SD from three specimen. The normative exchange rate across samples and from the previous chapter ($k = 140\ s^{-1}$) is drawn (orange line). The mean value after addition of ouabain, averaging cross specimen ($k = 36\ s^{-1}$), is also drawn (red line). (b) Percentage change in ADC_y over the same time period. Measurements of k and ADC_y were interleaved and repeated approximately once every 7 min. (Adapted from Ref. [146].)

failure in general [199]. Thus, the drop in ADC_y can be explained by cellular swelling (increased ICS, decreased ECS). The drop in k can also be partially explained by an increased ICS, but further mechanisms are likely present, considering the large difference in effect size (≈ 70 vs. 10%). Plausible explanations include the cessation of water co-transport due to the loss of ionic gradients or the disappearance of transient, local osmotic gradients induced by ion transport, though we cannot disentangle these mechanisms at this time. These results agree with previous reports that NMR measurements of exchange are sensitive to the activity of the Na^+/K^+–ATPase [175–181], though the measured effect size in our study is comparatively large, perhaps due to the isolation of exchange.

4.2.3 Oxygen-glucose deprivation model

Lastly, we studied the effect of oxygen-glucose deprivation (OGD) in live spinal cord, mimicking the effects of stroke and general energetic failure.

Methods

OGD was induced by switching the media inflow to glucose-free aCSF (made with 30 mM sucrose to keep osmolarity constant) bubbled with 1% O_2, 5% CO_2, and 94% N_2. Simultaneously, gas flowing into the top of the sealed chamber was switched from 95% O_2/5% CO_2 to humid 1% O_2, 5% CO_2, and 94% N_2. Two durations of OGD were tested, corresponding to different degrees of energetic failure. OGD was maintained for either 40 min ($n = 8$) or 70 min ($n = 9$) before switching back to normal aCSF and gas. Measurements of k and ADC_y were performed in the same manner as in Fig. 4.2, interleaving measurements. Saturation recovery experiments were also interleaved to measure $T_1 = 1/R_1$, which serves as a proximal measurement of the partial pressure of oxygen (pO_2) [200]. Specimen were observed at baseline over a period of 50 min and for several hours after switching back to normal conditions to monitor recovery.

Results

Time-courses of R_1, ADC_y, and k are presented in Fig. 4.3. Measurements of R_1 confirm the switching of OGD and normal conditions (Figs. 4.3a, b). Decreases in ADC_y of up to roughly $10-15\%$ (Figs. 4.3c, d) were observed, similar to the effect size observed for ouabain (Fig. 4.2b). The exchange rate k plateaus at about $45 \pm 7\ s^{-1}$ in the 70 min OGD experiment (Fig. 4.3f), which is not statistically different from the rate $k = 36 \pm 11\ s^{-1}$ observed for ouabain (Fig. 4.2a). These results indicate that similar effects were achieved via altogether different means of inducing energetic failure (ouabain vs. OGD).

We highlight the difference in the time-courses of ADC_y and k (Fig. 4.2). In the case of 70 min OGD, ADC_y shows a two-step decrease, with an initial decrease followed by a second decrease at $\approx 30-40$ min OGD (Fig. 4.3d). In contrast, k remains near baseline before dropping precipitously after ≈ 30 min OGD (Fig. 4.3f). Cross-correlation analyses (data not shown, see Ref. [146]) reveal that the initial drop in ADC_y precedes the drop in k by $\approx 20-30$ min.

We note that values of ADC_y were seen to recover to baseline (and can even overshoot the baseline, see Supplement in Ref. [146]) after switching back to normal

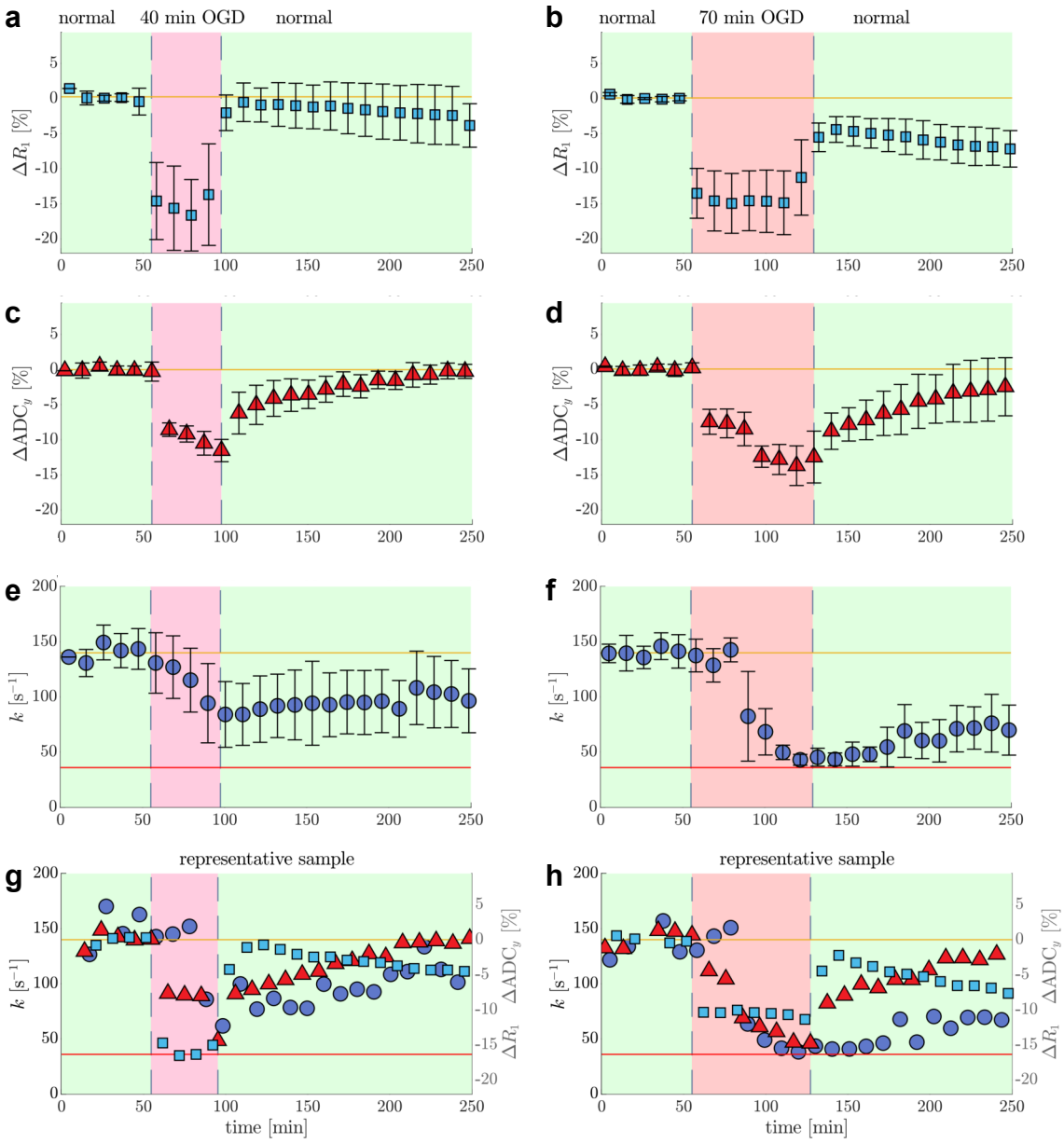

Figure 4.3: Time-courses of R_1, ADC_y, and k while switching from normal media bubbled with 95% pO_2 (green shading) to glucose-free media bubbled with 1% pO_2 (red/pink shading), before washing/switching back to normal conditions after 40 min (left column) or 70 min (right column), at 25°C. (a – f) Time-courses of R_1, ADC_y, and k. Error bars = mean ± SD from $n = 8$ samples for 40 min OGD (left column) and $n = 9$ samples for 70 min OGD (right). For k, the normative value ($k = 140\,s^{-1}$, orange line) and mean value after addition of ouabain ($k = 36\,s^{-1}$, red line) are drawn. In the 70 min OGD case, k plateaus near the line for ouabain. Note the differences in the time-course and recovery of ADC_y and k. (g, h) Time-course for a representative sample, with the axes for R_1 (light blue squares) and ADC_y (red triangles) on the right side and the axes for k (dark blue circles) on the left.

conditions, whereas k does not fully recover. The degree of recovery in k varied depending on the duration of OGD. Less recovery was observed after the 70 min OGD condition, wherein k eventually reached the plateau seen for oaubain ($k \approx 36\ \mathrm{s}^{-1}$, Fig. 4.2a). In comparison, in the 40 min OGD condition, OGD was halted before k fully decreased to this plateau, perhaps allowing for greater recovery. This suggests that k may be able to monitor recovery from stroke-like conditions.

We find as well that values of k under normal conditions ($k \approx 140\ \mathrm{s}^{-1}$) and conditions of energetic failure ($k \approx 36\ \mathrm{s}^{-1}$) were highly consistent between samples (see error bars in Figs. 4.3e, f, Fig. 4.2a), and thus k may serve as an absolute, intrinsic measurement of steady-state activity, rather than a relative measurement, and values between these two extremes may represent varying degrees of activity or recovery.

Summary of findings

Altogether, these findings form a strong case that exchange, measured as an AXR, is linked to (steady-state) metabolic activity — as evidenced by (i) a larger E_a in live vs. fixed tissue, (ii) a large decrease in k upon the introduction of ouabain, and (iii) a similar decrease under OGD, along with varying degrees of recovery depending on the severity (duration) of OGD. Furthermore, the information in k is evidently distinct from SDEs (ADC_y). The different effect sizes and behavior in the time-courses under ouabain and OGD support this conclusion. Of course, ADC_y is influenced by k (higher k corresponds to greater water mobility) and part of the variation in ADC_y can potentially be explained by changes in k — i.e., there is some overlap in information. Nonetheless, it is clear that k contains information beyond that which is communicated by ADC_y. While the mechanism(s) linking exchange and metabolic activity remain unclear, these findings suggest, at the least, that active exchange exists.

4.3 Measuring a distribution of exchange times

The existence of active exchange, supported by the results in the previous section, raises the question of whether passive and active exchange are separable in terms of exchange time. Indeed, there is no *a priori* reason to assume that different exchange

mechanisms would proceed at the same rate. If, for example, active exchange is linked to transient osmotic gradients produced by ion transport, then active exchange should proceed at a (potentially much) faster rate than passive exchange due to the increased driving force. Furthermore, passive and active exchange may correspond to different structures (e.g., neurites vs. soma) and thus have different SVRs and thereby AXRs. To explore whether passive and active exchange have different exchange times, we develop a method to measure *distributed* exchange times.

To do so, we employ ILT analysis and modify our signal model accordingly. The use of an ILT requires sufficient coverage in t_m, and many t_m may be required to obtain robust distributions. To that end, we also develop an improved phase cycling scheme which reduces the number of steps from 8 to 4, whilst also more comprehensively suppressing unwanted coherences. This allows for more t_m to be acquired in the same experiment time. We also explore the potential for sub-sampling in t_m to ascertain the minimal amount of data needed to produce robust distributions.

4.3.1 Signal modelling

To model a distributed exchange time, we can write the 3-parameter model of exchange (3.3.11) using a *probabilistic* exchange time with distribution $P(\tau_k)$:

$$\frac{S_{\text{mid}}}{S_{\text{end}}} = C_1 \int P(\tau_k) \exp\left(-\frac{t_m}{\tau_k}\right) d\tau_k + C_0, \tag{4.3.1}$$

If we remove the limit or floor (C_0), then we have an expression that is effectively identical to a T_2 relaxometry experiment (scaled by some factor C_1), where the time domain in question is t_m rather than the echo time,

$$\frac{S_{\text{mid}}}{S_{\text{end}}} - C_0 = C_1 \int P(\tau_k) \exp\left(-\frac{t_m}{\tau_k}\right) d\tau_k, \tag{4.3.2}$$

Note that the estimation and removal of the floor C_0 is essential to obtaining robust distributions. This is a well-known challenge in relaxometry experiments [201, 202], wherein the Rician noise floor from magnitude data can produce spurious, long T_2 components. Modelling and subtracting the floor, as we propose to do here, is one method to ameliorate this issue [202].

For this reason, we write (4.3.2) using the division approach $S_{\text{mid}}/S_{\text{end}}$ (see Sec. 3.3.4) rather than the T_1^{app} approach due to the tendency of the T_1^{app} approach to produce non-monotonic tail behavior, discussed previously (see Sec. 3.3.4, Fig. 3.11b). Such behavior will complicate the estimation of C_0 and should be avoided in this particular application. We will provide an example of this non-monotonic tail behavior in real data later in Sec. 4.3.3 and provide a clear justification for using $S_{\text{mid}}/S_{\text{end}}$, despite its aforementioned disadvantages (i.e., error propagation and removing exchange weighting).

Consider as well that the proportionality factor C_1 corresponds to the total amount of *observable* exchanging signal, or $f_{\text{SS}} - f_0$ in (3.2.10). Rather than presenting $P(\tau_k)$ in a normalized sense (integrates to 1), it is informative to scale $P(\tau_k)$ by C_1 in order to further distinguish distributions based on total exchange. The amplitude of the distribution will correspond to different amounts of exchange when scaled by C_1 and yield an additional source of visual contrast between conditions.

4.3.2 Phase cycling in DEXSY experiments

Let us first develop a more rapid, 4-step phase cycle for the SG-DEXSY experiment (Fig. 3.1). We can enumerate the unwanted coherences using the principle of Woessner decomposition, as we did in Table 2.1 for the STE experiment. Recall that this decomposition amounts to treating each pulse as being either an effective 0, 90-, or 180°-pulse.

Unwanted coherences

While many pathways can form echoes (indeed, up to 40 [33]), we need only consider those that are stored (or persist) longitudinally during t_m, as the static gradient will spoil any pathways that are in the transverse plane for any appreciable t_m. We also need only consider pathways which coincide with the desired coherence at the final echo. We will address the worst-case scenarios of either $\tau_1 = \tau_2$ ($b_1 = b_2$, S_{mid}) wherein certain STE pathways can refocus, and $\tau_2 \approx 0$ (S_{end}), wherein the FIDs from the second diffusion encoding may persist due to the short τ_2. With these

Table 4.1: Coherences in the 5-pulse DEXSY sequence

Pathway	1	2	3	4	5
SE-SE	90°	180°	90°	90°	180°
STE_1	90°	90°	0°	0°	90°
STE_2	90°	0°	90°	90°	0°
STE_3	0°	90°	90°	0°	90°
SE	0°	0°	0°	90°	180°
FID_1	0°	0°	0°	90°	0°
FID_2	0°	0°	0°	0°	90°

conditions in mind, a total of 6 unwanted pathways need be considered: (i – iii) three different STEs, (iv) the SE arising from only the second diffusion encoding, and (v – vi) FIDs from the final 90°- and 180°-pulses.

Recall as well that the SG-DEXSY sequence contains 5 pulses followed by a CPMG readout (90, 180, 90, 90, 180° → CPMG, Fig. 3.1). The CPMG train consists of 180°_y-pulses that will repeatedly refocus the magnetization along the same axis and can thus be ignored for the purpose of phase cycling. In Table 4.1, we show the effective pulses (numbered 1 – 5) for each unwanted pathway along with the desired pathway, denoted as SE-SE since it is a double SE with storage.

While it is difficult to systematically generate phase cycles, we can approach the problem in parts. We begin from all pulses being standard, i.e., 90°_x, 180°_y pulses with resulting receiver phase $\varphi_{\text{rec}} = \pi$. First, consider STE_1. It turns out that by using a $180^\circ_{\pm y}$-pulse (pulse 2) orthogonal to the excitation pulse, this pathway is not stored and is thus spoiled. Likewise, STE_3 will be spoiled because this pathway will be excited onto the $\pm x$-axis by a $180^\circ_{\pm y}$-pulse and will not be stored by subsequent $90^\circ_{\pm x}$-pulses, though we can suppress it anyway by cycling pulse 2. Next, consider FID_2, which sees the final 180°-pulse (pulse 5) as a 90°-pulse. Cycling this last pulse between 0 and π and setting $\varphi_{\text{rec}} = 0$ will suppress this FID. This leaves the STE_2, SE, and FID_1 pathways. To suppress STE_2, we can introduce a receiver cycle determined by the final 180°-pulse (which this pathway misses). This can be accomplished by introducing an additional cycle of the last pulse between $\pm\frac{\pi}{2}$ and setting the receiver phase back to $\varphi_{\text{rec}} = \pi$ for these steps. This brings the total number of steps to 4.

Table 4.2: Optimal 4-step SG-DEXSY phase cycling scheme

Step	φ_1	φ_2	φ_3	φ_4	φ_5	φ_{rec}
1	0	$+\pi/2$	π	π	0	0
2	π	$-\pi/2$	π	0	$+\pi/2$	π
3	0	$+\pi/2$	π	π	$-\pi/2$	π
4	π	$-\pi/2$	π	0	π	0

Finally, consider the SE pathway. This pathway does not see the first 90°-pulse such that cycling this pulse together with pulse 4 will suppress this pathway along with FID_1. This additional step does not interfere with the 4-step cycling of the last pulse and can be incorporated without introducing steps.

4-step phase cycle

We thus arrive at a 4-step phase cycle, shown in Table 4.2. This phase cycling scheme is comprehensive (when paired with spoiling during t_m and $b_1 > 0$) and can also be applied to PG-DEXSY experiments. We note the similarity between the phase cycling of the last pulse here and the common 4-step EXORCYCLE [28] scheme, as well as similarity to (parts of) the standard 4-step STE phase cycle [36], shown in Table 2.4. These similarities highlight that, despite the difficulty in designing phase cycles, certain phase cycling principles or 'tricks' can be broadly applied.

In Table 4.3, we work out the phase of the magnetization after each pulse and over the 4 phase cycle steps for every pathway in Table 4.1, and in so doing, verify the comprehensiveness of the phase cycling scheme. The phase of the magnetization during detection (i.e., after the last pulse) at each step is shown in parentheses, as well as the offset from the receiver phase φ_{rec}. Obviously, suppression is achieved when the offsets are opposed between steps (e.g., 0, π). All pathways considered are seen to be suppressed. As a finer detail, we point out that pathways storing along $+z$ and $-z$ are not necessarily equivalent — storing along $-z$ is akin to an inversion experiment and decreases signal by T_1 relaxation whereas storing along $+z$ recovers (some) signal. Thus, such pathways must be suppressed pair-wise to remove

Table 4.3: Location or phase of magnetization after each pulse for all pathways in Table 4.1 and phase cycle steps in Table 4.2. Note that STE_1 and STE_3 are spoiled because they are not stored during t_m.

.

Pathway	**Steps**	90°_x	180°_y	90°_{-x}	$90^\circ_{\pm x}$	$180^\circ_{\pm x,\pm y}$	φ_{rec}	**Offset**
SE-SE	1	$+y$	$+y$	$+z$	$-y$	$+y$ (0)	0	0
	2	$-y$	$-y$	$-z$	$-y$	$-y$ (π)	π	0
	3	$+y$	$+y$	$+z$	$-y$	$-y$ (π)	π	0
	4	$-y$	$-y$	$-z$	$-y$	$+y$ (0)	0	0
STE_1 (spoiled)	1	$+y$	$+y$	$+y$	$+y$	$-z$	0	N/A
	2	$-y$	$-y$	$-y$	$-y$	$-y$ (π)	π	0
	3	$+y$	$+y$	$+y$	$+y$	$+y$ (0)	π	π
	4	$-y$	$-y$	$-y$	$-y$	$-z$	0	N/A
STE_2	1	$+y$	$+y$	$+z$	$-y$	$-y$ (π)	0	π
	2	$-y$	$-y$	$-z$	$-y$	$-y$ (π)	π	0
	3	$+y$	$+y$	$+z$	$-y$	$-y$ (π)	π	0
	4	$-y$	$-y$	$-z$	$-y$	$-y$ (π)	0	π
STE_3 (spoiled)	1	$+z$	$-x$	$-x$	$-x$	$-x$ $(+\pi/2)$	0	$+\pi/2$
	2	$+z$	$+x$	$+x$	$+x$	$+z$	π	N/A
	3	$+z$	$-x$	$-x$	$-x$	$+z$	π	N/A
	4	$+z$	$+x$	$+x$	$+x$	$+x$ $(-\pi/2)$	0	$-\pi/2$
SE	1	$+z$	$+z$	$+z$	$-y$	$+y$ (0)	0	0
	2	$+z$	$+z$	$+z$	$+y$	$+y$ (0)	π	π
	3	$+z$	$+z$	$+z$	$-y$	$-y$ (π)	π	0
	4	$+z$	$+z$	$+z$	$+y$	$-y$ (π)	0	π
FID_1	1	$+z$	$+z$	$+z$	$-y$	$-y$ (π)	0	π
	2	$+z$	$+z$	$+z$	$+y$	$+y$ (0)	π	π
	3	$+z$	$+z$	$+z$	$-y$	$-y$ (π)	π	0
	4	$+z$	$+z$	$+z$	$+y$	$+y$ (0)	0	0
FID_2	1	$+z$	$+z$	$+z$	$+z$	$+y$ (0)	0	0
	2	$+z$	$+z$	$+z$	$+z$	$-x$ $(+\pi/2)$	π	$-\pi/2$
	3	$+z$	$+z$	$+z$	$+z$	$+x$ $(-\pi/2)$	π	$+\pi/2$
	4	$+z$	$+z$	$+z$	$+z$	$-y$ (π)	0	π

T_1-weighting and the phase cycles are designed to do so. Specifically, see how STE_2 is cycled in Table 4.3, with each pair of $+z$ or $-z$ steps being destructively added. To experimentally confirm the performance of the 4-step phase cycle, we measured the same S_0 ($b_s = 0.2, b_d = -0.02$ ms/μm^2) as well as symmetric endpoints along b_d using either the 4- vs. 8-step phase cycle, indicating that they are equally performant from a coherence selection standpoint (data not shown). We note, however, that Table 4.3 can stand on its own as a confirmation of coherence selection.

We are now well-positioned to re-evaluate the previous phase cycling schemes. In Appendix B, we show a similar table for the 8-step phase cycle confirming that it does not suppress STE_2. Thus, setting $b_1 \neq b_2$ is necessary to spoil this pathway, as we have done throughout and continue to do. There is also another pathway which is let through only when $b_1 = 0$ and is thus avoided in the SG-, but not the PG-DEXSY implementation and explains the asymmetry along b_d observed in Fig. 3.5. This pathway misses the first 180°-pulse and goes through the rest of the sequence (i.e., an STE-SE: 90, 90, 90, 180° — see Appendix B). Thus, the choice between the left and right endpoints along b_d is not entirely arbitrary, and $b_1 > 0$ is preferable for coherence selection.

General recommendations

Of course, this is not the only means to perform coherence selection in a DEXSY sequence and other schemes may work equally well. The investigation here, however, highlights some general principles for coherence selection in (both PG and SG) DEXSY sequences, and particularly those which utilize an SE-SE pulse sequence. We list some recommendations here:

- Spoiling during t_m drastically reduces the number of echo-forming pathways that need to be considered and is always recommended
- refocusing pulses $180^\circ_{\pm y}$ orthogonal to the excitation and storage pulses $90^\circ_{\pm x}$ prevent the formation of some STE pathways
- Setting $b_1 \neq b_2$ spoils STE pathways as does setting $b_1 > 0$. Given the expected

symmetry in the DEXSY signal (e.g., see Fig. 3.8), it is potentially preferable to acquire signal along the axis where $b_2 = 0$ rather than $b_1 = 0$, and to avoid acquiring data exactly along the $b_1 = b_2$ diagonal

- Cycling the storage pulses in some manner suppresses the SE pathway that sees only the second diffusion encoding

Finally, we stress that this is the first thorough investigation, to our knowledge, of phase cycling in the SG-DEXSY experiment using spin echoes. Although not directly comparable due to the additional coherence pathways introduced by using stimulated echoes instead of spin echoes, a drastically larger 128-step phase cycle list was published for a static gradient, double stimulated echo DEXSY sequence [203]. The proposed 4-step phase cycle is a novel result and a non-trivial advance in the experimental implementation of SG-DEXSY.

4.3.3 Distributions in live tissue

With a faster phase cycling scheme in hand, we present exchange time distributions $P(\tau_k)$ measured in live spinal cord. High repeatability within- and between-samples was observed. Importantly, live tissue was found to have a bimodal distribution of τ_k and only the faster of these peaks was affected by perturbations to activity, presented later in Sec. 4.4. These results strengthen the hypothesis that distinct active and passive exchange processes exist. Before presenting this data, we describe the inversion and normalization approaches and demonstrate them in simulated data.

Methods and simulations

For the ILTs, we used the Butler-Reeds-Dawson algorithm [204] implemented for a T_2-type decay [205, 206]. To demonstrate the robustness of the inversion, we present distributions $P(\tau_k)$ from simulated exchange-weighted decays in S_{mid}, following normalization of the diffusion-weighted T_1 by the division approach. Data was simulated as biexponential decays of the form:

$$\frac{S_{\text{mid}}}{S_{\text{end}}} = C_1 \left[f_{\text{fast}} \exp\left(-\frac{t_m}{\tau_k^{\text{fast}}} \right) + (1 - f_{\text{fast}}) \exp\left(-\frac{t_m}{\tau_k^{\text{slow}}} \right) \right] + C_0 \tag{4.3.3}$$

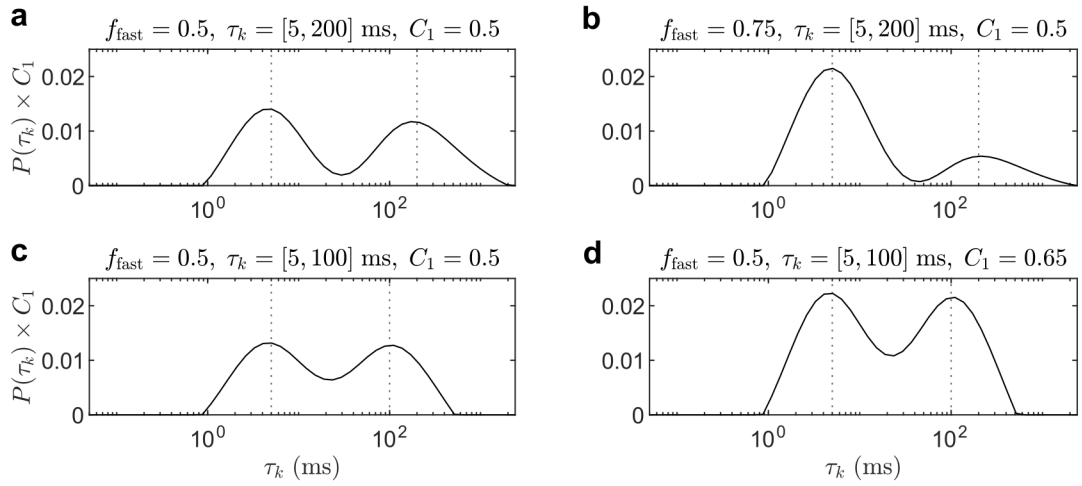

Figure 4.4: Exchange time distributions $P(\tau_k)$ scaled by C_1, obtained for data simulated using (4.3.3) with added Gaussian noise (SNR = 100) and various parameters (a – d). Dotted lines indicate the chosen exchange time parameters.

where f_{fast} is the fraction of the faster exchanging component, $\tau_k^{\text{fast}}, \tau_k^{\text{slow}}$ are exchange times, C_1 is the total (observable) exchanging signal, and C_0 is a floor or limit. Note that the fraction f_{fast} here does not correspond to a signal fraction in the conventional sense (i.e., a partial volume or proton density), but rather to the fraction of the observed exchange that is attributable to a given exchange process or rate. For instance, a tissue component may correspond to a large part of the observed signal, but if said component exhibits no exchange then it would not appear at all in this exchange-weighted decay. Gaussian noise with SNR = 100 was added prior to inversion in all simulated data. Data was simulated over 39 mixing times from $0.125 - 400$ ms.

In Fig. 4.4, we first show cases with no floor ($C_0 = 0$) to demonstrate that the inversion approach can produce accurate exchange times and fractions. In Fig. 4.4a, we set $f_{\text{fast}} = 0.5$, $[\tau_k^{\text{fast}}, \tau_k^{\text{slow}}] = [5, 200]$ ms, and $C_1 = 0.5$. The ILT produces, expectedly, two peaks centered at these times and roughly equal in amplitude. In Fig. 4.4b, the fraction is changed and the relative peak amplitudes are seen to change accordingly. In Fig. 4.4c, τ_k^{slow} is set to 100 ms and the longer τ_k peak is shifted to the left. Finally, in Fig. 4.4d, C_1 is increased to 0.65 and the peak amplitudes increase. The inversion approach is thus robust to noise (SNR = 100) and can reproduce the expected behavior

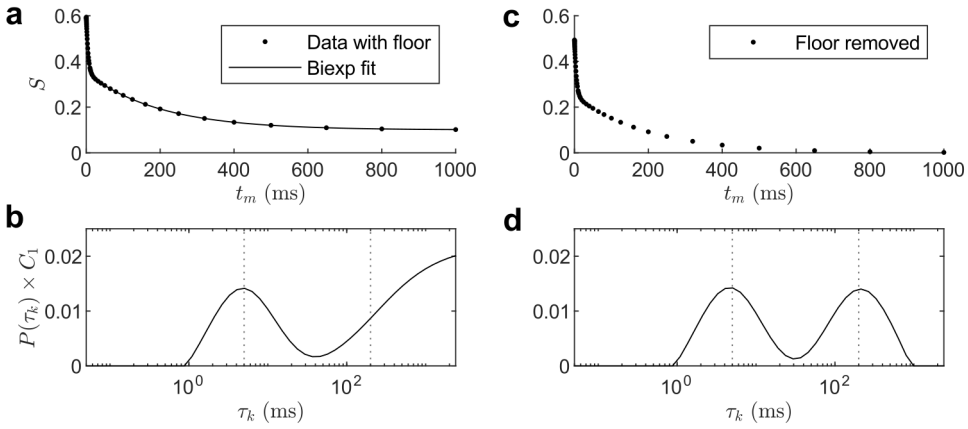

Figure 4.5: Demonstration of floor removal and floor-related artifacts in simulated data. (a) Data was simulated using the same parameters as in Fig. 4.4a ($f_{\text{fast}} = 0.5$, $[\tau_k^{\text{fast}}, \tau_k^{\text{slow}}] = [5, 200]$ ms, $C_1 = 0.5$) with added signal floor $C_0 = 0.1$. A biexponential fit to (4.3.3) is shown. (b) Obtained $P(\tau_k)$ without floor removal, demonstrating a long-τ_k artifact. (c) Simulated data from (a) after subtraction of C_0 estimated by the biexponential fit. (d) Obtained $P(\tau_k)$ after floor removal, similar to that obtained in Fig. 4.4a.

in $P(\tau_k)$. Note that C_1 was estimated by a biexponential fit of the simulated data to (4.3.3) and was not given *post hoc*. What if C_0 is not 0?

In Fig. 4.5, we demonstrate the importance of signal floor removal. Data was simulated using the same parameters as in Fig. 4.4a, but with an added signal floor of $C_0 = 0.1$. Without removing this signal floor, a spurious long τ_k component is estimated by the inversion (Fig. 4.5b) and the inversion cannot reproduce the expected parameters for the longer τ_k component. To remove this floor, the C_0 estimated from a biexponential fit was subtracted (Fig. 4.5c), after which a distribution similar to that obtained in Fig. 4.4a is recovered (Fig. 4.5d). It should be noted, however, that floor removal in this manner effectively constrains the inversion to the range of mixing times probed.

Normalization approaches revisited

We now apply this method to real data and argue that the $S_{\text{mid}}/S_{\text{end}}$ normalization approach is preferable to the T_1^{app} approach for this particular application. In Fig. 4.6, we show S_{mid} and S_{end} ($b_d = [-0.15, 4.3]$, respectively, at a fixed $b_s = 4.5$ ms/μm^2) acquired over 39 mixing times from $0.125 - 400$ ms on a *live* sample measured 5 times

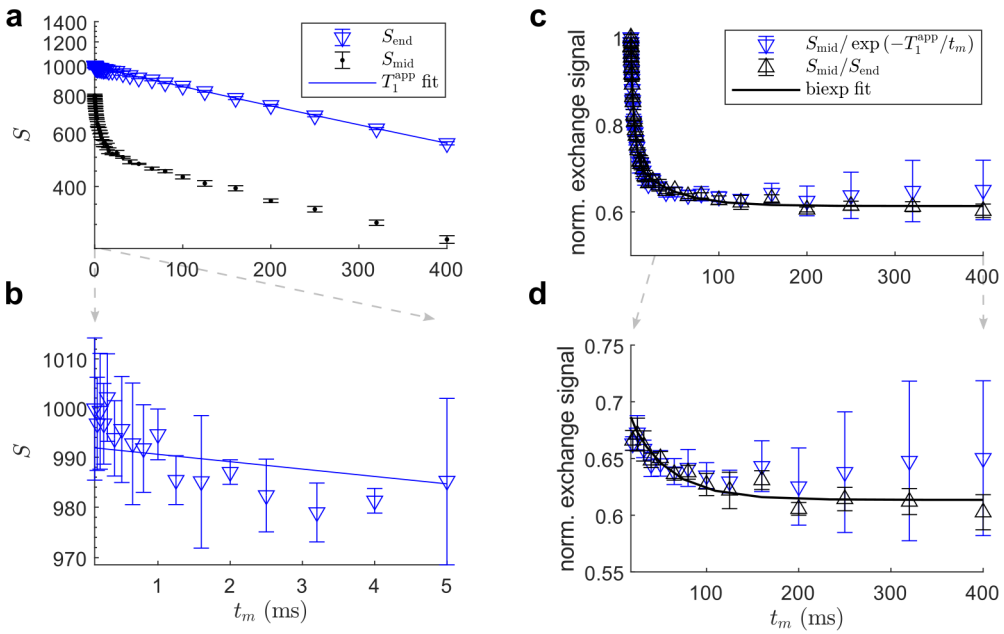

Figure 4.6: Normalization approaches and tail behavior for data acquired over 39 t_m from 0.125 – 400 ms in a live spinal cord. (a) The two points S_{mid} (black) and S_{end} (blue) plotted on a log-scaled y-axis. Error bars = mean ± SD from 5 experimental repeats. (b) Zoomed plot from (a), showing S_{end} up to $t_m = 5$ ms. Note the decrease due to exchange weighting. (c) Normalized exchange signal using either approach of S_{mid}/S_{end} (black) or estimating T_1^{app} (from each repetition, blue). A biexponential fit to the means of S_{mid}/S_{end} is shown (black line). (d) Zoomed plot of (c) at long t_m, highlighting the non-monotonic tail behavior from the T_1^{app} approach, which is not seen in the S_{mid}/S_{end} approach.

(Figs. 4.6a, b). A 4-step phase cycle similar to that presented in Table 4.2 was used (see Appendix B, Table B.6). The two normalization methods are compared (Figs. 4.6c, d), dividing by the mean of the first point ($t_m = 0.125$ ms) to obtain normalized exchanging signal decays starting from ≈ 1.

As discussed previously in Sec. 3.3.4, S_{end} contains some exchange weighting and thus decreases slightly with t_m, as seen in the zoomed plot in Fig. 4.6b. This exchange weighting biases the fit(s) for T_1^{app} and can lead to over-correction of the signal at long t_m, as seen in Figs. 4.6c and d (as well as previously in Fig. 3.11b). Such behavior is not detrimental when fitting a monoexponential AXR, but can be problematic when estimating $P(\tau_k)$. The observed non-monotonic tail behavior will make fitting and estimation of the floor difficult, leading to issues in the ILT such as those shown in Fig. 4.5. Therefore, the S_{mid}/S_{end} normalization approach is preferred.

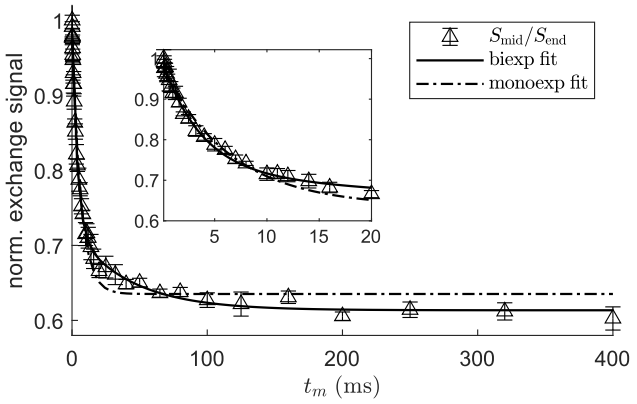

Figure 4.7: Normalized exchange signal using the $S_{\mathrm{mid}}/S_{\mathrm{end}}$ approach, shown in Fig. 4.6, fit using either a bi- or monoexponential model. The residual norm ($\sqrt{\mathrm{RSS}}$) for the biexponential is much smaller ($\approx 2\times10^{-3}$) than for the monoexponential fit ($\approx 1\times10^{-2}$).

A biexponential fit to this normalized exchange signal is shown in Figs. 4.6c, d and demonstrates that the floor C_0 can be accurately estimated and subtracted prior to inversion. While the T_1^{app} approach could potentially be improved by fitting a *bi*exponential to S_{end} in order to capture the exchange weighting (as we did for the results in Figs. 4.2, 4.3), we note that the SNR (≈ 50, 4-steps, 2000 CPMG echoes) between the two approaches is actually comparable due to variability in the estimated T_1^{app} between repeats (see error bars in Fig. 4.5d to the left of $t_m = 100$ ms), negating the SNR advantages of the T_1^{app} approach when using many t_m. Therefore, there is no advantage from taking this more complicated approach, and we can avoid the additional fitting step without loss in SNR.

Finally, we point out here that a biexponential fits better to the normalized exchange signal than a monoexponential. In Fig. 4.7, a bi- vs. monoexponential fit is compared for the $S_{\mathrm{mid}}/S_{\mathrm{end}}$ data in Fig. 4.6c. The monoexponential fit clearly diverges from the data at increasing t_m, indicating a failure to capture a slower exchange component. The residual norm for the biexponential fit ($\approx 2\times10^{-3}$) is much smaller than for the monoexponential fit ($\approx 1\times10^{-2}$). These data provide a preliminary suggestion that exchange time distributions $P(\tau_k)$ may be bimodal. This also suggests that the exchange-weighting in S_{end} may be biexponential, further complicating the T_1^{app} approach.

A bimodal distribution in live spinal cord

Methods

Proceeding with the $S_{\text{mid}}/S_{\text{end}}$ approach, we present data from 3 different live spinal cords (all dissected on P1, measured at 25 °C), each measured 5 times over mixing times from a wider range of $t_m = 0.125 - 1000$ ms. We are thus sensitive to τ_k over approximately this same range. Mixing times were spaced approximately log-linearly over 43 points. In addition, long-t_m points were over-sampled to ensure accurate estimation of the floor, acquiring up to 4 (averaged) repetitions of each t_m at longer values (i.e., $400 - 1000$ ms). Thus the 43 points actually correspond to 63 acquisitions. A 4-step phase cycle similar to Table 4.2 was used (see Appendix B). Normalized exchange data $S_{\text{mid}}/S_{\text{end}}$, dividing by the mean of the first point at $t_m = 0.125$ ms to obtain decays from ≈ 1, were fit to a biexponential (4.3.3) to estimate the floor, which was then subtracted prior to inversion. For the ILT, the range of τ_k was set to $0.05 - 2400$ ms (somewhat wider than the t_m range) with 50 points spaced log-linearly (similar to the 43 points in t_m). An implementation of the Butler-Reeds-Dawson algorithm [204] was used [206] with non-negativity constraints.

Results

In Fig. 4.8, we assess the repeatability of $P(\tau_k)$ both between- (Fig. 4.8a) and within-samples (Fig. 4.8b). Also shown are the raw, normalized exchange signals with the floor subtracted (bottom row). The decay of these signals to 0 indicates successful floor removal prior to inversion. The distributions are highly similar for the three P1 samples. Furthermore, the 95% confidence intervals (CI) are relatively narrow, indicating that the SNR is sufficient to measure $P(\tau_k)$ in a repeatable manner. In Fig. 4.8b, we show all 5 repeats from one of the samples to explicitly illustrate the degree of set-to-set variability. Note that the time required to acquire one set is about 17 min (2 s TR × 2 points × 63 t_m × 4 phase cycles), aided significantly by the shorter phase cycle list, which halves the experiment time. In Fig. 4.9, we assess the feasibility of sub-sampling the t_m domain by using every other mixing time in Fig. 4.8 for a total of 22 points, whilst also halving the resolution in τ_k to 25 points. This brings the

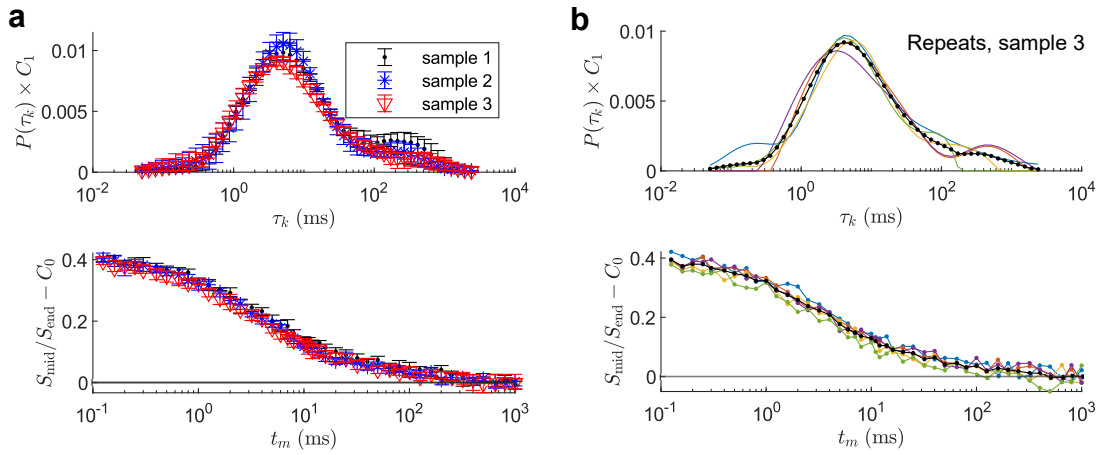

Figure 4.8: Normalized exchange data and exchange time distributions $P(\tau_k)$ from 3 live spinal cords (dissected P1), measured 5 times each. (a) Repeatability across samples. (top) Distributions $P(\tau_k)$ (50 points log-linearly spaced from 0.05 – 2400 ms) scaled by the total exchanging signal C_1. Error bars = means and 95% CIs estimated by bootstrapping. (bottom) Normalized exchange data $S_{\mathrm{mid}}/S_{\mathrm{end}}$, dividing by the mean at the shortest t_m, and with the floor C_0 removed, plotted on a log-t_m scale to demonstrate the log-linear sampling. Note the decay to 0, indicating successful floor removal. Altogether, 43 points from $t_m = 0.125 - 1000$ ms were acquired, with some repeated points at long t_m for a total of 63 acquisitions. The intercept is measured as $C_1 \approx 0.4$. (b) Repeatability within a sample. All 5 individual repeats are shown for sample 3 from part (a), (red). Colored lines correspond to different repeats. The mean is shown in black.

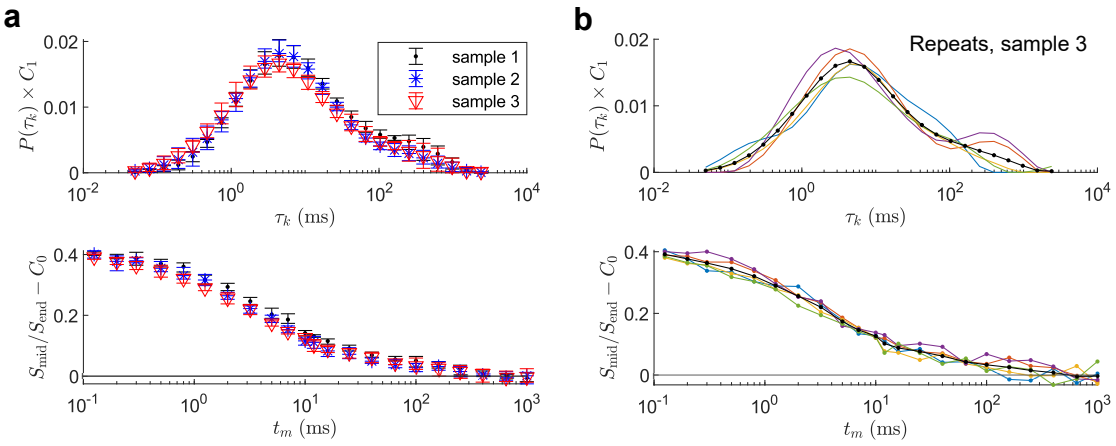

Figure 4.9: Analogous figure to Fig. 4.8, but sub-sampling t_m at every other point, reducing from 43 to 22 points and bringing the experiment time from ≈ 17 to 8 min. The τ_k domain was also reduced from 50 to 25 points. General characteristics in $P(\tau_k)$ are retained, but peaks are broadened.

experiment time down to approximately 8 minutes, potentially enabling time-course monitoring as we did in Figs. 4.2, 4.3 for ouabain and OGD. Sub-sampling the data to half as many t_m retains the general characteristics of $P(\tau_k)$, although the peaks are broader and less resolved. This analysis indicates the feasibility, at least, of data reduction. What are the characteristics of $P(\tau_k)$?

The distributions are bimodal with a larger, fast exchanging peak around $\tau_k = 3-5$ ms ($k = 200-250\ \mathrm{s}^{-1}$), and a much slower peak around $\tau_k = 200-500$ ms ($k = 2-5\ \mathrm{s}^{-1}$). The relative amplitude of the slower peak is $\approx 15-20\%$ of the larger peak, and its position is more variable (see Fig. 4.8b). This variability, however, may be due simply to the relative lack of signal at longer t_m, rather than actual differences in the long-time exchange, though we should mention again that the subtraction of the floor constrains $P(\tau_k)$ to the range of t_m probed (up to 1 s) and may flatten out any long-time behavior that may be present in the signal decay. The total exchange was consistently measured as $C_1 \approx 0.4$, corresponding to a large proportion of the diffusion-weighted signal exchanging in this time-frame. Note that these values are similar to the simulation parameters used in Fig. 4.4b. Recall that C_1 corresponds to the steady-state exchange fraction $f_{SS} = 2f_I(1-f_I)$ (3.2.9). Therefore, C_1 can in fact be interpreted as a proximal measurement of the structure (via the equilibrium signal fractions f_I and f_E), which is a point we will return to shortly in Sec. 4.10 and also elaborate upon in Chapter 5, Sec. 5.3.2..

Taking a weighted average of these two peaks produces $k \approx 180\ \mathrm{s}^{-1}$, which is similar to the normative $k \approx 140\ \mathrm{s}^{-1}$ observed previously in live tissue at this temperature (see results across Sec. 4.2). The discrepancy can potentially be explained by the fitting a monoexponential AXR in previous data, which fails to fully characterize the exchange process(es) (see Fig. 4.7). Thus, these distributions agree, roughly speaking, with previous results in live tissue, and indicate that the exchange rate k can be explained as arising from a weighted fraction of two exchange time components. Importantly, the observation of bimodal exchange times seems to confirm, qualitatively, that distinct exchange processes (perhaps, passive and active exchange) exist. Further experiments, however are necessary to confirm the nature of these peaks.

4.4 Effects on the distribution under perturbations

These distributions provide a richly detailed view into the overall exchange process and allow us to begin mechanistic investigations of active exchange. We will probe these distributions in a similar fashion to Sec. 4.2, first looking at temperature variation, then ouabain, and finally energetic failure conditions — in this case, tissue 'rundown', assessed by repeatedly measuring a sample as viability is lost. These results suggest that the effect(s) observed in Sec. 4.2 arise from shifting of the faster τ_k peak in Fig. 4.8, specifically, rather than the slower peak. In addition, we look at the effect of fixation and osmolarity perturbations. These final results shed light on the structural substrates of active exchange. We find that fixed tissue retains a bimodal distribution and that the addition of an osmolyte shifts both peaks towards faster times, consistent with the effect(s) of uniform ICS shrinkage. Thus, the two peaks likely arise from separate structures, rather than parallel processes within the same structure(s). Active exchange, therefore, is found to be associated with the structure(s) corresponding to the faster exchange peak, which we speculate to be high SVR structures such as neurites.

We stress, however, that the findings in this section are preliminary (i.e., not yet published) and are exploratory in nature. These perturbations were studied in only one or two specimen at a time and strong conclusions cannot yet be drawn. Despite this, the presented results provide some initial insight into the mechanism(s) underlying observed changes in the (monoexponential) AXR.

4.4.1 Temperature variation

Methods

Temperature was varied between $25 \rightarrow 11 \rightarrow 25$ °C for one specimen. The sampling scheme (43 points over $t_m = 0.125 - 1000$ ms) and analysis approach were the same as previously described for Fig. 4.8, and no sub-sampling was performed. One set was acquired at each temperature due to time constraints imposed by the longer experiment ($\approx$ 17 vs. 6 min), and the need to avoid subjecting the specimen to

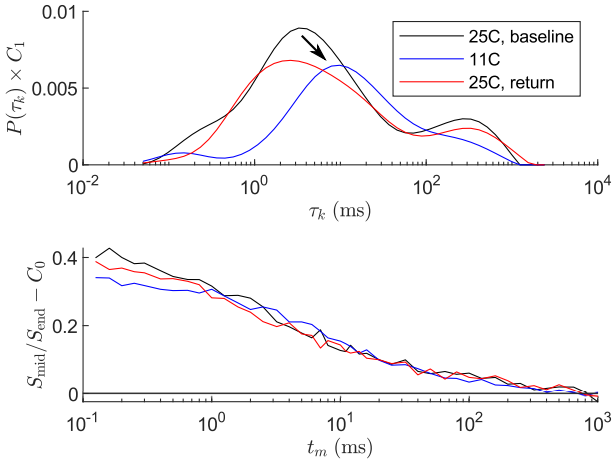

Figure 4.10: Variation in $P(\tau_k)$ for one live spinal spinal cord measured at 3 temperatures 25 (baseline, black) $\rightarrow$ 11 (blue) $\rightarrow$ 25 °C (return, red). One set was measured at each temperature, with each set corresponding to 43 points over $t_m = 0.125 - 1000$ ms (bottom). In the 11 °C condition, the faster peak shifts to the right from $\tau_k \approx 3-4$ to $\approx 6-20$ ms and the total exchange C_1 decreases from ≈ 0.4 to 0.35. Returning to 25 °C shifts this peak back to its approximate baseline position, but does not fully recover C_1.

cold temperatures for a long period of time. For the same reason, 11 °C was used rather than the 7 °C used previously (Fig. 4.1). The specimen was dissected on P2. Note that the day of dissection differs from Fig. 4.8, in which all specimen were dissected on P1. We found generally similar distributions for spinal cords from P1 – P3, though some deviations in the faster peak were observed for P4 (data not shown), perhaps due to decreased viability for spinal cords dissected on later days postnatal [144] and/or a different stage of development. In this section, we present data only from spinal cords dissected between P1 – P3 to avoid any potential confounding effects due to the day of dissection.

Results

In Fig. 4.10, we show the 3 sets acquired at 25 $\rightarrow$ 11 $\rightarrow$ 25 °C. Again, bimodal distribution(s) with peaks near $\tau_k \approx 3-4$ and $200-500$ ms are found, confirming the repeatability of these general characteristics in $P(\tau_k)$. Compared to the first (baseline) 25 °C condition, going to 11 °C produces a rightwards shift in the faster

peak (from $\tau_k \approx 3-4$ to $6-15$ ms) and an overall decrease in total exchange (C_1 decreases from ≈ 0.4 to 0.35, see intercept in bottom plot). Switching back to 25 °C recovers the location of the faster peak, but not the amplitude or total exchange, which recovers incompletely. Thus, the temperature-dependence of k in live tissue, and the resulting activation energy E_a, is seen to arise from a shifting of the faster peak, rather than a shift in the slower peak, which remains in approximately the same position ($\tau_k \approx 200-400$ ms). This data supports that active exchange corresponds to the fast exchange component for which $\tau_k \lesssim 5$ ms.

Interpretation of the total exchange

We emphasize the additional contrast afforded by scaling the distributions by the total exchange (C_1). With this contrast, the baseline and recovery 25 °C conditions are seen to be different, despite having a similar, un-scaled $P(\tau_k)$. Consider that C_1 reflects, in some sense, structural characteristics. Recall that the maximal total exchange is given by a quadratic relationship $f_{SS} = 2f_E f_I = 2f_I(1-f_I)$ (3.2.9) for two-site exchange. Assuming that steady state is reached (i.e., complete mixing), the maximal value of $C_1 = f_{SS}$ (after floor removal, i.e., subtracting C_0) is when $f_E = f_I = 0.5$, such that $C_1 = 0.5$. A value of $C_1 \approx 0.4$ is consistent with two-site exchange wherein the relative equilibrium signal fractions are $\approx 0.75, 0.25$: $C_1 = 2(0.75)(0.25) = 0.375$, with increasing *imbalance* in the signal fractions reducing C_1. Note that this is roughly in agreement with the freer compartment being the ECS, using the upper range of ECS fraction estimates in the literature $\approx 15-25\%$ [194, 207]. However, a two-site model may be insufficient to explain the exchange process (perhaps, > 2 sites), complicating such a facile interpretation. Nonetheless, changes in C_1 should be interpreted as being linked to structural changes, particularly in the relative balance of restricted and more mobile water. We will elaborate on this topic later in Sec. 5.3.2.

4.4.2 Suppression of the sodium-potassium pump

Next, we again study the effects of ouabain and find that ouabain also induces a shift in the faster peak, similar to the temperature perturbation.

Methods

Two spinal cords were studied, dissected on P2 and P3. Two sets were acquired at baseline (25 °C, normal aCSF) and then two sets were acquired after introduction of 100 μM ouabain, allowing some time for the ouabain to take effect prior to measurement. The analysis here is applied retrospectively to data acquired before the refinement of the t_m sampling scheme (i.e., to be log-linear and to over-sample the long t_m points). These data were acquired with a different set of 69 t_m from t_m = $0.2-1000$ ms that are less optimal for obtaining robust distributions. Nonetheless, the range of t_m is nearly identical to that used previously such that the range of τ_k probed is similar, and the data is still well-sampled. The resolution in τ_k was increased to 70 points from $\tau_k = 0.05-2400$ ms, in concordance with the increased sampling density in t_m. Despite these differences in experimental protocol, the distributions at baseline qualitatively resemble those obtained previously, and results can be directly compared.

Results

In Fig. 4.11, we show the distributions at baseline and after the introduction of 100 μM ouabain. Distributions and data are presented as means of the two acquired sets. Note that due to the different t_m sampling scheme, the data at long t_m are noisier (see bottom plots as $t_m > 100$ ms) than previous results (e.g., Fig. 4.10), but a floor was still able to be estimated, as shown by the decay going to 0. Once again, a bimodal distribution with peaks at $\tau_k \approx 3-4$ and $200-500$ ms was observed at baseline, affirming the high repeatability of these characteristics between samples, even across different days of dissection P1 – P3 and with a sub-optimal sampling scheme in t_m.

Similar to what was observed for the 11 °C condition (Fig. 4.10), the introduction of ouabain shifts the faster peak (here, from $\tau_k \approx 4-5$ to $30-50$ ms) while leaving the slower peak relatively unaffected ($\tau_k \approx 200-500$ ms). In this case, the faster peak is also broadened, smearing across smaller and higher τ_k. Interestingly, the total exchange is similar ($C_1 \approx 0.35$), and some of the faster peak is seen to be maintained after ouabain. The similar C_1 value indicates that ouabain does not induce any structural changes (over the time-frame observed). The persistence of

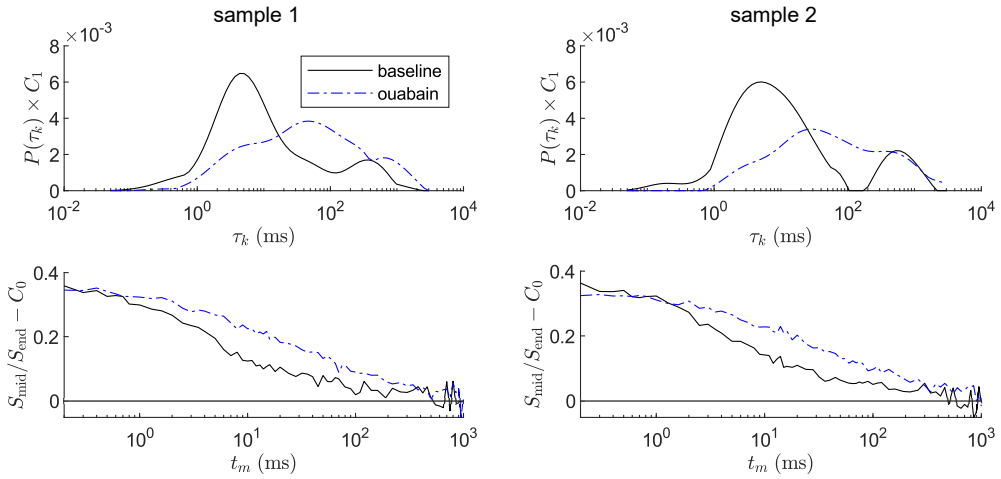

Figure 4.11: Variation in $P(\tau_k)$ for two spinal cords due to the introduction of 100 μM ouabain. Two sets were acquired at baseline (black) and two sets were acquired after adding ouabain (blue). Mean distributions and decay data from the two sets are shown. Sample 1 (left) was dissected on P2. Sample 2 (right) was dissected on P3. Ouabain suppresses, shifts (from $\tau_k \approx 4-5$ to $30-50$ ms), and broadens the faster peak, whereas the location and amplitude of the slower peak is approximately preserved. Total exchange is similar under both conditions. Effects are similar in both samples.

some degree of fast exchange with $\tau_k \approx 4-5$ ms indicates, perhaps, that ouabain suppresses only part of the active exchange process.

The effect of ouabain is seen to be similar between the two samples, highlighting the repeatability of the effect. While it is difficult to speculate what these changes might correspond to within tissue, the general conclusion that the shifting of the faster peak drives the changes observed in the AXR in Sec. 4.2 remains clear. Indeed, by taking a weighted average of the distribution after introducing ouabain: $\tau_k \approx 30$ ms, and $k \approx 33$ ms. This value roughly agrees with the plateaued AXR after ouabain observed across samples ($k \approx 36\ \mathrm{s}^{-1}$), shown previously in Fig. 4.2.

4.4.3 Tissue 'rundown'

Methods

To study a perturbation akin to energetic failure, we looked at one specimen, dissected on P2, measured repeatedly overnight until the loss of viability (i.e., death). Distributions were considered in blocks of time, with data being averaged within

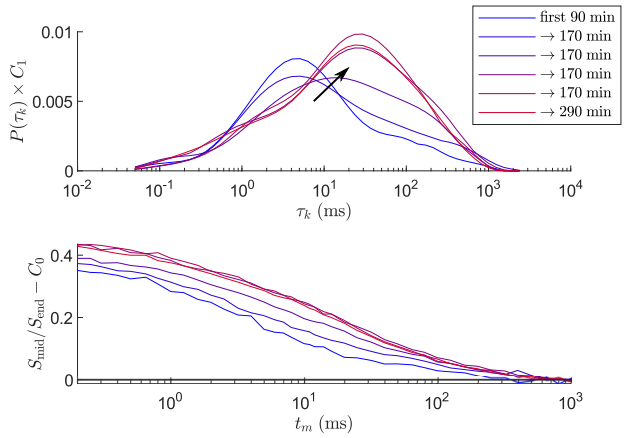

Figure 4.12: Variation in $P(\tau_k)$ for one specimen measured repeatedly overnight. Sets were averaged over blocks of time. The first 90 min (5 sets) are shown in blue, with later time blocks (10 sets) represented by the line color changing from blue to red. The final block (17 sets) is shown in red. The fast exchange peak drifts from $\tau_k \approx 4-5$ to $10-20$ ms over the first several blocks. Eventually, the two peaks homogenize, and $P(\tau_k)$ becomes approximately unimodal with a peak near $\tau_k \approx 30-40$ ms.

each block. The first block consists of the first 5 sets, corresponding to approximately the first 90 min, where the specimen is expected to be viable. For later times, blocks comprising 10 sets each ($\approx$ 170 min per block) were considered. Finally the last 17 sets ($\approx$ 290 min) comprise one block. Altogether, the sample was studied over a time period of $\approx$ 17 hrs following dissection, and complete loss of viability is expected by the final block according to electrophysiological measurements.

Results

In Fig. 4.12, the distributions are seen to drift towards longer exchange times (from $\tau_k \approx 4-5$ to $10-20$ ms), eventually settling around $\tau_k \approx 30-40$ ms. Note that for the first two sets, comprising $\approx$ 4.5 hrs, the distribution resembles the baseline distribution(s) seen previously, and complete viability is likely maintained over this initial time period. An effect in the total exchange is also seen, with C_1 increasing slightly (from $C_1 \approx 0.38$ to 0.42) over time. In addition, the resolution between the two peaks is slowly lost, and the final $P(\tau_k)$ is approximately unimodal with an exchange time of $\tau_k \approx 30-40$ ms.

The mechanism of tissue rundown is unclear, though we expect that some degree of cell death and apoptotic processes occur [186], leading, perhaps, to increased permeabilization and loss of the structural integrity of membrane structures. This potentially explains the homogenization of the two peaks (i.e., smaller compartments are lost). This may also explain the increase in C_1, as the effective ECS may increase as ICS structures break down. Furthermore, active processes will gradually cease, similarly to OGD or ouabain, perhaps explaining the shift towards slower exchange times over the first several time blocks. Indeed, the final position of the peak resembles that seen for 100 μM ouabain ($\tau_k \approx 30-40$ ms, Fig. 4.11). These results, while potentially interesting, are difficult to interpret due to a lack of clarity in what happens to the *ex vivo* tissue as it loses viability, and as such are presented here in a largely speculative manner.

4.4.4 Fixation

Having established that activity is linked to the faster exchange peak, we now turn towards investigating what these two peaks correspond to in terms of structure and/or function. Two plausible explanations should be considered: either (i) the peaks correspond to parallel active and passive processes which proceed throughout all relevant ICS structures, or (ii) the peaks correspond to different structures, with active exchange being linked to just one set of structure(s). To investigate which of these explanations is more plausible, we look at fixation (which fully eliminates any active exchange), and osmolarity perturbations (which perturb structure but not, necessarily, active exchange).

Methods

In this section, we compare a fixed to a live specimen. For the data acquired on the fixed specimen, the analysis is applied retrospectively, as was the case for the ouabain data (Fig. 4.11). These data were acquired with a different sampling scheme of 69 t_m from $t_m = 0.2-1000$ ms. For each specimen, 5 sets were acquired. Both were dissected on P1.

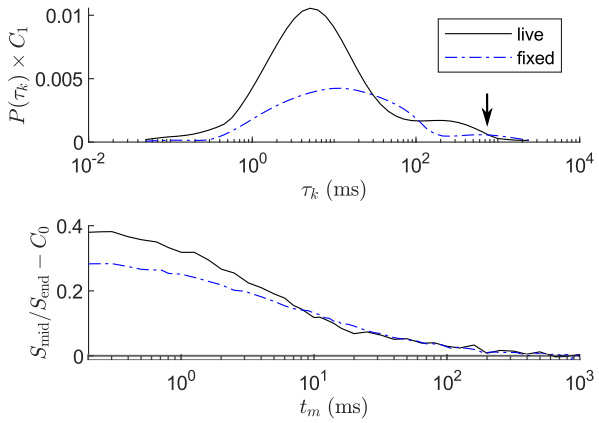

Figure 4.13: Distributions $P(\tau_k)$ in a live and fixed spinal cord from the means of 5 sets. Fixation retains the bimodal character, but shifts the faster and slower peaks from $\tau_k \approx 4-5$ to $7-20$ ms and $\tau_k \approx 200-300$ to $500-600$ ms, respectively, and also broadens the faster peak. The total exchange is also decreased from $C_1 \approx 0.38$ to 0.28. We highlight the presence of a slow component in $P(\tau_k)$ for fixed tissue (arrow).

Results

In Fig. 4.13, mean distributions from the 5 sets acquired in each sample are shown. The distribution observed following fixation retains the general bimodal character, wherein a faster peak dominates the overall exchange ($\gtrsim 80\%$), though the location of both peaks has shifted to longer times: for the faster peak from $\tau_k \approx 4-5$ to $7-20$ ms, and for the slower peak from $\tau_k \approx 200-300$ to $500-600$ ms. The total exchange has decreased (C_1 decreases from ≈ 0.38 to 0.28), consistent with a degree of shrinkage in the ECS induced by fixation. The shifting in both peaks is consistent with an increase in the ICS, resulting in decreased SVRs. Note that some biexponential character was also seen in Chapter 3, wherein we first applied the curvature method in fixed spinal cord (in particular, see the inset of Fig. 3.10), though this was not commented upon at the time because we did not have the tools nor the resolution in t_m to explore deviation from a monoexponential AXR. The fact that $P(\tau_k)$ in fixed tissue is bimodal is informative.

We interpret this finding as follows. Because fixed tissue retains broadly similar structural characteristics to live tissue in a compartmental sense, albeit with some

shrinkage of the ECS and permeation of membranes, the retention of bimodality in $P(\tau_k)$ in fixed tissue suggests that the two peaks correspond to different structures (e.g., neurites vs. soma — recall that this is a GM specimen and little to no myelination is expected at this stage of development [144]). We speculate, therefore, that the two peaks observed in live tissue may *also* correspond to different structures, rather than to parallel processes within the same structure(s). Consider that if the exchange processes were truly parallel in all ICS tissue components, and that this is what the two peaks represented, then $P(\tau_k)$ in fixed tissue would be unimodal (having eliminated one of the processes), which is clearly not the case.

For instance, it may be that the faster peak associated with active exchange corresponds to exchange between neurites (which have high SVRs and thus shorter expected τ_k) and the ECS, while the slower peak corresponds to exchange between larger compartments, such as soma, and the ECS. If this hypothesis is true, then the introduction of an osmolyte, which results in increased osmotic pressure and a uniform shrinking of ICS compartments, should shift the distribution *as a whole* towards faster times and potentially increase the total exchange via structural changes — i.e., increasing the ECS closer to a relative fraction of 0.5. On the other hand, if these peaks correspond to parallel active and passive processes, then an osmolyte should have an out-sized effect on the passive peak.

4.4.5 Osmolarity perturbation after ouabain

Methods

In the ouabain data presented previously (Fig. 4.11), 100 mM sucrose was added while keeping the previously added 100 μM ouabain. For each specimen (P2 and P3), 2 sets were acquired after addition of sucrose. Sucrose is known to be impermeant to the membranes of live tissue and is expected to increase the osmolarity of the ECS, inducing uniform shrinkage of ICS compartments via water outflow. This perturbation, therefore, can serve as a confirmation of the hypothesis that the two peaks in $P(\tau_k)$ correspond to different structures.

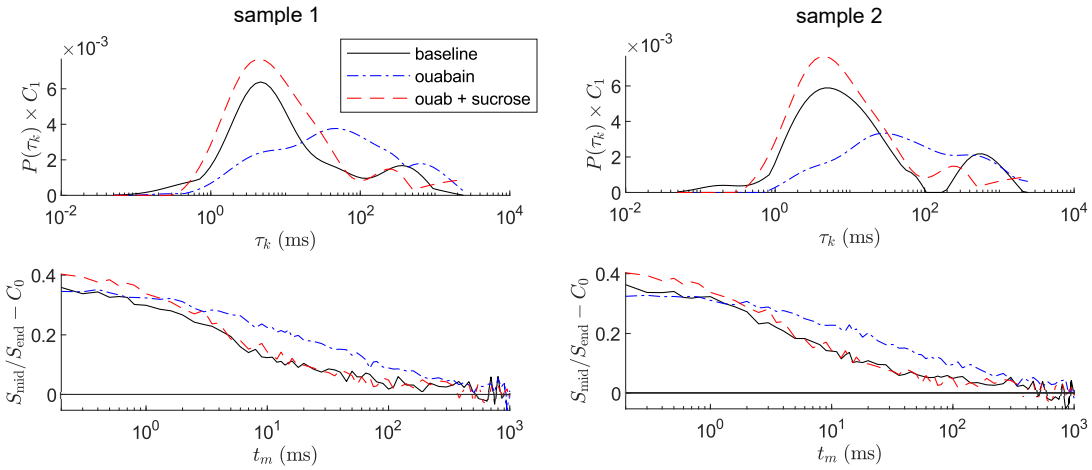

Figure 4.14: Variation in $P(\tau_k)$ for two spinal cords due to the introduction of 100 mM sucrose while maintaining the 100 μM concentration of ouabain. Two sets were acquired at each condition: baseline (black), after adding ouabain (blue), and after adding sucrose (red). Mean distributions and decay data from the two sets are shown. Sample 1 (left) was dissected on P2 and sample 2 (right) was dissected on P3. The baseline and ouabain conditions were first presented in Fig. 4.11. Sucrose is seen to shift the distribution as a whole to the left, approximately restoring the baseline fast τ_k peak (to $\tau_k \approx 4-5$ ms). This is consistent with ICS compartment shrinkage and an increase in the SVR. The total exchange increases as well (from $C_1 \approx 0.35$ to 0.4), consistent with an increase in the ECS. Note that the slow peak has shifted somewhat due to sucrose, from $\tau_k \approx 200-500$ to $100-300$ ms. Effects are consistent between samples.

Results

In Fig. 4.14, sucrose is seen to shift the entire distribution (both peaks) towards faster exchange times, consistent with the peaks being associated with different ICS structures. The total exchange also recovers. Qualitatively, sucrose appears to recover the effects of ouabain, restoring the fast peak to near its original position at $\tau_k \approx 4-5$ ms and bringing the AXR back to a similar value — i.e., the weighted average of the distribution is similar to baseline (c.f. the Supplement in Ref. [146]). If the two peaks truly corresponded to parallel active and passive processes, then sucrose would not be able to recover the 'active' peak to such an extent.

Indeed, the baseline and sucrose conditions are not equivalent. The slower peak has shifted somewhat (from $\tau_k \approx 200-500$ to $100-300$ ms) — which would be difficult to detect when fitting a monoexponential AXR — and the total exchange has increased

compared to baseline (C_1 increases from ≈ 0.35 to 0.4), both of which are effects that are consistent with an increase in the ECS and a shrinkage of the ICS. Thus, these distributions provide detail and mechanistic insight that would be invisible to a monoexponential AXR. Looking at an AXR might erroneously suggest that 100 mM sucrose simply reversed the effects of ouabain. Together with the findings in fixed tissue, these findings clarify the nature of and the structural substrates of active exchange.

Interpretation of active exchange

More specifically, we hypothesize that exchange into/out of the structure(s) associated with the faster τ_k peak is driven, partially, by active processes, as evidenced by the shifting of this peak under various perturbations (temperature, ouabain, rundown). In contrast, exchange for the structure(s) associated with the slower τ_k peak is predominantly passive, showing little to no change under the various perturbations to activity, but indeed showing changes under perturbations to structure (sucrose, Fig. 4.14). We stress, however, that we are less able to probe this slow exchange process due to decreased signal at long t_m and the position of this peak was generally found to be more variable. Within the faster peak, the two parallel active and passive processes can be written as a sum because both processes result in simultaneous turnover of signal. This additive property was pointed out by Springer *et al.* [179]: $k = k_{\text{active}} + k_{\text{passive}}$, or, equivalently,

$$\frac{1}{\tau_k} = \frac{1}{\tau_k^{\text{active}}} + \frac{1}{\tau_k^{\text{passive}}}. \tag{4.4.1}$$

With the presented findings in mind, the passive exchange time is estimated as $\tau_k^{\text{passive}} \approx 30-40$ ms, which is the final position of the faster peak after conditions which induce energetic failure (ouabain, rundown). That is, we interpret these perturbations as fully 'knocking down' the active exchange process such that $\tau_k = \tau_k^{\text{passive}}$. Thus, we estimate the active exchange time to be $\tau_k^{\text{active}} \approx 5-6$ ms (at 25°C), leading to an overall $\tau_k \approx 4-5$ ms, which is the peak position consistently observed at baseline across samples.

Comparing $\tau_k^{\text{passive}} \approx 30-40$ ms to the slower peak with $\tau_k \approx 200-500$ ms, these values suggest that the SVR of the structure(s) associated with the fast peak are approximately $7-10\times$ larger than the SVR for the slow peak, assuming $k = \kappa S/V$. This is roughly consistent with the difference in diameters between dendritic processes and soma [186] ($1.5-3$ μm for neurites, and ≈ 20 μm for soma). Indeed, the broadness in the observed peaks may be due to the size heterogeneity of these structures, rather than noise or issues with the inversion or regularization approach *per se*. However, we again caution against such direct interpretations with respect to structure due to the possibility of localized signal behavior, which will increase the effective SVR for the localized signal, and mention these values speculatively.

Summary

By looking at exchange in more detail using a distributed analysis of exchange times $P(\tau_k)$, we reveal insights about the active exchange detected previously in Sec. 4.2. The activity-dependence of the AXR is seen to be driven primarily by changes in a fast exchange component ($\tau_k \approx 4-5$ ms), which dominates the overall exchange ($\gtrsim 80\%$), rather than changes in a second, slower component ($\tau_k \approx 200-500$ ms). Temperature, ouabain, and tissue rundown perturbations primarily shift this faster peak and previous findings about the AXR can be adequately explained by this shifting. Distributions in fixed tissue and using osmolarity perturbations suggest that these two exchange components correspond to different structures (perhaps, neurites vs. soma), with fixed tissue retaining a bimodal $P(\tau_k)$ and sucrose inducing a shift in both components. However, we can only speculate what, exactly, these structural substrates are. Preliminarily, the fast exchange times seem to suggest a tissue component with high SVR, such as neurites. Nonetheless, we can reject the hypothesis that these two peaks correspond to parallel processes within the same structure(s). Rather, exchange within *only* the faster τ_k peak appears to consist of a combination of active and passive exchange processes that can be selectively 'knocked down' by perturbations to activity, while the slower peak is mainly passive, showing little to no change under the various perturbations to activity.

4.5 Discussion

We have presented a compendium of results (temperature variation, ouabain, OGD) which, when taken together, strongly suggest that exchange, measured as an AXR, has an active component. In particular, the activation energy E_a of the exchange rate k was found to be higher in live than in fixed tissue, and perturbations to activity produced decreases in k with an effect size much greater than those seen in the ADC. These findings suggest that the AXR probes processes and provides information beyond that which can be observed using SDEs (i.e., ADC measurements), and thus make the case that the AXR is linked to steady-state metabolic activity. We note as well that values of k were found to be highly reproducible across specimen, suggesting that k is an absolute, intrinsic biomarker, rather than a relative change in activity such as that observed using BOLD-based contrast [188].

To gain further insight into the activity-dependence of exchange, we developed a method to efficiently measure a distributed exchange time $P(\tau_k)$ in a reasonable time-frame (≈ 17 min, with potential for further sub-sampling), aided by the development of a novel, 4-step phase cycle of the SG-DEXSY experiment. Looking at the rich information provided in these distributions, we find that the activity-dependence of the AXR can be attributed to shifts in a fast exchange component ($\tau_k \approx 4-5$ ms) rather than a second, slower component ($\tau_k \approx 200-500$ ms), as evidenced by a similar set of perturbations to activity (temperature, ouabain, loss of viability). The presence of both peaks and their relative positions, even after perturbations (namely, in the case of ouabain, where two specimen were studied), were consistent across specimen, indicating the robustness of the methods. These results highlight once again that exchange rate(s) are intrinsic and absolute. We stress, however, that these findings are preliminary, and further studies with additional specimen are needed to confirm these findings.

The bimodality of $P(\tau_k)$ is in and of itself an interesting result, with different possible interpretations. Based on measurements in fixed tissue and after osmolarity perturbations, we hypothesize that the fast exchange component, which dominates the overall exchange, corresponds to particular structure(s) within tissue wherein

active and passive exchange processes coincide (i.e., proceed in parallel), as was hypothesized by Springer *et al.* [179]. In contrast, exchange within the structure(s) corresponding to the slower τ_k component appears to proceed mainly passively. Given the extremely short exchange time of the faster peak, we speculate that this peak may correspond to high SVR tissue components such as neurites, though this cannot be confirmed at this time. Plausible explanations for the active part of fast exchange include water co-transport with ions as well as transient, local osmotic gradients induced by ion transport, though these explanations likewise cannot be confirmed by our experiments and represent avenues of future study.

Comparison to other work

How does this work fit into the broader field of exchange measurements in central nervous system tissue? We point out once again that exchange times vary widely in the literature, ranging from $\tau_k = 25 - 620$ ms ([103, 147, 148]) or longer, and as short as $\tau_k = 15$ ms in GM [103]. More recently, even faster exchange times in GM (*ex vivo* rat brain) have been reported by Olesen *et al.* [101], at $\tau_k \approx 3 - 5$ ms. The fast exchange peak found here is consistent with this final report $\tau_k \lesssim 5$ ms, but seems, at first glance, to contradict other previous findings.

We point out again that our PM-10 system is uniquely situated to probe such fast exchange. The exchange-weighted point (S_{mid}, $b_d \approx 0, b_s = 4.5\ \text{ms}/\mu\text{m}^2$) uses diffusion encodings with $\tau \approx 0.7$ ms and mixing times as short as $t_m \approx 0.1$ ms, whereas typical PG-based methods have diffusion encoding times (Δ) that are much longer, on the order of $\Delta \gtrsim 10$ ms. Thus, such methods would have limited sensitivity to such fast exchange, and much of this exchange would transpire over the course of the encoding. In our case, the encoding and mixing time amount to $\lesssim 1$ ms, and most of this fast exchange (assuming $\tau_k = 5$ ms, $\gtrsim 80\%$) remains detectable. That is, it proceeds during the mixing time. On the other hand, for a PG diffusion encoding with a long diffusion time such as $\Delta = 15$ ms — which is what was used in Sec. 3.3.2, and which represents a typical value of Δ — nearly *all* of this exchange would occur during the encoding. This effectively leads to the high-permeability case ($\ell_\kappa \ll \ell_d, \ell_s$, see (2.3.4) and Fig. 2.11),

such that when the encoding is much longer than $\tau_k \approx 5$ ms, fast exchange would appear merely as hindered diffusion with, perhaps, some apparent time-dependence (i.e., dependence on Δ) corresponding to the decrease of $D(t)$ to D_∞ (2.3.4). We will return to this point in the discussion of Chapter 5 and in Chapter 7 (Sec. 7.1).

Indeed, the broad range of exchange times reported in the literature may simply be a result of variation in the utilized experimental parameters, at least in GM (we cannot and do not speculate about exchange in WM, which was not yet studied). For very long encoding and/or mixing times, only the second, slower exchange component may be detected, leading to estimates of τ_k on the order of $\tau_k \gtrsim 100$ ms. Intermediate encoding times $\Delta \sim 5 - 15$ ms may be able to detect some amount of fast exchange, and the overall AXR in this case would appear to be a weighted fraction of the two components, just as we observed in Sec. 4.2, where the normative AXR across samples at baseline was measured as $k \approx 140\,\mathrm{s}^{-1}$ ($\tau_k \approx 7$ ms), a value which lies between the fast ($k \approx 200\,\mathrm{s}^{-1}$) and slow peaks ($k \approx 3\,\mathrm{s}^{-1}$) in $P(\tau_k)$. The degree of activity-dependence detected in the AXR would also depend on the sensitivity to fast exchange. If only slow exchange was detected in a given measurement, then one might erroneously and prematurely conclude that exchange has no active contribution(s).

In comparing our findings to previous reports, we must also take into consideration the different methodologies (i.e., pulse sequences, SDEs vs. DDEs). We stress that findings using SDEs (e.g., Ref. [103]) are fundamentally limited by the inability of SDEs to fully decouple exchange from diffusion, and especially non-Gaussian diffusion. We have shown conclusively in our own work that SDEs do not possess the same contrast as DEXSY methods, as evidenced by comparison of the AXR to the ADC throughout Sec. 4.2. We reiterate as well the content of the previous chapter, showing that SDEs cannot reliably disentangle non-Gaussian diffusion and exchange (see Sec. 3.4): these effects are degenerate in SDEs. Thus, drawing direct comparisons between work performed using DEXSY sequences vs. SDE methods is difficult, and correspondence to the literature is not necessarily expected given these different methodologies. This is before even taking into account the vastly different experimental setup (and time- and lengthscales probed). Thus, we argue that this work should be considered as a set of novel observations.

Concluding remarks

The results and methods presented in this chapter represent a significant advance in the study of exchange using diffusion MR. In a series of experiments, we confirm the reported activity-dependence of exchange [175–181], highlighting the potential utility of the AXR as a biomarker of (steady-state) metabolic activity. We then develop and demonstrate a method that can yield robust estimations of a distributed exchange time $P(\tau_k)$, that is, to our knowledge, the first method of its kind. Using this method and the unique time- and lengthscales afforded by the PM-10 system — which can probe extremely fast exchange times on the order of ~ 1 ms — we investigated the mechanisms underlying active exchange. We find that the activity-dependence of exchange can be attributed to shifts in a fast exchange component ($\tau_k \approx 4-5$ ms) that is associated, we speculate, with a high SVR structure such as neurites. We emphasize that such exchange may be difficult to detect on more conventional systems and may help to explain, in part, the disparate exchange times reported in the literature.

5

Imaging of *In Vivo* Exchange in Mice

5.1 Introduction 140
5.1.1 Chapter outline and related works 141
5.2 Pulsed gradient exchange imaging 142
5.2.1 Stimulated echo DEXSY sequence 142
5.2.2 Choosing experimental parameters 144
5.2.3 Analysis pipeline 149
5.3 Exchange contrast and parameter maps 152
5.3.1 Apparent exchange contrast at a single mixing time 152
5.3.2 Total exchange and exchange rate maps 154
5.3.3 Repeatability 161
5.4 Discussion 166

5.1 Introduction

Almost all of the results to this point were acquired on the PM10 NMR-MOUSE system with its unique advantages, but also limitations. Most importantly, the inability to perform imaging severely limits the scope of applications that such a system can be used to study. In this chapter, we apply the curvature method to measure AXRs in the brain of live mice on a rodent imaging system (7T Bruker BioSpec 70/20 USR, Ettlingen, Germany), demonstrating, for the first time, the feasibility of *in vivo* imaging using our particular approach to sub-sample DEXSY data. This investigation

is also the first time in this thesis that differences between brain white matter (WM) and gray matter (GM) are studied, potentially broadening the scope of the findings presented herein to potentially include tissue-type comparisons.

Compared to other chapters, this work is in a more preliminary stage, with both data collection and methods development ongoing. While detailed analyses are not yet available, we present here representative data and assess the repeatability of exchange parameter maps. Despite the early stage of this work, we clearly demonstrate at least the feasibility of using the curvature method *in vivo* and, importantly, reproduce findings from the previous chapter that suggest extremely rapid exchange rates in live tissues ($\tau_k \lesssim 5$ ms).

5.1.1 Chapter outline and related works

We first develop a PG variation of DEXSY with an EPI readout. Here, we implement an STE sequence with bipolar gradients, rather than a double SE sequence as in Fig. 3.1. This allows us to avoid the use of refocusing RF pulses, simplifying the coherence selection problem, reducing eddy currents effects, and potentially allowing for shorter diffusion encoding. This final optimization in particular is critical if we are to detect fast exchange. We then select suitable experimental parameters for which we expect high exchange-weighted contrast and the ability to probe some degree of fast exchange. Finally, we describe the analysis pipeline, which, in addition to typical image processing steps (registration, etc.), utilizes a variation of the T_1^{app} approach (see Sec. 3.3.4) to measure an AXR.

With the methodology in place, difference maps containing exchange-weighted contrast ($S_{\text{end}} - S_{\text{mid}}$) are generated from pairs of images at a single mixing time, similar to the f_{exch} maps presented in Fig. 3.6 for the glass capillary array phantom. These results demonstrate the potential rapidity of the curvature method and serve as an initial confirmation of the sensitivity of the sequence and method to exchange. Then, from images acquired across multiple mixing times, apparent exchange time ($\tau_k = 1/k$) and total exchange maps (C_1) are generated. Finally, within- and between-subject variability is assessed.

Although the maps are too noisy at this stage to draw strong conclusions regarding tissue types (cortical GM vs. WM vs. hippocampus and thalamus), preliminary data seems to suggest that the highest total exchange is seen in cortical GM ($C_1 \approx 0.35-0.45$), somewhat less in hippocampus ($\approx 0.25-0.4$), and the least in WM ($\approx 0.15-0.25$). Perhaps surprisingly, exchange times are found to be similar, though not quite equal, throughout the brain, with fast exchange times observed in all tissue types ($\tau_k \lesssim 5$ ms), and perhaps slightly longer exchange times ($\tau_k \approx 4-7$ ms) in thalamus. Altogether, these findings form part of a first-authored publication in preparation, though, again, methods development and data collection is ongoing:

- **Cai, T. X.**, Williamson, N. H., Basser, P. J., Miller, K. L.*, & Tachrount, M.* *In vivo* imaging of the apparent exchange rate in mice under AQP4 suppression using equally diffusion-weighted double diffusion encodings.

We later intend to study the effect of an AQP4 inhibitor, TGN-020 (Cambridge Bioscience, Cambridge, UK) [208], in order to determine whether AQP4 is an important mediator of exchange in tissue as measured using our method(s). Experiments were performed in collaboration with Dr. Mohamed Tachrount, who also supervised the pulse sequence programming.

5.2 Pulsed gradient exchange imaging

In this section, we develop methods oriented towards measuring fast exchange *in vivo* and with imaging, prioritizing short diffusion encodings.

5.2.1 Stimulated echo DEXSY sequence

Rather than using a double SE preparation as in the previous investigations in this thesis, we choose here to use an STE sequence composed of three selective 90°-RF pulses with bipolar gradients in each encoding, mimicking a DDE, as proposed by Sønderby *et al.* [124] In using this sequence, we remove the need for (selective) refocusing pulses, along with the attendant slice-select and spoiler gradients on either side of the pulse, and can thus achieve diffusion times as short as $\Delta = 8.5$ ms.

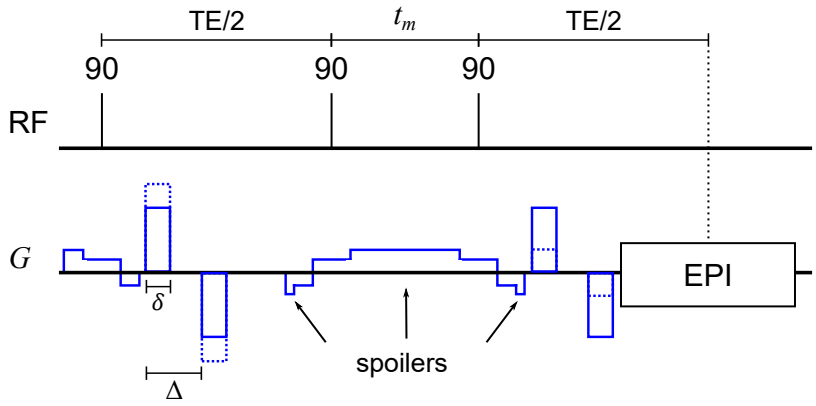

Figure 5.1: Schematic representation of the STE-DEXSY sequence using bipolar diffusion gradients with an EPI readout. All gradients are illustrated. Note the spoiler during t_m as well to the left and right of the storage 90°-pulses. The two diffusion-weighted points S_{mid} and S_{end} are illustrated with solid and dashed lines, respectively.

Importantly, this short encoding time leaves the possibility of detecting fast exchange. Being a highly customized sequence, the STE-DEXSY sequence was coded in-house in ParaVision 360 V1.1. The experiments were performed on a horizontal-bore 7T Bruker BioSpec 70/20 system (Ettlingen, Germany) using an 86 mm transmit RF coil and a 4-channel CryoProbe for the receive coil (Bruker, Germany). The system has a maximal gradient amplitude of $g_{\text{max}} = 660$ mT/m. For imaging, we utilized a standard EPI readout (Fig. 2.7) for rapid image acquisition. Slices were acquired in an interleaved manner.

The sequence diagram is depicted in Fig. 5.1. All of the utilized gradients, including the diffusion-weighting gradients, slice-select and rephase gradients, as well as various spoiler gradients (before, during, and after t_m), are illustrated. Gradients and timings are shown roughly to scale with the final experimental parameters used, discussed later. The two diffusion-weighted acquisitions, S_{mid} ($b_d = b_1 - b_2 \approx 0$) and S_{end} ($b_1 \approx b_s = b_1 + b_2$) are schematized by drawing two different gradient amplitudes: S_{mid} with equal b-values (solid lines), compared to S_{end}, wherein the vast majority of the diffusion-weighting is in b_1 (dotted lines). We found persistent structured artifacts during the development of this sequence (data not shown) and thus care was given to the incorporation of all the sequence elements necessary for effective coherence selection.

Coherence selection

The sequence incorporates multiple gradient elements as well as phase cycling to perform coherence selection and obtain well-behaved STEs centered about the EPI readout. As discussed in Secs. 2.1.2, 4.3.2, spoiling during t_m suppresses many unwanted coherences, and is done so here, keeping a small spoiler on during the entire duration of t_m. Additional spoiler gradients were incorporated on either side of the storage 90°-RF pulses in order to dephase or spread the transverse magnetization prior to storage. Such gradients are generally necessary to obtain well-behaved STEs [33]; otherwise the decomposition of transverse magnetization components shown in Fig. 2.4 may not apply, and the STE may exhibit unexpected behavior. As such, spoilers were implemented with an amplitude sufficient to produce a phase shift of 2π across the slice [209]. These gradients also serve to spoil the FID arising from the last RF pulse, as well as unwanted SE pathways (see Table 2.1). As a somewhat redundant measure, we also implemented a two-step phase cycle, cycling the two storage pulses together to $0, \pi$, as we did for the PG-DEXSY experiments in Chapter 3. Altogether, these coherence selection elements are expected to fully isolate the desired coherence and cancel the other ones. In addition to diffusion weighted acquisitions (S_{mid}, S_{end}), images without the bipolar diffusion-weighting gradients ($S_0, b = 0$) were acquired.

5.2.2 Choosing experimental parameters

In the interest of probing fast exchange, the diffusion encoding time Δ should be as short as possible. To determine what values of Δ are feasible, we must first determine what b-value produces the greatest exchange-weighted contrast *in vivo* and with good SNR, which can be measured as the signal difference $S_{\text{end}} - S_{\text{mid}}$ at some long t_m, for which a significant amount of exchange is expected. Recall that this difference is proportional to the curvature along $b_d = b_1 - b_2$ as estimated by finite differencing (3.3.9) and that — because these two acquisitions have the same timing parameters and total diffusion-weighting — taking such a difference removes the effects of non-exchanging, Gaussian diffusion as well as relaxation at a given t_m. That being said, we first conducted a pilot study with varying b-values.

Methods

In this initial study, diffusion encoding was performed using the following parameters: $\delta = 6$, $\Delta = 11$ ms, and total b-values (i.e., b_s) of [2.5, 3.5, 5, 6, 7] ms/μm^2, with the diffusion-weighting gradients oriented in the slice selection direction (rostral-caudal). For the S_{mid} image(s), we set $b_1 = b_2 = \frac{b_s}{2}$, and for the S_{end} image(s), b_2 was held constant at 0.1 ms/μm^2, with b_1 making up the rest of b_s. For example, for $b_s = 3.5$, S_{end} corresponds to $b_1 = 3.4$, $b_2 = 0.1$ ms/μm^2. Mixing times were set to 8 values: t_m = [5, 10, 20, 50, 100, 200, 300, 400] ms. EPI readout with partial sampling of the k-space (42/50 lines) was applied for the acquisition of 12 slices with an in-plane sagittal resolution of 0.3×0.3 mm^2 (FOV = 15×15 mm^2, matrix = 50×50) and 1 mm slice thickness. Spoiler gradients of 1 ms duration were incorporated on either side of the storage 90°-pulses as well as during t_m, with an amplitude of $g = 66$ mT/m (10% of g_{max}). TR/TE were 6 s/54 ms Two averages (two phase cycle steps) and 1 repetition (NR = 1) were acquired. Scan time was 3.2 min per b-value for a total scan time of $\approx$ 10 min.

Animal protocol

All animal procedures were approved by the local Animal Welfare and Ethical Review Body under approved personal and project licenses in accordance with the Animals (Scientific Procedures) Act, 1986 (UK) and associated regulations. C57BL6J wild-type adult mice ($n = 1$ for the pilot study, $n = 8$ for later results, 50% females) were housed in cages with up to 5 mice, maintained on a 12-hour light/dark cycle, and with *ad libitum* access to food and water. Animals were initially anaesthetized with 4% isofluorane and the concentration was then kept between 1.5 and 2% during scanning. Respiration and body temperature were monitored throughout scanning using an MR compatible monitoring and gating system (SA Instruments, Inc, NY, USA). The respiration rate was kept between 60 and 90 per minute. The temperature was maintained around 37.0 °C using heated water. To avoid motion-related artifacts the head was immobilized using a bite bar and ear pins. Animals were not scanned for longer than 2 hours.

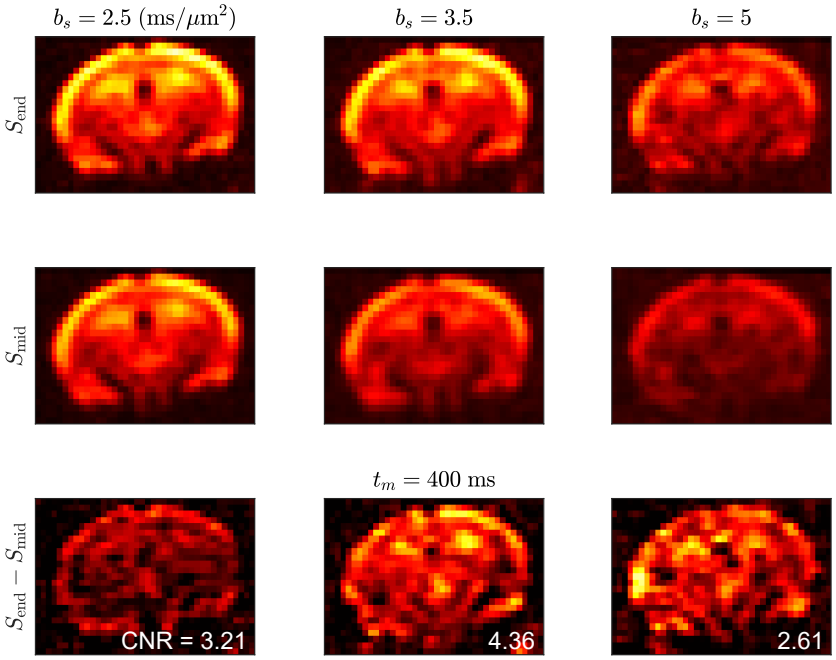

Figure 5.2: Images of S_{mid} ($b_1 = b_2 = \frac{b_2}{2}$) and S_{end} ($b_2 = 0.1$ ms/μm^2, $b_1 = b_s - b_2$) for a single animal, taken at a slice containing the corpus callosum and hippocampus, and at a long $t_m = 400$ ms. Diffusion parameters were $\delta/\Delta = 6/11$ ms and three values of b_s are shown, left-to-right: $b_s = [2.5, 3.5, 5]$ ms/μm^2. Gradients were oriented in the slice direction (rostral-caudal). Additional parameters were TR/TE = 6 s/54 ms, in-plane resolution 0.3×0.3 mm^2, 50×50 matrix size, 1 mm slice thickness. The same color scale is used for both the S_{end} and S_{mid} images. In the bottom row, difference maps $S_{\text{end}} - S_{\text{mid}}$ reflecting contrast due to exchange are shown (same color scale for the three maps). The CNR, calculated by dividing the mean of the difference map within the brain by the SD of the noise outside the brain, is calculated from left-to-right as $\approx 3.21, 4.36, 2.61$, indicating an optimum around $b_s = 3.5$ ms/μm^2 for obtaining exchange-weighted contrast.

Optimal b-value

In Fig. 5.2, we show raw images of S_{mid} and S_{end} (same color scale) acquired at $b_s = [2.5, 3.5, 5]$ ms/μm^2 and at a long mixing time of $t_m = 400$ ms for a representative animal. At such a long t_m, a large amount of exchange approaching steady state is expected, according to our prior findings in spinal cord across Chapters 3, 4. Note that these images were acquired within the same scan, and no receiver gain adjustment was made between the two acquisitions. A slice is chosen where cortex, WM (corpus callosum), and hippocampus are visible in order to assess the degree of

tissue-type contrast. Pairs of images were co-registered using a mutual information, intensity-based method (Image Processing Toolbox, MATLAB, Natick, MA, USA), and the resulting difference maps $S_{\text{end}} - S_{\text{mid}}$ are shown in the bottom row of Fig. 5.2.

These data indicate that the maximal sensitivity to exchange is achieved at around $b_s = 3.5$ ms/μm^2. Smaller b-values clearly show less exchange-weighted contrast, seen by comparing the difference maps for $b_s = 2.5$ vs 3.5 ms/μm^2 (same color scale across the bottom row of Fig. 5.2), while at larger b-values, the S_{mid} image decays towards lower signal levels, resulting in noisier difference maps. Comparing $b_s = 3.5$ vs. 5 ms/μm^2, the mean signal level within the brain for S_{mid} (middle row of Fig. 5.2) is approximately 4.9 as compared to 2.8× the noise floor, respectively, where the noise floor is calculated as the mean signal level outside the brain. Indeed, at the largest $b_s = 7$ ms/μm^2, the S_{mid} image (not shown) decays almost fully into the noise ($\approx 1.2\times$ the noise floor). The resulting contrast-noise-ratios (CNRs) — calculated as the mean difference $S_{\text{end}} - S_{\text{mid}}$ within the brain divided by the SD of the difference outside the brain — are approximately 3.21, 4.36, 2.61 for $b_s = [2.5, 3.5, 5]$ ms/μm^2, respectively, indicating an optimum around $b_s = 3.5$ ms/μm^2. In the $b_s = 3.5$ ms/μm^2 image, there is comparatively more structure-related contrast, with greater differences seen in cortex and hippocampus than in WM (see bottom row of Fig. 5.2).

Consider that these difference maps are in and of themselves a measurement of exchange (i.e., exchange-weighted contrast) and are perhaps sufficient for looking at *relative* differences between tissue types or between conditions. Such contrast can be generated extremely rapidly with just two images, highlighting the advantages of the curvature method. To confirm that these differences are, in fact, due to exchange, we now compare the difference maps presented in Fig. 5.2 to difference maps acquired at a shorter $t_m = 10$ ms, shown in Fig. 5.3.

The variation in the difference maps with respect to t_m in Fig. 5.3 confirms that this is an exchange effect, rather than an effect of non-Gaussian diffusion or $b^{1/3}$ signal scaling, which should manifest itself as a fixed intercept and scaling in the difference maps across t_m — i.e., such an effect does not vary with t_m (see Sec. 3.4). More specifically, this signal scaling would emerge for localized signal (3.4.3) for which $\ell_g \ll \ell_s, \ell_d$. Recall that motional averaging ($\ell_s \ll \ell_g, \ell_d$) will not show this scaling

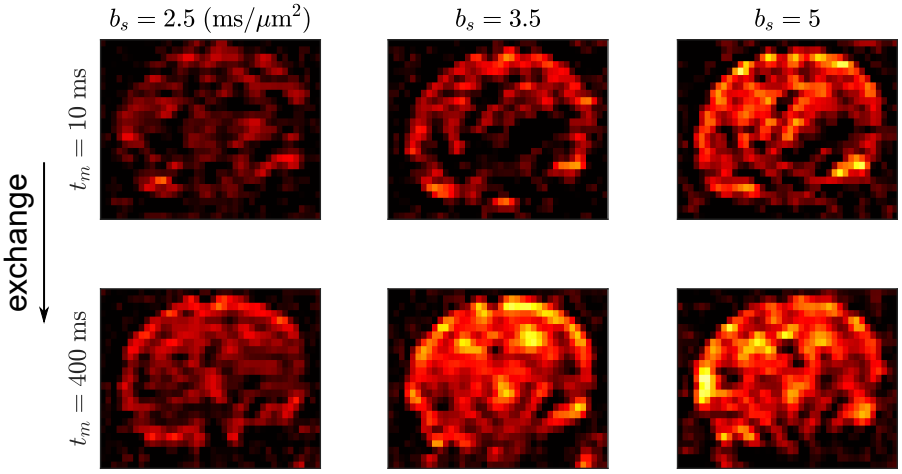

Figure 5.3: Difference maps $S_{\text{mid}} - S_{\text{end}}$ using the same parameters as in Fig. 5.2, but displaying both a short $t_m = 10$ ms (top) and the same long $t_m = 400$ ms (bottom). The same color scale is used. Note the increase in the difference with t_m, indicative of exchange. Note that some difference is observed even at short t_m, perhaps due to non-Gaussian diffusion and/or exchange during the encoding and for $t_m < 10$ ms.

for PG experiments wherein ℓ_d is fixed. While localization and fast exchange (i.e., between $t_m = 0 - 10$ ms) may both contribute to the differences observed in the first row of Fig. 5.3, the difference(s) *between* $t_m = 400$ ms and $t_m = 10$ ms (i.e. between the top and bottom row) are most likely due to exchange.

We should note, however, that these images were not normalized by S_0 ($b = 0$), such that T_1 effects, among others, may also be present. Nonetheless, because T_1 is long in the mouse brain at 7 T ($T_1 \approx 1.5$ s [210]) the vast majority of the change in the difference maps between short and long t_m can, to a first approximation, be attributed to exchange. Moreover, taking the log of these signal difference maps *would* remove the effect of T_1 (as the log of the difference is equivalent to taking the log of the quotient, i.e., the division approach in Sec. 3.3.4), and they can thus, in a proportional sense, be interpreted as a non-quantitative exchange measurement.

Methods revisited

This initial investigation determined that a small b-value relative to the capabilities of the system (i.e., g_{max}) can be used to probe exchange. Thus, we shortened

our diffusion timings from $\delta/\Delta = 6/11$ ms to $4/8.5$ ms in all subsequent results, potentially increasing our sensitivity to fast exchange by minimizing exchange during the encoding.

These results also indicate, however, that the CNR is low at around ~ 4, at least when combining images in this manner. The CNR would need to be increased to robustly measure AXRs and produce quantitative parameter maps. To increase the CNR, we reduced the in-plane resolution from 0.3×0.3 to 0.4×0.4 mm^2 (matrix size $= 64\times64$, FOV $= 25.6\times25.6$ mm^2), though also decreased the slice thickness from 1 to 0.75 mm, for an overall increase in SNR by a factor of $\frac{4}{3}$. Furthermore, we increased the number of repetitions to NR = 5, acquiring the 2 phase cycling steps 5 times. For averaging across repeats, we used the trimmed mean of co-registered repetitions of each image, removing the lowest and highest values and taking the mean of the remaining 3 repetitions for an increase in SNR by $\sqrt{3}$. To decrease the amount of T_2 relaxation, we shortened the TE from 52 ms to 43.2 ms ($T_2 \approx 40$ ms [210]), by adjusting the partial sampling of the k-space (42/64 lines). Altogether, these changes should bring the CNR to ≈ 10 ($\frac{4}{3}\times\sqrt{3}\times4 \approx 9.2$, along with decreased T_2-weighting) and enable the fitting of AXRs, but at the expense of scan time. A total of 11 mixing times were acquired t_m = [5, 10, 15, 20, 40, 60, 80, 120, 160, 200, 250, 300] ms, for a scan time of 26 min to acquire a whole brain volume across 18 slices. All subsequent data in $n = 8$ mice were acquired using these parameters. We next detail the analysis pipeline.

5.2.3 Analysis pipeline

Registration and masking

In order to fit across t_m, we need to both co-register the S_{end} and S_{mid} images as well as co-register each series of images across the 11 values of t_m. This was accomplished by first aligning S_{end} and S_{mid} at the shortest measured mixing time ($t_m = 5$ ms, where there is the least exchange weighting and thus intensity difference between images), and then registering all subsequent t_m images within each series to this first image. Again, registration was performed using a mutual information, intensity-based method (Image Processing Toolbox, MATLAB, Natick, MA, USA). Note as well that

in these data, STE-DEXSY images were first masked using an intensity threshold determined by Otsu's method [211], prior to analysis.

Modelling S_{end}

To fit exchange parameters, we adapt the T_1^{app} approach, first presented in Sec. 3.3.4. In this approach, the voxel-wise S_{end} and S_{mid} are fitted separately, rather than taking a (log) difference or quotient, which we have noted leads to error propagation (see Table 3.1). This also avoids the need to normalize by a $b = 0$ image. This approach estimates the variation in S_{end} with respect to t_m and then removes these effects from S_{mid} in order to isolate the effect of exchange. For this particular sequence, multiple signal evolution mechanisms are present in S_{end}. Because $b_2 \neq 0$ ($= 0.1$ ms/μm^2), S_{end} is slightly exchange-weighted, similar to the issue encountered in Sec. 3.3.4. In addition, the spoilers on either side of the storage pulses results in some (small) diffusion weighting during t_m (up to $b \approx 0.1$ ms/μm^2 for $t_m = 300$ ms) that can bias the exchange measurement [134, 209]. Of course, there is also the effect of the diffusion-weighted T_1.

All of these elements can be incorporated into a single fit. We note that for the experimental protocol used, the effect of T_1 is different than seen previously in Chapters 3, 4. This sequence was implemented in such a way that, for a given t_m, all slices are looped through before proceeding to the next t_m. The dominant effect of T_1, therefore, is actually as a saturation recovery. As t_m increases, more time elapses while the sequence loops through all slices, such that the *effective* TR (between repeats for the same slice) increases with t_m. Thus, we can model the signal variation in S_{end} as follows:

$$S_{\text{end}}(t_m) = C_2 \left[1 - \exp\left(-\frac{t_m}{T_1^{\text{app}}}\right)\right] \exp\left(-b_{\text{spoiler}}(t_m) D_{\text{app}}\right) \exp\left(-k_{\text{app}} t_m\right) + C_0, \qquad (5.2.1)$$

with three signal evolution mechanisms for (i) the overall T_1^{app} *recovery*, which is a combination of the diffusion-weighted T_1 relaxation during t_m and the saturation recovery due to increasing the effective TR, (ii) the diffusion weighting due to the spoilers on either side of the storage pulses $b_{\text{spoiler}} D_{\text{app}}$, where b_{spoiler} has $\Delta \approx t_m$,

$\delta = 1$ ms, $g = 66$ mT/m, and (iii) the exchange-weighting, represented by k_{app}, as well as the typical floor C_0 and limit C_2 terms. Here, we write C_2 to avoid confusion with the C_1 parameter corresponding to the total observable exchange in the previous chapter.

Fitting S_{end} to (5.2.1) will smooth out variation with respect to t_m due to noise and also ameliorate any slight mis-registration issues, as the evolution in S_{end} is likely to be similar between adjacent voxels. At least 5 values of t_m are needed to fit this model. Note that the estimated parameters from fits to (5.2.1) are not important for our application. The key point is to be able to remove the variation in $S_{\text{end}}(t_m)$ from S_{mid}, whatever particular form that variation may take, in order to isolate the variation due to exchange.

Fitting exchange

Dividing out the signal variation in the fitted S_{end} from S_{mid} results in a decay which contains only exchange weighting, and which can then be fit to some variation of the 3-parameter model for two-site exchange (3.2.10). To fit exchange parameters, we model exchange as a recovery (e.g., Fig. 3.8), beginning from the shortest observed mixing time at $t_m = 5$ ms. We treat this first point as $t = 0$ and normalize by it such that we obtain recoveries starting from $(0,0)$:

$$\frac{S_{\text{mid}}(t_m = 5\text{ ms}) - S_{\text{mid}}(t_m > 5\text{ ms})}{S_{\text{mid}}(t_m = 5\text{ ms})} = C_1\left[1 - \exp\left(-k t_m\right)\right]. \tag{5.2.2}$$

Normalizing by the first point at $t_m = 5$ ms removes the need to fit an intercept parameter and helps in obtaining robust fits. There is also some theoretical motivation for doing so. Attempting to fit an intercept (i.e., $t_m = 0$) is, in essence, an extrapolation towards mixing times that were not observed. While this may have been reasonable with the extremely short t_m used in the PM-10 experiments (minimum $t_m \leq 0.2$ ms), doing so here would constitute a major extrapolation of existing data. Thus, we choose not to do so and to limit our observations to the exchange process that *can* be experimentally probed. Note that there is no effective difference between fitting exchange as a decay or as a recovery, but the recovery is more intuitive, and corresponds to the notion of an increasing exchanging signal fraction f_{exch} (3.3.6).

As we do not need to estimate a floor or perform an ILT, as we did in Chapter 4, we choose here this more intuitive recovery representation.

In summary, the analysis proceeds as follows for each voxel: we first obtain a fit of S_{end} to (5.2.1), then divide out the fitted variation from S_{mid} — i.e., 'correcting' by the variation in S_{end} — and finally fit this corrected S_{mid} to (5.2.2), yielding an AXR and total exchange parameter (C_1) for every voxel.

5.3 Exchange contrast and parameter maps

We now present data acquired using this optimized protocol and analysis pipeline for a single animal, subject #1. Note that this is not the same animal as in Figs. 5.2, 5.3.

5.3.1 Apparent exchange contrast at a single mixing time

As a first result, we again present the exchange-weighted difference maps $S_{\text{end}} - S_{\text{mid}}$ at short and long t_m, shown in Fig. 5.4b. We also present corresponding high resolution, T_2-weighted images (RARE sequence, in-plane resolution 0.1×0.1 mm, matrix size $= 200 \times 200$, FOV $= 20 \times 20$ mm, slice thickness = 0.7 mm, RARE factor = 8, TE = 12 ms, effective TE = 36 ms, TR = 3 s, 4 averages) along with a $b = 0$ image (NR = 1) acquired using the STE-DEXSY sequence with the same parameters as for S_{mid}, S_{end} given in Sec. 5.2.2 (Fig. 5.4a). The concordance between this $b = 0$ image (denoted as b_0) and the RARE image serves as a confirmation of effective coherence selection, indicated by a lack of structured artifacts. As well, no severe EPI-related artifacts are seen (at least in this slice). Note that the T_2-weighting is greater for the $b = 0$ image (TE = 43.2 ms, as well as some T_2^*-weighting from the EPI readout), and thus greater contrast is observed between tissue types compared to the RARE image.

Looking at the difference maps in Fig. 5.4b, we again see the trend of an increasing difference/curvature with t_m, indicative of exchange. Importantly, the maps are less noisy than in Fig. 5.2. The CNR of the difference map at $t_m = 250$ ms presented here is calculated as ≈ 10 as compared to ≈ 4 acquired at a similarly long $t_m = 400$ ms in Fig. 5.2. This increase in CNR supports that the change(s) in experimental parameters successfully improved the signal-to-noise characteristics, in line with our predictions.

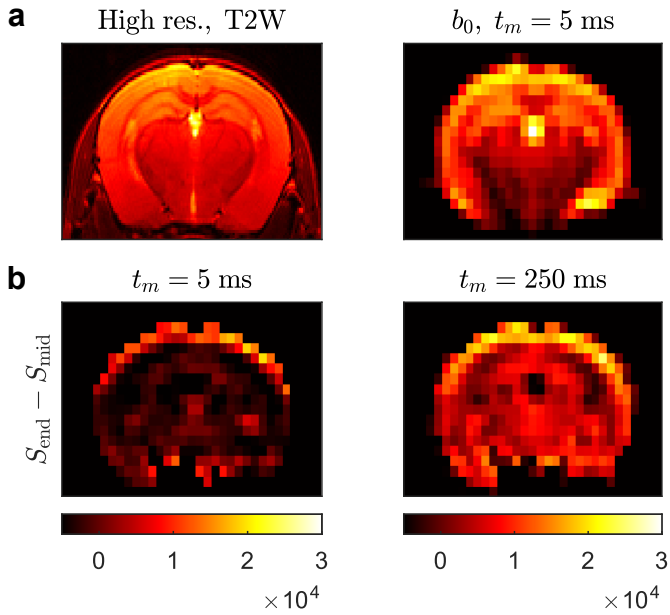

Figure 5.4: Difference maps and structural images for a slice containing the corpus callosum and hippocampus from subject #1. (a) High resolution T_2-weighted RARE image compared to a $b = 0$ image acquired using the STE-DEXSY sequence, denoted b_0 (see text for sequence parameters). Note the similar contrast between the two images. (b) Difference maps $S_{\text{end}} - S_{\text{mid}}$ acquired using the optimized sequence parameters. Of note, $\delta = 4$, $\Delta = 8.5$ ms. Two maps are compared: at the shortest $t_m = 5$ ms, and a long $t_m = 250$ ms. In both maps, structure-related contrast is visible, with the highest exchange-weighting in cortex, less in hippocampus, and the least in WM. Such contrast is visible at even $t_m = 5$ ms, with especially high values in cortex, indicative of fast exchange with $\tau_k \lesssim 5$ ms.

Once again, clear tissue-type contrast is visible, with the highest exchange-weighted difference(s) seen in the cortex, less in hippocampus, and the least in WM. We note, however, that this slice may have been shifted slightly towards the back of the brain compared to the $b = 0$ image.

Keep in mind that in fitting exchange parameters, we elect to fit only the signal variation from $t_m = 5$ ms onward (5.2.2) — avoiding data extrapolation. According to these difference maps, as much as half or more of the difference observed at $t_m = 250$ ms can already be seen at $t_m = 5$ ms. In particular, compare the cortical intensities near the top of the image in Fig. 5.4b: at $t_m = 5$ ms, differences as large as $1.5 - 2 \times 10^4$ are seen, and the limiting difference at $t_m = 250$ ms is less than twice that at $\approx 2.5 - 3 \times 10^4$. This serves as a preliminary indication that exchange is

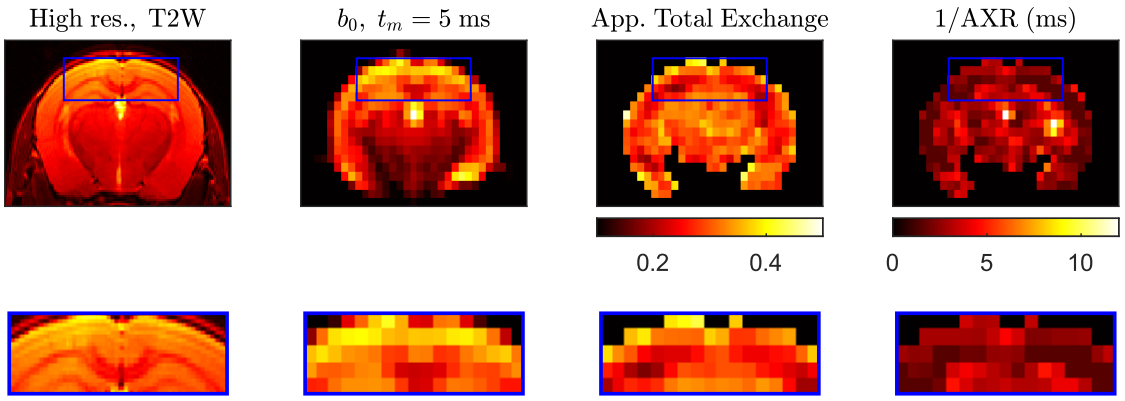

Figure 5.5: Exchange parameter maps generated by fitting S_{end} to (5.2.1), normalizing S_{mid} and fitting to (5.2.2) from subject #1. Corresponding high-resolution RARE images and the $b = 0$ image are shown alongside, though the difference maps appear to be slightly shifted towards the back of the brain. An ROI centered on the corpus callosum is shown in zoomed images.

extremely fast, and foretells that fitting an AXR, given the chosen range of mixing times ($t_m = 5 - 300$ ms) may be difficult due to a lack of information at the most relevant timescales for exchange (i.e., $t_m < 5$ ms).

5.3.2 Total exchange and exchange rate maps

We next present parameter maps of the apparent total exchange (C_1) and exchange time ($\tau_k = 1/k$ or 1/AXR) for the same animal as in Fig. 5.4, subject #1. In Fig. 5.5, we show the high-resolution RARE image and the $b = 0$ image alongside the generated parameter maps. An ROI centered roughly on the corpus callosum is highlighted and zoomed.

Assessing the fits

Before interpreting these parameter maps, let us first take a closer look at the fitting of exchange parameters and assess the overall fit quality by looking at the residuals across voxels. To provide a general idea of the fitting pipeline, a fit to the mean of the entire slice (within the brain) is shown in Fig. 5.6. In Fig. 5.6a, we show the fit to the mean $\bar{S}_{\text{end}}$, plotted in raw intensity units. We see that (5.2.1) is an appropriate model for S_{end}, as there are clearly both recovery (due to the increase in effective TR

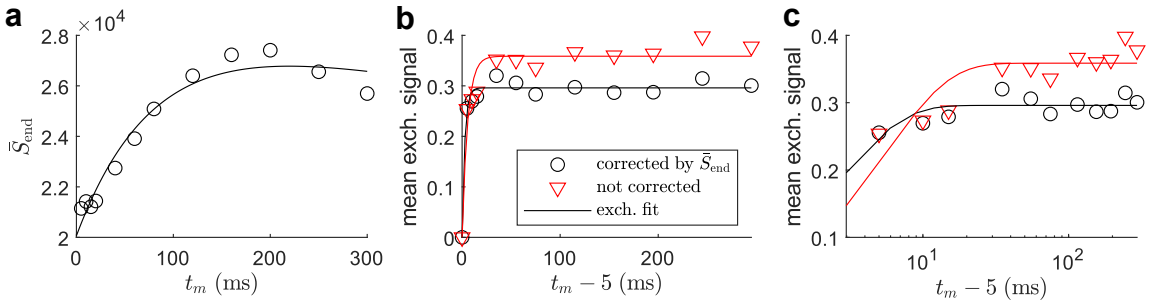

Figure 5.6: Analysis pipeline applied to the mean of the slice (within the brain) presented in Fig. 5.5. (a) Fitting of the mean $\bar{S}_{\text{end}}$ to (5.2.1). (b) Fitting of the mean exchange signal, i.e., S_{mid} normalized to the first point at $t_m = 5$ ms. Mean exchange signal after correction (black), i.e., removing the variation in $\bar{S}_{\text{mid}}$ in part (a), compared to the uncorrected (red) signal. This removes mainly a T_1 saturation recovery effect. Fitting to (5.2.2) yields $C_1 = 0.30$, $\tau_k = 2.7$ ms with RSS $= 2 \times 10^{-3}$ for the corrected signal and $C_1 = 0.36$, $\tau_k = 5.65$ ms, RSS $= 7 \times 10^{-3}$, indicating that the corrected signal (black) is better fit by the exchange model. (c) Same plot as in (b) on a log x-axis.

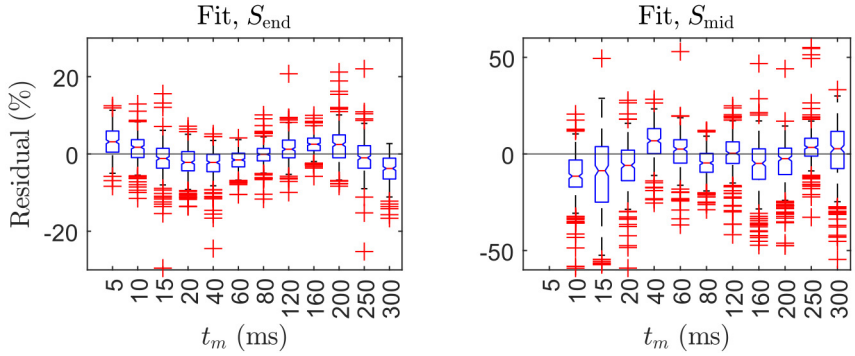

Figure 5.7: Fitting residuals across all voxels for the slice shown in Fig. 5.5. Overall, the fits are good, but there are many outliers, and some systematic bias may remain. In particular, note that the exchange fit (right) preliminarily supports a biexponential model of exchange.

with t_m) as well as decay elements (b-value from spoilers, exchange) which overtake the recovery at long $t_m > 200$ ms. While some systematic bias may remain (notably at the shortest $t_m = 5$ ms and longest $t_m = 300$ ms), the data is generally well-fit by this model, evidenced by the fitting residuals across all voxels shown in Fig. 5.7.

In Fig. 5.6b, we show the mean, normalized exchange signal (5.2.2) (i.e., the relative variation in S_{mid} from the shortest $t_m = 5$ ms onward). To demonstrate the effect of dividing out the variation in the fitted S_{end} — which we call here a correction for effects other than exchange — both the corrected (black) and uncorrected (red)

means are plotted. Without correction, a notable T_1 saturation recovery effect (see the increase of $\bar{S}_{\text{end}}$ in Fig. 5.6a) remains in the signal, and could be misinterpreted as being due to a slow exchange component, highlighting the necessity of both acquisitions S_{end} and S_{mid} to isolate exchange. The corrected exchange signal is well-fit by a monoexponential (5.2.2), yielding a total exchange of $C_1 = 0.30$, and $\tau_k = 2.7$ ms ($k \approx 370$ s^{-1}) with an RSS $= 2 \times 10^{-3}$, whereas the uncorrected signal is comparatively poorly fit (RSS $= 7 \times 10^{-3}$, see Fig. 5.6c) and estimates a longer exchange times $\tau_k = 5.65$ ms. The fitting residuals *across voxels* (right side of Fig. 5.7), however, indicate that there remains some systematic bias seen at short t_m which is consistent with a biexponential potentially being a better fit to the data (i.e., of the form (4.3.3), and consisting of a large signal fraction with a fast τ_k, and a smaller fraction with a longer τ_k). This would agree with the findings in Chapter 4, wherein we observed a consistent bimodality in $P(\tau_k)$ (see Fig. 4.8), though we stress that we do not have the SNR nor the range and sampling density in t_m necessary to explore this potential biexponentiality further.

Fits to exemplar voxels

Looking at individual voxel fits more clearly illustrates the degree of intra-voxel variability across t_m. In Fig. 5.8, we show fits to three voxels with markedly different fitted parameters. We compare voxels with (i) high total exchange and an intermediate exchange time ($C_1 = 0.40$, $\tau_k = 3.0$ ms, black circles), (ii) low total exchange and a longer exchange time ($C_1 = 0.19$ $\tau_k = 3.6$ ms, blue triangles), and (iii) low total exchange but a very fast exchange time near the minimum bound of $\tau_k = 1.5$ ms ($C_1 = 0.23$ $\tau_k = 1.6$ ms, magenta upside-down triangles). In Fig. 5.8a, the different shapes/colors representing these voxels are overlaid on the zoomed parameter maps from Fig. 5.5. In Figs. 5.8b and c, we show the voxel-wise fits to S_{end} and the normalized exchange signal from S_{mid}, respectively. In Fig. 5.8d, a zoomed range of t_m over the first 5 points $t_m = [5, 10, 15, 20, 40] - 5$ ms is shown to highlight the initial variation in the exchange signal and indicates that most of the variation proceeds over the first several, or even just the first two, points in t_m.

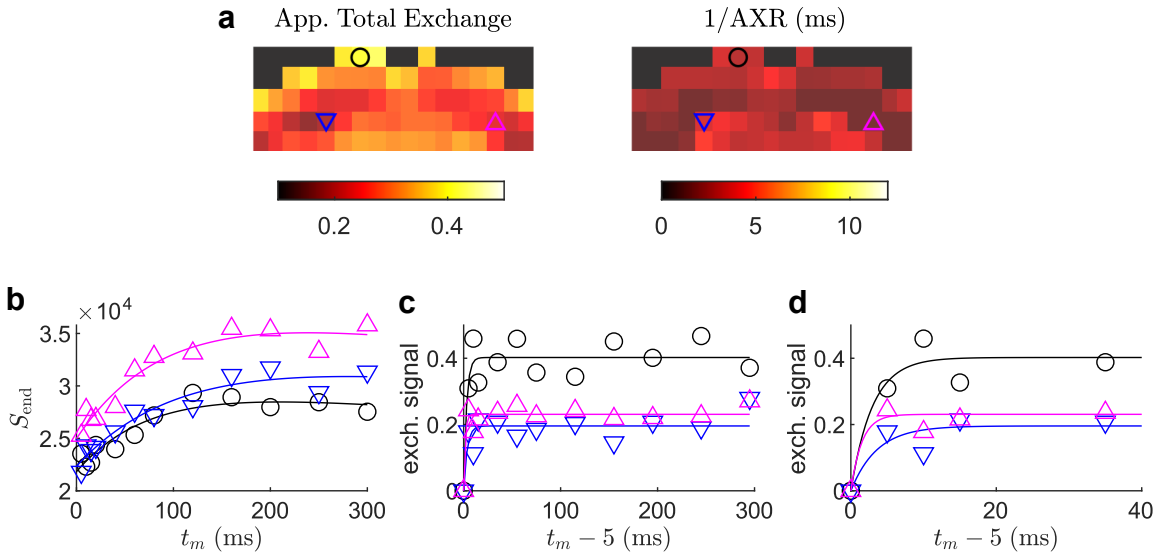

Figure 5.8: Fitting of exchange parameters in individual voxels. (a) Three voxels are compared (see text for fitted parameters), and the shapes/colors representing each are overlaid on the parameter maps presented in Fig. 5.5. (b) Fitting of S_{end} to (5.2.1). (c) Fitting of the normalized S_{mid} to (5.2.2). (d) A zoomed range of t_m highlighting the initial variation in (c). Note that almost all of the variation is captured in the first several points.

These individual voxel fits lead to two observations. Firstly, the variability in the exchange signal from S_{mid} remains high — i.e., there is large deviation from the expected monotonic behavior within a given time-series. For example, in the first voxel (Fig. 5.8c, black circles), the points at long t_m vary by as much as 0.1 about the fit, consistent with a CNR of ≈ 4 for the overall fitting of exchange (i.e., $C_1 \approx 0.4$ for this voxel). This greater variability (relative to the fit for S_{end}) may be due to the fact that the S_{mid} image has an intrinsically lower intensity than the S_{end} image (see Fig. 5.2), and furthermore any systematic bias or poor fitting of S_{end} ends up propagating into the exchange fit for S_{mid}. This difference in variability can be seen by comparing the size of the spread in the residuals in Fig. 5.7, noting the different y-axis ranges between S_{end} and S_{mid}. Second, and more critically, the information for the exchange fit is found to lie predominantly within the first several points due to the extremely short exchange times (see Fig. 5.8d). That is, exchange quickly reaches an apparent steady state by about $10-15$ ms. Thus, despite acquiring 11 values of t_m up to 300 ms, most of these points (where $t_m \geq 20$ ms) contribute little

to improving the fit of the AXR and are, in essence, repeated measurements of the limiting, or total observed exchange, C_1.

Overall, while we are able to fit the data reasonably well and generate quantitative parameter maps as shown in Fig. 5.5, the residual plots in Fig. 5.7 indicate a large number of outliers and some remaining systematic bias, suggesting that in many voxels, the fits may be poor. Moreover, the fitting of exchange is severely hamepred by a lack of information at short t_m. At this time, we must emphasize that the parameter maps should be interpreted with caution, and accordingly caveat our interpretations throughout. These issues arise from variation within voxels between different t_m, as well as our chosen range of $t_m = 5 - 300$ ms being insensitive to a large part of the exchange process, as we highlight in Figs. 5.6c and 5.8d, particularly.

Interpreting the total exchange map

That being said, let us now interpret the total exchange map presented in Fig. 5.5. While the maps are noisy, some structure-related contrast is visible. The highest values are seen in cortex ($\approx 0.35 - 0.45$), less in hippocampus ($\approx 0.25 - 0.4$), and the least in WM ($\approx 0.15 - 0.25$), although in the corpus callosum, specifically, the value appears to be higher ($\approx 0.3 - 0.35$, see zoomed plots in Fig. 5.5). Note that voxels where any value of S_{mid} across all t_m was below a certain noise threshold were omitted. Some voxels near the bottom and at the edge(s) of the brain in Fig. 5.5 were omitted for this reason.

Recall from Sec. 4.4.1 that we interpret the total exchange as being a proximal measurement of the (intra-voxel) signal fractions. We repeat and elaborate upon the argument here. Presuming that steady state (i.e., complete mixing) is reached within the observable t_m — this is indeed the case given the exchange time map in Fig. 5.5 — the total exchanging signal fraction is given by $f_{\text{SS}} = 2f_I f_E = 2f_I(1 - f_I)$ from (3.2.9), where I and E denote the exchanging compartments in a two-site exchange sense (perhaps, the ICS and ECS). Thus, the total *observed* exchange parameter C_1 (n.b., possibly $C_1 < f_{\text{SS}}$ due to exchange outside the observed range, i.e., $t_m < 5$ ms) is theoretically bounded between $[0, 0.5]$, where 0.5 corresponds to

$f_I = f_E$. The fitted total exchange values do in fact fall within the theoretical range of $[0, 0.5]$, lending credence to this interpretation. These bounds were not given in the fit and any parameter value was permitted. More specifically, values range from about $C_1 = 0.1 - 0.4$ throughout the brain.

Increasing imbalance between the relative signal fractions results in a smaller total exchange fraction (e.g., $f_I = 0.2$ leads to $f_{SS} = 2(0.8)(0.2) = 0.32$). Thus, we argue that the total exchange maps should be interpreted as a measurement of the ratio of strongly- vs. weakly-attenuating signal for these diffusion parameters (i.e., $\ell_s \ll \ell_d$ vs. $\ell_s \gtrsim \ell_d$). More specifically, the total exchange can be related to the (apparent) exchanging, weakly-attenuating signal fraction as

$$f_I^{\text{app}} = \tfrac{1}{2} \pm \tfrac{1}{2}\sqrt{1 - 2C_1}, \tag{5.3.1}$$

obtained by solving for the roots of $C_1 = 2f_I^{\text{app}}(1 - f_I^{\text{app}})$. Assuming $f_I^{\text{app}} \leq 0.5$ or $f_I^{\text{app}} \geq 0.5$ narrows this down to one solution, though we stress that these solutions are truly degenerate due to the symmetric nature of two-site exchange. Decreased total exchange is indicative of a greater imbalance between the strongly- and weakly-attenuating signal fractions and/or a large amount of exchange during times that are not visible (i.e., during Δ and/or $t_m < 5$ ms).

These results could therefore be interpreted as cortex having a greater fraction of exchanging, small compartments ($C_1 \approx 0.35 - 0.45$, $f_I^{\text{app}} \approx 0.2 - 0.35$), in comparison to hippocampus ($C_1 \approx 0.25 - 0.4$, $f_I^{\text{app}} \approx 0.15 - 0.25$) and WM ($C_1 \approx 0.15 - 0.25$, $f_I^{\text{app}} \approx 0.1 - 0.15$). However, we point out that due to the degeneracy of (5.3.1), this relationship would actually be flipped if we presume $f_I^{\text{app}} \geq 0.5$. That is, we could equivalently say that these are estimates of f_E^{app}, corresponding, perhaps, to an ECS fraction. It is more accurate to say that in GM, there is a greater apparent *balance* (i.e., closer to $f_I^{\text{app}} = f_E^{\text{app}} = 0.5$) between the strongly- and weakly-attenuating compartments. In the discussion at the end of this chapter, we will assess the lengthscales of the experiment to clarify what lengthscales f_I^{app} may correspond to.

Exchange time map

We now consider the map of the apparent exchange time ($\tau_k = 1/\mathrm{AXR}$) in Fig. 5.5. Throughout the brain, extremely fast exchange times of around $\tau_k \approx 2-5$ ms are seen. This is consistent with the hypothesis that whatever exchange is observed arises from a similar exchange process — i.e., similar compartment(s) and SVR(s) — regardless of the brain region. Although less tissue-type contrast is visible within this exchange time map, exchange times do appear to be somewhat longer in hippocampus and thalamus ($\tau_k \approx 4-7$ ms). Note that the fit for the AXR was given a minimum bound of $\tau_k = 1.5$ ms, motivated by $\Delta = 8.5$ ms. If τ_k were any shorter, then all of the exchange ($> 99\%$) would occur during the encoding and we would not expect our measurement to be able to meaningfully detect exchange due to full mixing, leading to the high-permeability, hindered diffusion case ($\ell_\kappa \ll \ell_d, \ell_s$, see (2.3.4) and Fig. 2.11). Even in this case, however, some t_m-dependence in the signal related to exchange may remain, corresponding to the decrease of $D(t)$ towards D_∞ for the hindered medium (2.3.4) [88]. We will revisit the topic of hindered diffusion in more detail in the discussion at the end of this chapter.

Regardless, the main observation from this map is that exchange times are estimated to be uniformly fast throughout the brain ($\tau_k \approx 2-5$ ms). These estimates are approximately consistent with the fast exchange peak ($\tau_k \approx 4-5$ ms) observed in the previous chapter, where we studied the distribution of $P(\tau_k)$ in live, *ex vivo* neonatal mouse spinal cord (see Fig. 4.8). Taking into account that these experiments were performed at a higher temperature of ≈ 37 °C (body temperature) compared to 25 °C for the *ex vivo* spinal cord specimen, the slightly faster exchange times observed here may be due to the temperature-dependence of the diffusivity D_0 as well as differences in the amount of physiological or metabolic activity. Note that in the temperature variation experiments shown in Fig. 4.1, we found that the exchange rate increased from $k \approx 140$ s^{-1} to ≈ 220 s^{-1} going from 25 °C to 37 °C (see Fig. 4.1a), which corresponds to a decrease in exchange time of $\tau_k \approx 7$ ms to 4.5 ms, in line with the values estimated here.

5.3.3 Repeatability

We next look at images acquired in different animals to assess the within- and between-subject repeatability of both the difference maps $S_{\text{end}} - S_{\text{mid}}$ and the exchange parameter maps. We also highlight issues with what are potentially structured artifacts in some of the short-t_m ($t_m = 5$ ms) images.

Within-subject repeatability, subject #2

To assess within-subject repeatability, we present the difference and parameter maps for two scans acquired back-to-back during the same scanning session (26 min per scan) for another animal (subject #2), shown in Fig. 5.9. In Fig. 5.9, we show the high-resolution RARE image and b_0 image for reference (Fig. 5.9a), alongside the difference maps $S_{\text{end}} - S_{\text{mid}}$ at short and long t_m ($t_m = 5$ vs. 250 ms, Figs. 5.9b, d) and the total exchange and exchange time parameter maps (Figs. 5.9c, d). The first scan (Figs. 5.9b, c, above) is compared to the second scan (Figs. 5.9d, e, below). A similar slice to Fig. 5.5 containing corpus callosum and hippocampus is chosen.

We see that the parameter maps for the second scan (Figs. 5.9e) resemble those presented prior in Fig. 5.5 for subject #1, with a lower total exchange in WM ($\approx 0.15 - 0.25$), and greater values in GM ($\approx 0.3 - 0.45$), with the highest values in cortex (up to ≈ 0.45). As before, generally fast exchange times of $\tau_k \approx 2 - 5$ ms are seen throughout the brain, though some voxels, mainly in thalamus, have up to $\tau_k \approx 5 - 10$ ms. However, in the first scan (Fig. 5.9c), the total exchange map seems to show a contradicting trend, with the *lowest* total exchange in thalamus ($\approx 0.15 - 0.3$) rather than WM, which has higher values than in the second scan ($\approx 0.2 - 0.35$ vs. $\approx 0.15 - 0.25$), though cortex values are consistent between scans. Thus, with the protocol and approach used at this time, these parameter maps do not appear to be highly reproducible.

What is the origin of this lack of reproducibility? Looking at the difference maps $S_{\text{end}} - S_{\text{mid}}$ sheds light on the source of parameter variations. In the first scan (Fig. 5.9b), the vast majority of the difference in the thalamus is already observed at the minimum $t_m = 5$ ms, leading to low total exchange in Fig. 5.9c. Likewise, there is

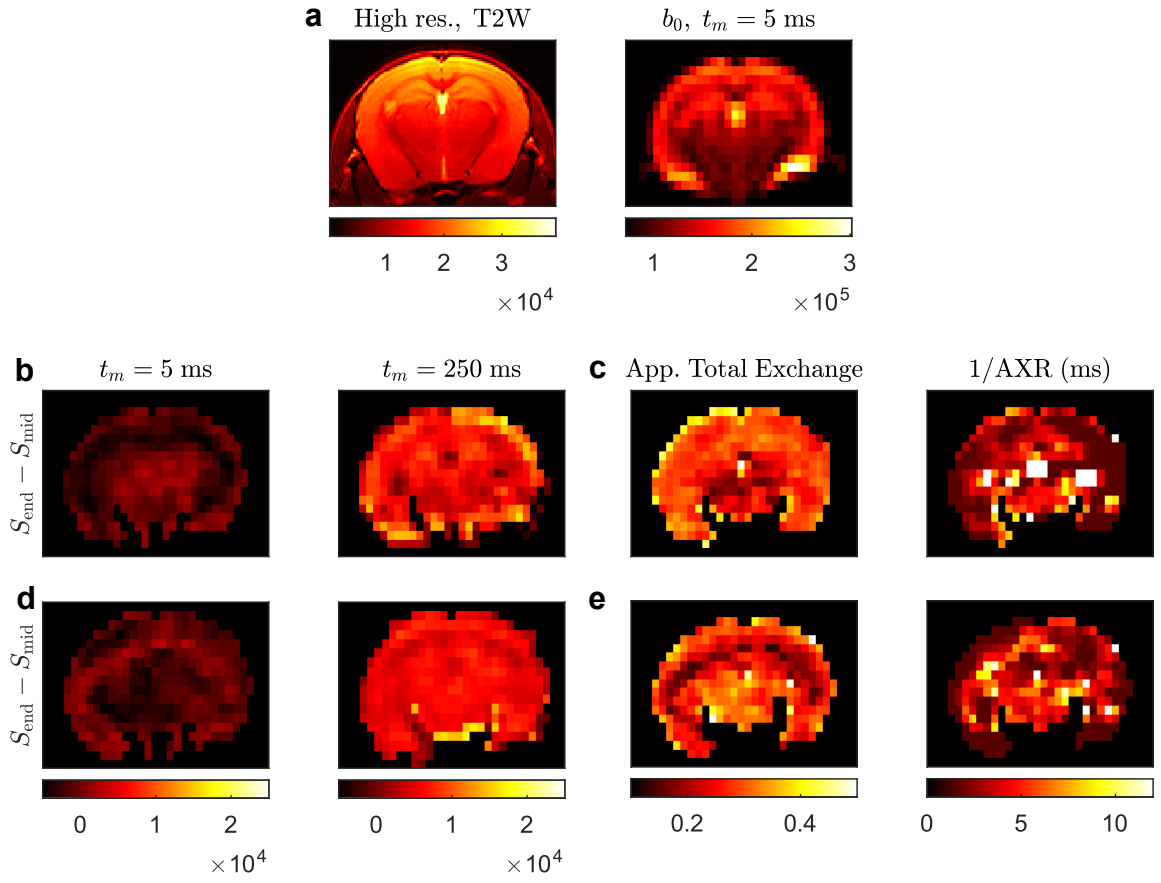

Figure 5.9: Difference maps $S_{\text{end}} - S_{\text{mid}}$ and parameter maps for two scans acquired back-to-back in subject #2. (a) High-resolution RARE and b_0 images for reference. (b – c) Difference and parameter maps for the first scan. (d – e) Difference and parameter maps for the second scan. Note the inconsistencies, particularly in the total exchange map, wherein the trend between WM and thalamus appears to be flipped. This can be attributed to differences in the difference map at $t_m = 5$ ms in parts (b, d). The feature seen in the second scan (bottom row) at $t_m = 5$ ms may be a structured artifact that is unstable over time.

almost no difference seen in WM at $t_m = 5$ ms such that greater total exchange values are ultimately fit. Exactly the opposite is seen for the second scan (Figs. 5.9d); there is a small difference in thalamus and a higher difference in WM at $t_m = 5$ ms, leading to a high total exchange in thalamus and a low total exchange in WM. That is, the initial acquisition at $t_m = 5$ ms appears to have an out-sized effect on the fitting because we normalize by this acquisition — modelling exchange as a recovery from that point onward (5.2.2). Thus, the issue of parameter reproducibility is more specifically an issue in the reproducibility of this first $t_m = 5$ ms acquisition, or the amount of

exchange-weighting seen at short t_m — which was particularly variable in this animal (compare Figs. 5.9b, d). We also cannot rule out that these inconsistencies are due to some form of structured artifact that is inconsistent over time and is present only at short t_m. Consider that short t_m is also when the spoiling during t_m is weakest and where off-resonance effects may become relevant. This highlights what changes would need to be made in order to improve the reproducibility. For instance, a greater number of points at across this range of t_m or a repeated measurement and/or greater averaging of the first point.

We should point out that one does not necessarily need to look at the fitted C_1 to assess the total exchange. Rather, the difference maps at long t_m (see the $t_m = 250$ ms case in Fig. 5.9b, d) are *also* a measurement of the maximal exchange-weighted contrast (i.e., proportional to the 'true' total exchange). These maps are more consistent between the two scans, and indicate a similar (though weaker) trend than that seen in Fig. 5.5: the most exchange-weighting in the cortex, slightly less in hippocampus and thalamus, and the least in WM. Thus, although the fitted C_1 may be unreliable, the difference maps at long t_m are seen to be comparatively repeatable. In Appendix C, we show these difference maps across all t_m and several slices for both scans in subject #1 and #2 to provide a sense of how these maps appear throughout the brain, as well as the behavior with respect to t_m.

Within-subject repeatability, subject #3

In Fig. 5.10, we present another set of two scans in a different animal, subject #3. Here, the total exchange maps (Figs. 5.10c, e) are more consistent, reproducing the hypointensity in WM ($\approx 0.15 - 0.25$ in both scans) seen originally in Fig. 5.5, and higher values in GM ($\approx 0.3 - 0.45$), with the highest values seen in cortex (up to ≈ 0.45). Indeed, the difference maps at $t_m = 5$ ms (Figs. 5.10b, d) are more consistent between scans in this case than in Fig. 5.9, supporting our hypothesis that differences in this first acquisition have a strong influence on the fit(s). However, some variation in the $t_m = 5$ ms acquisition is still visible, particularly in the second scan (Fig. 5.10d), where region(s) with high intensity at this first acquisition end up having low total exchange.

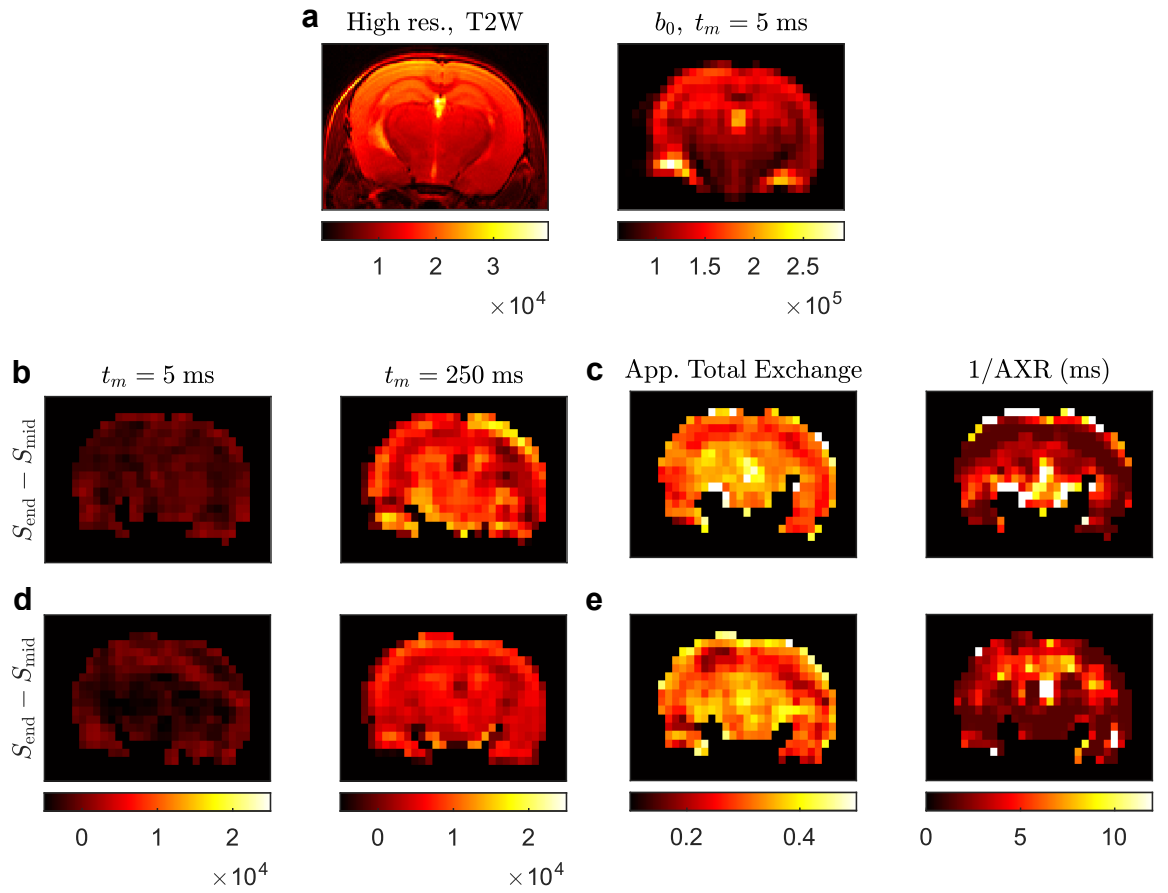

Figure 5.10: Difference and parameter maps for two scans acquired in subject #3. Images are presented in the same way as in Fig. 5.9. (a) High-resolution RARE and S_0 images. Difference and parameter maps for the first (b – c) and second (d – e) scan. Here, the total exchange maps are more consistent, though the exchange time maps are not. Note what may be a structured artifact in the second scan at $t_m = 5$ ms (d).

Again, we cannot rule out that this band of higher intensity represents some form of structured artifact. In contrast, the difference maps at long $t_m = 250$ ms are similar between scans and show the same general trend(s) observed in Figs. 5.4 and 5.9.

As in prior results, fast exchange is observed throughout the brain, with typical values of $\tau_k \approx 2-5$ ms, though in this case, the exchange time maps appear somewhat inconsistent between scans, and voxels with a longer τ_k of up to $\approx 7-10$ ms are not consistent in location. Therefore, taking into consideration all of the exchange time maps presented thus far, the only conclusion which can reliably be drawn is that exchange times are uniformly fast within the brain ($\tau_k \lesssim 5$ ms).

Table 5.1: Exchange parameters from fits to the mean of a slice containing the corpus callosum and hippocampus across animals, with two scans from each subject.

.

Subject #	**Scan**	**App. Total Exchange**	**Exchange Time** (ms)
1	1	0.295	2.75
	2	0.301	2.32
2	1	0.278	2.75
	2	0.263	2.60
3	1	0.318	3.16
	2	0.310	2.22
4	1	0.279	3.27
	2	0.275	1.51
5	1	0.327	1.69
	2	0.282	1.50 (min. bound)
6	1	0.280	1.53
	2	0.292	2.90
7	1	0.140	4.08
	2	0.159	2.42
8	1	0.293	1.51
	2	0.151	4.33
Mean ± SD		0.27 ± 0.06	2.6 ± 0.9

Between-subject repeatability

In light of these inconsistencies between animals, we conclude that the parameter maps are not yet sufficiently reproducible to make firm structural interpretations. As a more conservative assessment of exchange and the repeatability *between*-subjects, we will look only at fits to the *mean* of the slice (as was shown in Fig. 5.6), taking care in all animals to choose a similar slice intersecting the corpus callosum and hippocampus.

Fit parameters from all $n = 8$ animals are presented in Table 5.1. Subject #1 was presented in Fig. 5.5, and subjects #2 and #3 were presented in Figs. 5.9 and 5.10, respectively. Images for subjects 4 – 8 are not shown.

Across all subjects and scans, the total exchange within the brain is estimated as $C_1 = 0.27 \pm 0.06$ (mean ± SD) and the exchange time is estimated as $\tau_k = 2.6 \pm 0.9$ ms (omitting scan 2 for subject 5, which fit an exchange time below the minimum

bound). The total exchange value is fairly consistent between subjects and between the two repeat scans, with a mean difference between scans of ≈ 0.04. Notable deviations are subject #7, which is an outlier with respect to other subjects, but is consistent with itself, and subject #8, which shows poor scan-to-scan repeatability. This overall value of $C_1 \approx 0.27$ corresponds to f_I^{app} (or f_E^{app}) ≈ 0.17 (5.3.1). Given that this value was obtained by averaging through an entire slice, we speculate that $f_E^{\text{app}} \approx 0.17$ — i.e., a smaller, strongly-attenuating compartment — is a more plausible interpretation of the total exchange, and in line with estimates of the ECS occupying $\approx 20\%$ of the brain volume [194].

Compared to the total exchange, more relative variability is seen in the exchange time. For many subjects, a large variation between scans is seen. We mention again that this is due, probably, to the lack of information at $t_m < 5$ ms. Indeed, in some scans, exchange appears to be too fast to reliably fit, and τ_k is at or near the minimum bound of 1.5 ms.

5.4 Discussion

Interpretation of findings

Although we found that the parameter maps were not sufficiently reproducible to assess differences between tissue-types, there remain some general findings that can be considered robust. Exchange times were consistently found to be extremely fast and any voxel-to-voxel variability observed nonetheless fell within the range of $\tau_k \approx 1.5 - 10$ ms. Looking at the fits to the slice means in Table 5.1, all scans produced $\tau_k < 5$ ms. Such fast exchange agrees with some reports in the literature [101, 103]; notably, Olesen *et al.* [101] reported exchange times as fast as $\tau_k = 3 - 5$ ms in *ex vivo* rat brain, although SDE methods were used in that work. Critically, this range of τ_k agrees with our own findings in live, *ex vivo* neonatal mouse spinal cord (Chapter 4 and Ref. [146]), where we consistently found an overall $\tau_k \approx 6 - 7$ ms ($k \approx 140\ \text{s}^{-1}$) at 25 °C, and as fast as $\tau_k \approx 4.5$ ms at 37 °C (Fig. 4.1a). Thus, we speculate that the fast exchange component revealed in Chapter 4, and which dominates the overall exchange, remains detectable *in vivo*.

Considering our body of findings linking fast exchange to steady-state, metabolic activity (Secs. 4.2, 4.4, c.f. Springer *et al.* [180, 181]), this suggests that activity-dependent exchange may also be detectable *in vivo*. If the method(s) can be improved, we may be able to produce parameter maps that are linked to said activity, representing a unique and potentially useful biomarker.

The total exchange, while more consistent than the exchange time (see Figs. 5.5, 5.9, 5.10 and Table 5.1), was also noisy and found to be strongly influenced by the $t_m = 5$ ms acquisition, which may, in some cases contain a structured artifact (see Figs. 5.9d, 5.10d). The most consistent trend seen in our initial results is that of lower total exchange in WM ($\approx 0.15 - 0.25$) than in GM ($\approx 0.3 - 0.45$). If this is borne out by improved measurements (see discussion later), then this suggests that GM has greater relative ECS occupancy than WM. Recall that we hypothesize that the total exchange is an effective measurement of the ECS fraction from the relationship in (5.3.1). Taking a mean through the whole slice yielded an overall total exchange of ≈ 0.27 across subjects and scans (Table 5.1), corresponding to an estimated ECS signal fraction of $f_E^{\text{app}} \approx 0.17$.

There are also other issues with interpreting the total exchange. The possibility of multi-site exchange (e.g., involving soma, neurites, the extracellular space (ECS), or even membranous organelles) complicates the two-site interpretation in (5.3.1). The possibility of high exchange outside the observed range of t_m (see difference maps in Fig. 5.4), also affects estimates of C_1, effectively reducing this parameter. Consider as well that the fixed diffusion- ($b_s = 3.5$ ms/μm^2) and T_2-weighting of the sequence (TE = 43.2 ms) renders some signal components invisible due to complete dephasing, namely CSF, myelin water, and blood. The invisibility of these components could influence the estimated fraction(s) in ventricles or perivascular spaces, WM [103], or highly perfused regions, respectively, making direct comparisons between tissue types difficult. Thus, these results are presented speculatively and without strong interpretations beyond qualitative comparisons. Unfortunately, the resolution is too low to compare cortical layers, which could potentially facilitate stronger interpretations by probing voxels with predominantly soma vs. neurites, but this represents an avenue of future study.

Despite these challenges with regards to the parameter maps, we can consider the difference maps $S_{\text{end}} - S_{\text{mid}}$ at long values of t_m, as shown in Figs. 5.4b, 5.9b, c, 5.10b, c, and Appendix C — i.e., exchange-weighted contrast maps — as a robust finding and a sufficient validation of the curvature method in and of themselves. We confirm that these are, in fact, a measurement of exchange due to variation with respect to t_m; the difference maps at shorter t_m across all presented subjects were always (much) lower in intensity than at long t_m. Difference maps at a long t_m can be interpreted in a similar manner to the total exchange maps (though not quantitatively), and were more repeatable between scans (see Figs. 5.9, 5.10, Appendix C). Therefore, these data serve as a more robust indication of higher relative ECS occupancy in GM than WM. These difference maps are generated using just two images at a single t_m and thus avoid the issues associated with attempting to combine data across t_m. More generally, these images demonstrate the feasibility of attaining exchange-specific contrast by holding the total b-value constant in a DDE, as we conclusively demonstrated in Chapter 3. Recent theoretical developments for DDEs [111–114] also support the general idea that DDEs can be used to isolate exchange.

While not a finding *per se*, we have also demonstrated the development of methods to measure fast exchange *in vivo*, including the testing and development of an STE-DEXSY sequence (similar to the implementation by Bai *et al.* [129] for FEXSY imaging) on a rodent imaging system as well as determination of parameters and analysis approaches oriented towards this end-goal. Thus, while the results may be preliminary, the methods development represents a crucial first step towards eventually probing fast exchange — and potentially steady-state activity — in a robust manner, *in vivo* and with imaging. We should consider more closely, however, the sensitivity of our measurement to fast exchange, and whether this is truly the phenomenon that we are detecting.

Experimental lengthscales

To provide a sense of the lengthscales probed by the experiment, and whether they are consistent with fast exchange, let us evaluate the diffusion and dephasing lengths:

ℓ_d, ℓ_g. For PG experiments, we have that $\ell_d \approx \sqrt{2D_0\Delta}$. Using $D_0 \approx 3\ \mu\text{m}^2/\text{ms}$ and $\Delta = 8.5$ ms, this gives $\ell_d \approx 7.1\ \mu$m. The dephasing length ℓ_g for the exchange-weighted S_{mid} acquisition (where $b_1 = b_2 = 1.75\ \text{ms}/\mu\text{m}^2$) is calculated as $\ell_g = (D_0/\gamma g) \approx 3\ \mu$m. We again find ourselves in a complicated intermediate regime ($\ell_d \gtrsim 2\ell_g$) where the motional averaging ($\ell_s < \ell_g$), localization ($\ell_g < \ell_s < \ell_d$), and free diffusion ($\ell_s > \ell_d$) regimes may all be present to some degree, depending on the underlying distribution of structure sizes ℓ_s. Localization thus cannot be excluded as an explanation for some of the observed curvature (or difference between S_{end} and S_{mid}) at short t_m. Note that although the theory for these three regimes was developed for the extended gradient case of $\tau = \delta = \Delta$ [69] (n.b., additional phenomena may be present here due to the separation between gradients, i.e., diffraction-like effects [212]), we point out that $\delta = 4$, $\Delta = 8.5$ ms lies much closer to the extended gradient case than to the narrow pulse approximation ($\delta \ll \Delta$), for which a different set of theoretical developments apply [75, 213]. Thus, to a first approximation, we may apply here the theoretical principles for the extended gradient case.

This value of $\ell_d \approx 7.1\ \mu$m is much longer than $\ell_d \approx 1.7\ \mu$m (at 25°C) for the PM-10 experiments across Chapters 3, 4. On this system, we may therefore be measuring exchange into/out of relatively larger structures and may not be able to observe the fast exchange reported for live, *ex vivo* spinal cord ($\tau_k \lesssim 5$ ms) if the relevant structure size ℓ_s lies between these two values of ℓ_d. However, if the exchanging structure(s) are smaller than *both* of these ℓ_d values, then the possibility of detecting fast exchange remains. That is, if the motionally averaged, barrier-limited exchange condition ($\ell_\kappa, \ell_d \gg \ell_s$, see Fig. 2.11) holds in the PM-10 system, it would *also* hold in this system. Recall that in our investigation of diffusion in fixed spinal cord (Sec. 3.4, Fig. 3.12), we hypothesized that the signal behavior was more consistent with motional averaging than with localization ($\ell_s \lesssim \ell_g \approx 0.8\ \mu$m). We recently reported similar diffusion decay behavior in live spinal cord (see Supplement in Ref. [146], c.f. Ref. [44]). These findings suggest that the ℓ_s of fast-exchanging structures may indeed be very small and potentially in the sub- to single-micron range (e.g., small neurites). Therefore, we hypothesize that fast exchange may still be detected in the results presented here, despite the relatively longer time- and lengthscales

probed. If this is the case, the main limiting factor would be exchange during the encoding Δ and achievable (short) mixing times. That is, is the permeability low enough (long ℓ_κ) to observe exchange?

A closer look at fast exchange

The exchange times estimated ($\tau_k \lesssim 5$ ms) seem, upon closer inspection, to be outside the range of sensitivity for our measurement with diffusion time $\Delta = 8.5$ ms and minimum $t_m = 5$ ms. Indeed, we should point out that there is some additional time between the end of the first diffusion encoding and the storage pulse (see Fig. 5.1) such that our effective t_m is actually even longer. If exchange is truly this fast, as it appears to be across subjects (see Table 5.1), then complete mixing and the high-permeability, hindered diffusion case is expected ($\ell_\kappa \ll \ell_s, \ell_d$). We must ask how, then, can we measure such fast exchange at all?

Recall that hindered diffusion is *also* time-dependent before the long-time limit of $D_{\text{inst}}(t) = D_\infty$ is reached (2.2.48), (2.3.4), with $D_{\text{inst}}(t)$ taking some approach towards D_∞. More specifically, Novikov *et al.* derived different power law (2.2.49) and/or exponential approaches towards D_∞, depending on the characteristic structural disorder of the medium [83, 88–90]. Thus, the barriers and their permeability can play a role in the apparent time-dependence of the DEXSY signal via the time-dependence of hindered diffusion as it approaches steady state, *even in the case of near complete mixing*. This implies that exchange can still, to some degree, be probed at intermediate timescales between τ_k and the limiting hindered diffusion behavior at $t \to \infty$, which our measurement may fall within. It is perhaps this decrease in $D_{\text{inst}}(t)$ that our measurement probes, rather than exchange in a barrier-limited sense *per se*. Later in Chapter 7 (Sec. 7.1), we will derive and show that the curvature method is in fact a measurement of the approximate *slope* in $D_{\text{inst}}(t)$ at a point in the proximity of $t = t_m + \Delta$, provided that the signal representations in Table 2.6 hold (i.e., the GPA and mass balance are valid assumptions), and thus cogently illustrate how our measurement can probe exchange-related behavior even at longer timescales beyond τ_k.

Nonetheless, we should keep in mind the experimental issues, particularly at short-t_m, that were encountered here (e.g., see Fig. 5.9a, 5.10b). We cannot at this point rule out that our results are biased or contaminated by short-t_m artifacts that could potentially suffice to explain the fast exchange time estimates. Further experiments and modifications to the sequence are necessary.

Ongoing developments

Finally, let us describe some avenues of future development for this work. First and foremost, the need to probe even shorter mixing times is seen to be paramount. The relative lack of information (and potentially structured artifacts) at short t_m is the probable cause of many of the fitting issues and the lack of reproducibility in parameter maps. We could potentially utilize the same STE-DEXSY sequence and shorten the t_m. However, this may lead to issues of insufficient spoiling and thereby incomplete coherence selection. The width of the two storage 90°-pulses also imposes a hard limit on the minimum t_m and such an approach can only go so far. Another possibility is to use an analogous SE-DEXSY sequence with bipolar gradients in each half, collapsing the two 90°-pulses into a single refocusing pulse, and further shortening the t_m by eliminating one pulse altogether (such a sequence was suggested by Chakwizira *et al.* [114] for exchange measurement). Switching to an SE preparation would also avoid the signal loss inherent to STEs (recall that only half the signal is stored — see Fig. 2.4). Yet another approach is to forego *any* refocusing and instead utilize a twice-refocused GRE after the excitation pulse. This approach could produce even shorter mixing times, although will suffer from T_2^* dephasing. All of these experimental approaches/pulse sequences merit investigation and will be implemented and tested in future.

Alternatively or in tandem, we could simply acquire more data in the information-rich, short-t_m range to improve the noise characteristics of the initial point(s), similar to what we did in Chapter 4 (Sec. 4.3.3), where we over-sampled the long-t_m points in order to improve floor estimation prior to the ILT analysis. Indeed, because many of the longer t_m points are effectively redundant here (see Figs. 5.6, 5.8), we could

potentially acquire more data in the short-t_m range while keeping the same or a similar overall scan time (26 min) by discarding some of the longer t_m points. Of course, we could also simply acquire more data and/or analyze over ROIs to increase the effective SNR by pooling voxels, but not to the degree of taking entire slice means. Another possibility is to revisit the selection of $b_s = 3.5$ ms/μm^2. While such a b-value was found to be CNR optimal in terms of the difference maps (Fig. 5.2), the shorter diffusion times permitted by a smaller b-value may ultimately be more important than the CNR itself. Presumably, once such experimental or analysis adjustments have been made, we will be able to obtain more reproducible parameter maps that permit stronger structural interpretations of exchange parameters.

Further experiments

In addition to these experimental improvements, we intend to study the role of AQP4 in the measured exchange process in order to gain further mechanistic insight into exchange, i.e., whether the measured exchange is primarily glial in origin. Reports in the literature suggest that the ADC and apparent exchange time are linked to the expression of AQP4 on membranes [214–217]. Debaker *et al.*, for example, report ADC decreases of about 9% in cortex upon the suppression of AQP4 using an inhibitor, TGN-020 [215]. We observed similar changes of around 10% in the ADC under ouabain and OGD (stroke-like) perturbations (Figs. 4.2, 4.3, respectively), which coincided with a much larger decrease of $\approx 70\%$ in the AXR. We speculate, therefore, that the ADC changes under AQP4 suppression reported in other works may be amplified in the AXR, and animals for which AQP4 is inhibited (or AQP4-deficient animals [216]) may have drastically different exchange characteristics than wild-type. Results along these lines were reported by Eriksson *et al.* [127], who found that expression of human AQP1 in yeast cells led to a ~ 10-fold reduction in τ_k.

Concluding remarks

In this chapter, we demonstrated for the first time, the use of the curvature method *in vivo* and with imaging. Methods were developed on a pre-clinical system to probe

the fast exchange reported in Chapter 4, prioritizing short encoding times. Initial results suggest that we can successfully probe fast exchange despite the change in experimental lengthscales, and exchange times were estimated to be uniformly fast throughout the brain ($\tau_k \lesssim 5$ ms) confirming our previous findings. However, parameter maps remain too noisy to identify clear trends between tissue-types. Nonetheless, these preliminary findings provide a clear path forward towards the robust measurement of fast exchange and suggest the possibility, at least, of probing exchange linked to steady-state, metabolic activity *in vivo*.

6

Rapid measurement of sub-millisecond, time-dependent diffusion

6.1 Introduction 174
6.1.1 Chapter outline and related works 177
6.2 Time-incremented echo train 178
6.2.1 Avoiding off-resonances 178
6.2.2 Estimating the instantaneous diffusivity 184
6.3 Experimental findings 188
6.3.1 Findings in simple liquids 188
6.3.2 Findings in yeast 194
6.4 Discussion 197

6.1 Introduction

In this chapter, we change course to the measurement of time-dependent diffusion in general, rather than exchange specifically. The theory underlying the measurement of time-dependent diffusion $D(t)$ and some of the methods to do so were described in Chapter 2 (Sec. 2.2). The most common approach toward measuring time-dependent diffusion utilizes the frequency-domain representation of the signal

(2.2.24), originating from the work(s) of Stepišnik [16, 17], which is repeated here:

$$\frac{S}{S_0} = \exp\left(-\frac{1}{2\pi}\int_0^\infty |F(\omega)|^2 \widetilde{\mathcal{D}}(\omega) d\omega\right),$$

where

$$|F(\omega)|^2 = \left|\int_0^{\mathrm{TE}} F(t)\exp(i\omega t)dt\right|^2,$$

is the truncated power spectrum of the time-integral of the gradient waveform $F(t)$ and $\widetilde{\mathcal{D}}(\omega)$ is the spectrum of the velocity autocorrelation. Oscillating gradients such as sine-wave modulation in time can thus be used to probe $\widetilde{\mathcal{D}}(\omega)$, which can then be related back to $D_{\mathrm{inst}}(t)$ via the series of operations outlined in (2.2.35). Indeed, the various time-dependent signal models presented, such as Neuman's expressions for restricted diffusion (2.2.43) or Mitra's short-time limit (2.2.50), have frequency-domain analogues in terms of $\widetilde{\mathcal{D}}(\omega)$ [17, 64]. These frequency-domain expressions can then be used to relate the measured $\widetilde{\mathcal{D}}(\omega)$ to structural parameters (e.g., axon [20] and cell [21] diameters, or the surface-to-volume ratio [64]). These works are numerous and form a sub-field of diffusion MR in their own right, and have been collectively referred to as 'temporal diffusion spectroscopy' (TDS) [15]. A non-exhaustive list of works utilizing this signal representation and some variation of this experimental paradigm are given here: [15, 17, 20, 21, 61, 62, 64, 66, 67, 218–224] (c.f. reviews by Reynaud [68] and Xu [225]).

On conventional MRI scanners, however, such an approach is limited by the low gradient slew rates on PG systems, as well as the maximal gradient amplitude, making the observation of short diffusion times (i.e., high ω) difficult. Generally, maximal frequencies of around $100-200$ Hz, or $\sim 5-10$ ms in the time domain can be observed on clinical PG systems [68]. We should also mention that the attendant point-wise sampling approach of TDS is slow, and many acquisitions may be needed to trace out the variation in $\widetilde{\mathcal{D}}(\omega)$. Thus, there are two shortcomings in these methods which we hope to improve upon: (i) first, and more importantly, the short-time behavior is difficult to detect — indeed, most of the signal variation (i.e., the decay in $D_{\mathrm{inst}}(t)$ from D_0 towards D_∞) may reside at these time- and lengthscales, making this a serious shortcoming — and (ii) secondly, the approach may be slow because only one time or frequency is probed per acquisition.

The first issue (i) can be resolved by utilizing the very same SG or constant gradient methods we have used throughout this thesis in Chapters 3, 4. The *effective* gradient switching by refocusing pulses is potentially much faster than oscillating, pulsed-field gradients. Thus, a CPMG sequence under a strong SG (such that there is still appreciable signal attenuation due to diffusion) is a means to probe the short-time, high-frequency diffusion. Consider that such a sequence (i.e., SG-CPMG) produces a triangle-wave $F(t)$, which, over successive cycles, will produce a sharp power spectrum centered at $\omega = 1/(2\tau_{\mathrm{CPMG}})$ Hz (though with odd harmonics). Values of τ_{CPMG} can be as short as ~ 0.1 ms, permitting the observation of $\omega \sim 1-10$ kHz [221], which is far in excess of what can be probed with PG systems (up to $100-200$ Hz). This approach was suggested by Callaghan & Stepišnik [61] and is utilized in some of the works mentioned above [17, 64, 67, 219–221, 223].

Using the SG-CPMG experiment comes with complications, however. The large number of (selective) pulses (e.g., 20 180°-pulses to produce 10 triangle-wave $F(t)$ cycles) leads to potentially very strong off-resonance effects. Recall that the number of pathways generated by N total pulses is given by 2×3^N via Woessner decomposition, which is clearly an intractably large number of pathways to consider comprehensively and analytically. The diffusion behavior measured by SG-CPMG may therefore consist of a combination of many STE and SE pathways in addition to the desired coherence, which has the (intended) sharp power spectrum. Nonetheless, the use of CPMG sequences in inhomogeneous fields (i.e., with an SG) is well-studied [71, 226–228], and attempts have been made to account for these effects. In particular, Song [229] has categorized the various off-resonance pathways in the SG-CPMG sequence, and various methods have been proposed to correct for these effects *post hoc* [229–232]. Finally, we should note that the second limitation (ii) of point-wise sampling still applies to the SG-CPMG experiment.

We thus arrive at the motivation for this work. We ask: is it possible to leverage the advantages of the SG-CPMG experiment whilst avoiding off-resonance effects? In addition, can we measure many timescales at once? It turns out that both of these goals can accomplished simultaneously. Unwanted pathways in the SG-CPMG experiment can be avoided by successively incrementing the inter-pulse timings in

a carefully considered manner. We call this the SG, time-incremented echo train acquisition (SG-TIETA). At the same time, this produces a variety of effective echo times and diffusion weightings within the same acquisition. Indeed, the decay of the SG-TIETA signal contains a broad range of time-sensitivity such that $D_{\text{inst}}(t)$ can be estimated in potentially a single shot. We detail the theory underlying this method and provide a range of validation experiments in simple liquids and yeast suspensions in this chapter.

6.1.1 Chapter outline and related works

We first describe how pulse timings can be designed to avoid off-resonance effects. We design a sequence in which we avoid the *majority* of relevant unwanted pathways up to a certain order, and provide exemplar inter-pulse timings to achieve this avoidance. We also describe how SG-TIETA decays can be normalized to produce effectively on-resonant signal behavior.

We then present data which confirms the avoidance of off-resonance effects. Looking at normalized decays in simple liquids of varying diffusivity, we find that SG-TIETA can reproduce the expected decay due to Gaussian diffusion, thereby indirectly demonstrating the avoidance of unwanted pathways. Consider that one would expect different decay behavior for liquids of different diffusivities if off-resonance pathways such as STEs were not avoided. We also provide more direct evidence of the avoidance of pathways. We find that the evolving echo shape of SG-TIETA decays is consistent with a decreasing frequency band, which in turn is consistent with off-resonance pathways arising from the side lobes of the pulse (i.e., flip angles less than 180°) being suppressed. Finally, raw time-domain data illustrates how unwanted pathways refocus at times away from the desired echo.

We next develop a regularized, least-squares approach to measure $D_{\text{inst}}(t)$ from single-shot (averaged) SG-TIETA experiments. The fitting method is first validated in synthetic data from Monte Carlo simulations and is then applied to study $D_{\text{inst}}(t)$ in yeast cell suspensions using the PM-10 system over a sub-millisecond range of diffusion times.

Elements of this work were first presented in

- **Cai, T. X.**, Williamson, N. H., Witherspoon, V. W., Ravin, R., & Basser, P. J. Single-shot measurement of sub-millisecond, time-dependent diffusion using optimized, unequal pulse spacings in a static field gradient. (2021, May). *Proceedings of the 30th Annual Meeting of the ISMRM*, Online, Abstract #2468,

and subsequently a more comprehensive work was published in

- **Cai, T. X.**, Williamson, N. H., Witherspoon, V., Ravin, R., & Basser, P. J. (2021). A single-shot measurement of time-dependent diffusion over sub-millisecond timescales using static field gradient NMR. *The Journal of Chemical Physics*, *154*, 111105.

Experiments were performed in collaboration primarily with Dr. Nathan Williamson.

6.2 Time-incremented echo train

In this section, we describe the design of the SG-TIETA sequence as well as the fitting approach to yield $D_{\text{inst}}(t)$ from a single SG-TIETA decay.

6.2.1 Avoiding off-resonances

Let us investigate how inter-pulse timings can be successively incremented to avoid off-resonant pathways. Following Song [229] and Woessner decomposition in general, we will consider separate categories of pathways and how each can be avoided.

Incremented timings

In particular, we propose to acquire acquire an echo train wherein every inter-pulse interval (2τ in a typical CPMG experiment) is incremented by some integer multiple $m \in \mathbb{Z}$ of a fixed, discrete time offset, δ. This multiple varies for the interval following each refocusing pulse (numbered n), such that the inter-pulse intervals take the following form:

$$2\tau + m_n\delta, \tag{6.2.1}$$

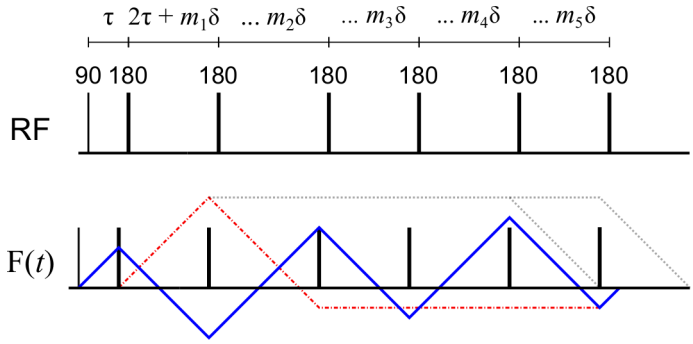

Figure 6.1: Example of an SG-TIETA sequence with timings: $m_n = [1,3,1,2,1]$ and $\tau = 4\delta$. The time-integral of the (constant) gradient $F(t)$ is drawn for the desired coherence (blue) and for example unwanted pathways emerging from the first 180°-pulse which either refocus at the final echo (red, dash-dot) or do not refocus (gray, dotted).

i.e., the time between the n^{th} and the $(n+1)^{\text{th}}$ refocusing pulse. An example of an SG-TIETA sequence is shown in Fig. 6.1, illustrated along with the resulting time-integral of the static gradient $F(t)$. Such a graph is similar in notion to 'extended phase graphs' [33] used to track off-resonant pathways. Note how the evolving pulse timings determine the TE for the echoes formed, which is proportional to the height of the peaks in $F(t)$. The initial echo formed has $\text{TE} = 2\tau$, while the echo after the first refocusing pulse has $\text{TE} = 2(\tau + m_1\delta)$, increased by the increment. We will call these two echo times TE_1 and TE_2 because they form during the first and second inter-pulse intervals. For every echo thereafter ($n > 2$), the TE is determined by the *difference* between the previous offset and the current offset, which results in a recursive relationship:

$$\text{TE}_{n>2} = 2\left[\tau + (m_n - m_{n-1})\delta\right], \quad \text{TE}_2 = 2(\tau + m_1\delta), \quad \text{TE}_1 = 2\tau. \tag{6.2.2}$$

The time that the n^{th} echo is formed is given by $\sum_{j=1}^{n} \text{TE}_j$.

In Fig. 6.1, we have also drawn example unwanted coherences emerging from the first refocusing pulse which either refocus (red) or do not refocus (gray) at the final echo (i.e., coincide with the desired pathway drawn in blue at the final echo). Recall that by Woessner decomposition (see Sec. 2.1.2, Fig. 2.4), we can consider pathways as undergoing either 0, 90, or 180°-pulses. In the domain of $F(t)$, this corresponds to piece-wise linear functions, where dephasing and rephasing correspond to positive

and negative slopes (of $\pm\gamma g = G$, to be precise), and longitudinal storage corresponds to a horizontal line, as drawn for the exemplar pathways in Fig. 6.1.

Recall as well that the echo width in the time domain for hard, refocusing pulses is approximately equal to the width of the pulse τ_p [48]. Thus, to separate the desired echo-forming pathway from the undesired pathways, it is sufficient to separate them by at least $2\tau_p$ (i.e., the points where these pathways intersect $F(t) = 0$ is at least $2\tau_p$ apart). The idea that timings can be used to isolate the desired coherence is obvious, and indeed, many unwanted pathways are avoided by the exemplar sequence in Fig. 6.1. With this discretely incremented timing framework in place, we now turn towards the systematic design of m_n and δ to avoid unwanted pathways, broken into different categories [229]. This principle of avoiding pathways via timings is inspired by preceding works by Song [233] and Sigmund *et al.* [234].

Freshly excited transverse magnetization

The first category of unwanted pathway we consider is that of magnetization which was not excited onto the transverse plane by the initial 90°-pulse, and is excited by some later pulse. The pathways illustrated in Fig. 6.1, for example, are excited onto the transverse plane by the first refocusing pulse. Consider the following: any sum of TEs (i.e., the time of echo formation) for the desired pathway contains an *even* multiple of τ and some multiple of δ according to (6.2.2). On the other hand, any pathway that is excited by a refocusing pulse *misses the τ interval* between the 90°-pulse and the first refocusing pulse, such that these pathways will always form at a time with an *odd* multiple of τ instead. Therefore, if δ does not divide evenly into τ — $(\tau \bmod \delta) \neq 0$ — then there will always be an offset between these pathways and the desired pathway. We thus arrive at our first 'rule' for timings:

(1) δ and τ satisfy $(\tau \bmod \delta) = \delta/2$ and $\delta > 2\tau_p$.

If we set $(\tau \bmod \delta) = \delta/2$, then the separation in the time of echo formation between the desired pathway and these pathways will always be at least $\delta/2$. Keeping in mind that the echo width is τ_p, then $\delta > 2\tau_p$ ensures no echo overlap. This first rule eliminates an entirely family of off-resonance pathways at once and we now

need only consider magnetization that is already in the transverse plane after the initial 90°-pulse.

Singly stimulated echoes

Another category of pathways undergoes a single storage period and then is brought back in alignment with the desired pathway. Looking at Fig. 6.1, we can see that this situation can occur if any of the TEs are repeated. Visually, this corresponds to a horizontal line drawn between two peaks in $F(t)$ (or the peak flipped across the $F = 0$ line). Therefore these pathways can be avoided by the simple rule:

(2) TE_n may not be repeated across all n.

Higher order pathways

We can also consider higher order pathways with multiple deviations, such as storage, from the desired pathway. To do so, we introduce the concept of the phase *relative* to the desired SG-TIETA pathway that is accrued over some interval n: $\Delta F(t)$. This deviation in phase can take only one of three values by Woessner decomposition:

$$\Delta F(t) = G(-1)^{n-1}(2\tau + m_n\delta) \times \{0, 1, 2\}. \tag{6.2.3}$$

Note that the $(-1)^{n-1}$ term captures the alternating dephasing and rephasing of the desired pathway (slopes of $\pm G$ in time, respectively). The three values $\{0, 1, 2\}$ correspond to three cases: (i) the pathway accrues no relative phase $\Delta F(t)$ (sees the 180°-pulse as intended), (ii) the pathway is stored and acquires $\Delta F(t)$ of $\pm G(2\tau + m_n\delta)$ — i.e., it is stored whilst the desired pathway phases by $\pm G(2\tau + m_n\delta)$ — or (iii) the pathway misses the pulse and acquires a phase of $\pm 2G(2\tau + m_n\delta)$ because it continues to dephase after the desired pathway begins rephasing.

According to (6.2.3), avoiding higher order pathways is seen to be equivalent to preventing $\Delta F(t)$ from summing back to 0. Because the $G\tau$ term is always present, this really amounts to preventing combinations of m_n from summing to zero, also taking into account the even and odd alternation by $(-1)^{n-1}$. We can come up with a variety of rules to avoid higher-order pathways (here, up to fourth-order, i.e.,

deviating from the desired pathway over up to 4 intervals), where Δn denotes the difference between intervals (e.g., the first and fourth interval have $\Delta n = 3$):

(3) m_n and $m_{n\pm\Delta n}$ with odd Δn may not be the same.

(4) Any two m_n with even n may not equal the sum of any two m_n with odd n

(5) Twice any m_n with even n may not equal the sum of any two m_n with odd n, and vice versa.

(6) Twice any m_n may not equal the sum of $m_{n+\Delta n}$ and $m_{n-\Delta n}$ for even Δn.

These rules avoid many pathways comprising various SE and STE elements and are based on preventing the values of $(-1)^{n-1}m_n$ from summing to zero. While we could account for even higher-order pathways, consider that the diffusion-weighting of these pathways is strictly greater than for the desired SG-TIETA pathway. Since $b = \int |F(t)|^2 dt$, the area under $F(t)$ will *always* be greater whenever a pathway does not see a refocusing pulse as it is. Not seeing a refocusing pulse will *always* result in relatively more phase accrual or diffusion weighting. Thus, very high-order pathways will dephase much more rapidly, and can effectively be considered as 'lost' signal. Such pathways, are in a sense, avoided anyway. This brings us to the topic of pulse 'accuracy'.

Pulse 'accuracy'

As argued by Song [229], one can consider for a given system and refocusing pulse that each pulse produces a certain ratio of on- vs. off-resonance signal, which is captured by a pulse accuracy term, A_p (e.g., $A_p = 0.95$, corresponding to 5% off-resonant excitation). For an SG-TIETA sequence, however, we expect that A_p will increase with n — i.e., it is a function of n, $A_p(n)$ — because off-resonant pathways are avoided. This corresponds to repeatedly convolving the pulse spectrum with itself, resulting in a narrower and narrower frequency band as n increases. We will confirm this behavior later in Sec. 6.3.1. Consider that higher-order pathways that are much more diffusion-weighted than the desired pathway will also be captured by $A_p(n)$,

because this signal effectively vanishes. Thus, in order to obtain SG-TIETA decays that correspond only to the on-resonant signal, one can experimentally estimate $A_p(n)$ using a system with known Gaussian diffusivity (such as a simple liquid) and then 'correct' the SG-TIETA decay (of the echoes) $S(n)$ by a factor

$$\frac{S(n)}{S_0} = S(n)\left(\prod_{j=1}^{n} A_p(n)\right)^{-1}, \tag{6.2.4}$$

to obtain what corresponds to a typical, normalized diffusion-weighted decay $S(n)/S_0$.

Exemplar timing sequence

Here, we provide an SG-TIETA sequence which satisfies all of the presented rules (1 – 6). Note that satisfying these rules generally requires increasing m_n, and thus TE_n, because an increasingly large ($\sim 3^n$) number of pathways must be avoided as more pulses are added. Put simply, more 'space' between pulses is needed to avoid the growing number of unwanted pathways. A possible sequence forming a total of $N = 20$ echoes is as follows:

$$\begin{gathered} \tau = 49\,\mu\mathrm{s}, \quad \delta = 14\,\mu\mathrm{s}, \\ m_n = \begin{Bmatrix} 1 & 3 & 6 & 7 & 10 & 12 & 11 & 15 & 20 & 21 \\ 24 & 26 & 20 & 21 & 33 & 35 & 33 & 34 & 33 & \ldots \end{Bmatrix}, \end{gathered} \tag{6.2.5}$$

See how τ and δ are chosen such that $(\tau \bmod \delta) = \delta/2 = 7\ \mu$s, which would satisfy rule (1) for $\tau_p \lesssim 5\ \mu$s. See also how m_n increases. These timings result in the following TEs:

$$\mathrm{TE}_n = 2 \times \begin{Bmatrix} 49 & 63 & 77 & 105 & 91 & 147 & 119 & 133 \\ 175 & 203 & 189 & 245 & 217 & 161 & 231 & 329 \\ 259 & 301 & 273 & 287 & \ldots & & & \end{Bmatrix} \mu\mathrm{s}. \tag{6.2.6}$$

This sequence is sensitive to diffusion times over $t \sim 50 - 500\ \mu$s, i.e., diffusion over sub-millisecond timescales. In terms of experimental lengthscales, the ℓ_d for the various TEs, using $D_0 = 2.15\ \mu\mathrm{m}^2/\mathrm{ms}$, varies from $\ell_d = 0.3\ \mu$m for the first TE = 98 μs, to up to $\ell_d = 0.8\ \mu$m at the longest TE = 602 μs. Thus, this sequence also measures diffusion over sub-micron lengthscales. See Supplement in Ref. [47] for Python code to generate these sequences.

6.2.2 Estimating the instantaneous diffusivity

With the experimental paradigm in place, we now turn towards how $D_{\text{inst}}(t)$ can potentially be estimated from single-shot SG-TIETA decays, which evidently probe a large range of diffusion times all at once. We utilize Ning's [65] signal representation in terms of $D_{\text{inst}}(t)$ and the cumulative gradient autocorrelation $C(t)$, which we solved for the SG-SE experiment in (2.2.34), see also Fig. 2.10 for the shape of $C(t)$. More specifically, we will presume that each *inter*-echo decay (i.e., over each TE_n) can be approximated as an independent measurement of the time-varying diffusivity, i.e., starting from $t = 0$:

$$C_n(t) = \begin{cases} t\left(-\frac{3}{2}t + \text{TE}_n\right) & 0 \le t \le \frac{\text{TE}_n}{2} \\ \frac{t}{2}\left(t - \text{TE}_n\right) + \text{TE}_n^2 & \frac{\text{TE}_n}{2} \le t \le \text{TE}_n \end{cases}. \tag{6.2.7}$$

This amounts to assuming that the previous intervals can be ignored and that each TE_n is a measurement of the steady-state magnetization as though it had just been excited. This is valid for simple liquid systems. Of course, this assumption may not hold in spatially heterogeneous systems such as tissue, where the signal will in reality become increasingly weighted towards smaller compartments as n increases. For heterogeneous systems, ideally the whole decay (i.e., considering the whole of $F(t)$ or $G(t)$ at once) would be ideal, but this greatly complicates the calculation of $C(t)$. To a first approximation, (6.2.7) may suffice, particularly in the short-time regime of $\ell_d \ll \ell_s$.

The short-time $D_{\text{inst}}(t)$

Over the very short times probed, the universal short-time behavior of $D(t)$ (2.2.50) may perhaps be observed,

$$D(t) \simeq D_0\left[1 - \frac{S}{V}\left(\frac{4\sqrt{D_0 t}}{3\sqrt{\pi}} - \kappa t\right)\right], \quad \ell_d \ll \ell_s, \tag{6.2.8}$$

modified here to include a correction for the permeability κ [88]. From $D_{\text{inst}}(t) = \partial_t\left[2tD(t)\right]$, we retrieve the analogous expression:

$$D_{\text{inst}}(t) \simeq D_0\left[1 - \frac{S}{V}\left(\frac{2\sqrt{D_0 t}}{\sqrt{\pi}} - 2\kappa t\right)\right], \quad \ell_d \ll \ell_s. \tag{6.2.9}$$

If this regime is observed, then spatial heterogeneity will not greatly affect the decay behavior, such that (6.2.7) is a good approximation.

Fitting $D_{\text{inst}}(t)$

We cast the problem of estimating $D_{\text{inst}}(t)$ from SG-TIETA decays as a weighted and regularized log-linear least squares (LLS) inversion by discretizing the time domain into J intervals of variable width, $\Delta t(j)$:

$$\underset{\mathbf{X}}{\operatorname{argmin}} \, ||\mathbf{W}^{1/2}\left(\mathbf{AX}-\mathbf{B}\right)||_2^2+\lambda||\mathbf{\Gamma X}||_2^2, \tag{6.2.10}$$

with coefficients

$$\mathbf{A}=\begin{bmatrix} \int_0^{\Delta t(1)} C_1(t)\,dt & \dots & \int_{\Delta t(J-1)}^{\Delta t(J)} C_1(t)\,dt \\ \vdots & & \vdots \\ \int_0^{\Delta t(1)} C_N(t)\,dt & \dots & \int_{\Delta t(J-1)}^{\Delta t(J)} C_N(t)\,dt \end{bmatrix},$$

where $\mathbf{X}$ consists of time-interval $D_{\text{inst}}(t)$ averages,

$$\mathbf{X}=\begin{bmatrix} \frac{1}{\Delta t(1)}\int_0^{\Delta t(1)} D_{\text{inst}}(t)\,dt \\ \vdots \\ \frac{1}{\Delta t(J)-\Delta t(J-1)}\int_{\Delta t(J-1)}^{\Delta t(J)} D_{\text{inst}}(t)\,dt \end{bmatrix},$$

$\mathbf{B}^{\mathrm{T}}=-\ln\left[S(n=1)/S_0 \quad \dots \quad S(N)/S(N-1)\right]$ is the (log) SG-TIETA decay after normalization by $A_p(n)$ using (6.2.4) and setting $S_0=1$, $\mathbf{W}$ is the corresponding $N\times N$ weights matrix composed of the inter-echo signal differences, i.e., $S(n-1)-S(n)$, and finally $\mathbf{\Gamma}$ is a regularization matrix with regularization parameter λ.

In implementing this inversion, we can take into consideration known theoretical characteristics of $D_{\text{inst}}(t)$. Because $D_{\text{inst}}(t)$ is expected to be monotonically decreasing (from D_0 to D_∞) as well as smooth, strong regularization has some theoretical motivation, and $\mathbf{\Gamma}$ is therefore chosen to consist of first- and second-order finite difference matrices (see Supplement of Ref. [47] for details). The choice of J and $\Delta t(j)$ (i.e., how to discretize the time-domain) should also account for how $D_{\text{inst}}(t)$ varies. Consider that $\Delta t(j)$ should be chosen such that $D_{\text{inst}}(t)$ does not vary greatly over any interval, such that the averaging in $\mathbf{X}$ is valid. Thus, $\Delta t(j)$

should start out small (when the variation in $D_{\text{inst}}(t)$ is greatest), and may gradually lengthen as $D_{\text{inst}}(t)$ approaches D_∞. As well, estimated values of D_0 and D_∞ from separate ADC measurements can be given as initial guesses in $\mathbf{X}$. The choice of N, of course, is dictated by when the SG-TIETA signal decays to the noise floor, and J should be similar or smaller than N.

Monte Carlo simulations to test inversion

To test the LLS inversion (6.2.10), SG-TIETA decays were generated from Monte Carlo simulations of the MSD in cylindrical geometries and (6.2.7), shown in Fig. 6.2. Simulations were performed in the following geometries: impermeable cylinders with $R = 1$ μm looking at the displacement orthogonal to the cylinders (blue), the same geometry but with a 4% cross-over probability upon collision with the wall to model permeability (red), the same geometry but looking at the displacement parallel to the cylinders (i.e., free diffusion, black), and, finally, impermeable cylinders with a larger $R = 1.5$ μm (magneta). The generated MSD curves are shown in Fig. 6.2a. The corresponding $D_{\text{inst}}(t)$ curves — which is merely the time-derivative of the MSD — are shown in Fig. 6.2c (solid lines). In all simulations, 2.5×10^4 walkers were simulated with time steps of 1 μs and up to $t = 700$ μs. Walkers were randomly and uniformly distributed at the start of the simulation.

The predicted SG-TIETA decay was then calculated from (6.2.7) using the timings provided in (6.2.5), yielding echo-to-echo decays (same colors) shown in Fig. 6.2b. The overall time-domain weighting of the sequence, represented as $\sum_{n=3}^{20} C_n(t)$, is overlaid in Fig. 6.2a in order to give a sense of the time-domain sensitivity of the sequence (omitting the first two echoes which show very little attenuation). In an inset of Fig. 6.2b, the difference between adjacent echoes n and $n-1$ is shown, which forms the weights matrix, $\mathbf{W}^{1/2}$. For the inversion, the time domain spanning $t \approx 0-600$ μs was discretized into intervals of width $\Delta t(j) = [50, 50, 50, 50, 75, 75, 125, 139]$ μs, gradually lengthening the intervals such that $D_{\text{inst}}(t)$ can be approximated as constant within each interval. Also shown is the resulting weights matrix $\mathbf{A}$ (Fig. 6.2b), which illustrates how each inter-echo interval's $C_n(t)$ probes a different range of times.

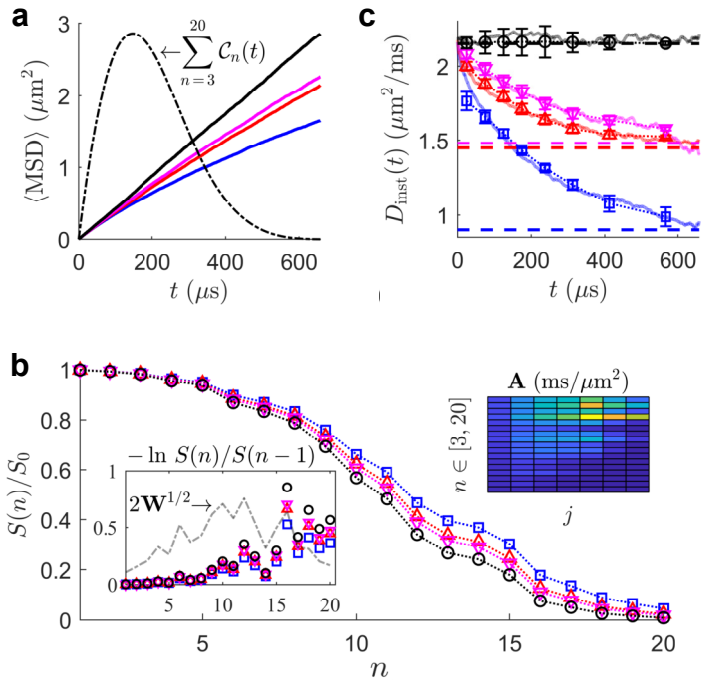

Figure 6.2: LLS inversion tested on SG-TIETA data generated from Monte Carlo simulations. (a) Simulated $\langle \mathrm{MSD} \rangle$ ($D_0 = 2.15\ \mu\mathrm{m}^2/\mathrm{ms}$) for free diffusion (black) and various restricted geometries (see text for simulation details). The overall time-domain weighting of the SG-TIETA sequence with timings given in (6.2.5), $\sum C_n(t)$, is overlaid (units of b, scaled to fit the graph), omitting the first two echoes. (b) Generated SG-TIETA decays from the same color curves in (a), using $g = 15.3$ T/m, corresponding to the PM-10. An inset shows the (log) inter-echo decay $\mathbf{B}$ and the scaled weights $2\mathbf{W}^{1/2}$ for the black curve. The coefficients matrix $\mathbf{A}$, with the time-domain split into $J = 8$ intervals of width $\Delta t(j) = [50, 50, 50, 50, 75, 75, 125, 139]$ μs is also shown. (c) $D_{\mathrm{inst}}(t)$ from the gradient of $\langle \mathrm{MSD} \rangle$ curves in (a) (solid lines) compared to $\mathbf{X}$ inverted from decays in (b) with added Gaussian noise (SNR = 25). Error bars = mean ± SD from 100 repeated inversions. Initial guesses of $\mathbf{X}$ were D_0 for the first point and D_∞ (dashed lines, $[0.9, 1.45, 1.48]$ μm^2/ms) for all remaining points. The regularization parameter $\lambda = 2 \times 10^{-6}$ was selected approximately by the L-curve method for the free diffusion case (black) and held constant for other cases. See Eq. (S1) in Ref. [47] for the exact form of $\mathbf{\Gamma}$.

Recall from (6.2.7) and Fig. 2.10 that $C_n(t)$ has a peak at $t = \frac{2}{3}\mathrm{TE}_n$.

Finally, the LLS inversion was performed after first adding Gaussian noise to the simulated signal (SNR = 25). The regularization parameter was chosen approximately as $\lambda = 2 \times 10^{-6}$ by the L-curve method [151] for the free diffusion case (black) and then held the same for the other cases. The inversion was repeated 100 times, and the predicted values of $\mathbf{X}$ (i.e., $D_{\mathrm{inst}}(t)$ averaged over discrete $\Delta t(j)$ intervals) are overlaid on the simulated $D_{\mathrm{inst}}(t)$ in Fig. 6.2c. Note that D_0 was given as an initial guess for

the first point of **X** and an estimated D_∞ was given as the initial guess for remaining points (dashed lines in Fig. 6.2c). Setting these initial guesses aids in stabilizing the inversion, as the L_2 norm in (6.2.10) is more likely to evolve monotonically; later points in **X** are 'pulled up' from D_∞, minimizing both the error term *and* the regularization term simultaneously to ultimately yield an apparent decay in $D_{\text{inst}}(t)$ starting from $\approx D_0$. Good agreement is observed between the simulations and the inversions even with relatively low SNR = 25, indicating the feasibility of estimating $D_{\text{inst}}(t)$ over a broad range of times from SG-TIETA decays, provided that (6.2.7) holds and the short-time regime is observed. See Supplement in Ref. [47] for inversion code as well an investigation of using different initial guesses.

6.3 Experimental findings

We now present experimental findings with the SG-TIETA method. Before studying a system with variation in $D_{\text{inst}}(t)$ (yeast suspensions), we first assess whether the method truly avoids off-resonance pathways by looking at data in simple liquids, for which the expected diffusion behavior is known: $-bD_0$. A variety of experimental data, including raw echo data, is presented which supports that SG-TIETA (largely) isolates the on-resonant signal.

6.3.1 Findings in simple liquids

Materials and methods

NMR methods were the same as previously described for the PM-10 system using the solenoid RF coil (see Fig. 3.7). Of note, hard RF pulses were used with duration $\tau_p = 1.6\ \mu$s. We acquired SG-TIETA decays using the timings given in (6.2.5), but extended up to $N = 40$ in some cases (not shown, see Supplement in Ref. [47]). Data was collected from twice-distilled water, decane (Sigma-Aldrich, St. Louis, MO, USA.), 1-octanol (Sigma-Aldrich), and dodecamethylcyclohexasiloxane. The liquids were transferred to 2 cm glass capillary sections (1.1 mm OD, Kwik-Fil™, World Precision Instruments, Inc., Sarasota, FL, USA) and the capillaries were sealed with a hot glue

Table 6.1: Relaxation times of simple liquids.

Sample	T_1 (ms)	T_2 (ms)
water	3250	133
decane	1340	166
octanol-1	440	217

gun. A CPMG measurement with $\tau_{\mathrm{CPMG}} = 48\ \mu$s was also acquired in 1-octanol in order to compare the SG-TIETA decays to the conventional SG-CPMG measurement. Both SG-TIETA and CPMG measurements utilized the standard two-step phase cycle of the first pulse between 0 and π [48]. Additional diffusion measurements to measure D_0 involved an SE diffusion encoding block followed by the usual CPMG readout (see methods surrounding Fig. 3.7). The value of τ was varied linearly over 22 points from $\tau_{\mathrm{min}} = 0.05$ ms to $\tau_{\mathrm{max}} = [1, 1, 2.2]$ for water, decane, and 1-octanol, respectively.

Relaxation

Note that T_2 relaxation will affect SG-TIETA decays. However, given the range of TEs (the longest TE_n are up to ~ 2 ms for the 1-octanol SG-TIETA decay), the effect of T_2 relaxation *between* echoes — which is what is ultimately fit — is small, and can, to a first approximation, be ignored. Relaxation times measured by inversion recovery and CPMG experiments are shown in Table 6.1. Note as well that TRs were variable between liquids, and chosen to be between $3-5\times$ the measured T_1 ($\mathrm{TR} = [10, 5, 2]$ s for water, decane, 1-octanol).

SG-TIETA vs. CPMG

We noted previously that if SG-TIETA truly avoids off-resonance pathways, then this would manifest itself as a narrower band of frequencies as n increases. That is, the slice would thin out in the spatial domain with each successive pulse, corresponding to a repeated convolution of the pulse spectrum. This would result in an *increasing echo width* in the time domain. This would not be the case for the CPMG experiment, wherein off-resonant pathways are expected to repeatedly refocus due to the equal

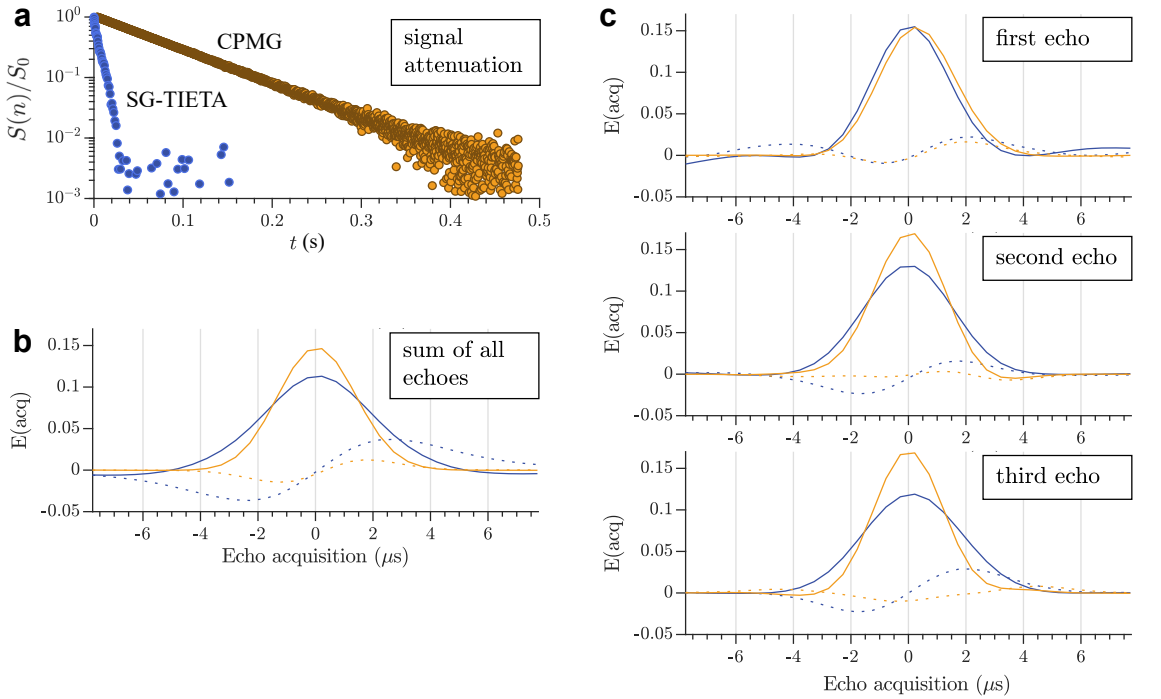

Figure 6.3: Comparison of the SG-TIETA (blue) — timings up to $N = 20$ are given in (6.2.5) — and CPMG (orange) for 1-octanol with 2τ = TE = 98 ms. (a) Comparison of the log-signal attenuation plotted vs. the total experiment time. (b) Overall echo shapes from summing all echoes ($N = 40$ for SG-TIETA, $N = 2000$ for CPMG). The real (solid lines) and imaginary (dotted lines) signal components are plotted, normalized by the area under the real signal curve in a 16 μs window. (c) Echo shape over the first three echoes. The CPMG echo width decreases with n and stabilizes around $n = 3$, consistent with the approach to asymptotic behavior described in Ref. [227]. In contrast, the SG-TIETA echo width *increases* and stabilizes around $n = 3$, consistent with isolation of the on-resonant signal or desired pathway.

inter-pulse intervals, bringing in potentially more signal from the sides of the slice (more frequencies). Indeed, the CPMG echo width has been reported to *decrease* with n and eventually stabilize, consistent with a wider observed frequency band, as described by Hürlimann & Griffin [227].

In Fig. 6.3, we experimentally verify these contrasting behaviors for the SG-TIETA and CPMG sequence in 1-octanol. The two decays are plotted vs. the overall experiment time in Fig. 6.3a. Note that the SG-TIETA decay is faster due to the increasing TE with n. Here, the SG-TIETA sequence was extended to $N = 40$ (timings not shown) to achieve complete decay of the signal for 1-octanol, which has a low diffusivity. These extended timings nonetheless satisfy the presented rules (1 – 6).

What is important to note here is the evolution of the echo shape. In Fig. 6.3b, we plot the echo shape over a 16 μs window (with a time resolution given by the dwell time of 0.5 μs), summing over all acquired echoes ($n = 2000$ for CPMG). Echo data was normalized such that the area under the real signal curve is 1. The SG-TIETA echo is wider than the CPMG echo, consistent with slice thinning and a loss of frequency content via avoidance of off-resonance pathways. Looking over the first three echoes in Fig. 6.3c is especially informative. The first echo is of course nearly identical, but the CPMG echo rapidly converges to a narrower shape, consistent with the behavior predicted by Hürlimann & Griffin [227], whereas the SG-TIETA echo widens. This investigation provides experimental confirmation of the signal-isolating properties of the SG-TIETA sequence.

It may also be informative to look at the raw SG-TIETA signal. Recall that the sequence is designed in such a way that unwanted pathways refocus at an offset of at least $\delta/2 = 7$ μs away from the desired pathway. Thus, we would expect that there is variation in the signal intensity in the time *between* echoes, consistent with coherent refocusing of these unwanted pathways. In Fig. 6.4, we show the raw echoes for an SG-TIETA decay in 1-octanol, stitched together in 16 μs windows. If, indeed, unwanted pathways refocus ≥ 7 μs away from the desired coherence, then there should be high variation in the intensities at the edge of this window ± 8 μs. In the zoomed plot in Fig. 6.4, we can see clearly that this is the case, with variation (up to approx 0.05, or $\sim 2\%$ of the signal) seen at the edges of adjacent windows. This serves as another indication that the sequence avoids pathways.

Measuring the pulse accuracy

We next look at the estimated pulse accuracy $A_p(n)$ from SG-TIETA decays of water, 1-octanol, and decane. To do so, we compare SG-TIETA decays to what would be expected given Gaussian diffusion and the values of TE_n (6.2.5). Dividing the observed decay between each echo by the *expected* decay according to $\exp(-bD_0)$ yields the decay due to pulse (in-)accuracy, i.e., the additional loss of signal due to the pulse and which captures the effect of avoiding off-resonance pathways. Dividing

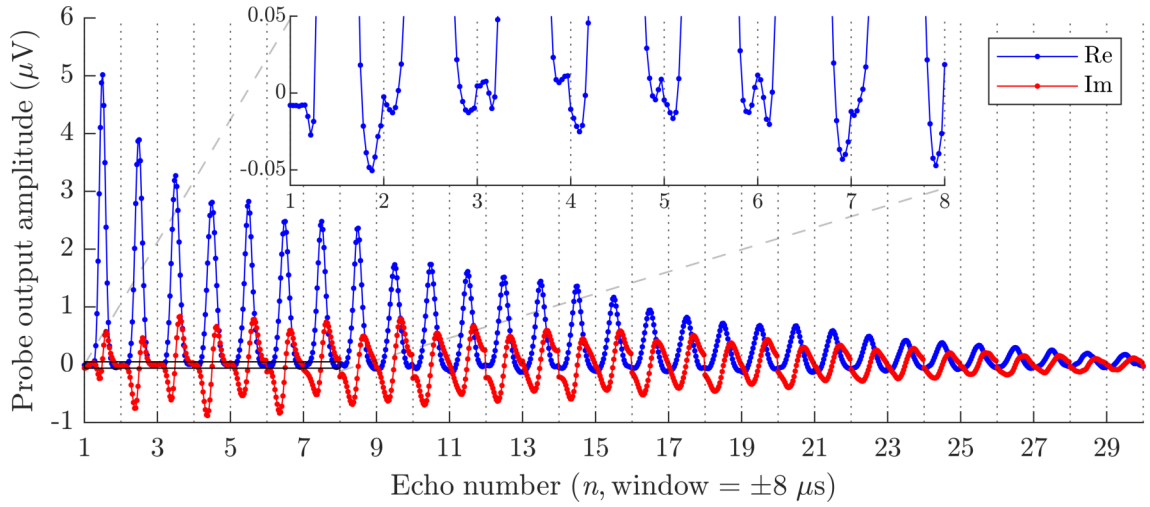

Figure 6.4: Exemplar SG-TIETA echo decay for 1-octanol up to $n = 29$. Real (blue) and imaginary (red) signal is shown in raw probe amplitude units. Echoes are stitched together in 16 μs windows and splotted by echo number n. The interval between 1 and 2, for example, corresponds to the first echo with TE_n. Zoomed inset highlights amplitude variations at the edges of the echoes which may arise from avoided pathways refocusing at least $\delta/2 = 7$ μs away from the desired pathway.

by adjacent echoes then yields $A_p(n)$, or the loss in signal after the nth pulse. In Fig. 6.5, $A_p(n)$ is estimated in this way from SG-TIETA decays in 1-octanol (magenta), decane (blue), and water (black).

In Fig. 6.5a, the observed SG-TIETA decay normalized to the first echo $S(n)/S_0$ is plotted alongside the expected decay $\exp(-bD_0)$ according to diffusivities measured by separate SG-SE experiments: $D_0 = 2.22 \pm 0.01, 1.27 \pm 0.01, 0.121 \pm 0.002$ $\mu\mathrm{m}^2/\mathrm{ms}$ for water, decane, and 1-octanol, respectively. SG-TIETA decays were averaged 32× to boost SNR. An inset shows the first 6 echoes. In Fig. 6.5b, the ratio is plotted. We find that the behavior is highly consistent across all three liquids studied (despite the vastly different D_0), suggesting that the additional decay seen in SG-TIETA experiments is not diffusion-weighted, i.e., not weighted by off-resonance pathways such as STEs. This, as well as previous results (Figs. 6.3, 6.4) confirms the avoidance of unwanted pathways. An inset shows a cubic spline fit to further highlight the similarity between liquids.

Finally, the estimated $A_p(n)$ is calculated by dividing adjacent values in Fig. 6.5b (not fitted values), and is plotted in Fig. 6.5c. If $A_p(n)$ corresponds to repeated

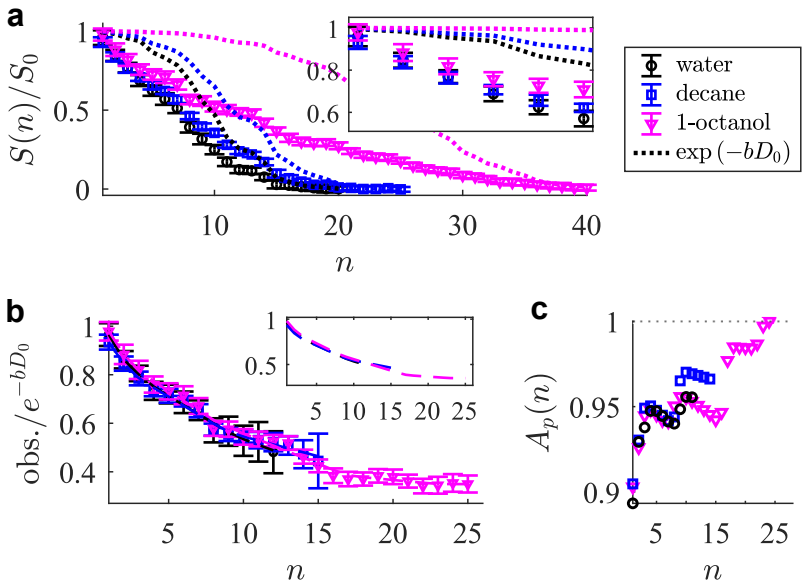

Figure 6.5: SG-TIETA decays and estimation of $A_p(n)$ using pure liquids. (a) Observed SG-TIETA decays compared to $\exp(-bD_0)$. D_0 was measured using an SG-SE sequence (see methods text) in legend order as $2.22 \pm 0.01, 1.27 \pm 0.01, 0.121 \pm 0.002\ \mu m^2/ms$. Error bars = ±1 SD for 25, 38, 70 repetitions, respectively. Each repetition consisted of a 32× average. (b) The ratio of the observed SG-TIETA decay vs. $\exp(-bD_0)$ truncated once the signal reached the noise floor at $n = 12, 15, 25$, respectively. Inset shows cubic spline fits. (c) $A_p(n)$ approximated using adjacent fitted ratios.

convolution of a pulse spectrum, it should monotonically increase towards 1. That is, the slice should approach some asymptotic shape or bandwidth where effectively all of the signal is on-resonance, consistent with the approach to a stable echo shape seen in Fig. 6.3b. This approximate behavior is observed, although some degree of non-monotonic variation with the echo number n remains for all three liquids studied. This may indicate that some pathways are not fully avoided and may re-converge with the desired pathway ($\sum \Delta F(t) = 0$) at some later echo, leading to jaggedness in $A_p(n)$. Of course, the presented rules (1 – 6) do not exhaustively avoid unwanted pathways (which would be nearly impossible for longer sequences), so some imperfections are expected due to the refocusing of pathways of a higher order than 4. Nonetheless, we can, from these estimates of $A_p(n)$, yield the calibration $\prod_{j=1}^{n} A_p(n)$ (6.2.4) necessary to study SG-TIETA decays with these effects removed, leaving primarily the effect of diffusion weighting in the intended pathway. This then

permits the study of $D_{\text{inst}}(t)$ in heterogeneous systems such as yeast via the inversion described in 6.2.10, which we present in the following section.

6.3.2 Findings in yeast

In this section, we estimate $D_{\text{inst}}(t)$ in yeast as well another simple liquid that was not previously studied to validate that a flat $D_{\text{inst}}(t)$ is produced in this case. If a flat curve is produced, this suggests that $\prod_{j=1}^{n} A_p(n)$ is an accurate correction.

Materials and methods

Another simple liquid, dodecamethylcyclohexasiloxane (D6, kinematic Viscosity = 6.6 cSt at 25 °C, Gelest, inc. Morrisville, PA, USA), was studied and prepared in the same manner as previous simple liquids. For measurements on yeast (*S. cerevisiae*), 1.72 g of dry yeast was mixed in 10 ml of tap water and stored in a 50 ml tube with the lid screwed on loosely to allow gas to escape. After three days (72 hr), the yeast was re-suspended and samples were taken for NMR experiments and for cell density measurement. The density of the first sample (yeast #1) was measured to be 2.84×10^9 cells/ml using a hemocytometer. The remaining yeast was centrifuged, the pellet was re-diluted to 2× the initial concentration, and a second sample (yeast #2) was taken for NMR experiments. Immediately prior to experiments, yeast was transferred to 2 cm KrosFlow® Implant Membrane sections (500 kDa molecular weight cut off, 1 mm outer diameter, SpectrumLabs, Waltham, MA, USA) and the membranes were sealed by pinching the membrane with heated forceps. Yeast was kept from drying out by performing measurements immediately upon filling and sealing the capillary and by lining the inside of the chamber with wet tissue paper to increase humidity.

SG-TIETA decays using the timings given in (6.2.5) were acquired and averaged 32×. For the data analysis, we used the $A_p(n)$ values from 1-octanol in Fig. 6.5 to calibrate the SG-TIETA decays, i.e., dividing by $\prod_{j=1}^{n} A_p(j)$, such that (predominantly) the effects of diffusion remain. Given the shorter T_2 in yeast, however, some T_2 effects may also be present between echoes, particularly for the higher cell density sample. Calibrated SG-TIETA decays can then be fit using (6.2.10), yielding estimates

Table 6.2: Relaxation times in yeast and D6.

Sample	T_1 (ms)	T_2 (ms)
D6	788	292
yeast #1 (2.84×10^9 cells/mL)	625	59
yeast #2 (5.68×10^9 cells/mL)	319	41

of $D_{\text{inst}}(t)$. Relaxation times are presented in Table 6.2. The TR was was [10, 2, 2] s for water, yeast, and D6, respectively. The number of repetitions was [38, 3, 4, 25] for water, yeast #1, yeast #2, and D6, respectively.

Due to noise and variation in $A_p(n)$ dominating the decay behavior for small n (i.e., low diffusion weighting), the SG-TIETA decays were also constrained to monotonically decrease by fitting to a piecewise linear function over each interval, with the slopes constrained to be strictly decreasing [235] — see Ref. [47] for details. Total measurement time for the yeast samples was ≈ 10 min, taking into account the $32\times$ averaging.

Results

In Fig. 6.6a, we present the SG-TIETA decays normalized by $\prod_{j=1}^{n} A_p(j)$ from the 1-octanol data in Fig. 6.5 and averaged over experimental repetitions. The inter-echo decays, which are what is fit in (6.2.10), are shown in the inset. The estimated $D_{\text{inst}}(t)$ from an LLS inversion (6.2.10) are shown in Fig. 6.6b. As stated before for Fig. 6.2, initial guesses were provided of D_0 for the first point in $\mathbf{X}$ and some D_∞ for the remaining points (dashed lines). For yeast #1 and yeast #2, initial guesses of $D_0 = 2.22$, $D_\infty = [0.9, 1.1]$ μm^2/ms, respectively, were provided. For D6, SG-SE diffusion measurements were used to estimate D_0, and this was given as the guess for D_0, D_∞: for D6, $D_0 = D_\infty = 0.114$ μm^2/ms, for water $D_0 = D_\infty = 2.22$ μm^2/ms. The same regularization parameter $\lambda = 2\times10^{-6}$ was used as in Fig. 6.2.

Importantly, $D_{\text{inst}}(t)$ for water and D6 are correctly estimated as having no time-dependence by the inversion and have mean values $\bar{\mathbf{X}}$ nearly identical to the measured diffusivities, suggesting that the $\prod_{j=1}^{n} A_p(j)$ correction removed effects other than

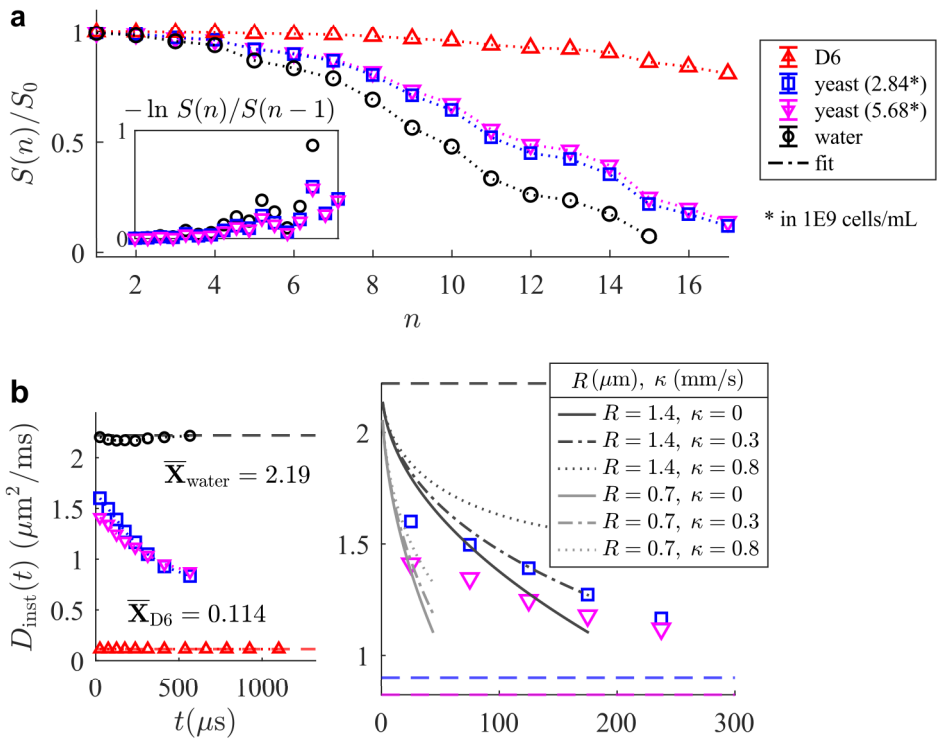

Figure 6.6: SG-TIETA decays and inverted **X** for D6, yeast, and water. (a) Decays analyzed and calibrated by $A_p(n)$ as described in the text. Data shown are the means of [38, 3, 4, 25] repetitions truncated at $N = [34, 17, 17, 15]$, in legend order. (b) Inverted values of $D_{\text{inst}}(t)$ over each interval $\Delta t(j)$, **X** in (6.2.10). Inversion parameters were identical to Fig. 6.2 other than $\Delta t(j)$ for D6, which was lengthened. For yeast #1 and yeast #2, initial guesses of $D_0 = 2.22$, $D_\infty = [0.9, 1.1]$ μm^2/ms, respectively, were provided. For D6 and water: $D_0 = D_\infty = 0.114$ μm^2/ms and $D_0 = D_\infty = 2.22$ μm^2/ms, respectively. Zoomed plot compares the yeast values to the predicted short-time $D_{\text{inst}}(t)$ (6.2.9) for different parameter values.

diffusion, despite being generated from a different set of data in 1-octanol. In yeast, $D_{\text{inst}}(t)$ is estimated to have rapidly decreased from D_0 over the initial points, after which the decay slows down, bearing similarity to the simulated data in Fig. 6.2 and to the expected behavior of $D_{\text{inst}}(t)$ in heterogeneous systems in general [89]. For comparison, we also show in the zoomed plot the predicted $D_{\text{inst}}(t)$ from (6.2.9) — i.e., the short-time limit [2] with a permeability correction [88] — for two values of $R = 3V/S = [0.7, 1.4]$ μm and several values of κ. The deviation of the estimated $D_{\text{inst}}(t)$ from the prediction indicate that we likely are not able to probe, truly, within this universal short-time limit, even in this sub-millisecond range. Nonetheless, the

separation between the two yeast samples at short times seems to suggest a difference in the SVR by a factor of $\sim 2\times$, consistent with the doubling in cell density between the two samples. These approximate cell radii $R \sim 0.5 - 2.5\ \mu$m agree with other diffusion MR studies of yeast at similar densities [11, 133, 236–238].

6.4 Discussion

While the yeast results appear to be consistent with previous reports, we note that the results may be affected by T_2. In particular, we measured a small (5%) water population in yeast by relaxometry methods that had a very fast $T_2 \sim 500\ \mu$s, which could potentially confound these results [47]. Relaxation effects are not accounted for by $A_p(n)$ and may lead to a slight overestimation in the decay of $D_{\text{inst}}(t)$. Furthermore, we stress once again that the inversion approach assumes that each inter-echo interval is an independent measurement of $D_{\text{inst}}(t)$ (6.2.7), i.e., we assume that the decay behavior is invariant with n. This, of course, is not actually the case, and the later intervals may become increasingly weighted towards smaller components or components with a longer T_2. Thus, these results in yeast fall short of being quantitative and should be regarded as apparent estimates of $D_{\text{inst}}(t)$. Despite these shortcomings, it remains clear that SG-TIETA and this LLS inversion approach were able to probe differences between the two yeast cell densities that were approximately consistent with the expected trend of a doubled SVR.

These results serve as an initial proof-of-principle of the SG-TIETA method and suggest that time-dependent diffusion can be probed over very short, sub-millisecond times from (averaged) single-shot decays, overcoming challenges with conventional TDS experiments [68]. In addition, we demonstrate that the advantages of a CPMG-styled sequence under an SG can be leveraged whilst ostensibly avoiding the majority of off-resonance effects. Indeed, the methods and timing principles developed in Sec. 6.2.1 may be the more interesting finding of this chapter, and illustrate how off-resonance pathways can be systematically considered and duly avoided in the context of this experiment. Correcting for or avoiding such pathways remains, to this day, a challenging problem in the application of TDS using SG-CPMG sequences

[232]. Elements of the SG-TIETA sequence may suffice to improve the current state-of-the-art. For instance, just incorporating the first rule, where the refocusing pulse timings are offset by δ with $(\tau \bmod \delta) = \delta/2$ — thereby eliminating pathways arising from magnetization not excited by the first $90°$-pulse — may improve SG-CPMG experiments considerably.

This investigation also demonstrates the utility of the time-dependent signal representations summarized in Table 2.6 and developed by Ning *et al.* [65]. The typical frequency-domain representation (2.2.24) used by essentially all TDS studies [68, 225] to this point is seen to be experimentally constrictive. One does not, necessarily, need to probe time-dependent diffusion at a single timescale or frequency to yield useful information. Indeed, *any* pulse sequence (provided that the GPA and mass balance hold) will have some weighting in the time domain and can be considered as a measurement of $D_{\text{inst}}(t)$, characterized by the cumulative gradient autocorrelation $C(t)$. Even a sequence with broad time-domain weighting(s) like the SG-TIETA sequence is shown to be able to produce robust estimates of $D_{\text{inst}}(t)$ (in simulated data, Fig. 6.2) by concatenating data from various effective TEs. This leads us into the future directions for our work, the most notable of which is a bridging of time-dependent diffusion and exchange.

7
Future Work and Conclusions

7.1 Revisiting the 'curvature' method 199
7.2 Further experiments 203

In this final chapter, we present some preliminary insights regarding exchange, time-dependent diffusion, non-Gaussian diffusion, and how these are all linked. We also mention ongoing or planned work, both *in vivo* (pre-clinical) and *ex vivo* (PM-10), and provide concluding remarks.

7.1 Revisiting the 'curvature' method

Exchange and time-dependent diffusion are typically measured and analyzed using separate paradigms, namely DEXSY and TDS, respectively. From a theoretical point-of-view, however, exchange and $D_{\text{inst}}(t)$ are intrinsically linked and exchange is a fundamental and inextricable part of what determines the behavior in $D_{\text{inst}}(t)$ [88, 113]. Exchange *is* time-dependence. It is natural to ponder, therefore, how the curvature method relates to measuring $D_{\text{inst}}(t)$ and in particular what timescales the exchange-weighted difference $S_{\text{end}} - S_{\text{mid}}$ (which is proportional to the curvature along b_d at a given t_m) measures.

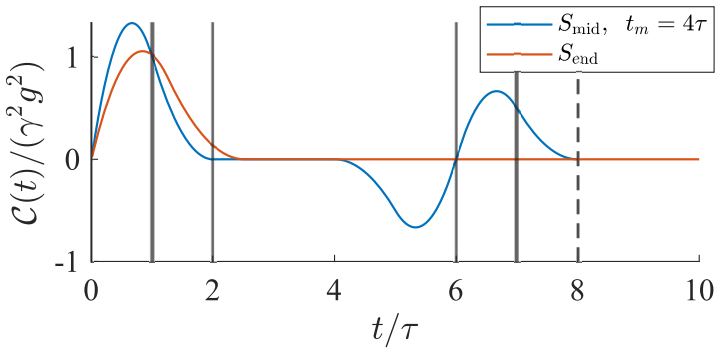

Figure 7.1: Calculated $C(t)$ for the S_{mid} and S_{end} acquisitions in an SG-DEXSY experiment with encoding time τ for S_{mid}, and $t_m = 4\tau$. Pulses are indicated by gray lines (thicker lines correspond to refocusing pulses). The exchange signal as measured, for example, by $\ln S_{\text{mid}}/S_{\text{end}}$, is seen to be a measurement in the slope of $D_{\text{inst}}(t)$, shedding new light on our exchange measurement.

Curvature in the time domain

The $C(t)$ for S_{end}, presuming $b_2 \approx 0$, has already been calculated (2.2.34) for the SG-DEXSY experiment. Let us calculate the $C(t)$ for an S_{mid} acquisition (i.e., equal b-values and encoding time τ). We obtain:

$$C_{\text{mid}}(t) = \gamma^2 g^2 \begin{cases} t\,(-3t+4\tau) & 0 \le t < \tau \\ t\,(t-4\tau)+4\tau^2 & \tau \le t < 2\tau \\ 0 & 2\tau \le t < t_m \\ t\left(-\frac{1}{2}t+t_m\right)-\frac{1}{2}t_m^2 & t_m \le t < t_m+\tau \\ t\left(\frac{3}{2}t-3t_m-4\tau\right)+\left(\frac{3}{2}t_m+\tau\right)(t_m+2\tau) & t_m+\tau \le t < t_m+2\tau \\ t\left(-\frac{3}{2}t+3t_m-8\tau\right)-\left(\frac{3}{2}t_m+5\tau\right)(t_m+2\tau) & t_m+2\tau \le t < t_m+3\tau \\ t\left(\frac{1}{2}t-t_m-4\tau\right)+\left(\frac{1}{2}t_m+2\tau\right)(t_m+4\tau) & t_m+3\tau \le t < t_m+4\tau \end{cases} . \quad (7.1.1)$$

In Fig. 7.1, we plot the $C(t)$ for S_{mid} as compared to S_{end} for the case of $t_m = 4\tau$ and on a normalized $C(t)/G^2$ axis. We see that taking the log of the signal difference $S_{\text{end}} - S_{\text{mid}}$ (i.e., $\ln S_{\text{end}}/S_{\text{mid}}$) will approximately cancel the short-time lobe and leave just the positive and negative lobes on either side of $t = 2\tau + t_m$. Note that in the case of a PG experiment where g is varied, perfect cancellation would be achieved. Note as well that taking the difference will flip the signs so that the lobe at shorter times is positive. This measurement can thus be thought of as *approximating the slope*

in $D_{\text{inst}}(t)$ *at* $t = (2\tau + t_m)$, or, equivalently, the curvature in the MSD. This sheds an entirely new light on the measurement of exchange using the curvature method.

The curvature method, however S_{mid} is chosen to be normalized, is seen to be equivalent to probing $\partial_t D_{\text{inst}}(t)$ at longer and longer times as t_m is increased. We thus bridge the notions of exchange (as measured in this way) and time-dependent diffusion, and can bring to bear the body of theoretical work studying $D_{\text{inst}}(t)$ to interpret our measurements, in particular work by Novikov [89] on structural disorder. This framing of our measurement clarifies how we were able to measure fast exchange times *in vivo* in Chapter 5 ($\tau_k \lesssim 5$ ms), despite such an exchange time indicating near complete mixing during the encoding and minimum mixing time ($\Delta = 8.5$ ms, $t_m = 5$ ms). It may be that $D_{\text{inst}}(t)$ continues to decay exponentially over intermediate timescales even after mixing, and the rate of this decay is what our measurements were probing, rather than exchange in a barrier-limited sense *per se*. Taking into consideration the exponential time-dependence in the exchange signal seen throughout this thesis in Chapters 3, 4, 5 — rather than some form of power-law behavior — this suggests that exponential decay in $D_{\text{inst}}(t)$ is a general feature across the specimen studied, at least for the chosen experimental parameters. Therefore, the disorder of the medium might best be described as periodic domains, which are expected to produce such an exponential and rapid decrease in $D_{\text{inst}}(t)$ (see Ref. [89], Eq. S25).

Periodic domains

More specifically, for periodic barriers separated by some distance a in 1D and with permeability κ, Novikov [89] found that

$$D_{\text{inst}}(t) = D_\infty + D_0 \sum_{n=1,3,\ldots} \frac{\zeta^2 \exp(-t/t_n)}{1 + \zeta + (\zeta k_n a/2)^2}, \quad t_n = \frac{1}{D_0 k_n^2}, \tag{7.1.2}$$

where $\zeta = \ell_\kappa a$ characterizes the ability of barriers to impede diffusion, $\ell_\kappa = D_0/\kappa$, and k_n are the positive roots of $\cos k_n a = \cos qa + k_n \ell_\kappa \sin \kappa a$, where $q = \delta G/2\pi$. Although this theory was developed with the narrow pulse approximation (i.e., assuming $\delta \ll \Delta$), the general principle applies. If the domains are periodic, then spins do not need to

sample the whole domain to reach D_∞, and the approach to D_∞ proceeds rapidly (i.e., exponentially), as above. Such behavior is also predicted directly by the Ornstein-Uhlenbeck model of diffusion [65, 239, 240]. On the other hand, for a disordered medium, spins must sample the whole volume in order to truly reach D_∞, and some long-time dependence, taking the form of a power-law tail, is to be expected [89].

Our data throughout Chapters 3, 4, 5 appears to be consistent with periodic domains, and little to no signal variation indicative of power-law scaling was seen at longer t_m values. However, it may be the case that at even longer t_m, such behavior would emerge. We generally did not probe $t_m > 400$ ms and the longest t_m probed were in Chapter 4, where we acquired up to $t_m = 1$ s for the distributed $P(\tau_k)$ results (e.g., Fig. 4.8). Indeed, we should note that the exchange-weighted decays in this work generally did not reach 0, which would correspond, according to Fig. 7.1, to $\partial_t D_{\text{inst}}(t) = 0$, and thus $D_{\text{inst}}(t) = D_\infty$ (if the GPA holds). Therefore, the signal floor(s) estimated in Chapter 4 may in fact correspond to some long-time, power law behavior, which we chose to subtract out of the signal and are thus insensitive to.

This leads to a different possible interpretation of the slow peak in the distributions $P(\tau_k)$ presented in Chapter 4. It is perhaps the case that the fast peak corresponds to the initial exchange between approximately periodic domains and an external space (ECS), while the slow peak may represent an additional power-law tail due to structural disorder of the overall medium (i.e., a deviation from periodic domains), rather than a different set of structure(s) with smaller SVRs such as soma, as we speculated. Such power law behavior would merely be approximated by the ILT, leading to a broad peak, similar to how restriction and $b^{1/3}$ scaling was seen to result in broadened peak(s) in ILT-derived spectra, as shown in Chapter 3 (Sec. 3.4, Fig. 3.13). The broadness and less consistent location of this slower peak (e.g., as seen in Fig. 4.8) can perhaps be explained in a similar manner, i.e., the signal behavior is better explained by a power law. While we have not yet explored these hypotheses in detail, the benefits of being able to potentially link our data to the wealth of literature on time-dependent diffusion — which we referenced throughout Chapters 2, 6 — are clear, and open the door to different possible explanations of our data.

Localization?

Of course, the above only holds if the GPA holds, which may break down if localized signal is present. Generally speaking, we found throughout that higher b-values in the regime of $\ell_d > \ell_g$ were necessary to achieve maximal exchange weighting (see, for instance, Figs. 3.8, 5.4). More specifically, $\ell_d \approx 2\ell_g$ was found to be optimal for measuring exchange. Unfortunately, the use of high b-values leads invariably to the possibility of localized signal behavior ($\ell_g < \ell_s < \ell_d$), which we have pointed out as a caveat throughout this thesis. However, localization can also be seen as a *beneficial* phenomenon [74, 80, 81, 152]. To quote Grebenkov [152]: "[localization] makes the signal more sensitive to the boundaries and thus opens new ways of probing the microstructure." Indeed, for localized signal, the dominant effect on the signal may be exchange.

Given that the possibility of localized signal appears to be unavoidable when choosing b-values with maximal exchange weighting and CNR, incorporating localization into signal models of exchange in a rigorous manner represents another promising direction of theoretical development, though stands somewhat in contrast to the GPA-based signal models used above. In our own work, we have recently begun to study whether localization or motional averaging are better explanations of the weakly-attenuating signal tissue by using permanent magnets with different gradient strengths or ℓ_g (see our recent publication, Ref. [44]). We find, preliminarily, that localized signal is likely to be present in our studies of exchange in *ex vivo* spinal cord, constituting an important effect at the b-values used. These findings highlight the need to better understand how localization interacts with exchange at short- to intermediate timescales.

7.2 Further experiments

In addition to the above theoretical developments, further experimental work is also currently being undertaken or is planned.

Active exchange

While we have shown that active exchange exists, the biological substrates remain unclear. We hypothesized that active exchange is linked to water cotransport and/or osmotic gradients induced by ion cotransport. To further test these hypotheses, we can selectively knockdown such cotransporters, rather than knocking out activity and/or the resting membrane potential as a whole as we did with ouabain and the oxygen-glucose deprivation experiments. We could, for instance, target specific neurotransmitter systems, such as the AMPA receptor system, which mimics glutamate and results in partial inhibition of activity [186]. We have obtained preliminary results on the PM-10 system studying live spinal cord which indicate that the AXR is in fact decreased upon the introduction of AMPA, further supporting the existence of active exchange. At the same time, we can study these effects in tandem with osmolarity perturbations using impermeant solutes such as sucrose, as we did in Chapter 4, to try and disambiguate the mechanisms of direct, ion co-transport vs. osmotic gradients.

In vivo imaging

We mentioned in Chapter 5 that sequence developments were ongoing with regards to measuring exchange *in vivo* in mouse brain. We also mentioned our intent to study the effects of AQP4 inhibition. If these sequence improvements and AQP4 studies turn out to be fruitful, we could later look at perturbations to activity *in vivo* (e.g., stroke models) and observe whether the AXR is more sensitive than the ADC — as it appeared to be for the results in Chapter 4, Sec. 4.2. These studies would represent an important step towards ascertaining whether exchange is linked to activity *in vivo* and towards assessing the clinical utility of our methods. That is, can these methods measure active exchange without the unique capabilities of the PM-10 system? Or are these effects only visible due to the uniqueness of the PM-10, and disappear upon the usage of longer diffusion times and weaker gradients? While the pre-clinical rodent imaging system is still very different from clinical systems (much higher $g_{\max}$), this would be a first step towards potential clinical studies and work is ongoing towards this end.

Another interesting direction is to vary the direction of diffusion encoding to probe exchange in anisotropic systems, namely WM. Some work has been performed along these lines [124, 241] that indicate that the AXR does depend on the direction of encoding, with faster exchange being observed when the gradients are oriented perpendicular to the enclosing structure. One might envision a tensor exchange quantity that could serve, perhaps, to distinguish ambiguous WM structures such as crossing vs. kissing fibers.

Validating exchange measurements

While the curvature method was validated in Chapter 3 using a microcapillary system (Sec. 3.3.2), exchange in heterogeneous systems was not characterized with a phantom study in this thesis. Given the results in Chapter 4 which suggest the presence of multiple exchange components, phantom or even simulation studies which could replicate such heterogeneous exchange characteristics would be a valuable validation of our methods. Recent work has aimed to develop such exchange phantoms from hollow fiber fabrication methods [242]. Simpler approaches using yeast cells, as we did in Chapter 6, may also be pursued [243].

Developing SG-TIETA

The inversion approach used for the SG-TIETA data [47] can be considered incomplete. Really, one would need to calculate the $C(t)$ arising from the whole of the modulated triangle-wave in $F(t)$ with its evolving TEs. While this would be challenging, it also represents an interesting measurement that spans very short ($< 100\,\mu$s) to rather long timescales (> 100 ms) all at once — see Fig. 6.3a. The sequence itself is ostensibly capable of following the on-resonant signal over a very large number of sequential diffusion encodings ($N \geq 40$) such that, perhaps the whole of the short- ($\sim D_0$) to long-time ($\sim D_\infty$) diffusion behavior could be observed in such a measurement. The inversion could also be improved by collecting SG-TIETA data with different timings (i.e., different lists of integer offsets m_n), and then collating these data such that the timescales probed are in effect more finely sampled due to the staggered lists.

Development of SG-TIETA sequence variants and studies of polymer systems and other samples using SG-TIETA are ongoing in Dr. Basser's lab.

Final remarks

We set out at the beginning of this thesis 'In Search of Lost Time', meaning we wanted to probe diffusion as it is — time-dependent — and to make such measurements as time-efficient as possible. To that end, we have developed a method to measure exchange which, to our knowledge, is the fastest such diffusion MR measurement in the literature. The method is based on the relatively simple principle that, by holding the *total* diffusion weighting constant and varying the measurement time, the difference between two such signals isolates exchange. As a result of these and other methodological developments, we have been able to show that exchange in tissue is linked to activity, paving the way for exciting future developments and potential applications. As well, we have developed a means to probe the time-varying diffusivity from just a single signal decay. We hope that these methods can, in time, help to reveal interesting biological phenomena.

Appendices

A
Additional derivations

In Sec. 2.2, we presented several models for the diffusion attenuation S/S_0 in terms of time-dependent transport quantities such as the mean-squared displacement (MSD) and the instantaneous diffusivity $D_{\text{inst}}(t)$. Here we provide additional derivations for these expressions, particularly (2.2.27) and (2.2.29), which are summarized in Table 2.6. These derivations follow the supplement of the original work by Ning *et al.* [65] though are expanded in detail here for clarity.

Mean-squared displacement and gradient autocorrelation

We will first derive the signal representation in terms of the MSD. Let us begin by writing the MSD between times t' and t:

$$\langle [r(t) - r(t')]^2 \rangle = \langle r^2(t) \rangle - 2\langle r(t) r(t') \rangle + \langle r^2(t') \rangle, \tag{A.1}$$

and by stationarity we also have

$$\langle [r(t) - r(t')]^2 \rangle = \langle [r(|t-t'|) - r(0)]^2 \rangle = \langle r^2(|t-t'|) \rangle, \tag{A.2}$$

where, by self-normalization, we may say that $r(0) = 0$ for each spin isochromat. Combining the above, we may write the position autocorrelation as:

$$\langle r(t) r(t') \rangle = \frac{1}{2} \left[\langle r^2(t) \rangle + \langle r^2(t') \rangle - \langle r^2(|t-t'|) \rangle \right]. \tag{A.3}$$

By the echo condition $F(t = \mathrm{TE}) = 0$, we have that

$$\int_0^{\mathrm{TE}} G(t)\langle r^2(t)\rangle G(t')dt = \int_0^{\mathrm{TE}} G(t)\langle r^2(t')\rangle G(t')dt' = 0, \tag{A.4}$$

which leaves only the $\langle r^2(|t-t'|)\rangle$ term upon substitution of (A.3) into (2.2.20),

$$\frac{S}{S_0} = \exp\left(\frac{1}{4}\int_0^{\mathrm{TE}}\int_0^{\mathrm{TE}} G(t)\langle r^2(|t-t'|)\rangle G(t')dt\,dt'\right). \tag{A.5}$$

Recall that the general goal is to get this double integral representation to collapse into a single integral. To do so, we can perform a series of substitutions. We first split the integral into two parts, from $t = [0, t']$ and then from $[t', \mathrm{TE}]$

$$\begin{aligned}&\int_0^{\mathrm{TE}}\int_0^{\mathrm{TE}} G(t)\langle r^2(|t-t'|)\rangle G(t')dt\,dt' \\ &= \int_0^{\mathrm{TE}}\int_0^{t'} G(t)\langle r^2(t'-t)\rangle G(t')dt\,dt' + \int_0^{\mathrm{TE}}\int_{t'}^{\mathrm{TE}} G(t)\langle r^2(t-t')\rangle G(t')dt\,dt'.\end{aligned} \tag{A.6}$$

For the second integral on the right-hand-side, let $u = \mathrm{TE} - t$ and $u' = \mathrm{TE} - t'$ and perform a change of variables,

$$\int_0^{\mathrm{TE}}\int_{t'}^{\mathrm{TE}} G(t)\langle r^2(t-t')\rangle G(t')dt\,dt' = \int_0^{\mathrm{TE}}\int_0^{u'} G(\mathrm{TE}-u)\langle r^2(u'-u)\rangle G(\mathrm{TE}-u')du\,du'. \tag{A.7}$$

Therefore (A.6) can be re-grouped into the same integral as follows:

$$\int_0^{\mathrm{TE}}\int_0^{t'} \langle r^2(t'-t)\rangle \left[G(t)G(t') + G(\mathrm{TE}-t)G(\mathrm{TE}-t')\right] dt\,dt'. \tag{A.8}$$

Changing the order of integration yields

$$\int_0^{\mathrm{TE}}\int_t^{\mathrm{TE}} \langle r^2(t'-t)\rangle \left[G(t)G(t') + G(\mathrm{TE}-t)G(\mathrm{TE}-t')\right] dt'\,dt. \tag{A.9}$$

Now, let $s = t' - t$, i.e., we integrate along the level set of $t' - t$:

$$\int_0^{\mathrm{TE}}\int_0^{\mathrm{TE}-t} \langle r^2(s)\rangle \left[G(t)G(t+s) + G(\mathrm{TE}-t-s)G(\mathrm{TE}-t)\right] ds\,dt. \tag{A.10}$$

At this point, we note that $\langle r^2(s)\rangle$ is simply the MSD and depends only on s. We can again swap the order of integration such that

$$\int_0^{\mathrm{TE}} \langle r^2(s)\rangle \int_0^{\mathrm{TE}-s} \left[G(t)G(t+s) + G(\mathrm{TE}-t-s)G(\mathrm{TE}-t)\right] dt\,ds, \tag{A.11}$$

which pulls out the MSD from the inner integral. Finally, we consider that in

$$\int_0^{\mathrm{TE}-s} [G(t)G(t+s)+G(\mathrm{TE}-t-s)G(\mathrm{TE}-t)]\,dt,$$

each of the gradient products contains two terms shifted between one another by s. The first product is integrated over $t=[0,\mathrm{TE}-s]$ while the second is integrated over $t=[\mathrm{TE}-s,0]$. Therefore, the two terms are equal and simply evaluated in opposite directions. That is,

$$\int_0^{\mathrm{TE}-s} [G(t)G(t+s)+G(\mathrm{TE}-t-s)G(\mathrm{TE}-t)]\,dt = 2\int_0^{\mathrm{TE}-s} G(t)G(t+s)dt. \quad \text{(A.12)}$$

Note that $s=t'-t\in[-\mathrm{TE},\mathrm{TE}]$ such that the interval $t=[0,\mathrm{TE}-s]$ is equivalent to $[0,2\mathrm{TE}]$. If we assume that $G(t)=0$ for $t\geq\mathrm{TE}$ then we can simply change the integration bounds to be over $[0,\mathrm{TE}]$. Thus, we arrive at (2.2.27) by substituting the above times the MSD back into (A.5), reproduced here:

$$\frac{S}{S_0}=\exp\left(\frac{1}{2}\int_0^{\mathrm{TE}}\langle r^2(t)\rangle\mathcal{G}(t)dt\right),$$

where

$$\mathcal{G}(t)=\int_0^{\mathrm{TE}} G(s)G(s+t)ds$$

Instantaneous diffusivity and cumulative gradient autocorrelation

To arrive at (2.2.29) which is written in terms of $C(t)$ and $D_{\mathrm{inst}}(t)$, we simply integrate the above (2.2.27) by parts, yielding, for the term inside the integral:

$$\int_0^{\mathrm{TE}}\langle r^2(t)\rangle\mathcal{G}(t)dt=\langle r^2(t)\rangle\int_0^{\mathrm{TE}}\mathcal{G}(t)dt-\int_0^{\mathrm{TE}}\partial_t\langle r^2(t)\rangle\int_0^{\mathrm{TE}}\mathcal{G}(t')dt'\,dt. \quad \text{(A.13)}$$

By the echo condition $F(\mathrm{TE})=0$, the gradient autocorrelation integrates to 0 such that the first term on the right-hand-side vanishes. Substituting the definition of $D_{\mathrm{inst}}(t)=\frac{1}{2}\partial_t\langle r^2(t)\rangle$ yields

$$\int_0^{\mathrm{TE}}\langle r^2(t)\rangle\mathcal{G}(t)dt=-2\int_0^{\mathrm{TE}}D_{\mathrm{inst}}(t)\rangle\int_0^{\mathrm{TE}}\mathcal{G}(t')dt'\,dt. \quad \text{(A.14)}$$

Substituting the above back into (2.2.27) yields (2.2.29):

$$\frac{S}{S_0}=\exp\left(-\int_0^{\mathrm{TE}}D_{\mathrm{inst}}(t)C(t)dt\right),\ C(t)=\int_0^{\mathrm{TE}}\mathcal{G}(t')dt'.$$

B

DEXSY phase cycles

Throughout this work, a variety of phase cycling schemes were implemented and used. Here, we provide the phase cycles not given in the main text and elaborate on which unwanted coherences are let through by certain phase cycling schemes.

PG-DEXSY phase cycling

In Chapter 3, for the results regarding the glass capillary phantom (e.g., Fig. 3.3.2, a 2-step phase cycle was implemented, shown in Table B.1. We noted that this phase cycling scheme fails to suppress certain unwanted pathways, in particular STE pathways. The unwanted pathways in a 5-pulse spin echo DEXSY sequence (90, 180, 90, 90, 180°, numbered 1 – 5) were given in Table 4.1. Although in the case of $b_1 = 0$, another pathway is also relevant: an STE-SE. The pathways in Table 4.1 are reproduced here in Table B.2 along with this additional pathway.

It is easy to see that if a pathway misses either of the storage pulses (3 or 4), then it will be suppressed by this two-step phase cycle (as well as spoiled by the

Table B.1: 2-step PG-DEXSY phase cycling scheme

Step	φ_1	φ_2	φ_3	φ_4	φ_5	φ_{rec}
1	0	$+\pi/2$	π	π	$+\pi/2$	π
2	0	$+\pi/2$	0	0	$+\pi/2$	π

Table B.2: Coherences in the 5-pulse DEXSY sequence

Pathway	1	2	3	4	5
SE-SE	90°	180°	90°	90°	180°
STE_1	90°	90°	0°	0°	90°
STE_2	90°	0°	90°	90°	0°
STE_3	0°	90°	90°	0°	90°
STE-SE	90°	0°	90°	90°	180°
SE	0°	0°	0°	90°	180°
FID_1	0°	0°	0°	90°	0°
FID_2	0°	0°	0°	0°	90°

Table B.3: Location or phase of magnetization after each pulse for relevant pathways and phase cycle steps in Table B.1.

Pathway	**Steps**	90°_x	180°_y	$90^\circ_{\pm x}$	$90^\circ_{\pm x}$	180°_y	φ_{rec}	**Offset**
STE_2	1	$+y$	$+y$	$+z$	$-y$	$-y$	π	0
	2	$+y$	$+y$	$-z$	$-y$	$-y$	π	0
STE-SE	1	$+y$	$+y$	$+z$	$-y$	$-y$	π	0
	2	$+y$	$+y$	$-z$	$-y$	$-y$	π	0

spoiler during t_m). STE_1 is not stored due to the orthogonal refocusing pulses and will thus be spoiled, as noted in Table 4.3. Therefore, the only relevant pathways to consider are STE_2 and the STE-SE. In Table B.3, we show that this phase cycling scheme fails to suppress these two pathways and they sum coherently with the desired SE-SE pathway. Failing to suppress the STE-SE results in the asymmetry seen in Fig. 3.5 because this pathway is not spoiled only when $b_1 = 0$ and it exhibits greater attenuation than the SE-SE due to having net T_2^* dephasing by missing the first refocusing pulse (2). The STE_2 pathway will only refocus when $b_1 = b_2$ and thus removes some exchange weighting from the midpoint in Fig. 3.5a because it sees the experiment as a diffusion-weighted STE rather than a DEXSY sequence. In combination, these pathways and their respective effects may suffice to explain the slight underestimation of exchange parameters compared to prediction in Fig. 3.5b.

Table B.4: 8-step SG-DEXSY phase cycles

Step	φ_1	φ_2	φ_3	φ_4	φ_5	φ_{rec}
1	0	$+\pi/2$	0	0	$+\pi/2$	π
2	π	$-\pi/2$	0	0	$+\pi/2$	0
3	0	$+\pi/2$	π	0	$+\pi/2$	0
4	π	$-\pi/2$	π	0	$+\pi/2$	π
5	0	$+\pi/2$	0	π	$-\pi/2$	0
6	π	$-\pi/2$	0	π	$-\pi/2$	π
7	0	$+\pi/2$	π	π	$-\pi/2$	π
8	π	$-\pi/2$	π	π	$-\pi/2$	0

Table B.5: Location or phase of magnetization after each pulse for relevant pathways and phase cycle steps in Table B.4.

Pathway	**Steps**	90°_x	180°_y	$90^\circ_{\pm x}$	$90^\circ_{\pm x}$	180°_y	φ_{rec}	**Offset**
STE_2	1	$+y$	$+y$	$-z$	$-y$	$-y$	π	0
	2	$-y$	$-y$	$+z$	$+y$	$+y$	0	0
	3	$+y$	$+y$	$+z$	$+y$	$+y$	0	0
	4	$-y$	$-y$	$-z$	$-y$	$-y$	π	0
	5	$+y$	$+y$	$-z$	$+y$	$+y$	0	0
	6	$-y$	$-y$	$+z$	$-y$	$-y$	π	0
	7	$+y$	$+y$	$+z$	$-y$	$-y$	π	0
	8	$-y$	$-y$	$-z$	$+y$	$+y$	0	0

SG-DEXSY phase cycles

Most of the PM-10 experiments utilized an 8-step phase cycle given here in Table B.4. This phase cycling scheme is almost comprehensive and fails to suppress only STE_2, which we show in Table B.5. Thus, one must set $b_1 \neq b_2$ in order to spoil this pathway. We have done so throughout such that all presented results with the PM-10 can be considered as not containing off-resonance effects.

In Chapter 4 (Sec. 4.3.2), we developed a 4-step phase cycle which does suppress all relevant pathways when $b_1 > 0$. The cycle presented as a result in Table 4.2 is slightly different to the phase cycles that were actually utilized throughout Sec. 4.3.1. The actual phase cycles are given here in Table B.6. The phase cycles are largely the

Table B.6: 4-step SG-DEXSY phase cycling scheme

Step	φ_1	φ_2	φ_3	φ_4	φ_5	φ_{rec}
1	π	$+\pi/2$	π	π	0	0
2	π	$-\pi/2$	0	0	$+\pi/2$	π
3	π	$+\pi/2$	π	π	π	0
4	π	$-\pi/2$	0	0	$-\pi/2$	π

Table B.7: Location or phase of magnetization after each pulse for relevant pathways and phase cycle steps in Table B.4.

Pathway	**Steps**	90°_x	180°_y	$90^\circ_{\pm x}$	$90^\circ_{\pm x}$	180°_y	φ_{rec}	**Offset**
STE_2	1	$-y$	$-y$	$-z$	$+y$	$+y$	0	0
	2	$-y$	$-y$	$+z$	$+y$	$+y$	π	π
	3	$-y$	$-y$	$-z$	$+y$	$+y$	0	0
	4	$-y$	$-y$	$+z$	$+y$	$+y$	π	π

same and both suppress all unwanted pathways, except for a minor difference in how STE_2 ends up being cycled. In these phase cycles, we can see from B.7 that over the 4 steps, the pathway is added when it is stored along $-z$ and subtracted when it is stored along $+z$ and thus this will result in a T_1-weighting from this pathway. This minor issue was resolved in the phase cycles presented in Table 4.2. Note, however, that because we set $b_1 \neq b_2$ throughout the PM-10 experiments anyway, the phase cycles used (Table B.6) should still suffice to isolate the desired coherence and off-resonance effects should not affect the presented results.

C

Difference maps *in vivo*

Here, we present exchange-weighted difference maps $S_{\text{end}} - S_{\text{mid}}$ ($b_s = 3500\ \text{ms}/\mu m^2$) across all 11 values of t_m = [5, 10, 15, 20, 40, 60, 80, 120, 160, 200, 250, 300] ms and several slices for both scans in subject #1 and #2 as shown in Figs. 5.5 and 5.9, respectively. Throughout Chapter 5, we looked only at a similar slice containing hippocampus and the corpus callosum. We extend those observations here to other parts of the brain. We also highlight how these maps increase in intensity with t_m, with most of the variation happening over the first several t_m, consistent with fast exchange. However, variability with respect to t_m remains high, as we noted in Fig. 5.8. Tissue-type contrast is not always consistent between t_m. The same color scale from is used in all images presented in this appendix.

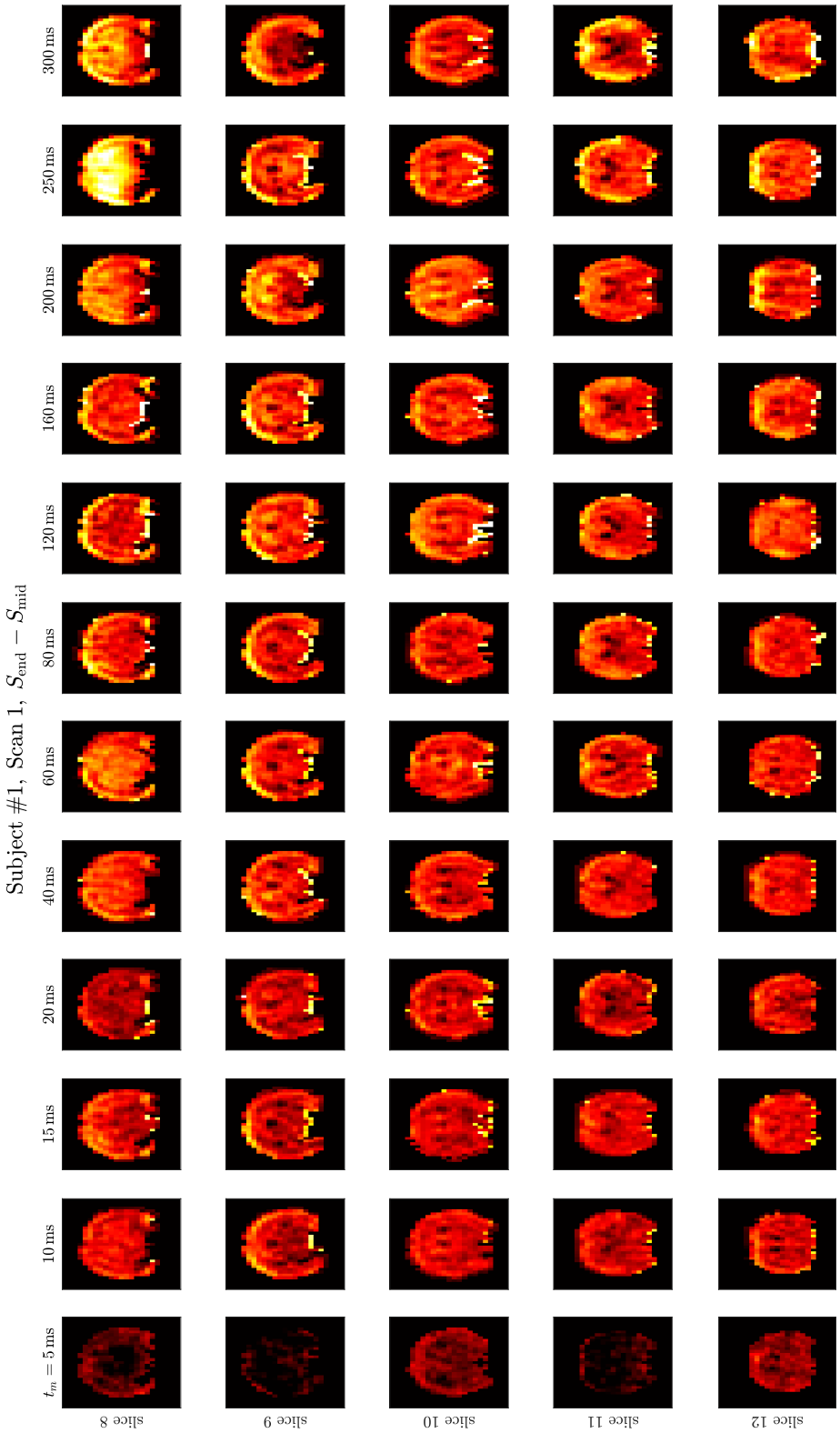
Subject #1, Scan 1, $S_{\text{end}} - S_{\text{mid}}$
$t_m = 5$ ms
10 ms
15 ms
20 ms
40 ms
60 ms
80 ms
120 ms
160 ms
200 ms
250 ms
300 ms
slice 8
slice 9
slice 10
slice 11
slice 12

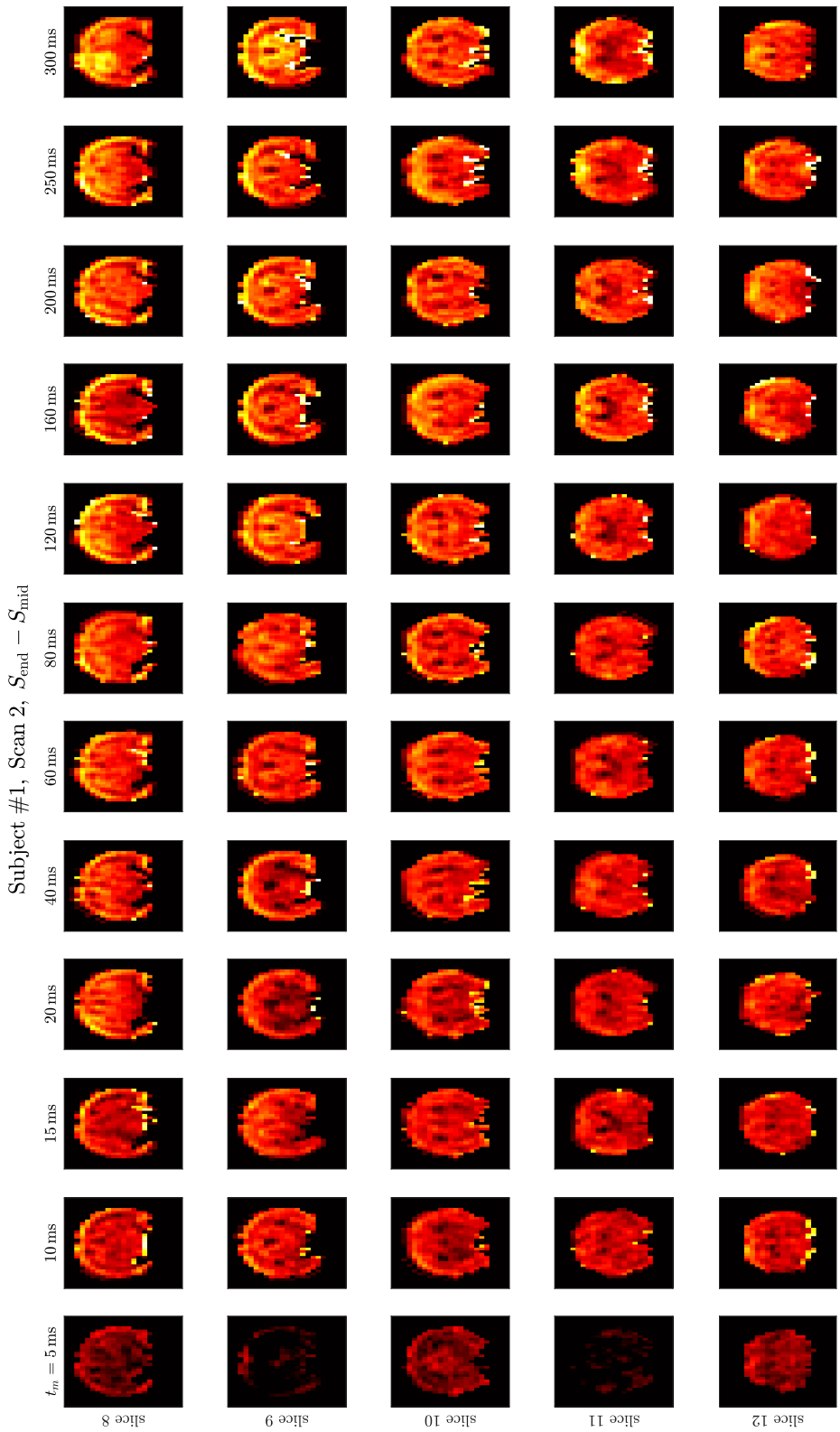
Subject #1, Scan 2, $S_{\text{end}} - S_{\text{mid}}$
$t_m = 5$ ms
10 ms
15 ms
20 ms
40 ms
60 ms
80 ms
120 ms
160 ms
200 ms
250 ms
300 ms
slice 8
slice 9
slice 10
slice 11
slice 12

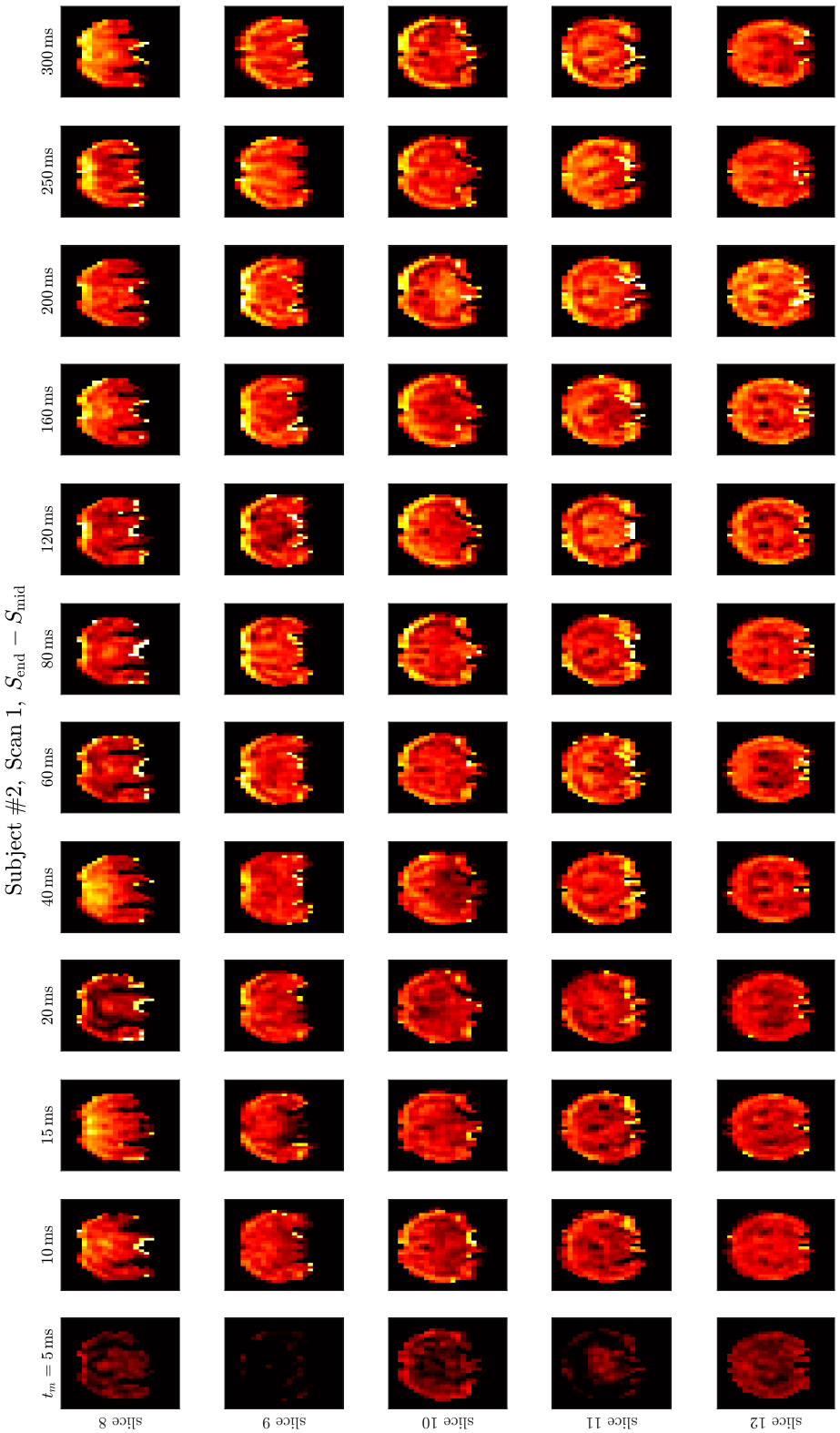
Subject #2, Scan 1, $S_{\text{end}} - S_{\text{mid}}$
$t_m = 5$ ms
10 ms
15 ms
20 ms
40 ms
60 ms
80 ms
120 ms
160 ms
200 ms
250 ms
300 ms
slice 8
slice 9
slice 10
slice 11
slice 12

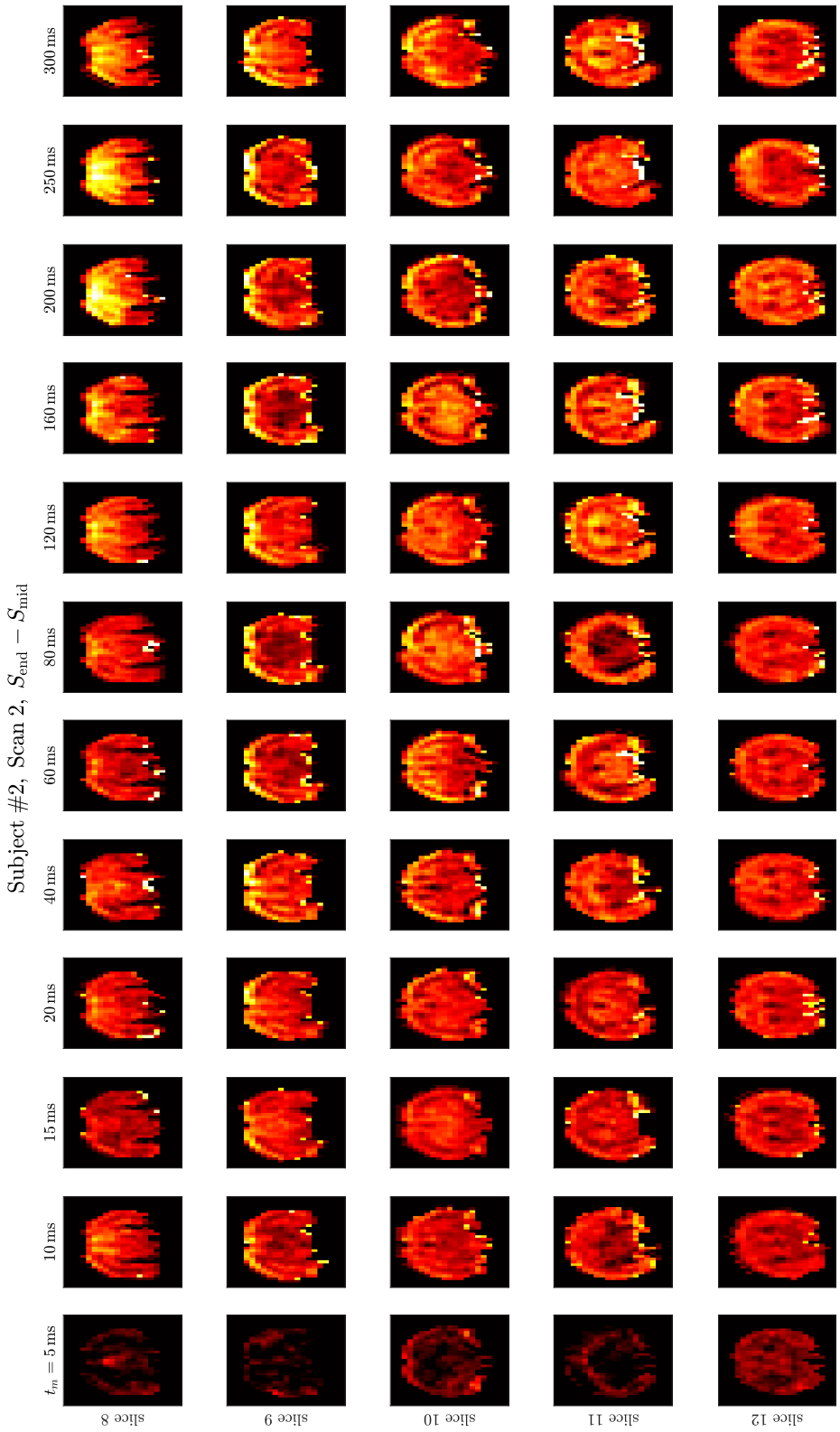
Subject #2, Scan 2, $S_{\text{end}} - S_{\text{mid}}$
$t_m = 5$ ms
10 ms
15 ms
20 ms
40 ms
60 ms
80 ms
120 ms
160 ms
200 ms
250 ms
300 ms
slice 8
slice 9
slice 10
slice 11
slice 12

References

1. Kac, M. Can One Hear the Shape of a Drum? *Amer. Math. Monthly* **73,** 1–23 (1966).
2. Mitra, P. P., Sen, P. N. & Schwartz, L. M. Short-time behavior of the diffusion coefficient as a geometrical probe of porous media. *Phys. Rev. B* **47,** 8565–8574 (14 1993).
3. Sen, P. N. Time-dependent diffusion coefficient as a probe of geometry. *Concepts Magn. Reson., Part A* **23A,** 1–21 (2004).
4. Mitra, P. P., Sen, P. N., Schwartz, L. M. & Le Doussal, P. Diffusion propagator as a probe of the structure of porous media. *Phys. Rev. Lett.* **68,** 3555–3558 (24 1992).
5. Latour, L. L., Mitra, P. P., Kleinberg, R. L. & Sotak, C. H. Time-Dependent Diffusion Coefficient of Fluids in Porous Media as a Probe of Surface-to-Volume Ratio. *J. Magn. Reson.* **101,** 342–346 (1993).
6. Hurlimann, M. D., Helmer, K. G., Latour, L. L. & Sotak, C. H. Restricted Diffusion in Sedimentary Rocks. Determination of Surface-Area-to-Volume Ratio and Surface Relaxivity. *J. Magn. Reson.* **111,** 169–178 (1994).
7. Tanner, J. E. Transient diffusion in a system partitioned by permeable barriers. Application to NMR measurements with a pulsed field gradient. *J. Chem. Phys.* **69,** 1748–1754 (1978).
8. Tanner, J. E. Self diffusion of water in frog muscle. *Biophys. J.* **28,** 107–116 (1979).
9. Latour, L. L., Svoboda, K., Mitra, P. P. & Sotak, C. H. Time-dependent diffusion of water in a biological model system. *Proc. Natl. Acad. Sci. U.S.A.* **91,** 1229–1233 (1994).
10. Sen, P. N. Time-dependent diffusion coefficient as a probe of the permeability of the pore wall. *J. Chem. Phys.* **119,** 9871–9876 (2003).
11. Tanner, J. E. & Stejskal, E. O. Restricted Self-Diffusion of Protons in Colloidal Systems by the Pulsed-Gradient, Spin-Echo Method. *J. Chem. Phys.* **49,** 1768–1777 (1968).
12. Le Bihan, D. Apparent Diffusion Coefficient and Beyond: What Diffusion MR Imaging Can Tell Us about Tissue Structure. *Radiology* **268,** 318–322 (2013).
13. Basser, P. J., Mattiello, J. & LeBihan, D. MR diffusion tensor spectroscopy and imaging. *Biophys. J.* **66,** 259–267 (1994).
14. Callaghan, P. T. & Furó, I. Diffusion-diffusion correlation and exchange as a signature for local order and dynamics. *J. Chem. Phys.* **120,** 4032–4038 (2004).

15. Parsons Jr., E. C., Does, M. D. & Gore, J. C. Temporal diffusion spectroscopy: Theory and implementation in restricted systems using oscillating gradients. *Magn. Reson. Med.* **55,** 75–84 (2006).

16. Stepišnik, J. Analysis of NMR self-diffusion measurements by a density matrix calculation. *Physica B+C* **104,** 350–364 (1981).

17. Stepišnik, J. Time-dependent self-diffusion by NMR spin-echo. *Physica B Condens. Matter* **183,** 343–350 (1993).

18. Lasič, S. *et al.* Apparent exchange rate for breast cancer characterization. *NMR Biomed.* **29,** 631–639 (2016).

19. Schilling, F. *et al.* MRI measurements of reporter-mediated increases in transmembrane water exchange enable detection of a gene reporter. *Nat. Biotechnol.* **35,** 75–80 (2016).

20. Li, H., Gore, J. C. & Xu, J. Fast and robust measurement of microstructural dimensions using temporal diffusion spectroscopy. *J. Magn. Reson.* **242,** 4–9 (2014).

21. Jiang, X. *et al.* Quantification of cell size using temporal diffusion spectroscopy. *Magn. Res. Med.* **75,** 1076–1085 (2016).

22. Callaghan, P. T. *Principles of nuclear magnetic resonance microscopy* (Clarendon Press, Oxford, U.K., 1993).

23. Rigden, J. S. Quantum states and precession: The two discoveries of NMR. *Rev. Mod. Phys.* **58,** 433–448 (2 1986).

24. Bloch, F. Nuclear Induction. *Phys. Rev.* **70,** 460–474 (7-8 1946).

25. Bloembergen, N., Purcell, E. M. & Pound, R. V. Relaxation Effects in Nuclear Magnetic Resonance Absorption. *Phys. Rev.* **73,** 679–712 (7 1948).

26. Brownstein, K. R. & Tarr, C. E. Importance of classical diffusion in NMR studies of water in biological cells. *Phys. Rev. A* **19,** 2446–2453 (1979).

27. Damadian, R. Tumor Detection by Nuclear Magnetic Resonance. *Science* **171,** 1151–1153 (1971).

28. Keeler, J. *Understanding NMR spectroscopy* (John Wiley and Sons, Chichester, U.K, 2010).

29. Hahn, E. L. Spin Echoes. *Phys. Rev.* **80,** 580–594 (4 1950).

30. Carr, H. Y. & Purcell, E. M. Effects of Diffusion on Free Precession in Nuclear Magnetic Resonance Experiments. *Phys. Rev.* **94,** 630–638 (3 1954).

31. Meiboom, S. & Gill, D. Modified Spin-Echo Method for Measuring Nuclear Relaxation Times. *Rev. Sci.* **29,** 688–691 (1958).

32. Woessner, D. E. Effects of Diffusion in Nuclear Magnetic Resonance Spin-Echo Experiments. *J. Chem. Phys.* **34,** 2057–2061 (1961).

33. Weigel, M. Extended phase graphs: dephasing, RF pulses, and echoes - pure and simple. *J. Magn. Reson. Imaging* **41,** 266–295 (2015).

34. Kaiser, R., Bartholdi, E. & Ernst, R. R. Diffusion and field-gradient effects in NMR Fourier spectroscopy. *J. Chem. Phys.* **60,** 2966–2979 (1974).

35. Burstein, D. Stimulated echoes: Description, applications, practical hints. *Concepts Magn. Reson.* **8,** 269–278 (1996).

36. Kingsley, P. B. Product operators, coherence pathways, and phase cycling. Part III: phase cycling. *Concepts Magn. Reson.* **7,** 167–192 (1995).

37. Mansfield, P. Multi-planar image formation using NMR spin echoes. *J. Phys. C: Solid State Phys.* **10,** L55–L58 (1977).

38. Mansfield, P. & Pykett, I. L. Biological and medical imaging by NMR. *J. Magn. Reson.* **29,** 355–373 (1978).

39. Edelstein, W. A., Hutchison, J. M., Johnson, G. & Redpath, T. Spin warp NMR imaging and applications to human whole-body imaging. *Phys. Med. Biol.* **25,** 751–756 (1980).

40. Pykett, I. L. & Rzedzian, R. Instant images of the body by magnetic resonance. *Magn. Reson. Med.* **5,** 563–571 (1987).

41. Liu, G. & Ogawa, S. EPI image reconstruction with correction of distortion and signal losses. *J. Magn. Reson. Imaging* **24,** 683–689 (2006).

42. Eidmann, G., Savelsberg, R., Blümler, P. & Blümich, B. The NMR MOUSE, a Mobile Universal Surface Explorer. *J. Magn. Reson.* **122,** 104–109 (1996).

43. Blümich, B. *et al.* The NMR-mouse: construction, excitation, and applications. *Magn. Reson. Imaging* **16,** 479–484 (1998).

44. Williamson, N. H. *et al.* Low-field, high-gradient NMR shows diffusion contrast consistent with localization or motional averaging of water near surfaces. *Magn. Reson. Lett.* **3,** 90–107 (2023).

45. Williamson, N. H. *et al.* Magnetic resonance measurements of cellular and sub-cellular membrane structures in live and fixed neural tissue. *eLife* **8,** e51101 (2019).

46. Williamson, N. H. *et al.* Real-time measurement of diffusion exchange rate in biological tissue. *J. Magn. Reson.* **317,** 106782 (2020).

47. Cai, T. X., Williamson, N. H., Witherspoon, V. J., Ravin, R. & Basser, P. J. A single-shot measurement of time-dependent diffusion over sub-millisecond timescales using static field gradient NMR. *J. Chem. Phys.* **154,** 111105 (2021).

48. Casanova, F., Blümich, B. & Perlo, J. *Single-Sided NMR* (Springer, Heidelberg, New York, 2011).

49. Stejskal, E. O. & Tanner, J. E. Spin Diffusion Measurements: Spin Echoes in the Presence of a Time-Dependent Field Gradient. *J. Chem. Phys.* **42,** 288–292 (1965).
50. Stejskal, E. O. Use of Spin Echoes in a Pulsed Magnetic-Field Gradient to Study Anisotropic, Restricted Diffusion and Flow. *J. Chem. Phys.* **43,** 3597–3603 (1965).
51. Torrey, H. C. Bloch Equations with Diffusion Terms. *Phys. Rev.* **104,** 563–565 (3 1956).
52. Bennett, K. M. *et al.* Characterization of continuously distributed cortical water diffusion rates with a stretched-exponential model. *Magn. Reson. Med.* **50,** 727–734 (2003).
53. Jensen, J. H., Helpern, J. A., Ramani, A., Lu, H. & Kaczynski, K. Diffusional kurtosis imaging: The quantification of non-gaussian water diffusion by means of magnetic resonance imaging. *Magn. Reson. Med.* **53,** 1432–1440 (2005).
54. Jensen, J. H. & Helpern, J. A. MRI quantification of non-Gaussian water diffusion by kurtosis analysis. *NMR Biomed.* **23,** 698–710 (Aug. 2010).
55. Bai, Y. *et al.* Grading of Gliomas by Using Monoexponential, Biexponential, and Stretched Exponential Diffusion-weighted MR Imaging and Diffusion Kurtosis MR Imaging. *Radiology* **278,** 496–504 (2015).
56. Casella, G. C. & Berger, R. L. *Statistical Inference* 2nd ed. (Brooks/Cole, Florence, KY, 1990).
57. Douglass, D. C. & McCall, D. W. Diffusion in Paraffin Hydrocarbons. *J. Phys. Chem.* **62,** 1102–1107 (1958).
58. Kubo, R. Statistical-Mechanical Theory of Irreversible Processes. I. General Theory and Simple Applications to Magnetic and Conduction Problems. *J. Phys. Soc. Jpn.* **12,** 570–586 (1957).
59. Kampen, N. G. V. *Stochastic Processes in Physics and Chemistry (North-Holland Personal Library)* (North Holland, 2007).
60. Einstein, A. *Investigations on the theory of Brownian movement* (Dover Publications, New York, N.Y, 1956).
61. Callaghan, P. T. & Stepišnik, J. Frequency-Domain Analysis of Spin Motion Using Modulated-Gradient NMR. *J. Magn. Reson.* **117,** 118–122 (1995).
62. Callaghan, P. T. & Stepišnik, J. in *Advances in Magnetic and Optical Resonance* (ed Warren, W. S.) 325–388 (Academic Press, 1996).
63. Stepišnik, J. Validity limits of Gaussian approximation in cumulant expansion for diffusion attenuation of spin echo. *Physica B Condens. Matter* **270,** 110–117 (1999).

64. Novikov, D. S. & Kiselev, V. G. Surface-to-volume ratio with oscillating gradients. *J. Magn. Reson.* **210,** 141–145 (2011).

65. Ning, L., Setsompop, K., Westin, C.-F. & Rathi, Y. New insights about time-varying diffusivity and its estimation from diffusion MRI. *Magn. Reson. Med.* **78,** 763–774 (2017).

66. Schachter, M., Does, M. D., Anderson, A. W. & Gore, J. C. Measurements of Restricted Diffusion Using an Oscillating Gradient Spin-Echo Sequence. *J. Magn. Reson.* **147,** 232–237 (2000).

67. Stepišnik, J., Lasič, S., Mohorič, A., Serša, I. & Sepe, A. Spectral characterization of diffusion in porous media by the modulated gradient spin echo with CPMG sequence. *J. Magn. Reson.* **182,** 195–199 (2006).

68. Reynaud, O. Time-Dependent Diffusion MRI in Cancer: Tissue Modeling and Applications. *Front. Phys.* **5,** 58 (2017).

69. Hürlimann, M. D., Helmer, K. G., de Swiet, T. M. & Sen, P. N. Spin echoes in a constant gradient and in the presence of simple restriction. *J. Magn. Reson.* **113,** 260–264 (1995).

70. De Swiet, T. M. & Sen, P. N. Decay of nuclear magnetization by bounded diffusion in a constant field gradient. *J. Chem. Phys.* **100,** 5597–5604 (1994).

71. Hürlimann, M. D. Diffusion and Relaxation Effects in General Stray Field NMR Experiments. *J. Magn. Reson.* **148,** 367–378 (2001).

72. Axelrod, S. & Sen, P. N. Nuclear magnetic resonance spin echoes for restricted diffusion in an inhomogeneous field: Methods and asymptotic regimes. *J. Chem. Phys.* **114,** 6878–6895 (2001).

73. Sukstanskii, A. L. & Yablonskiy, D. A. Gaussian approximation in the theory of MR signal formation in the presence of structure-specific magnetic field inhomogeneities. *J. Magn. Reson.* **163,** 236–247 (2003).

74. Grebenkov, D. S. NMR survey of reflected Brownian motion. *Rev. Mod. Phys.* **79,** 1077–1137 (3 2007).

75. Yablonskiy, D. A. & Sukstanskii, A. L. Theoretical models of the diffusion weighted MR signal. *NMR Biomed.* **23,** 661–681 (2010).

76. Woessner, D. E. NMR spin-echo self-diffusion measurements on fluids undergoing restricted diffusion. *J. Chem. Phys.* **67,** 1365–1367 (1963).

77. Neuman, C. H. Spin echo of spins diffusing in a bounded medium. *J. Chem. Phys.* **60,** 4508–4511 (1974).

78. Mitra, P. P. & Halperin, B. I. Effects of Finite Gradient-Pulse Widths in Pulsed-Field-Gradient Diffusion Measurements. *J. Magn. Reson. Ser. A* **113,** 94–101 (1995).

79. Stoller, S. D., Happer, W. & Dyson, F. J. Transverse spin relaxation in inhomogeneous magnetic fields. *Phys. Rev. A* **44,** 7459–7477 (11 1991).

80. Moutal, N., Demberg, K., Grebenkov, D. S. & Kuder, T. A. Localization regime in diffusion NMR: Theory and experiments. *J. Magn. Reson.* **305,** 162–174 (2019).

81. Moutal, N. & Grebenkov, D. S. The localization regime in a nutshell. *J. Magn. Reson.* **320,** 106836 (2020).

82. Grebenkov, D. S. & Helffer, B. On Spectral Properties of the Bloch–Torrey Operator in Two Dimensions. *SIAM J. Math. Anal.* **50,** 622–676 (2018).

83. Novikov, D. S., Fieremans, E., Jespersen, S. N. & Kiselev, V. G. Quantifying brain microstructure with diffusion MRI: Theory and parameter estimation. *NMR Biomed.* **32,** e3998 (2018).

84. Carslaw, H. S. & Jaeger, J. C. *Conduction of heat in solids* 2nd ed. (Oxford University Press, London, England, 1959).

85. Robertson, B. Spin-Echo Decay of Spins Diffusing in a Bounded Region. *Phys. Rev.* **151,** 273–277 (1 1966).

86. Murday, J. S. & Cotts, R. M. Self-Diffusion Coefficient of Liquid Lithium. *J. Chem. Phys.* **48,** 4938–4945 (1968).

87. Shen, L. & Chen, Z. Critical review of the impact of tortuosity on diffusion. *Chem. Eng. Sci.* **62,** 3748–3755 (2007).

88. Novikov, D. S., Fieremans, E., Jensen, J. H. & Helpern, J. A. Random walk with barriers. *Nat. Phys.* **7,** 508–514 (2011).

89. Novikov, D. S., Jensen, J. H., Helpern, J. A. & Fieremans, E. Revealing mesoscopic structural universality with diffusion. *Proc. Natl. Acad. Sci. U.S.A* **111,** 5088–5093 (2014).

90. Sigmund, E. E. *et al.* Time-dependent diffusion in skeletal muscle with the random permeable barrier model (RPBM): application to normal controls and chronic exertional compartment syndrome patients. *NMR Biomed.* **27,** 519–528 (2014).

91. Jian, B., Vemuri, B. C., Özarslan, E., Carney, P. R. & Mareci, T. H. A novel tensor distribution model for the diffusion-weighted MR signal. *NeuroImage* **37,** 164–176 (2007).

92. Provencher, S. W. CONTIN: A general purpose constrained regularization program for inverting noisy linear algebraic and integral equations. *Comput. Phys. Commun* **27,** 229–242 (1982).

93. Venkataramanan, L., Song, Y.-Q. & Hurlimann, M. Solving Fredholm integrals of the first kind with tensor product structure in 2 and 2.5 dimensions. *IEEE Trans. Signal Process.* **50,** 1017–1026 (2002).

94. Galvosas, P. & Callaghan, P. T. Multi-dimensional inverse Laplace spectroscopy in the NMR of porous media. *C. R. Phys.* **11,** 172–180 (2010).

95. Le Bihan, D. & Turner, R. Intravoxel incoherent motion imaging using spin echoes. *Magn. Reson. Med.* **19,** 221–227 (1991).

96. Novikov, D. S., Fieremans, E., Jespersen, S. N. & Kiselev, V. G. Quantifying brain microstructure with diffusion MRI: Theory and parameter estimation. *NMR Biomed.* **32,** e3998 (2019).

97. Assaf, Y. & Basser, P. J. Composite hindered and restricted model of diffusion (CHARMED) MR imaging of the human brain. *NeuroImage* **27,** 48–58 (2005).

98. Kroenke, C. D., Ackerman, J. J. & Yablonskiy, D. A. On the nature of the NAA diffusion attenuated MR signal in the central nervous system. *Magn. Reson. Med.* **52,** 1052–1059 (2004).

99. Jelescu, I. O., Palombo, M., Bagnato, F. & Schilling, K. G. Challenges for biophysical modeling of microstructure. *J. Neurosci. Methods,* 108861 (2020).

100. Papadopoulos, M. C. & Verkman, A. S. Aquaporin water channels in the nervous system. *Nat. Rev. Neurosci.* **14,** 265–277 (2013).

101. Olesen, J. L., Østergaard, L., Shemesh, N. & Jespersen, S. N. Diffusion time dependence, power-law scaling, and exchange in gray matter. *NeuroImage* **251,** 118976 (2022).

102. Palombo, M. *et al.* SANDI: A compartment-based model for non-invasive apparent soma and neurite imaging by diffusion MRI. *NeuroImage* **215,** 116835 (2020).

103. Jelescu, I. O., de Skowronski, A., Geffroy, F., Palombo, M. & Novikov, D. S. Neurite Exchange Imaging (NEXI): A minimal model of diffusion in gray matter with inter-compartment water exchange. *NeuroImage* **256,** 119277 (2022).

104. Grebenkov, D. S. Exploring diffusion across permeable barriers at high gradients. II. Localization regime. *J. Magn. Reson.* **248,** 164–176 (2014).

105. Kärger, J. Zur Bestimmung der Diffusion in einem Zweibereichsystem mit Hilfe von gepulsten Feldgradienten. *Annalen der Physik* **479,** 1–4 (1969).

106. Kärger, J. NMR self-diffusion studies in heterogeneous systems. *Adv. Colloid Interface Sci.* **23,** 129–148 (1985).

107. Moutal, N., Nilsson, M., Topgaard, D. & Grebenkov, D. The Kärger vs bi-exponential model: Theoretical insights and experimental validations. *J. Magn. Reson.* **296,** 72–78 (2018).

108. Price, W. S., Barzykin, A. V., Hayamizu, K. & Tachiya, M. A Model for Diffusive Transport through a Spherical Interface Probed by Pulsed-Field Gradient NMR. *Biophy. J.* **74,** 2259–2271 (1998).

109. Nilsson, M. *et al.* Evaluating the accuracy and precision of a two-compartment Kärger model using Monte Carlo simulations. *J. Magn. Reson.* **206,** 59–67 (2010).

110. Jelescu, I. O., Veraart, J., Fieremans, E. & Novikov, D. S. Degeneracy in model parameter estimation for multi-compartmental diffusion in neuronal tissue. *NMR Biomed.* **29,** 33–47 (Nov. 2015).

111. Coelho, S., Pozo, J. M., Jespersen, S. N., Jones, D. K. & Frangi, A. F. Resolving degeneracy in diffusion MRI biophysical model parameter estimation using double diffusion encoding. *Magn. Reson. Med.* **82,** 395–410 (Mar. 2019).

112. Henriques, R. N. *et al.* Double diffusion encoding and applications for biomedical imaging. *J. Neurosci. Methods* **348,** 108989 (2021).

113. Ning, L., Nilsson, M., Lasič, S., Westin, C.-F. & Rathi, Y. Cumulant expansions for measuring water exchange using diffusion MRI. *J. Chem. Phys.* **148,** 074109 (2018).

114. Chakwizira, A. *et al.* Diffusion MRI with pulsed and free gradient waveforms: Effects of restricted diffusion and exchange. *NMR Biomed.* **36,** e4827 (2023).

115. Cai, T. X., Benjamini, D., Komlosh, M. E., Basser, P. J. & Williamson, N. H. Rapid detection of the presence of diffusion exchange. *J. Magn. Reson.* **297,** 17–22 (2018).

116. Åslund, I., Nowacka, A., Nilsson, M. & Topgaard, D. Filter-exchange PGSE NMR determination of cell membrane permeability. *J. Magn. Reson.* **200,** 291–295 (2009).

117. Qiao, Y., Galvosas, P., Adalsteinsson, T., Schönhoff, M. & Callaghan, P. T. Diffusion exchange NMR spectroscopic study of dextran exchange through polyelectrolyte multilayer capsules. *J. Chem. Phys.* **122,** 214912 (2005).

118. Petrella, J. R. & Provenzale, J. M. MR Perfusion Imaging of the Brain. *AJR Am. J. Roentgenol.* **175,** 207–219 (2000).

119. Tsougos, I. *Advanced MR neuroimaging* en (CRC Press, London, England, 2019).

120. Breen-Norris, J. O. *et al.* Measuring diffusion exchange across the cell membrane with DEXSY (Diffusion Exchange Spectroscopy). *Magn. Reson. Med.* **84,** 1543–1551 (2020).

121. Mankinen, O. *et al.* Ultrafast diffusion exchange nuclear magnetic resonance. *Nat. Commun* **11,** 3251 (2020).

122. Lasič, S., Nilsson, M., Lätt, J., Ståhlberg, F. & Topgaard, D. Apparent exchange rate mapping with diffusion MRI. *Magn. Reson. Med.* **66,** 356–365 (2011).

123. Nilsson, M. *et al.* Noninvasive mapping of water diffusional exchange in the human brain using filter-exchange imaging. *Magn. Reson. Med.* **69,** 1572–1580 (2013).

124. Sønderby, C. K., Lundell, H. M., Søgaard, L. V. & Dyrby, T. B. Apparent exchange rate imaging in anisotropic systems. *Magn. Reson. Med.* **72,** 756–762 (2013).

125. Lampinen, B. *et al.* Optimal experimental design for filter exchange imaging: Apparent exchange rate measurements in the healthy brain and in intracranial tumors. *Magn. Reson. Med.* **77,** 1104–1114 (2017).

126. Tian, X. *et al.* Evaluation and comparison of diffusion MR methods for measuring apparent transcytolemmal water exchange rate constant. *J. Magn. Reson.* **275,** 29–37 (2017).

127. Eriksson, S. *et al.* NMR quantification of diffusional exchange in cell suspensions with relaxation rate differences between intra and extracellular compartments. *PloS One* **12,** e0177273 (2017).

128. Scher, Y., Reuveni, S. & Cohen, Y. Constant gradient FEXSY: A time-efficient method for measuring exchange. *J. Magn. Reson.* **311,** 106667 (2020).

129. Bai, R. *et al.* Feasibility of filter-exchange imaging (FEXI) in measuring different exchange processes in human brain. *NeuroImage* **219,** 117039 (2020).

130. Schillmaier, M., Kaika, A. & Schilling, F. Disentangling Intercompartment Exchange from Restricted Diffusion. *Advanced Diffusion Encoding Methods in MRI* **24,** 154 (2020).

131. Ludwig, D., Laun, F. B., Ladd, M. E., Bachert, P. & Kuder, T. A. Apparent exchange rate imaging: On its applicability and the connection to the real exchange rate. *Magn. Reson. Med.* **86,** 677–692 (2021).

132. Fieremans, E. *et al.* In vivo observation and biophysical interpretation of time-dependent diffusion in human white matter. *NeuroImage* **129,** 414–427 (2016).

133. Åslund, I. & Topgaard, D. Determination of the self-diffusion coefficient of intracellular water using PGSE NMR with variable gradient pulse length. *J. Magn. Reson.* **201,** 250–254 (2009).

134. Ohene, Y. *et al.* Filter exchange imaging with crusher gradient modelling detects increased blood–brain barrier water permeability in response to mild lung infection. *Fluids Barriers CNS* **20** (2023).

135. Washburn, K. E. & Callaghan, P. T. Tracking Pore to Pore Exchange Using Relaxation Exchange Spectroscopy. *Phys. Rev. Lett.* **97,** 175502 (17 Oct. 2006).

136. Van Landeghem, M., Haber, A., D'espinose De Lacaillerie, J.-B. & Blümich, B. Analysis of multisite 2D relaxation exchange NMR. *Concept Magn. Reson. A* **36A,** 153–169 (2010).

137. Bai, R., Cloninger, A., Czaja, W. & Basser, P. J. Efficient 2D MRI relaxometry using compressed sensing. *J. Magn. Reson.* **255,** 88–99 (2015).

138. Bai, R., Benjamini, D., Cheng, J. & Basser, P. J. Fast, accurate 2D-MR relaxation exchange spectroscopy (REXSY): Beyond compressed sensing. *J. Chem. Phys.* **145,** 154202 (2016).

139. Benjamini, D. & Basser, P. J. Use of marginal distributions constrained optimization (MADCO) for accelerated 2D MRI relaxometry and diffusometry. *J. Magn. Reson.* **271,** 40–45 (2016).

140. Benjamini, D., Komlosh, M. E. & Basser, P. J. Imaging Local Diffusive Dynamics Using Diffusion Exchange Spectroscopy MRI. *Phys. Rev. Lett.* **118,** 158003 (15 2017).

141. LeVeque, R. J. *Finite difference methods for ordinary and partial differential equations* (Society for Industrial and Applied Mathematics, 2007).

142. Lampinen, B. *et al.* Probing brain tissue microstructure with MRI: principles, challenges, and the role of multidimensional diffusion-relaxation encoding. *NeuroImage* **282,** 120338 (2023).

143. Sengul, G., Puchalski, R. B. & Watson, C. Cytoarchitecture of the Spinal Cord of the Postnatal (P4) Mouse. *Anat. Rec.* **295,** 837–845 (2012).

144. Henry, A. M. & Hohmann, J. G. High-resolution gene expression atlases for adult and developing mouse brain and spinal cord. *Mamm. Genome* **23,** 539–549 (2012).

145. Bai, R. *et al.* Simultaneous calcium fluorescence imaging and MR of ex vivo organotypic cortical cultures: a new test bed for functional MRI. *NMR Biomed.* **28,** 1726–1738 (2015).

146. Williamson, N. H. *et al.* Water exchange rates measure active transport and homeostasis in neural tissue. *PNAS Nexus* **2,** pgad056 (2023).

147. Yang, D. M. *et al.* Intracellular water preexchange lifetime in neurons and astrocytes. *Magn. Reson. Med.* **79,** 1616–1627 (2018).

148. Nilsson, M., van Westen, D., Ståhlberg, F., Sundgren, P. C. & Lätt, J. The role of tissue microstructure and water exchange in biophysical modelling of diffusion in white matter. *MAGMA* **26,** 345–370 (2013).

149. Godefroy, S. & Callaghan, P. 2D relaxation/diffusion correlations in porous media. *Magn. Reson. Imaging* **21,** 381–383 (2003).

150. Mitchell, J., Chandrasekera, T. C. & Gladden, L. F. Numerical estimation of relaxation and diffusion distributions in two dimensions. *Prog. Nucl. Magn. Reson. Spectrosc.* **62,** 34–50 (2012).

151. Hansen, P. C. & O'Leary, D. P. The Use of the L-Curve in the Regularization of Discrete Ill-Posed Problems. *SIAM J. Sci. Comput.* **14,** 1487–1503 (1993).

152. Grebenkov, D. S. Diffusion MRI/NMR at high gradients: Challenges and perspectives. *Microporous Mesoporous Mater.* **269,** 79–82 (2018).

153. Carlton, K. J., Halse, M. R. & Strange, J. H. Diffusion-Weighted Imaging of Bacteria Colonies in the STRAFI Plane. *J. Magn. Reson.* **143,** 24–29 (2000).

154. Pfeuffer, J., Flögel, U., Dreher, W. & Leibfritz, D. Restricted diffusion and exchange of intracellular water: theoretical modelling and diffusion time dependence of1H NMR measurements on perfused glial cells. *NMR Biomed.* **11,** 19–31 (1998).

155. Cai, T. X., Williamson, N. H., Ravin, R. & Basser, P. J. Disentangling the Effects of Restriction and Exchange With Diffusion Exchange Spectroscopy. *Front. Phys.* **10** (2022).

156. Callaghan, P. *Translational dynamics and magnetic resonance : principles of pulsed gradient spin echo NMR* (Oxford University Press, Oxford, New York, 2011).

157. Benjamini, D. & Basser, P. J. Multidimensional correlation MRI. *NMR Biomed.* **33** (2020).

158. Ordinola, A., Cai, S., Lundberg, P., Bai, R. & Özarslan, E. On the sampling strategies and models for measuring diffusion exchange with a double diffusion encoding sequence. *Magn. Reson. Lett.* **3,** 232–247 (2023).

159. Cheng, Z. *et al.* Using deep learning to accelerate magnetic resonance measurements of molecular exchange. *J. Chem. Phys.* **159** (Aug. 2023).

160. Koch, M. A. & Finsterbusch, J. Compartment size estimation with double wave vector diffusion-weighted imaging. *Magn. Reson. Med.* **60,** 90–101 (2008).

161. Shemesh, N., Özarslan, E., Adiri, T., Basser, P. J. & Cohen, Y. Noninvasive bipolar double-pulsed-field-gradient NMR reveals signatures for pore size and shape in polydisperse, randomly oriented, inhomogeneous porous media. *J. Chem. Phys.* **133** (2010).

162. Henriques, R. N., Jespersen, S. N. & Shemesh, N. Correlation tensor magnetic resonance imaging. *NeuroImage* **211,** 116605 (2020).

163. Li, C., Fieremans, E., Novikov, D. S., Ge, Y. & Zhang, J. Measuring water exchange on a preclinical MRI system using filter exchange and diffusion time dependent kurtosis imaging. *Magn. Reson. Med.* **89,** 1441–1455 (2022).

164. Ulloa, P., Methot, V. & Koch, M. A. Experimental validation of a bias in apparent exchange rate measurement. *Curr. Dir. Biomed. Eng.* **3,** 529–532 (2017).

165. Khateri, M., Reisert, M., Sierra, A., Tohka, J. & Kiselev, V. G. What does FEXI measure? *NMR Biomed.* **35** (2022).

166. Powell, E. *et al.* Blood-brain barrier water exchange measurements using FEXI: Impact of modeling paradigm and relaxation time effects. *Magn. Reson. Med.* **90,** 34–50 (2023).

167. King, L. S., Kozono, D. & Agre, P. From structure to disease: the evolving tale of aquaporin biology. *Nat. Rev. Mol. Cell Biol.* **5,** 687–698 (2004).

168. Loo, D. D. F., Zeuthen, T., Chandy, G. & Wright, E. M. Cotransport of water by the Na+/glucose cotransporter. *PNAS* **93,** 13367–13370 (1996).

169. Meinild, A.-K., Klaerke, D. A., Loo, D. D. F., Wright, E. M. & Zeuthen, T. The human Na+-glucose cotransporter is a molecular water pump. *Physiol. J.* **508,** 15–21 (1998).

170. Zeuthen, T. & MacAulay, N. in *Molecular Mechanisms of Water Transport Across Biological Membranes* 259–284 (Academic Press, 2002).

171. Zeuthen, T. Water-Transporting Proteins. *J. Membr. Biol.* **234,** 57–73 (2009).

172. MacAulay, N. & Zeuthen, T. Water transport between CNS compartments: contributions of aquaporins and cotransporters. *Neuroscience* **168,** 941–956 (2010).

173. Steffensen, A. B. *et al.* Cotransporter-mediated water transport underlying cerebrospinal fluid formation. *Nat. Commun* **9** (2018).

174. MacAulay, N. Molecular mechanisms of brain water transport. *Nat. Rev. Neurosci.* **22,** 326–344 (2021).

175. Springer Jr, C. S. *et al.* Intratumor mapping of intracellular water lifetime: metabolic images of breast cancer? *NMR Biomed.* **27,** 760–773 (2014).

176. Rooney, W. D. *et al.* Mapping human brain capillary water lifetime: high-resolution metabolic neuroimaging. *NMR Biomed.* **28,** 607–623 (2015).

177. Bai, R., Springer, C. S., Plenz, D. & Basser, P. J. Fast, Na^+/K^+–pump driven, steady-state transcytolemmal water exchange in neuronal tissue: A study of rat brain cortical cultures. *Magn. Reson. Med.* **79,** 3207–3217 (Nov. 2017).

178. Bai, R., Springer Jr, C. S., Plenz, D. & Basser, P. J. Brain active transmembrane water cycling measured by MR is associated with neuronal activity. *Magn. Reson. Med.* **81,** 1280–1295 (2019).

179. Springer, C. S. Using 1H2O MR to measure and map sodium pump activity in vivo. *J. Magn. Reson.* **291,** 110–126 (2018).

180. Springer Jr, C. S. *et al.* Metabolic Activity Diffusion Imaging [MADI]: II. Non-Invasive, High-Resolution Human Brain Mapping of Sodium Pump Flux and Cell Metrics. *NMR Biomed.* **36,** e4782 (2022).

181. Springer Jr, C. S. *et al.* Metabolic activity diffusion imaging (MADI): I. Metabolic, cytometric modeling and simulations. *NMR Biomed.* **36,** e4781 (2023).

182. Bihan, D. L., Urayama, S., Aso, T., Hanakawa, T. & Fukuyama, H. Direct and fast detection of neuronal activation in the human brain with diffusion MRI. *PNAS* **103,** 8263–8268 (2006).

183. Tsurugizawa, T., Ciobanu, L. & Bihan, D. L. Water diffusion in brain cortex closely tracks underlying neuronal activity. *PNAS* **110,** 11636–11641 (2013).

184. Abe, Y., Tsurugizawa, T. & Bihan, D. L. Water diffusion closely reveals neural activity status in rat brain loci affected by anesthesia. *PLoS Biol.* **15,** e2001494 (2017).

185. Bihan, D. L. Diffusion, confusion and functional MRI. *NeuroImage* **62,** 1131–1136 (2012).

186. Kandel, E. R., Koester, J. D., Mack, S. H. & Siegelbaum, S. A. *Principles of neural science* 6th ed. (McGraw-Hill Education/Medical, 2021).

187. Abe, Y., Tsurugizawa, T. & Bihan, D. L. Water diffusion closely reveals neural activity status in rat brain loci affected by anesthesia. *PLoS Biol.* **15** (ed Rushworth, M.) e2001494 (2017).

188. Ogawa, S., Lee, T. M., Kay, A. R. & Tank, D. W. Brain magnetic resonance imaging with contrast dependent on blood oxygenation. *PNAS* **87,** 9868–9872 (1990).

189. Bai, R., Stewart, C. V., Plenz, D. & Basser, P. J. Assessing the sensitivity of diffusion MRI to detect neuronal activity directly. *PNAS* **113** (2016).

190. Miller, K. L. *et al.* Evidence for a vascular contribution to diffusion FMRI at high *b*-value. *Proceedings of the National Academy of Sciences* **104,** 20967–20972 (2007).

191. Mills, R. Self-diffusion in normal and heavy water in the range 1-45. deg. *J. Chem. Phys.* **77,** 685–688 (1973).

192. Apell, H.-J. & Roudna, M. Partial Reactions of the Na, K-ATPase: Determination of Activation Energies and an Approach to Mechanism. *J. Membr. Biol.* **253,** 631–645 (2020).

193. Esmann, M. & Skou, J. C. Temperature-dependencies of various catalytic activities of membrane-bound Na^+/K^+–ATPase from ox brain, ox kidney and shark rectal gland and of C12E8-solubilized shark Na^+/K^+–ATPase. *Biochim. Biophys. Acta - Biomembr.* **944,** 344–350 (1988).

194. Syková, E. & Nicholson, C. Diffusion in brain extracellular space. *Physiol. Rev.* **88,** 1277–1340 (2008).

195. Shepherd, T. M., Thelwall, P. E., Stanisz, G. J. & Blackband, S. J. Aldehyde fixative solutions alter the water relaxation and diffusion properties of nervous tissue. *Magn. Reson. Med.* **62,** 26–34 (2009).

196. Howarth, C., Gleeson, P. & Attwell, D. Updated energy budgets for neural computation in the neocortex and cerebellum. *J. Cereb. Blood Flow Metab.* **32,** 1222–1232 (2012).

197. Edwards, I. J. *et al.* Na^+/K^+–ATPase $\alpha 1$ and $\alpha 3$ isoforms are differentially expressed in α-and γ-motoneurons. *J. Neurosci.* **33,** 9913–9919 (2013).

198. Buckley, D. L. *et al.* The effect of ouabain on water diffusion in the rat hippocampal slice measured by high resolution NMR imaging. *Magn. Reson. Med.* **41,** 137–142 (1999).

199. Benveniste, H., Hedlund, L. W. & Johnson, G. A. Mechanism of detection of acute cerebral ischemia in rats by diffusion-weighted magnetic resonance microscopy. *Stroke* **23,** 746–754 (1992).

200. Lu, H., Clingman, C., Golay, X. & van Zijl, P. C. Determining the longitudinal relaxation time (T1) of blood at 3.0 Tesla. *Magn. Reson. Med.* **52,** 679–682 (2004).

201. Hernando, D., Kramer, J. H. & Reeder, S. B. Multipeak fat-corrected complex $R2^*$ relaxometry: Theory, optimization, and clinical validation. *Magn. Reson. Med.* **70,** 1319–1331 (2013).

202. Hernando, D., Levin, Y. S., Sirlin, C. B. & Reeder, S. B. Quantification of liver iron with MRI: State of the art and remaining challenges. *J. Magn. Reson. Imaging* **40,** 1003–1021 (2014).

203. Neudert, O., Stapf, S. & Mattea, C. Diffusion exchange NMR spectroscopy in inhomogeneous magnetic fields. *J. Magn. Reson.* **208,** 256–261 (2011).

204. Butler, J. P., Reeds, J. A. & Dawson, S. V. Estimating Solutions of First Kind Integral Equations with Nonnegative Constraints and Optimal Smoothing. *SIAM J. Numer.* **18,** 381–397 (1981).

205. Su, G. *et al.* Improved Butler-Reeds-Dawson Algorithm for the Inversion of Two-Dimensional NMR Relaxometry Data. *Math. Probl. Eng.* **2019,** 1–11 (2019).

206. Ohkubo, T. *Open Source 1D/2D Inverse Laplace Program* in *Bulletin of the Nuclear Magnetic Resonance Society of Japan* **9** (2018), 92–98.

207. Nicholson, C. & Hrabětová, S. Brain Extracellular Space: The Final Frontier of Neuroscience. *Biophys. J.* **113,** 2133–2142 (2017).

208. Verkman, A. S., Smith, A. J., Phuan, P., Tradtrantip, L. & Anderson, M. O. The aquaporin-4 water channel as a potential drug target in neurological disorders. *Expert Opin. Ther. Targets* **21,** 1161–1170 (2017).

209. Lasič, S., Lundell, H., Topgaard, D. & Dyrby, T. B. Effects of imaging gradients in sequences with varying longitudinal storage time—Case of diffusion exchange imaging. *Magn. Reson. Med.* **79,** 2228–2235 (2017).

210. Guilfoyle, D. N., Dyakin, V. V., O'Shea, J., Pell, G. S. & Helpern, J. A. Quantitative measurements of proton spin-lattice (T1) and spin-spin (T2) relaxation times in the mouse brain at 7.0 T. *Magn. Reson. Med.* **49,** 576–580 (2003).

211. Otsu, N. A Threshold Selection Method from Gray-Level Histograms. *IEEE Trans. Syst. Man. Cybern.* **9,** 62–66 (1979).

212. Callaghan, P. T., Coy, A., MacGowan, D., Packer, K. J. & Zelaya, F. O. Diffraction-like effects in NMR diffusion studies of fluids in porous solids. *Nature* **351,** 467–469 (1991).

213. Mair, R. *et al.* The Narrow Pulse Approximation and Long Length Scale Determination in Xenon Gas Diffusion NMR Studies of Model Porous Media. *J. Magn. Reson.* **156,** 202–212 (2002).

214. Tourdias, T. *et al.* Aquaporin 4 correlates with apparent diffusion coefficient and hydrocephalus severity in the rat brain: A combined MRI–histological study. *NeuroImage* **47,** 659–666 (2009).

215. Debaker, C., Djemai, B., Ciobanu, L., Tsurugizawa, T. & Bihan, D. L. Diffusion MRI reveals in vivo and non-invasively changes in astrocyte function induced by an aquaporin-4 inhibitor. *PLoS One* **15,** e0229702 (2020).

216. Urushihata, T. *et al.* Exploring cell membrane water exchange in aquaporin-4-deficient ischemic mouse brain using diffusion-weighted MRI. *Eur. Radiol. Exp.* **5** (2021).

217. Gomolka, R. S. *et al.* Loss of aquaporin-4 results in glymphatic system dysfunction via brain-wide interstitial fluid stagnation. *eLife* **12** (2023).

218. Parsons, E. C., Does, M. D. & Gore, J. C. Modified oscillating gradient pulses for direct sampling of the diffusion spectrum suitable for imaging sequences. *Magn. Reson. Imaging* **21,** 279–285 (2003).

219. Zielinski, L. J. & Hürlimann, M. D. Short-time restricted diffusion in a static gradient and the attenuation of individual coherence pathways. *J. Magn. Reson.* **171,** 107–117 (2004).

220. Zielinski, L. J. & Hürlimann, M. D. Probing short length scales with restricted diffusion in a static gradient using the CPMG sequence. *J. Magn. Reson.* **172,** 161–167 (2005).

221. Lasič, S., Stepišnik, J. & Mohorič, A. Displacement power spectrum measurement by CPMG in constant gradient. *J. Magn. Reson.* **182,** 208–214 (2006).

222. Gore, J. C. *et al.* Characterization of tissue structure at varying length scales using temporal diffusion spectroscopy. *NMR Biomed.* **23,** 745–756 (2010).

223. Stepišnik, J., Mohorič, A., Serša, I. & Lahajnar, G. Analysis of Polymer Dynamics by NMR Modulated Gradient Spin Echo. *Macromol. Symp.* **305,** 55–62 (2011).

224. Baron, C. A. & Beaulieu, C. Oscillating gradient spin-echo (OGSE) diffusion tensor imaging of the human brain. *Magn. Reson. Med.* **72,** 726–736 (2013).

225. Xu, J. Probing neural tissues at small scales: Recent progress of oscillating gradient spin echo (OGSE) neuroimaging in humans. *J. Neurosci. Methods* **349,** 109024 (2021).

226. Goelman, G. & Prammer, M. The CPMG Pulse Sequence in Strong Magnetic Field Gradients with Applications to Oil-Well Logging. *J. Magn. Reson.* **113,** 11–18 (1995).

227. Hürlimann, M. D. & Griffin, D. D. Spin dynamics of Carr–Purcell–Meiboom–Gill-like sequences in grossly inhomogeneous B0 and B1 fields and application to NMR well logging. *J. Magn. Reson.* **143,** 120–135 (2000).

228. Zielinski, L. J. & Sen, P. N. Combined effects of diffusion, nonuniform-gradient magnetic fields, and restriction on an arbitrary coherence pathway. *J. Chem. Phys.* **119,** 1093–1104 (2003).

229. Song, Y.-Q. Categories of Coherence Pathways for the CPMG Sequence. *J. Magn. Reson.* **157,** 82–91 (2002).

230. Hürlimann, M. D. Optimization of timing in the Carr-Purcell-Meiboom-Gill sequence. *Magn. Reson. Imaging* **19,** 375–378 (2001).

231. Ross, A., Czisch, M. & King, G. Systematic Errors Associated with the CPMG Pulse Sequence and Their Effect on Motional Analysis of Biomolecules. *J. Magn. Reson.* **124,** 355–365 (1997).

232. Serša, I., Bajd, F. & Mohorič, A. Effects of off-resonance spins on the performance of the modulated gradient spin echo sequence. *J. Magn. Reson.* **270,** 77–86 (2016).

233. Song, Y.-Q. Multiple modulation multiple echoes: A one-shot method. *Magn. Reson. Imaging* **23,** 301–303 (2005).

234. Sigmund, E. E., Cho, H. & Song, Y.-Q. Multiple-modulation-multiple-echo magnetic resonance. *Concepts Magn. Reson., Part A* **30A,** 358–377 (2007).

235. D'Errico, J. D. *SLM - Shape Language Modeling* (ed MATLAB Central File Exchange) 2017. `https://www.mathworks.com/matlabcentral/fileexchange/24443-slm-shape-language-modeling` (2020).

236. Suh, K.-J. *et al.* Water self-diffusion behavior in yeast cells studied by pulsed field gradient NMR. *Biophys. Chem.* **104,** 121–130 (2003).

237. Mazur, W. & Krzyżak, A. T. Attempts at the Characterization of In-Cell Biophysical Processes Non-Invasively—Quantitative NMR Diffusometry of a Model Cellular System. *Cells* **9,** 2124 (Sept. 2020).

238. Karunanithy, G. *et al.* INDIANA: An in-cell diffusion method to characterize the size, abundance and permeability of cells. *J. Magn. Reson.* **302,** 1–13 (2019).

239. Uhlenbeck, G. E. & Ornstein, L. S. On the Theory of the Brownian Motion. *Phy. Rev.* **36,** 823–841 (1930).

240. Ning, L., Westin, C.-F. & Rathi, Y. Estimation of Bounded and Unbounded Trajectories in Diffusion MRI. *Front. Neurosci.* **10** (2016).

241. Li, Z. *et al.* The direction-dependence of apparent water exchange rate in human white matter. *NeuroImage* **247,** 118831 (2022).

242. Li, X., Bai, Y., Liao, Y. & Xin, S. X. Assessment of the effects of mimicking tissue microstructural properties on apparent diffusion coefficient and apparent exchange rate in diffusion MRI via a series of specially designed phantoms. *Magn. Reson. Med.* **87,** 292–301 (2021).

243. Schillmaier, M., Kaika, A., Topping, G. J., Braren, R. & Schilling, F. Repeatability and reproducibility of apparent exchange rate measurements in yeast cell phantoms using filter-exchange imaging. *MAGMA,* 1–18 (2023).